

JAERI-M

88-086

A CONCEPTUAL DESIGN OF  
A NEGATIVE-ION-GROUNDED ADVANCED  
TOKAMAK REACTOR  
—— NAVIGATOR (FER) ——

May 1988

Shin YAMAMOTO, Yoshihiro OHARA, Keiji TANI, Satoshi NISHIO  
Yoshikazu OKUMURA, Masanori ARAKI, Masafumi AZUMI, R.S. DEVOTO\*<sup>1</sup>  
Noboru FUJISAWA, Shigehisa HITOKI\*<sup>2</sup>, Tsutomu HONDA, Tomoyoshi HORIE  
Hiroshi HORIIKE, Takashi INOUE, Takeshi KOBAYASHI, Mika MASUZAWA\*<sup>3</sup>  
Shinzaburo MATSUDA, Nobuharu MIKI, Makoto MIZUNO, Tadanori MIZOGUCHI  
Kunihiko NAKASHIMA, Masao OKAMOTO\*<sup>4</sup>, Kunihiko OKANO\*<sup>5</sup>, Ryusei SAITO  
Yasushi SEKI, Kiyoshi SHIBANUMA, Yasuo SHIMOMURA, Kichiro SHINYA  
Masayoshi SUGIHARA, Katsuhiro TACHIKAWA, Shigeru TADO\*<sup>2</sup>  
Shigeru TANAKA, Tatsuzo TONE, Taisei UEDE\*<sup>6</sup>, Kazuhiro WATANABE  
Masao YAMADA and Hiromasa IIDA

JAERI-Mレポートは、日本原子力研究所が不定期に公刊している研究報告書です。  
入手の問合わせは、日本原子力研究所技術情報部情報資料課（〒319-11 茨城県那珂郡東海村）あて、  
お申しこしください。なお、このほかに財団法人原子力弘済会資料センター（〒319-11 茨城県那珂郡  
東海村日本原子力研究所内）で複写による実費領布をおこなっております。

JAERI-M reports are issued irregularly.  
Inquiries about availability of the reports should be addressed to Information Division Department  
of Technical Information, Japan Atomic Energy Research Institute, Tokaimura, Naka-gun, Ibaraki-  
ken 319-11, Japan.

© Japan Atomic Energy Research Institute, 1988

編集兼発行 日本原子力研究所  
印刷 日青工業株式会社

A Conceptual Design of  
a Negative-Ion-Grounded Advanced Tokamak Reactor  
- NAVIGATOR\* (FER) -

Shin YAMAMOTO, Yoshihiro OHARA<sup>+1</sup>, Keiji TANI<sup>+2</sup>, Satoshi NISHIO  
Yoshikazu OKUMURA<sup>+1</sup>, Masanori ARAKI<sup>+1</sup>, Masafumi AZUMI<sup>+2</sup>, R. S. DEVOTO<sup>\*1</sup>  
Noboru FUJISAWA<sup>+2</sup>, Shigehisa HITOKI<sup>\*2</sup>, Tsutomu HONDA, Tomoyoshi HORIE  
Hiroshi HORIIKE<sup>+2</sup>, Takashi INOUE<sup>+1</sup>, Takeshi KOBAYASHI, Mika MASUZAWA<sup>\*3</sup>  
Shinzaburo MATSUDA, Nobuharu MIKI, Makoto MIZUNO<sup>+3</sup>  
Tadanori MIZOGUCHI, Kunihiro NAKASHIMA, Masao OKAMOTO<sup>\*4</sup>, Kunihiro OKANO<sup>\*5</sup>  
Ryusei SAITO, Yasushi SEKI<sup>+2</sup>, Kiyoshi SHIBANUMA, Yasuo SHIMOMURA<sup>+2</sup>  
Kichiro SHINYA, Masayoshi SUGIHARA, Katsuhiko TACHIKAWA<sup>+2</sup>  
Shigeru TADO<sup>\*2</sup>, Shigeru TANAKA<sup>+1</sup>, Tatsuzo TONE<sup>+4</sup>, Taisei UEDE<sup>\*6</sup>  
Kazuhiro WATANABE<sup>+1</sup>, Masao YAMADA and Hiromasa IIDA

Fusion Experimental Reactor Team  
Naka Fusion Research Establishment, JAERI

(Received April 12, 1988)

The NAVIGATOR concept is based on the negative-ion-grounded 500 keV 20 MW neutral beam injection system (NBI system), which has been proposed and studied at JAERI. The NAVIGATOR concept contains two categories; one is the NAVIGATOR machine as a tokamak reactor, and the other is the NAVIGATOR philosophy as a guiding principle in fusion research. The NAVIGATOR machine implies an NBI heated and full inductive ramped-up reactor. The NAVIGATOR concept should be applied in a phased approach to and beyond the operating

---

\* NAVIGATOR (NegAtive-Ion-Grounded Advanced Tokamak Reactor)

- +1 Department of Thermonuclear Fusion Research
- +2 Department of Large Tokamak Research
- +3 Department of JT-60 Facility
- +4 Office of Planning
- \*1 Lawrence Livermore National Laboratory
- \*2 Mitsubishi Fusion Center
- \*3 Northwestern University
- \*4 Institute of Plasma Physics, Nagoya University
- \*5 Toshiba Corporation
- \*6 Hitachi, Ltd.

goal for the FER (Fusion Experimental Reactor, the next generation tokamak machine in Japan). The mission of the FER is to realize self-ignition and a long controlled burn of about 800 seconds and to develop and test fusion technologies, including the tritium fuel cycle, superconducting magnet, remote maintenance and breeding blanket test modules.

The NAVIGATOR concept is composed of three major elements, that is, reliable operation scenarios, reliable maintainability and sufficient flexibility of the reactor. The NAVIGATOR concept well supports the ideas of phased operation and phased construction of the FER, which will result in the reduction of technological risk.

The NAVIGATOR concept is expected to bring forth the fruits growing up in the present large tokamak machines in the form of next generation machines. In addition, the NAVIGATOR concept will supply many required databases for the DEMO reactor.

The details of the NAVIGATOR concept is described in this paper, and the concept may indicate a feasible strategy for developing fusion research.

Keywords: Guiding Principle, NAVIGATOR Concept, Conceptual Design, Negative-Ion-Grounded, FER, Next Generation Tokamak Machines, Operation Scenarios, Reliability, Maintainability, Flexibility, Phased Operation, Phased Construction, DEMO Reactor

負イオンビーム・システムに基づいた先進トカマク炉の  
概念設計  
— NAVIGATOR (FER) —

那珂研究所核融合実験炉特別チーム

山本 新・小原祥裕<sup>+1</sup>・谷 啓二<sup>+2</sup>・西尾 敏  
奥村義和<sup>+1</sup>・荒木政則<sup>+1</sup>・安積正史<sup>+2</sup>・R.S.DEVOTO<sup>\*1</sup>  
藤沢 登<sup>+2</sup>・一木繁久<sup>\*2</sup>・本田 力・堀江知義  
堀池 寛<sup>+2</sup>・井上多加志<sup>+1</sup>・小林武司・増沢美佳<sup>\*3</sup>  
松田慎三郎・三木信晴・水野 誠<sup>+3</sup>・溝口忠憲  
中島国彦・岡本正雄<sup>\*4</sup>・岡野邦彦<sup>\*5</sup>・斉藤龍生  
関 泰<sup>+2</sup>・柴沼 清・下村安夫・新谷吉郎  
杉原正芳・立川克浩<sup>+2</sup>・田戸 茂<sup>\*2</sup>・田中 茂<sup>+1</sup>  
東稔達三<sup>+4</sup>・上出泰生<sup>\*6</sup>・渡辺和弘<sup>+1</sup>・山田政男  
飯田浩正

( 1988 年 4 月 12 日受理 )

NAVIGATOR 概念は、原研で提案され、研究が進められている 500 KeV, 20 MW の中性粒子入射 ( NBI ) システムに基礎を置いている。NAVIGATOR 概念は、2 つのカテゴリーを包含する；一方は、トカマク装置としての NAVIGATOR machine であり、他方は、核融合研究における指導原理 ( guiding principle ) としての NAVIGATOR

---

那珂研究所：〒311-01 茨城県那珂郡那珂町大字向山 801-1

+ 1 核融合研究部

+ 2 臨界プラズマ研究部

+ 3 JT-60 試験部

+ 4 企画室

\* 1 ローレンスレヴェアモア国立研究所

\* 2 三菱核融合センター

\* 3 ノースウェスタン大学

\* 4 名古屋大学プラズマ研究所

\* 5 ㈱東芝

\* 6 ㈱日立製作所

philosophy である。NAVIGATOR machine は自己点火条件を得るための加熱手段としてはNBI加熱を用い、電流立上げとしては、完全誘導立上げが可能な炉を意味する。NAVIGATOR 概念は、日本の次期大型装置であるFERのミッション達成のための一つの方法論を提示している。FERのミッションは、800 秒の長時間にわたって制御された自己点火プラズマの実現および、核融合炉技術の開発を行なうことにある。核融合炉システムの開発の中には、トリチウム循環システム、超電導コイル、遠隔操作技術および増殖ブランケットのテスト・モジュールを含む。

NAVIGATOR 概念は、主要な三つの要素から構成されている。すなわち、その炉において信頼できるオペレーション・シナリオが描けること、信頼できる分解保守修理が保証されていること、十分なフレキシビリティが確保されているということである。NAVIGATOR概念は、FERでの段階的運転（phased operation）や段階的建設（phased construction）の考え方をよく助ける。それはとりもなおさず技術的なリスクの軽減へとつながる。

本論文において、NAVIGATOR 概念の詳細を述べる。それにより、この概念が核融合研究の発展のための実行可能な戦略を与えていることがわかる。

## Contents

1. Introduction .....	1
2. Overview of the NAVIGATOR Concept .....	5
2.1 The NAVIGATOR Philosophy as a Guiding Principle .....	5
2.2 The NAVIGATOR Machine as a Tokamak Reactor .....	12
3. Operation Scenario .....	20
3.1 Model of Calculation for Beam Driven Current .....	21
3.2 Current Profile Control .....	29
3.3 Self-Consistent Plasma Profile of Beam Driven High $\beta$ Plasma .....	33
3.3.1 Calculational Procedure .....	33
3.3.2 Calculated Results .....	34
3.4 Current Ramp-Up Operation .....	37
3.4.1 Simulation Model and Formulation .....	37
3.4.2 Current Ramp-Up under $\beta_T$ and $\beta_p$ Limitations .....	40
3.4.3 Full Non-Inductive Current Ramp-Up .....	42
3.5 Quasi-Steady State Operation .....	47
3.6 Cold and Dense Divertor Plasma during Non-Inductive Current Ramp-Up and Quasi-Steady State Operation .....	50
3.6.1 Calculational Procedure .....	50
3.6.2 Calculated Results .....	53
3.7 Steady State Operation .....	57
3.7.1 Steady State Operation for Next Generation Tokamak .....	57
3.7.2 Steady State Operation for Power Reactor .....	57
3.8 Bootstrap Current Effect .....	63
3.9 Plasma Rotation Effect .....	69
3.10 Summary .....	72
4. A 500 keV/20 MW Negative-Ion-Grounded Neutral Beam Injection System .....	74
4.1 Beam Line Design .....	74
4.2 Major Components of Beam Line System .....	78
4.2.1 Ion Source .....	78
4.2.2 Beam Profile Controller .....	80
4.2.3 Neutralizer .....	81
4.2.4 Ion Dump .....	83

4.2.5 Cryopump .....	83
4.2.6 Power Supply System .....	84
4.3 Summary .....	85
5. Reactor Design .....	95
5.1 Mission of Next Generation Tokamak (FER) .....	95
5.2 Location of Beam Line System .....	99
5.3 Injection Port and Shine-through Armor Plate .....	105
5.3.1 Structural Concepts of Injection Port and Shine-through Armor Plate .....	105
5.3.2 Thermal and Erosion Estimations of Shine-through Armor Plate .....	106
5.4 Neutron Shield Structure .....	112
5.4.1 Calculational Model .....	112
5.4.2 Calculational Procedure .....	113
5.4.3 Results .....	113
5.5 Tritium Processing System for Ion Source Room and Ion Dump Room .....	121
5.5.1 Operation Scenario and Mass Flows .....	121
5.5.2 Gas Handling Conditions .....	123
5.5.3 Selection of Gas Handling Scenario .....	124
5.6 Summary .....	131
6. Discussion and Conclusions .....	132
Acknowledgements .....	135
References .....	137
Appendices .....	142
A. 1 Confinement Scaling Law and H-Mode Phenomenon .....	142
A. 2 Overall Efficiency of Heating and Current Drive Facilities .....	160
A. 3 Present Status of Negative Ion Source Development .....	164
A. 4 Beam Divergence in a Volume Negative Ion Source .....	171
A. 5 Analytic Expression of Beam-Driven Ion Current .....	172
A. 6 Toroidal Equilibrium with Non-Inductive Current Drive .....	177
A. 7 High Heat Flux Components .....	180

## 目 次

1. 序 言 .....	1
2. NAVIGATOR 概念の概説 .....	5
2.1 指導原理としてのNAVIGATOR philosophy .....	5
2.2 トカマク装置としてのNAVIGATOR machine .....	12
3. オペレーション・シナリオ .....	20
3.1 ビーム駆動電流に対する計算モデル .....	21
3.2 電流分布制御 .....	29
3.3 ビーム電流駆動 高 $\beta$ plasma の自己無撞着のプラズマ分布 .....	33
3.3.1 計算方法 .....	33
3.3.2 計算結果 .....	34
3.4 電流立上げオペレーション .....	37
3.4.1 シミュレーション・モデル及び定式化 .....	37
3.4.2 $\beta_T$ と $\beta_P$ 制限のもとでの電流立上げ .....	40
3.4.3 完全非誘導電流立上げ .....	42
3.5 準定常オペレーション .....	47
3.6 非誘導電流立上げ及び再充電オペレーション時での 低温・高密度ダイバータ・プラズマ .....	50
3.6.1 計算方法 .....	50
3.6.2 計算結果 .....	53
3.7 定常運転 .....	57
3.7.1 次期装置に対する定常運転 .....	57
3.7.2 動力炉に対する定常運転 .....	57
3.8 ブート・ストラップ電流効果 .....	63
3.9 プラズマ回転効果 .....	69
3.10 要 約 .....	72
4. 500 KeV / 20MW 負イオン源中性粒子入射システム .....	74
4.1 ビーム・ライン設計 .....	74
4.2 ビーム・ライン システムの主コンポーネント .....	78
4.2.1 イオン源 .....	78
4.2.2 電流分布制御装置 .....	80
4.2.3 中性化セル .....	81
4.2.4 イオン・ダンプ .....	83

4.2.5	クライオ・ポンプ .....	83
4.2.6	電力供給系 .....	84
4.2.7	要 約 .....	85
5.	炉 設 計 .....	95
5.1	次期装置 ( FER ) のミッション .....	95
5.2	ビーム・ライン・システムの位置 .....	99
5.3	入射ポートおよびシャイン・スルー・アーマ板 .....	105
5.3.1	入射ポートおよびシャイン・スルー・アーマ板の構造概念 .....	105
5.3.2	シャイン・スルー・アーマ板の熱およびエロージョン計算 .....	106
5.4	ニュートロン遮蔽構造 .....	112
5.4.1	計算モデル .....	112
5.4.2	計算手順 .....	113
5.4.3	結 果 .....	113
5.5	イオン源室とイオン・ダンプ室に対するトリチウム処理システム .....	121
5.5.1	オペレーション・シナリオとマス・フロー .....	121
5.5.2	ガス取扱い条件 .....	123
5.5.3	ガス取扱いシナリオの選択 .....	124
5.6	要 約 .....	131
6.	議論および結論 .....	132
謝 辞	.....	135
参考文献	.....	137
付 録	.....	142
A. 1	閉込め則とHモード現象 .....	142
A. 2	加熱電流駆動装置の全体効率 .....	160
A. 3	負イオン源開発の現状 .....	164
A. 4	負イオン源でのビーム発散 .....	171
A. 5	ビーム駆動イオン電流の解析解 .....	172
A. 6	非誘導電流駆動のトロイダル平衡 .....	177
A. 7	高熱流束コンポーネント .....	180

## 1. Introduction

Japan has few natural resources for energy and therefore depends on import for most of its energy supply. Japan is very eager to pursue the development of new energy sources by fusion. The Atomic Energy Committee (ACE) set up a division for nuclear fusion research in 1958 under the chairmanship of the late Professor Hideki Yukawa, Nobel Prize winner in Physics, which division began to inquire into the general direction that the scientific activities within ACE might take. Thus the Institute of Plasma Physics (IPP) was established at Nagoya University in 1961, with Koji Hushimi as director, as the center of cooperative research activities throughout the country. In the mid-1970s, the AEC decided to proceed with fusion R&D as a national project and authorized the construction of a "large-tokamak project" (JT-60) at the Japan Atomic Energy Research Institute (JAERI). In parallel with the decision of constructing the JT-60, the importance of tokamak alternatives was also recognized, and specific developmental projects on hot plasma were initiated in the university sector as extensions of past individual achievements, in addition to those at the IPP, Nagoya University. Those include the heliotron project (D, DM and E devices) at Kyoto University, the inertial confinement fusion project (glass-laser GEKKO series, CO<sub>2</sub>-laser LEKKO series, and light-ion beam REIDEN series) at Osaka University, and the tandem-mirror project (GAMMA 6 and 10) at The University of Tsukuba. More recently, the new-laser development project at the University of Electro-communications, the high-field (superconducting) tokamak project at Kyushu University, and others have also been initiated. Many Japanese contributions to fusion research have been made, and may be found in the proceedings of the International Conference on Plasma Physics and Controlled Nuclear Fusion Research under the auspices of the International Atomic Energy Agency (IAEA). Especially, during this decade, significant progress has been done in the tokamak field, using JFT-2a (DIVA), JFT-2, JFT-2M at JAERI, D-III (JAERI) at GA technology and JIPP-T2/T2U at IPP, and many original works have been made at JAERI in the physics field and engineering field. These works resulted in the success of the JT-60 project.

The JT-60 experiment started in April 1985. The net period of the experiment was one year because of the installations of heating devices, diagnostics, armor plates and so on. The following successful results were obtained not only in the physics field but also engineering field.

- 1) Impurity, particle and heat fluxes are successfully controlled under the condition of a the maximum power input of 30 MW and a maximum energy input of 80 MJ.
- 2) The wall conditioning technique is well developed and several tens hours are sufficient for wall conditioning not only for the metallic wall but also for the graphite wall. A wide range of averaged plasma densities of  $\bar{n}_e = (1 - 120) \times 10^{18} \text{ m}^{-3}$  is obtained.
- 3) Stable discharges of 3.23 MA plasma current with a safety factor  $q_\psi = 2.2$  are obtained by saving the flux swing using lower hybrid (LH) current drive and by stabilizing the  $m/n = 3/1$  kink like mode by neutral beam injection (NBI) heating.
- 4) A maximum stored energy of 3.1 MJ is obtained by NBI of about 20 MW and an energy confinement time of 0.18 - 0.15 sec is obtained using 20 MW NBI power in hydrogen discharges.
- 5) A plasma current of 2 MA was driven by the lower hybrid current drive (LHCD) and the efficiency, defined as  $\eta = \bar{n}_e [10^{20} \text{ m}^{-3}] R [\text{m}] I_{CD} [\text{MA}] / P_{AD} [\text{MW}]$ , is very high, e.g. 0.1 - 0.17 in the case without additional heating and 0.2 - 0.28 with NBI heating.
- 6) Electron heating up to 6 keV is obtained only by lower hybrid range of frequency (LHRF) heating.
- 7) Injected high energy ions by NB is effectively heated by ICRF with the second harmonic.
- 8) Several possibilities of improving confinement are demonstrated, e.g. H-mode transitions in diverted and non diverted discharges with NBI, NBI+LH or NBI+ICRF (ion cyclotron range of frequencies), improvement of energy confinement time by controlling the current profile with LHCD, improvement of the energy multiplication factor  $Q$  value and confinement of high energy ions by simultaneous heating of NBI and ICRF.

- 9) The maximum power input of NBI was obtained after only twenty days net operation. 20 MW x 5 sec. injections are routinely obtained from 28 ion sources after several conditioning shots.
- 10) The maximum total heating power of 30 MW including NBI, ICRF and LH was obtained one year after the installation without many special tokamak discharges for aging.

Beyond the present, we are planning to go forward to the next step of fusion power development. A committee to review the basic issues in fusion development was composed under the Nuclear Fusion Council and has discussed the mission and guidelines for the next step after JT-60. According to the internal report of the review subcommittee in February 1986, the next major device, which employs tokamak confinement, aims at achieving self-ignited, long-burn DT plasma and related technology to demonstrate the engineering feasibility of nuclear fusion as a power reactor.

As already mentioned, significant progress has been made in fusion research during this decade. The success of a big project depends not only on personal abilities but also especially on the budget owing to scientific policy. There are sufficient human resources in Japan. Thus, remarkable progress will be expected during the next decade, if the budget is enough. The next step project will need a long term and much money compared with that of the JT-60 project. In order to make the design of the next generation machine attractive, sufficient innovative ideas should be adopted. At the same time, the design should be based on the present databases. In order to reconcile the differences between innovative ideas and realistic ideas, we proposed the NAVIGATOR concept. The NAVIGATOR concept is based on the negative-ion-grounded 500 keV 20 MW neutral beam injection system (NBI system), which has been proposed and studied at JAERI. The word "NAVIGATOR" has the meaning found in O.E.D., "one who conducts explorations by sea". A boat concept plays an important role in the NAVIGATOR concept. We compare the present large tokamak machine to a pier and the innovative next generation machine to a ship. The boat is a medium, which belongs to both sides of the present large tokamak machine and the innovative next generation machine. The NAVIGATOR concept contains two categories; one is the NAVIGATOR machine as a tokamak reactor, and the other is the

NAVIGATOR philosophy as a guiding principle in fusion research. At present, the NAVIGATOR machine implies an NBI heated and full inductive ramped-up reactor. The NAVIGATOR concept is composed of three major elements, that is, reliable operation scenarios, reliable maintainability and sufficient flexibility of the reactor. The NAVIGATOR concept well supports the ideas of phased operation and phased construction of the next generation machine, which will result in the reduction of technological risk and initial cost and in the enhancement of cost benefit.

Section 2 provides a detailed description of the NAVIGATOR concept. Section 3 describes operation scenarios based on the negative-ion-grounded neutral beam injection system. Section 4 presents detailed description of a 500 keV/20 MW negative-ion-grounded neutral beam injection system. Section 5 deals with the reactor design based on the NBI system. Discussion and conclusions are given in Sec. 6.

In conclusion, we are preparing many appendices in order to bridge the gap between the physics field and engineering field. We are now constructing the dockyard for the boat belonging in common to the FER team, JT-60 experiment, operation and engineering team, JFT-2M experiment group, theory group and technological R&D groups.

## 2. Overview of the NAVIGATOR Concept

### 2.1 The NAVIGATOR Philosophy as a Guiding Principle

Japan needs nuclear fusion from the security point of view. Japan has already the JT-60, one of the three present large tokamak machines in the world. Recently, the scientific feasibility of the fusion reactor, that is, the break-even condition, has been successfully demonstrated by the JT-60. The result is encouraging in promoting the realization of the fusion reactor. Next, the engineering feasibility of nuclear fusion as a power reactor should be clarified as soon as possible by the next generation tokamak machine. The initiation of the project for the next generation machine tightly depends on national demand, because it takes a long term and much money compared with other scientific projects.

In order to make the design of the next generation machine attractive and cost effective, sufficient innovative ideas should be adopted. In cost estimation, not only the total cost but also the initial cost and cost benefit should be considered. Cost benefit is defined as the ratio of the sum of the evaluation of databases and know-how to the total cost. Databases consist of physics databases obtained from the self-ignited long-burn plasma, engineering databases obtained from the required neutron fluence and databases for the DEMO reactor. Know-how is obtained through the construction of the next generation tokamak machine and the operation of the machine. On the other hand, the design should be based on the present databases. In order to reconcile the difference between innovative ideas and realistic ideas, the NAVIGATOR concept has been proposed at JAERI. The NAVIGATOR concept is a guiding principle in fusion research and should be applied in a phased approach to and beyond the operating goal for the FER (Fusion Experimental Reactor, the next generation machine in Japan).

In the design of the next generation machine, the three following items should be mainly examined, that is, energy confinement time, heating method for realizing the self-ignited plasma and the first wall materials, including the divertor material. Many experimental and theoretical scaling laws of energy confinement time have been proposed (see Appendix 1). At present, no commonly accepted view on how the

tokamak confinement properties can be quantified as a function of the parameters of the plasma and of the device. Thus, it is necessary to study the effect of the scaling law on the reactor size and on the reactor concept. However, if the scaling law does not decisively affect the reactor concept, there is no problem in choosing a particular scaling law in order to design the next machine as a tentative measure. The most important thing to be considered is to study the commonly used concept for the next machine even if the reactor size is changed.

The NAVIGATOR concept is composed of three major elements, that is, reliable operation scenarios, reliable maintainability and sufficient flexibility of the reactor. In this report, the NAVIGATOR machine is shown to satisfy the above three elements.

NBI, LHRF, ICRF and ECRF (electron cyclotron range of frequencies) are candidates for the heating facility to realize a self-ignited plasma condition. H-mode confinement is obtained without exception in the NBI heated tokamak with a separatrix magnetic surface (see Appendix 1). The overall efficiency of the negative-ion-grounded NBI system is expected to become comparable with that of ICRF and much better than those of other RF facilities (see Appendix 2). This value can be improved further by employing a plasma neutralizer and/or an energy convertor system. The progress in the R&D of the negative ion source is remarkable (see Appendix 3). The negative-ion-grounded NBI system has many functions of heating, current ramp-up, transformer recharge, steady state and current profile control, as described in Section 3. However, in order to support the reliable operation scenarios, at first, only the heating function of the NBI system is demanded in the NAVIGATOR machine. That is, the NAVIGATOR machine implies an NBI heated and full-inductive ramped-up reactor. In addition, in order to support the reliable operation scenarios, low-Z material is used as plasma side material. Low z materials are preferable for the first wall material. Considering sputtering and thermo-mechanical characteristics, the carbon would be the best choice for the surface of the divertor plate. The carbon surface and its in-situ and vacuum repair are adopted in the NAVIGATOR machine. And removable carbon guard limiters are used for the protection of the vacuum chamber.

In order to realize a disruption free and self-ignited controlled long burn plasma, phased operation and phased construction are attached

great importance in the design of the FER. The phased operation consists of three phases; the first is a cold phase with hydrogen and/or deuterium discharges, in which a person can enter into the vacuum vessel of the FER, the second is a semi-hot phase with deuterium and tritium discharges in order to realize very short self-ignited plasma, in which a person can enter into the vacuum vessel after many hydrogen and/or deuterium discharges and the last is a hot phase with deuterium and tritium discharges in order to make a mission-oriented long self-ignited plasma.

Figures 2.1.1a and b show the fusion ocean without the NAVIGATOR concept and with the NAVIGATOR concept, respectively. A boat concept plays an important role in the NAVIGATOR concept. The present large tokamak machine and the next generation machine are compared to a pier and to a ship, respectively. The ship navigates across the fusion ocean in order to find out a new world DEMO, after stopping at an ignition island or steady state island. The boat is a medium, which belongs to both sides of the present large tokamak machine and the next generation machine. The boat symbolizes the phased operation and phased construction. A dockyard for the boat belonging in common to the FER team, JT-60 experiment, operation and engineering team, JFT-2M experimental group, theory group and technological R&D groups is constructed. The boat consists of four elements, that is, a hull, engine, cargo and crew. A detailed description of the elements are given in Table 2.1.1. The hull is JT-60, JT-60 up-grade or the FER flexible reactor in cold and semi-hot phases. The JT-60 up-grade well simulates the FER flexible reactor, as shown in Table 2.1.2.

In the cold phase of the NAVIGATOR machine, a simple vacuum vessel without a neutron shield, as shown in Fig. 2.1.2, will be used. The vacuum chamber should be easily exchanged without interference of the heating facility, if the negative-ion-grounded NBI system is used. The vacuum of the NBI system is maintained during the exchange of the vacuum vessel, and full power injection is possible just after the work. Thus, the NAVIGATOR machine involves the present large tokamak machine in itself and has sufficient flexibility. When well-accustomed diagnostics and simple RF launchers without a neutron shield, developed in JT-60 or JT-60 up-grade, are set up on the flexible reactor, the plasma in the cold-phase and plasma-antenna coupling will be able to be well examined,

and the databases and know-how in the cargo of the boat will become abundant. In the NAVIGATOR machine, the reference plasma configuration is a single null divertor configuration with a medium elongation of around  $\kappa = 1.7$  and triangularity of around  $\delta = 0.2$ . The vertical positional instability is expected to be well stabilized. Horizontal access for the maintenance of the movable shell, including the divertor segment, is possible. Horizontal access is reliable compared with the vertical access. In the medium elongation case, the poloidal field power supply for horizontal access is possible to be smaller than that for vertical access. In the flexible reactor, plasma parameters around the reference value will be examined, using a high elongation plasma of up to 2.0, high triangularity up to 0.3, a larger plasma size and higher plasma current. Through this examination, disruption free plasma is expected in the hot phase. The NAVIGATOR cold and semi-hot phase flexible reactor is used for the NAVIGATOR hot phase mission oriented reactor in order to make the plasma well-accustomed, except for thermal instability and to confirm the specification for the reactor components.

We can obtain information concerning the slowing down process and the ripple-loss mechanism, for high energy hydrogen and deuterium particles, in the cold phase. For example, by using the simultaneous injection of 500 keV NBI and ICRF (second harmonic ICRF heating or minority heating), information on alpha particles in the semi-hot phase and estimation of the plasma behavior of the hot phase may be obtained by using both the databases for the cold and semi-hot phases and simulation codes. Therefore, it may not be necessary any longer that the mechanical configuration of the NAVIGATOR machine be changed, after going into the hot operation. Even if the ignition condition were not realized, the NAVIGATOR concept will satisfy the technological mission of next generation tokamak machines and will supply databases for the DEMO reactor. Well-considered phased operation and phased construction will result in the reduction of technological risk and initial cost and in the enhancement of cost benefit.

Table 2.1.1 Elements of boat

Hull	JT-60. JT-60 Upgrade The FER flexible reactor in cold & semi-hot phases
Engine	Well-accustomed diagnostics Simple RF launcher Power supply system Carbon divertor Fuel injection system Evacuation system
Cargo	Databases Know-how
Crew	

Table 2.1.2 Parameters of JT-60, JT-60 up-grade and FER

	JT-60	JT-60 up-grade	FER
Plasma current	2.7 MA	6.0 MA	~ 10 MA
Input power	30 MW	40 MW	~ 50 MW
Magnetic field in the plasma	4.8 T	4.5 T	~ 5 T
Aspect ratio	3.4	3.4	~ 3.5
Position of x-point	Out side	Lower	Lower

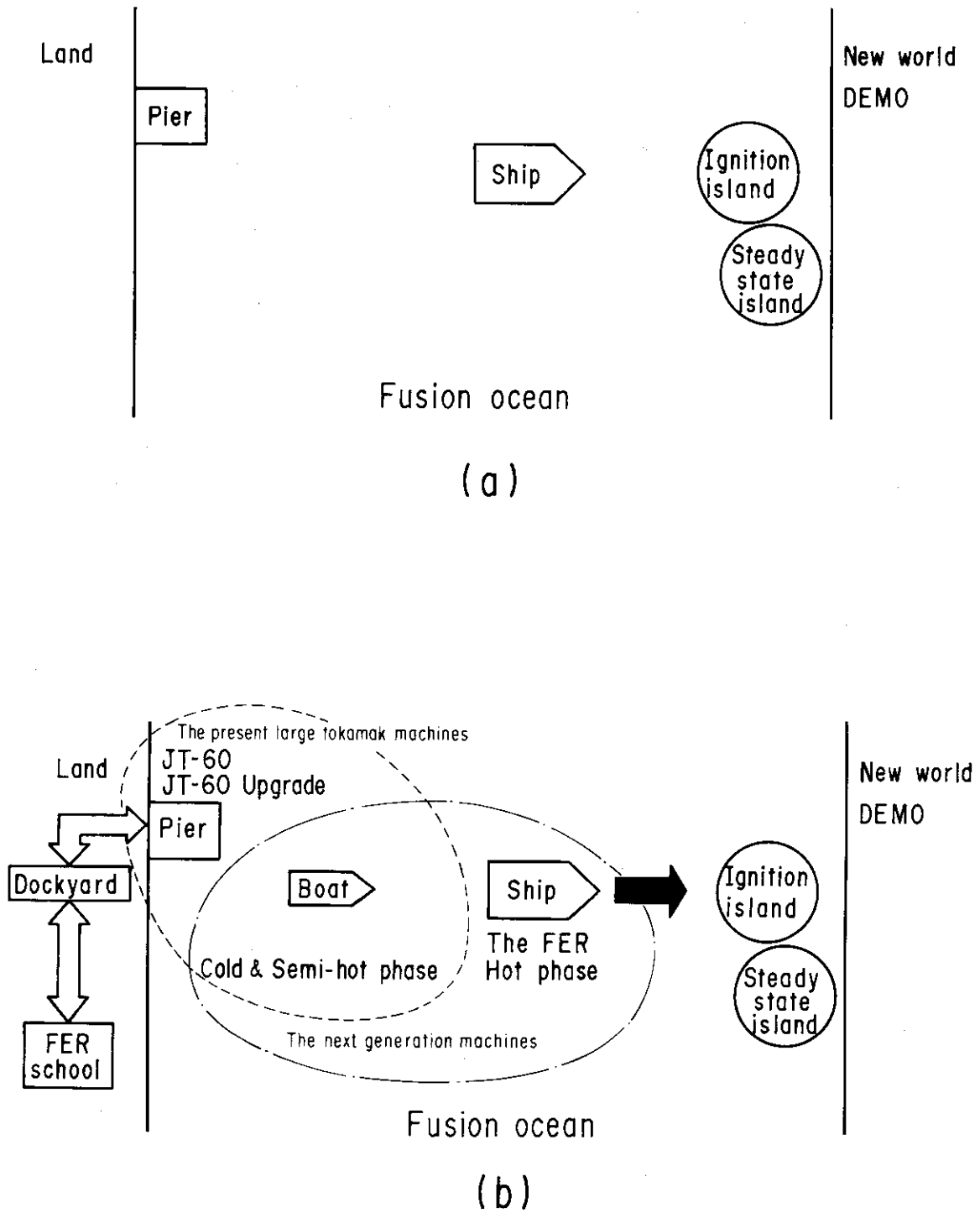


Fig. 2.1.1 Fusion ocean; (a) without the NAVIGATOR concept, (b) with the NAVIGATOR concept

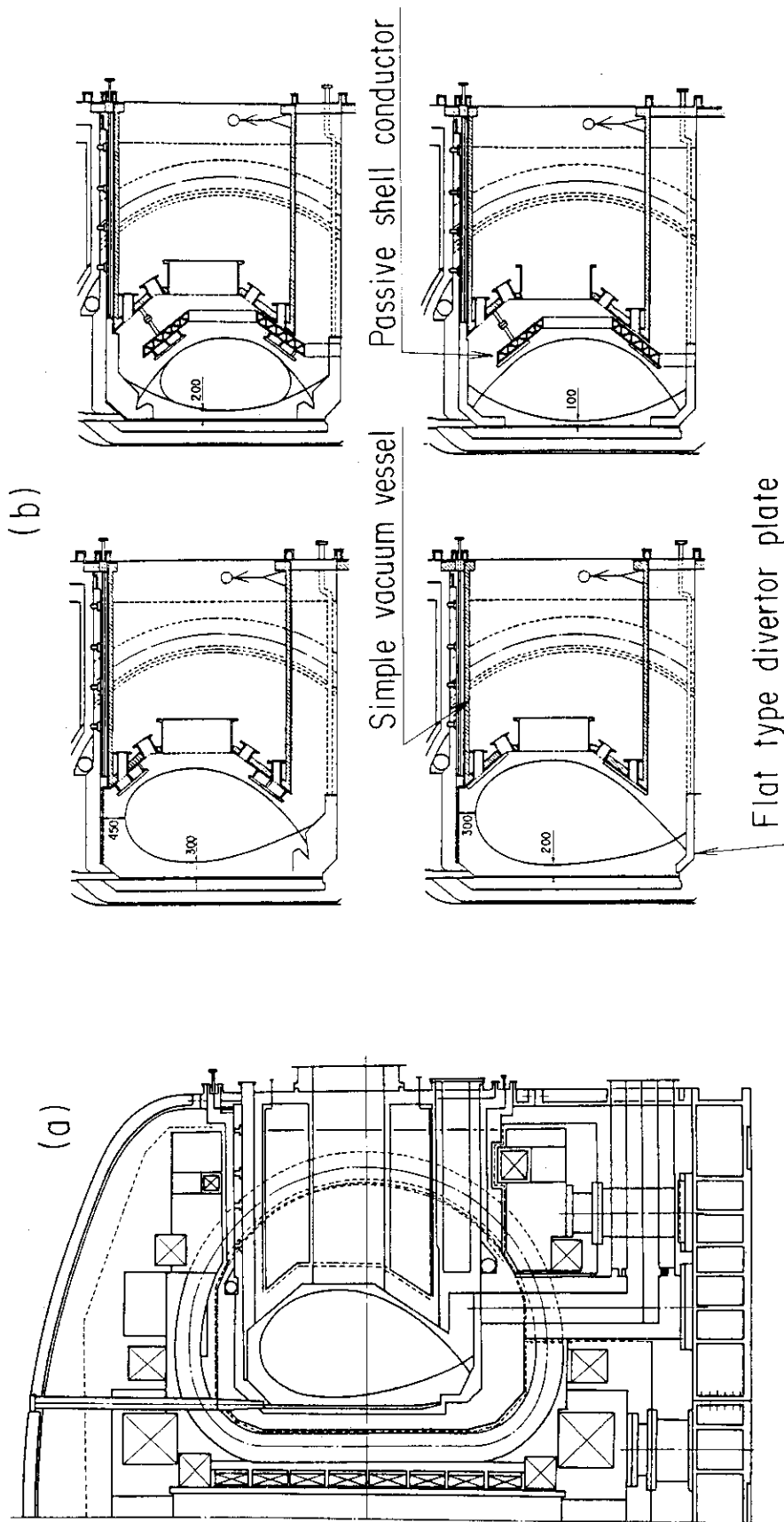


Fig. 2.1.1.2 Phased operation and phased construction of the reactor (a) Hot phase reactor (b) Simple vacuum vessel without neutron shield during the cold phase. During the cold phase, various types of plasma configurations are obtained by exchanging the position of the passive shell conductor and the configuration of the divertor plate including a flat type divertor plate. Notations of the hot phase reactor are shown in Fig. 2.2.2.

## 2.2 The NAVIGATOR Machine as a Tokamak Reactor

Positive-ion-based neutral beam injection technology is well established [1] and plays an important role in high power plasma heating of the JT-60 [2]. Recent experiments on the beam driven current in present large tokamaks [3,4] have increased the potentiality in applying the NBI system to the fusion reactor. These injectors utilize positive ion beams with energies up to 100 keV/nucleon. Higher beam energies are required for future fusion devices in order to realize deep beam penetration and current drive in the tokamak devices. The existing positive-ion-based injectors, however, cannot be used in such a high energy regime because of their extremely low conversion efficiency of positive ions to neutrals as shown in Fig. 2.2.1. The efficiency is below 20% at 200 keV deuterium and decreases further with beam energy. This low efficiency increases the circulating power in the system, even if an energy recovery system is used, and makes the injector system too complicated and too big to be used. The most promising method, and the only possible method, to overcome this problem is to use negative ions which have high neutralization efficiency at a high energy regime; the efficiency is higher than 60% at such energies depending on the neutralization methods, as shown in Fig. 2.2.1.

Another fundamental problem confronting the neutral beam injector is a problem on neutronics. Since the existing injector is situated near the fusion device and connected with the device through a big straight tube, the neutrons from the plasma directly hit the complex internal structure in the neutral beam system. This would not only cause serious damage of the structure but also make maintenance difficult and expensive due to induced radioactivity. In order to overcome this problem, the LBL group has proposed a TFF (transverse field focusing) beam acceleration and transport system, where the beam line has several bends to avoid direct exposure against the neutrons [5]. The proposed TFF-based neutral beam system utilizes negative ions and is able to produce 400 keV, 2 MW/m sheet beams with a high power efficiency. Another solution against the neutronics problem is to place the ion source and complex beam line components at a position far from the fusion devices and to transport the beams straightforward to a long distance through a narrow transport duct so as to minimize the solid

angle from the plasma. This was considered to be impossible in both the positive-ion-based injectors and the injectors using the negative ions produced by the process of double-charge exchange and surface conversion, because of their large beam divergences. However, recent experimental studies on negative ion sources and high energy beam extraction have shown that the negative ions produced by volume processes have a capability of realizing this concept because of good beam divergence (see Appendix A.3). Based on this prospect, a negative-ion-grounded 500 keV/20 MW neutral beam injection system, which has a long, straight beam line, has been proposed at JAERI. Applying the NBI system technology to FER represents a reasonable step from the present data base [6].

The top and side views of a negative-ion-grounded advanced tokamak reactor are shown in Fig. 2.2.2. Two beam line systems are enough for realizing a self-ignition plasma in the H-mode confinement case. Three beam line systems are prepared for the FER, considering flexibility in operation scenarios and redundancy. The NBI system consists of a beam line, a 500 keV power supply system, an evacuating system including a tritium handling system, a cooling water circulating system and auxiliary sub-systems. The beam line consists of an intense negative ion source, a beam profile controller, a long gas neutralizer, an ion beam dump, a neutron shutter, a drift duct including an injection port of the torus and a shine-through armor plate against the neutral beams into the torus. In both the ion source room and the beam dump room, cryopanel is mounted. The neutralizer and the ion source room are shielded magnetically, and the beam line is covered with neutron shields. The  $D^-$  ions are produced by a volume production method and extracted by DC acceleration. The beam energy is variable in the 200 keV to 500 keV range during the beam injection phase.

The most important feature of the NBI system is characterized by a long, slender neutralizer, which is 0.3 meter wide and 24 meters long. The required beam divergence is 0.3 deg or 5 mrad. Such a low beam divergence can be realized by using a volume  $D^-$  ion source (see Appendix A.4). The long, slender neutralizer concept results in a considerable reduction in required pumping speed and in neutron damage of the ion sources. The total pumping speed is 850 m<sup>3</sup>/s for 20 MW injection, while that for the JT-60 NBI, for example, is 1400 m<sup>3</sup>/s for 1.4 MW injection.

The neutron flux above 1 MeV is estimated to be  $10^7$  n/cm<sup>2</sup>·s at the position of the ion source insulator. The database on which to judge the performance limits of the NBI components, especially for organic materials, is poor. Concerning mechanical strength, the radiation exposure limit under  $\gamma$ -ray irradiation for epoxy may be supposed to be 1 MGy ( $10^8$  rad) or less. Then, under neutron irradiation, assuming that the irradiation limit value for mechanical life time estimation is  $10^{16}$  n/cm<sup>2</sup>, it may be expected to have a life time (operation time) of the magnitude of  $10^9$  s. But the limit value for electrical resistivity has a tendency to be reduced by a few orders of magnitude. Thus, it is desirable that the ion source insulator has enough distance from the axis to have a moderate life time. For an operation time of a magnitude of  $10^7$  s (for several years), it is expected that it will be necessary to exchange the ion source insulator only a few times. The thickness of the neutron shield for the NBI system has been estimated to satisfy a dose value of less than 2.5 mrem/hour one day after shutdown following a 2-year full power operation.

Another feature is that the poloidal magnetic field from the tokamak is used to deflect the unneutralized negative ions and reionized positive ions toward the ion dump near the injection port. Therefore, no bending magnet, which takes much space, is used in this design. The space for the ion dump room is designed to be narrow in order to make the reactor maintenance easier. In the FER case, the bore of the TF coils, set by the ripple condition of 0.75% enables a part of the first wall (removable shield) to be withdrawn by a radial straight-line motion through the access port, as shown in Fig. 2.2.3 [7]. The divertor is also segmented into 12 sectors toroidally and withdrawn by a single straight-line radial motion. The divertor segment is withdrawn without interference of the NBI system. The movable shield with the drift duct is also withdrawn, after taking off only a part of the neutron shutter, as shown in Fig. 2.2.4. Each shine-through armor plate is installed on the same movable shield for another NBI injection port, which keeps the number of ports employed by such NBI systems minimum. The shine-through armor plate is extractable while keeping vacuum condition of the reactor vacuum chamber, as shown in Fig. 2.2.5. If these design concepts are adopted, the NBI system will become more reliable, have much longer lifetime and will be more easily maintained.

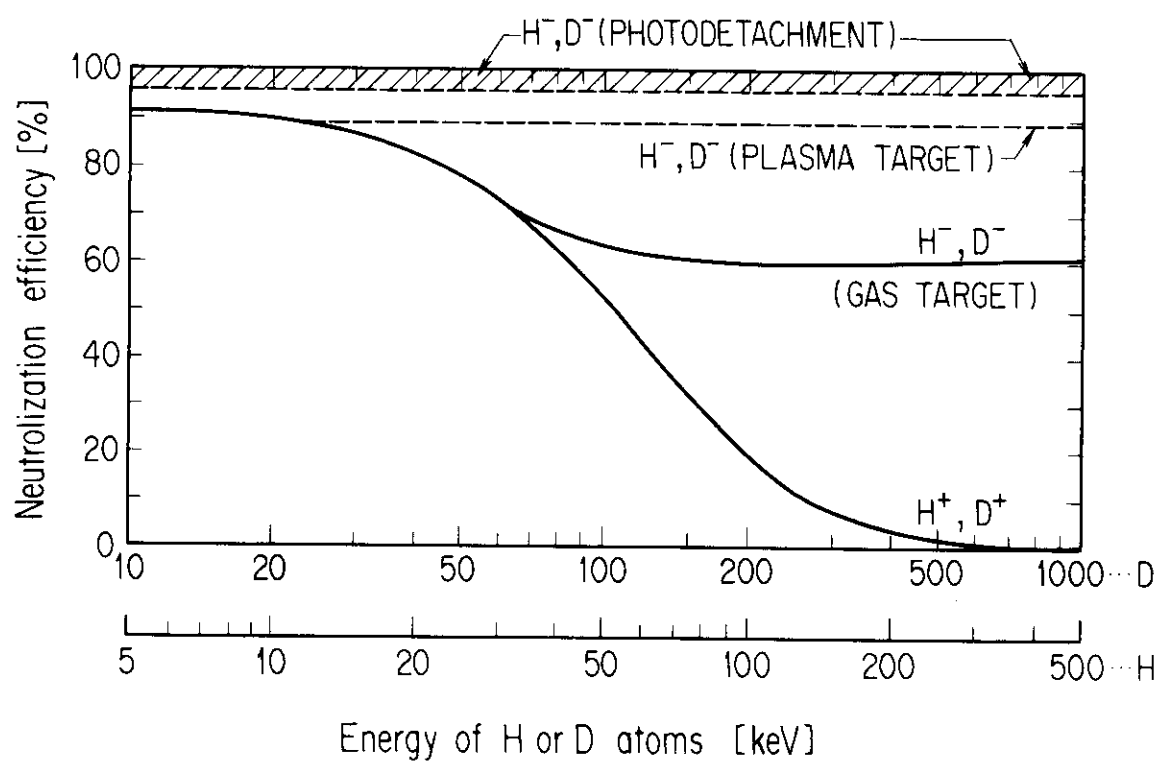


Fig. 2.2.1 Dependence of maximum neutralization efficiency on beam energy.

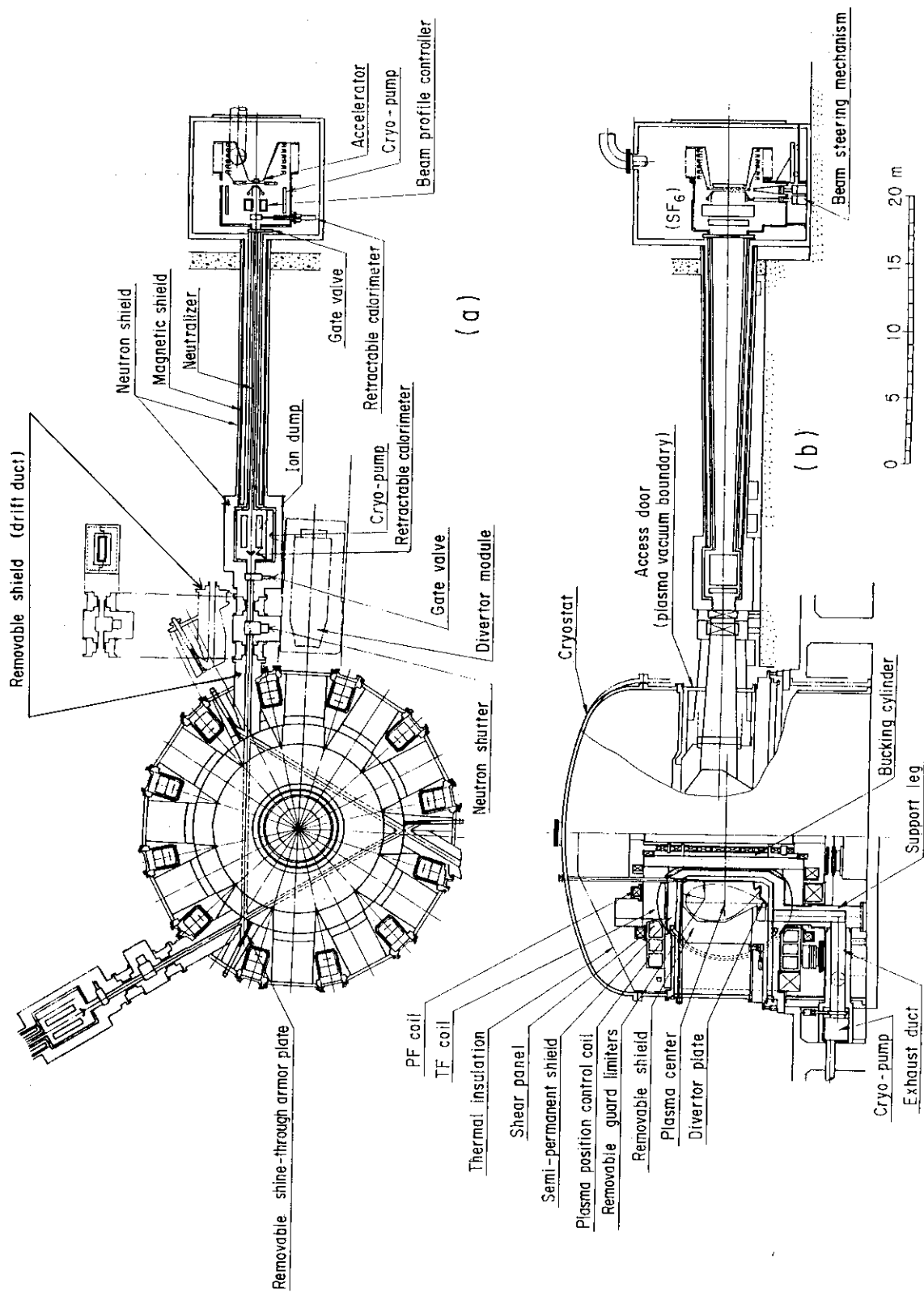


Fig. 2.2.2 Top and side view of the Negative-Ion-Grounded Advanced Tokamak Reactor

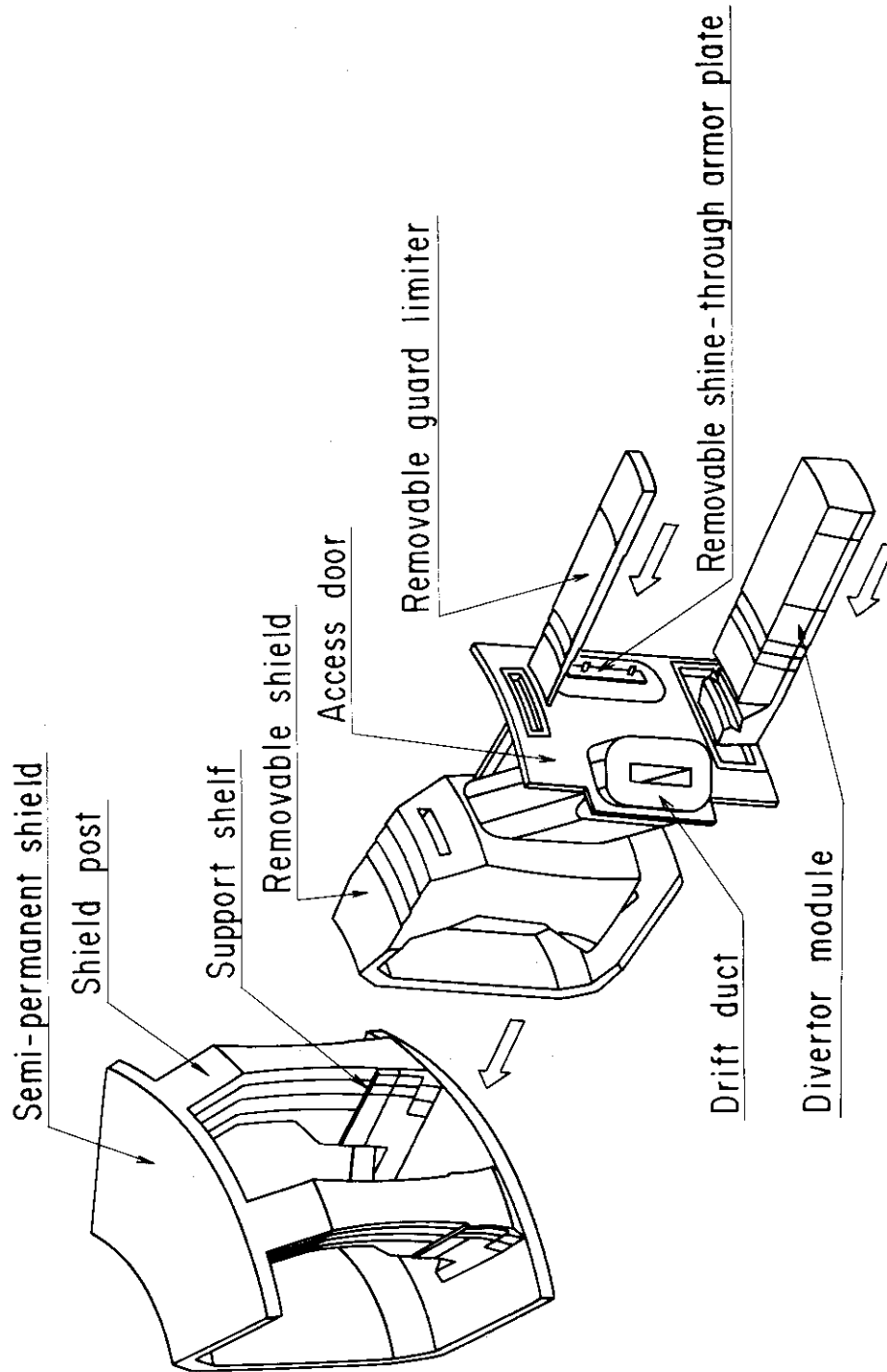


Fig. 2.2.3 Torus segmentation and structural concept of injection port, including the access door

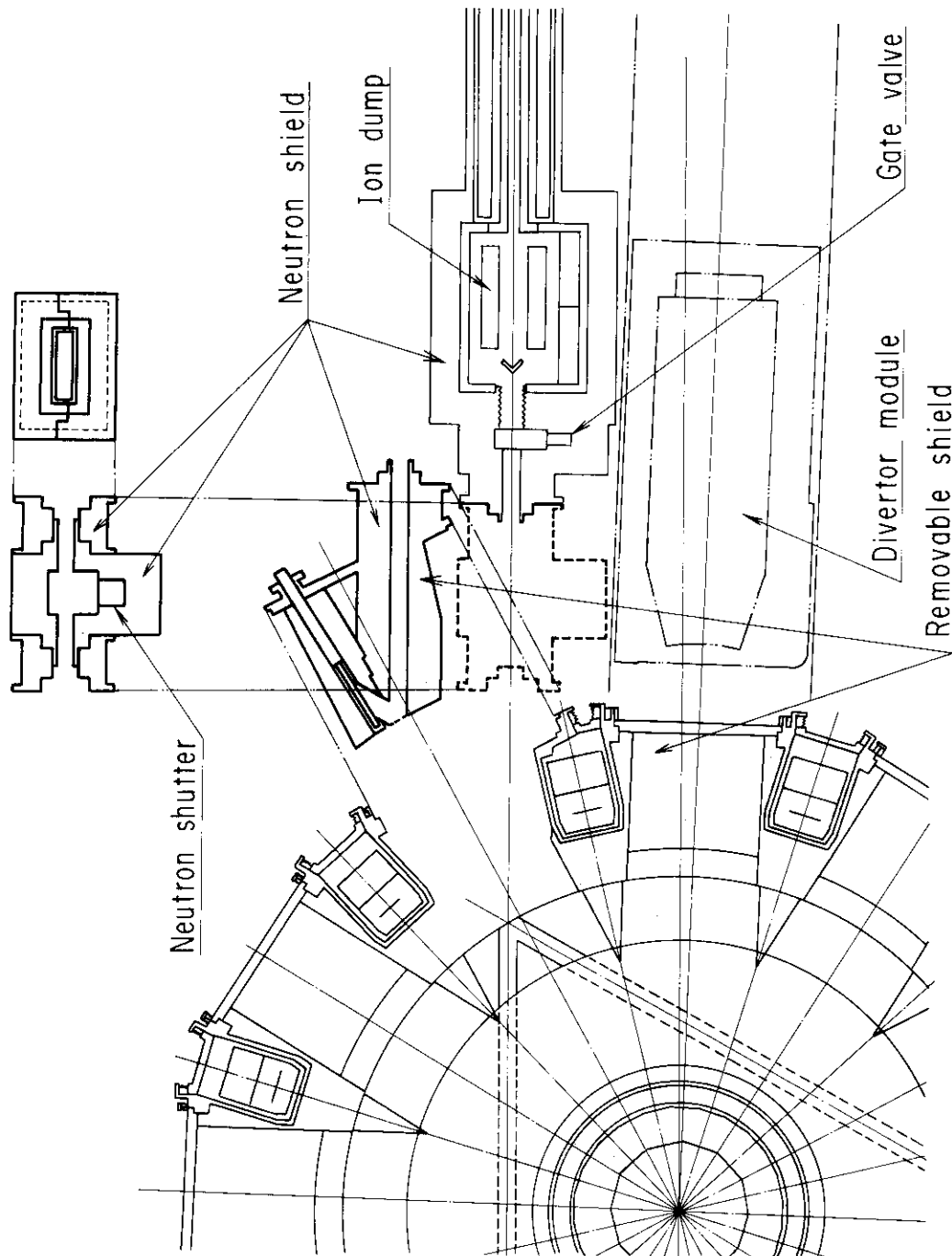


Fig. 2.2.2.4 The divertor segment is withdrawn without interference of the NBI system. The movable shield with the drift duct is also withdrawn without interference of the NBI system, after taking off only a part of the neutron shutter.

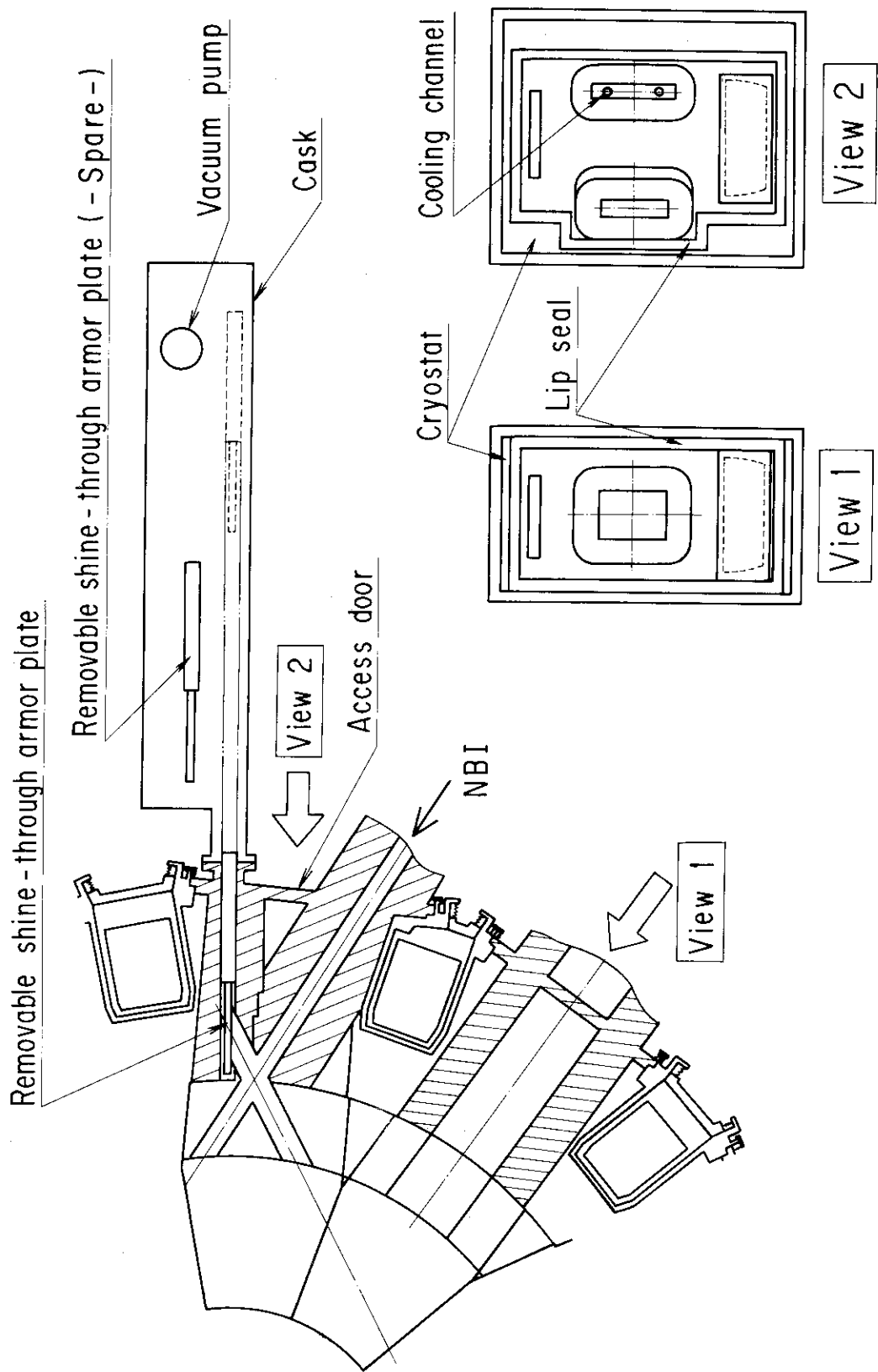


Fig. 2.2.5 Shine-through armor plate and access door

### 3. Operation Scenario

The most efficient and reliable way to drive toroidal current in a tokamak is by electromagnetic induction, using a set of external coils, including OH (ohmic) transformer coils and equilibrium coils. Thus, in the NAVIGATOR machine, a full inductive current ramp-up operation is adopted in order to make the operation reliable. This inductive operation necessitates pulsed operation, because the current in the external coils cannot be ramped indefinitely. The disadvantages of pulsed operation are discussed. It is generally believed that in a power reactor, non-inductive current ramp-up and steady state operations are necessary. The most straightforward way to overcome the problems of pulsed operation is to drive toroidal plasma current in a strictly steady-state device with externally supplied NBI particles or RF waves. More recently, it has been recognized that merely employing the non-inductive current drive technique during the current ramp-up phase of a tokamak can result in a considerable saving of volt-seconds and in a reduction of the reactor size. High  $\beta$  is also essential to reducing cost, since considerable capital is invested in the large toroidal field magnet. One key to achieving high beta in a tokamak may be the proper control of the plasma pressure and current density profiles.

In this section, tokamak reactor operation scenarios based on plasma heating, current drive and current profile control by a 500 keV/20 MW negative-ion-grounded neutral beam injection system are examined. The bootstrap current effect on the Q value and the rotation effect on current drive efficiency and plasma confinement are also examined. The negative-ion-grounded NBI system will be shown to have many functions of heating, current ramp-up, transformer recharge, steady state and current profile control. However, in order to support the reliable operation scenarios, at first, only the heating function of the NBI is demanded in the NAVIGATOR machine. That is, the NAVIGATOR machine implies an NBI heated and full inductive ramped-up reactor. Some parts of the operation scenarios have already been presented at the IAEA conference held in Kyoto [8].

### 3.1 Model of Calculation for Beam Driven Current

Ohkawa suggested the use of fast ions for current drive [9]. High-energy neutral particle beams can be injected into plasmas across a strong magnetic field. The neutral particles are converted into high-energy ions by means of charge exchange with plasma ions or ionization, as shown in Fig. 3.1.1 [10,11]. The high-energy ions running through the plasma are slowed down by Coulomb collisions with the plasma ions and electrons and the beam energy is thus transferred to the plasma. The change rate of energy  $\epsilon_b$  for a fast ion is given by

$$\frac{1}{v_b} \frac{d\epsilon_b}{dt} = - \frac{Z^2 e^4 \ln \Lambda}{8\pi \epsilon_0^2} \left[ \frac{A}{\epsilon_b} \left\{ \frac{n_i Z_i^2}{A_i} + \frac{4n_e}{3\pi^{1/2}} \left( \frac{A_e}{A} \right)^{1/2} \frac{\epsilon_b^{1/2}}{T_e^{3/2}} \right\} \right] = - \frac{\alpha}{\epsilon_b} - \beta \epsilon_b^{1/2}$$

when the beam ion's velocity  $v_b$  is much less (say 1/3) than the plasma electron thermal velocity  $(T_e/m_e)^{1/2}$  and is much larger than the plasma ion thermal velocity  $(T_i/m_i)^{1/2}$ .

The symbols  $A$ ,  $A_i$ , and  $A_e$  give the atomic weights of the injected ion, plasma ion, and electron, respectively.  $Z_b$  and  $Z_i$  are the charge states of the injected and the plasma ion. The first term on the right  $(-\alpha/\epsilon_b)$  is due to beam-ion collisions, and the second term  $(-\beta\epsilon_b^{1/2})$  is due to beam electron collisions. A critical energy  $\epsilon_{cr}$  of the beam ion, at which the plasma ion and electrons are heated at equal rates, is given by

$$\epsilon_{cr} = 15T_e \left( A^{3/2} \left\{ \frac{n_i Z_i^2}{n_e} \frac{1}{A_i} \right\} \right)^{2/3}$$

In the following, we will describe the mechanism of the beam driven current. We assumed that the energy of the injected fast ions is larger than the above mentioned critical energy. Thus, the injected beams mainly interact with the plasma electrons much more than the plasma ions. The plus direction on the coordinate is taken to be in the same direction as the fast ion velocity. It is easy for us to understand the interaction between injected fast ions and plasma electrons, using a moving coordinate with the same speed as that of the fast ions.

In a moving coordinate, the friction force is given by

$$F_1 = \frac{n_e m_e v_b}{\tau_B^{eb}},$$

where  $\tau_B^{eb}$  is the Braginskii collision time [12]. Plasma electrons are accelerated due to friction force. But these plasma electrons are decelerated due to collisions with the plasma ions. The friction force is given by

$$F_2 = - \frac{n_e m_e v_d}{\tau_B^{ei}},$$

where  $v_d$  is the electron drift velocity. A steady state is obtained in the condition of  $F_1 + F_2 = 0$ . From this relation, the following equation is derived.

$$j_e = - \frac{\tau_B^{ei}}{\tau_B^{eb}} \frac{n_e}{Z_b n_b} j_b,$$

where  $j_e$  and  $j_b$  are the beam-induced reverse electron current and beam-induced ion current and expressed as

$$j_b = n_b Z_b e v_b$$

$$j_e = -n_e e v_d.$$

Consequently, the total induced current due to the injected fast ions becomes to be

$$j_{db} = j_b + j_e = j_b \left( 1 - \frac{\tau_B^{ei}}{\tau_B^{eb}} \frac{n_e}{Z_b n_b} \right).$$

Using the following relations,

$$\tau_B^{eb} \propto \frac{1}{Z_b^2 n_b}, \quad \tau_B^{ei} \propto \frac{1}{Z_{eff} n_e},$$

where  $Z_{\text{eff}}$  is the effective charge state defined as  $Z_{\text{eff}} = \sum_i n_i Z_i^2 / n_e$ , the total induced current is reduced to the following equation.

$$j_{\text{db}} = j_b \left( 1 - \frac{Z_b}{Z_{\text{eff}}} \right)$$

Thus, in the classical description, i.e., when trapped electrons are not considered, this collisional electron current will cancel the ion current if  $Z_b = Z_{\text{eff}}$ . When trapped electron orbits are included, the electron current is reduced and  $Z_b$  need not differ from  $Z_{\text{eff}}$  in order to drive a net current. The beam driven current is estimated by

$$I_B = I_{fi} \left\{ 1 - Z_b / Z_{\text{eff}} [1 - G(Z_{\text{eff}}, \epsilon)] \right\},$$

where the trapped electron correction,  $G(Z_{\text{eff}}, \epsilon)$ , depends on the inverse aspect ratio,  $\epsilon = r/R_0$ , and on  $Z_{\text{eff}}$  [13]. The finite aspect ratio calculation [14] of  $G(Z_{\text{eff}}, \epsilon)$  is approximated by

$$G(Z_{\text{eff}}, \epsilon) \approx (1.55 + 0.85/Z_{\text{eff}}) \sqrt{\epsilon} - (0.20 + 1.55/Z_{\text{eff}}) \epsilon$$

This approximation is in error by <1% for  $1 < Z_{\text{eff}} < 3$  and  $0 \leq \epsilon < 0.2$ .

For the estimation of the beam driven current, an accurate knowledge of the fast-ion distribution function is necessary. In most of the old analytical treatments [15,16], the fast ion current induced during slowing down of the injected beams has been estimated by using an analytical solution of the non-bounce averaged Fokker-Plank equation without the energy diffusion term (see Appendix A.5). J.G. Cordey has reported that the effect of particle trapping on the distribution of fast ions in a tokamak is very important [17]. In the presence of banana trapped particles, the pitch angle of passing particles can change its sign in a time interval much shorter than in a plasma without banana particles. A precise treatment of banana particles requires that the Coulomb collision operator must be bounce averaged. The effect of energy diffusion might be important in a high temperature plasma. The effect of fast ion loss during slowing down on the beam induced current is very interesting. These problem may lead us to estimate the beam driven current by using an orbit-following Monte-Carlo code (hereafter

simply referred to as OFMC code) which can precisely describe the behavior of fast ions during slowing down.

Our OFMC code consists of four parts [18,19];

- 1) beam deposition
  - 2) simulation of Coulomb collisions,
  - 3) calculation of the guiding center orbit
- and 4) simulation of charge-exchange reactions of fast ions and succeeding reionization of fast neutrals.

One of the problems in the use of the OFMC code is that it takes a very long CPU time. For example, it takes about 2 hours to analyze the beam driven current in the FER for 2000 test particles. The OFMC code, however, may provide many important information for analyzing the beam driven current. The OFMC code is a very useful tool to analyze the slowing down process of fast ions. We have found some important effects from the comparison of the calculation results derived by the OFMC code with those by the old analytical treatment. Taking these information into consideration, we have developed a new analytical code. One is the code in which the analytical eigenfunctions of the bounce-averaged Fokker-Planck equation solved by J.G. Cordey [17] are adopted. In the other code, the eigenfunctions of the Fokker-Planck equation are numerically derived by using a variational method. We employed an analytical expression for the energy diffusion term given by J.D. Gaffey (see Appendix 5) in both codes. Detailed descriptions are given in Ref. [20] and in Appendix 5. Thus, in the following, we will simply describe the calculation result.

Calculations are made for these parameters appropriate to JT-60. Fast ions are launched from a specific point  $(R, Z) = (4.0, 0.0)$  with an initial pitch of  $\eta_0 = 1.0$  and a beam energy of 160 keV. The banana size of fast ions are assumed to be zero. The beam driven current as a function of the initial pitch angle given by Gaffey's model with the energy diffusion term (old analytical treatment), is shown by the broken line in Fig. 3.1.2. The dash-dotted line is the one given by Cordey's analytical expressions of the eigen function with the energy diffusion term. The closed circles are the results from the OFMC code. The results from Cordey's model agree very well with those from the OFMC code near the tangential injection (pitch angle  $\sim 9^\circ$ ). In the pitch angle near the banana region, however, one can find a difference of

10~30% between the results of the OFMC code and Cordey's model. The solid curve in Fig. 3.1.2 shows the results from the improved analytical model with numerical eigenfunctions which can describe the effect of barely trapped ions [17]. One can see that the results from the improved analytical code agree very well with those from the OFMC code in a wide range of pitch angles. Another interesting thing about the comparison of the results from those two methods lies in the effect of loss during slowing down. The effect of a finite banana size on the distribution of the beam driven current is also of great interest. The calculation results for the FER are shown in Fig. 3.1.3. We cannot find out any significant difference between the results with and without charge-exchange loss. This is because charge-exchange loss usually occurs when fast ions slow down to the energy range  $E < 50$  keV, where the contribution of fast ions to the ion current becomes very small. In order to clarify the effect of the finite banana size  $\rho_B$  on the spatial distribution of the beam induced current, calculations with and without the banana size were made. Results are shown in Fig. 3.1.3. What is evident from Fig. 3.1.3 is that the effect of the finite banana size on the distribution of the beam driven current is not essential. Figure 3.1.3 shows that, in the FER case, the calculation results between the three modes are small. This is because the effect of energy diffusion on the current drive efficiency becomes low, because the increment of the injected beam energy and injection angle is relatively large. Thus, in the FER case, the old treatment can be used. The characteristics for each model are summarized in Table 3.1.1.

Table 3.1.1.1 Summary of characteristics of beam driven current models

Physics Model	Electron	Ion				
		Trapped effect	Birth		Trapped effect	Energy diffusion
			H ( r )	Monte Carlo		
Mikkelsen - Singer	○	○				
Start	○			○		
JAERI New code	○			○	○	○

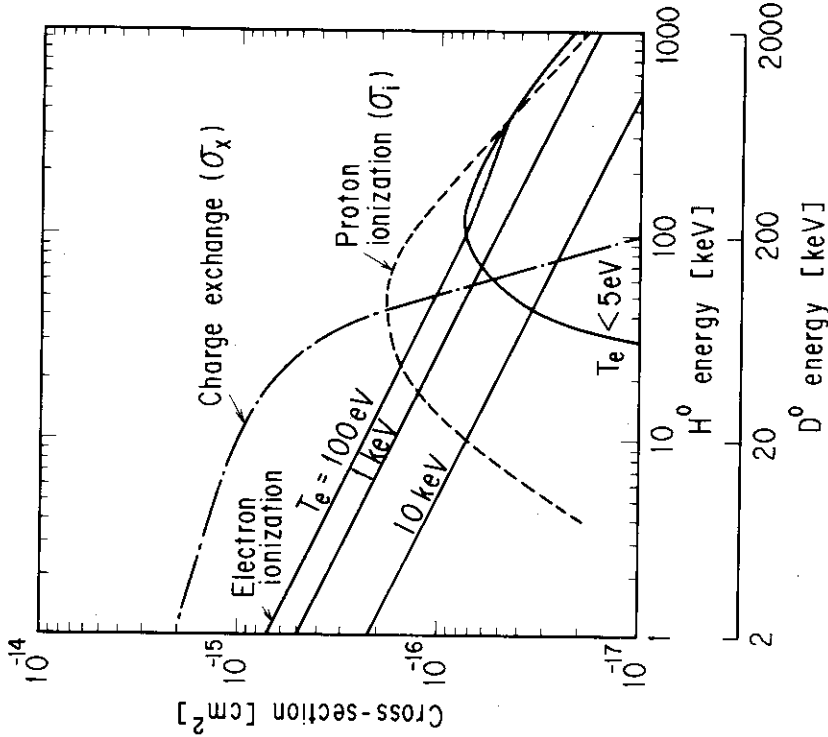


Fig. 3.1.1 The separated cross-sections for ionization of the injected neutral beam versus energy. In the case of electron ionization, when  $v_e \gg v_0$ ,  $\sigma_{e^+} v_e / v_0$  is shown for a Maxwellian electron-velocity distribution at temperature  $T_e$ : for  $v_e \ll v_0$ , the cross-section  $\sigma_e$  is shown for a velocity  $v_0$  [10,11]

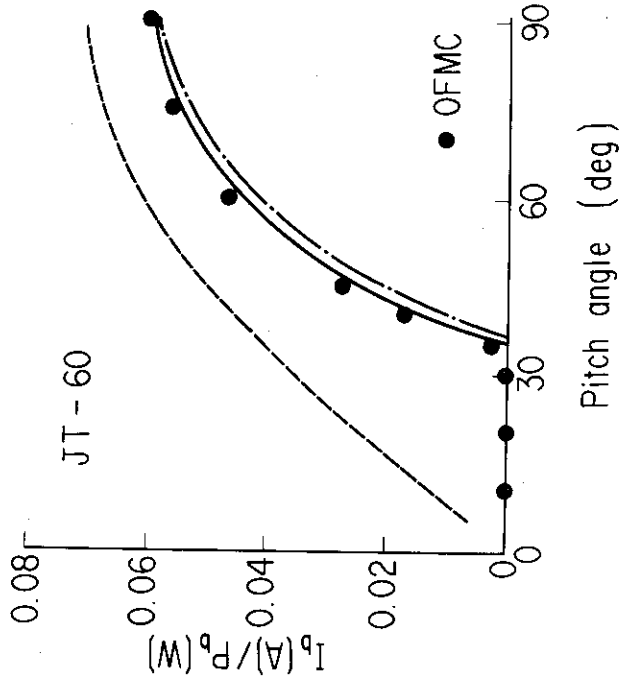
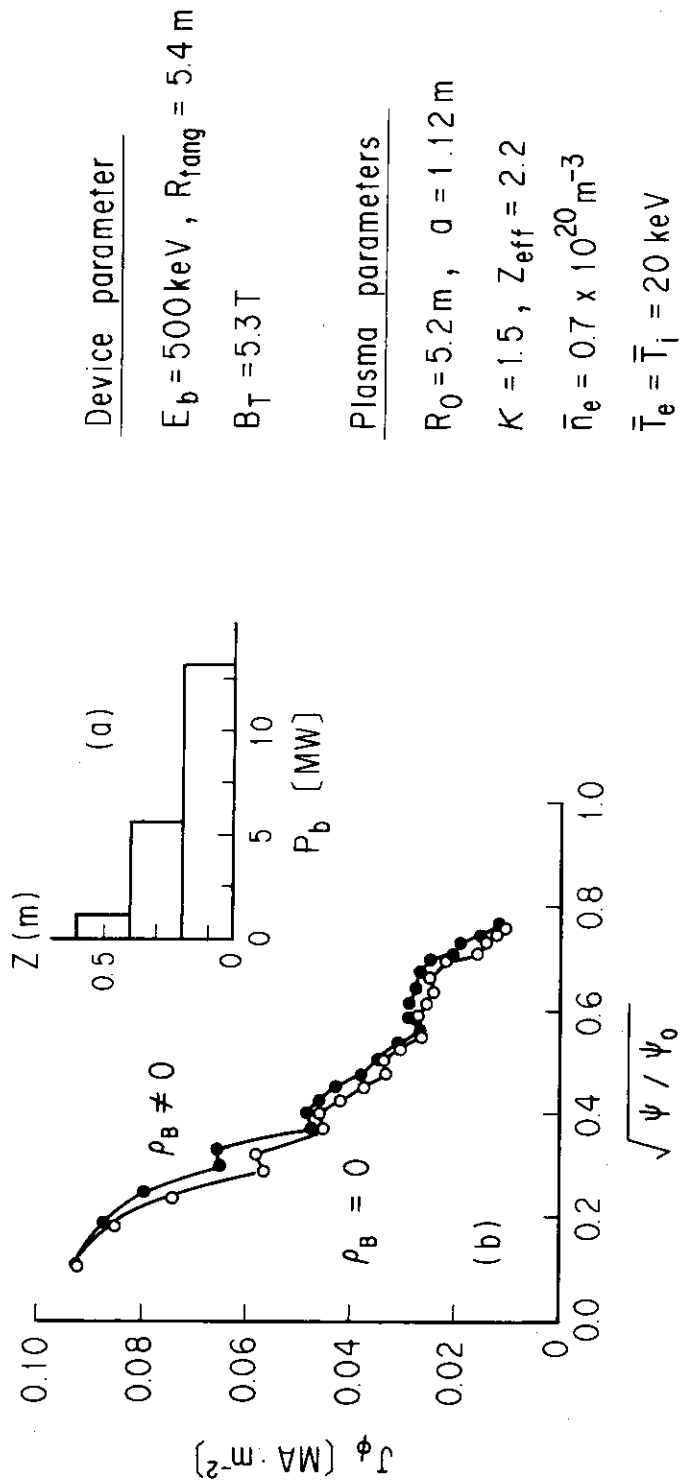


Fig. 3.1.2 Beam driven current versus initial pitch angle of fast ions. Calculations are made for a point source in the equatorial plane. Injection energy  $E_b = 160$  keV,  $n_e = 10^{20} \text{ m}^{-3}$ ,  $T_e = T_i = 8$  keV and  $Z_{\text{eff}} = 2$ . Broken and dash-dotted lines correspond to the results of Gaffey's model with an energy diffusion term (old analytical treatment) and Cordey's model with analytical eigenfunctions. The solid line corresponds to the new analytical model with numerically derived eigenfunctions. Results from OFMC code are shown by closed circles.



#### Device parameter

$E_b = 500 \text{ keV}$ ,  $R_{\text{tang}} = 5.4 \text{ m}$

$B_T = 5.3 \text{ T}$

#### Plasma parameters

$R_0 = 5.2 \text{ m}$ ,  $a = 1.12 \text{ m}$

$K = 1.5$ ,  $Z_{\text{eff}} = 2.2$

$\bar{n}_e = 0.7 \times 10^{20} \text{ m}^{-3}$

$\bar{T}_e = \bar{T}_i = 20 \text{ keV}$

$I_b [A] / P_b [W]$	CX - off		CX - on
	$\rho_B = 0$	$\rho_B \neq 0$	$\rho_B \neq 0$
OFMC	0.123	0.130	0.125
New AM	0.137		
Old AM	0.133		

Fig. 3.1.3 Effect of finite banana size and charge-exchange loss on beam driven current in the FER case.

### 3.2 Current Profile Control

Current profile control is important for beta enhancement [21], control of sawtooth oscillation [22,23] and suppression of major disruption. In the NBI system, almost all beams are not neutralized at the entrance of the neutralizer, because of low system pressure. Hence, the beam driven current profile is easily controlled by changing the beam power profiles with horizontal magnetic fields, less than 0.03 T, produced by coils in the beam profile controller shown in Fig. 2.2.2. A detailed description of the beam profile controller is given in subsection 4.2.2. Figures 3.2.1a and b show the cross-sectional view of the drift duct, the neutralizer and the ion source. The abscissa is scaled down one-tenth of the ordinate. The size of the FER ion source is 0.2 meter wide and 2.4 meters high. The ion source is divided into three ion sources ( $IS_U$ ,  $IS_O$ ,  $IS_D$ ) for calculation. Multiple focused beams from the ion source make Gaussian type power profiles, of which e-holding half width is  $X \tan \omega$ , where  $\omega$  is the beam divergence and  $X$  is the distance from the ion source to the position of  $R_{tang}$ .  $R_{tang}$  is the minimum major radius along the beam path. Figure 3.2.1c shows the power ratio to the total power of the rectangular ion source, the beam divergence, the vertical position and e-holding half width of each ion source. Usually, neutral beams are focused to the focal point A and makes a peaked power profile, as shown in Fig. 3.2.1a. In this case, the beam divergence of the ion source of  $IS_O$  at  $Z=0$  does not change, that is,  $\omega=0.3$  deg (5 mrad). When horizontal fields are applied, a hollow power profiles is made, as shown in Fig. 3.2.1b. In this case, the beam divergence of the ion source  $IS_O$  at  $Z=0$  is assumed to change from 0.3 deg to 0.5 deg, due to the fringing field near the equatorial plane. However, the perturbation can be minimized (see subsection 4.2.2).

Figure 3.2.2 shows typical beam driven current profiles  $J_O^{NBI}$  corresponding to three beam power profiles along the vertical direction at  $R_{tang}$ . The OFMC beam driven code has been used. The global beam driven current efficiency  $I_b[A]/P_b[W]$  and beam shine-through fraction  $f_s$  are also shown. Figure 3.2.2 shows only the capability of current profile control, because the target plasma parameters are fixed. The upper and lower beam profiles with respect to the equatorial plane can be controlled independently. The required total beam driven current and

its desirable profile, depending on scenarios, can be obtained by the combination of individual current profiles as obtained in a few units of the NBI system. The drift duct is 0.44 meter wide and 1.2 meter high at the reactor entrance and is 0.5 meter wide and 2 meters high at the first wall, respectively. The drift duct does not have a serious impact on the reactor structure such as toroidal field coils, shield structure, passive shell conductors, coolant channels and electrical insulators for one-turn resistance (see Section 5.2).

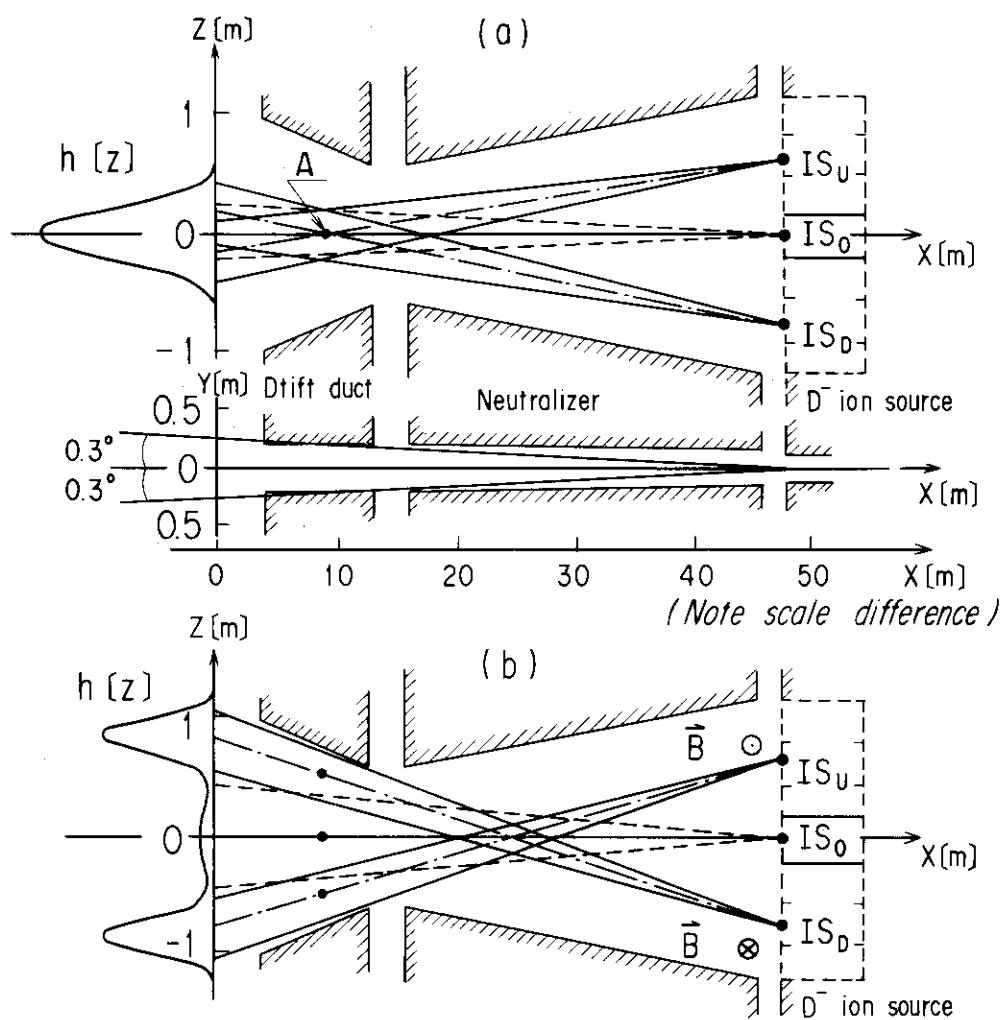


Fig. 3.2.1 Control of beam power profile. (a) Peaked power profile. (b) Hollow power profile. (c) Characteristics of modelled ion source, (IS<sub>U</sub>, IS<sub>0</sub>, IS<sub>D</sub>);  $P/P_{\text{rec}}$ : Power ratio of each ion source to total power of original rectangular ion source,  $\omega$ : Beam divergence,  $Z$ : Vertical position,  $r$ : e-holding half-width, that is,  $r=X \cdot \tan \omega$ , where  $X$  is the distance from the ion source to the position of  $R_{\text{tang}}$ .

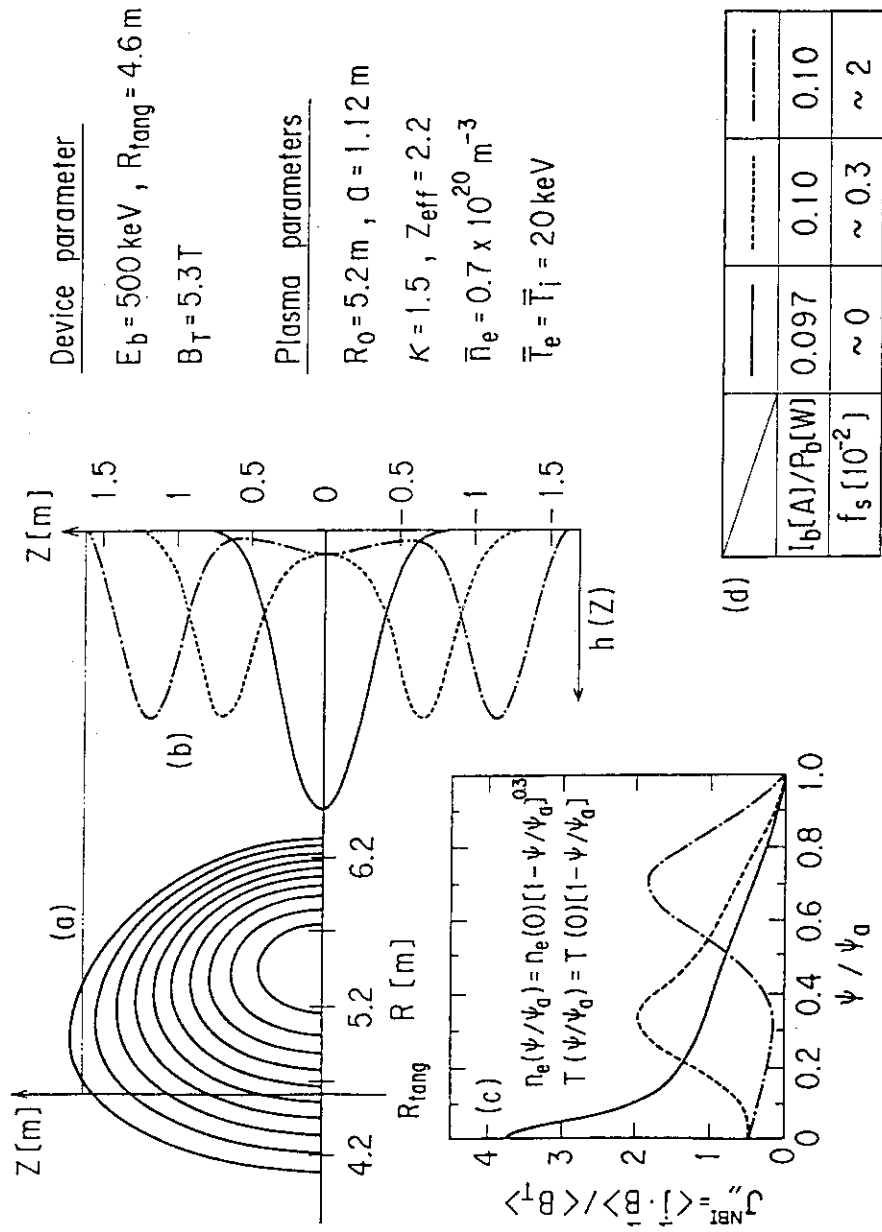


Fig. 3.2.2 Current profile control. (a) Magnetic surface, (b) Beam power profile  $h(Z)$ , (c) Beam-driven current profile  $j_{NBI}$  and poloidal flux function  $\psi$ , (d) Beam shine-through fractions  $f_s$  and global beam-driven current efficiency  $I_b[A]/P_b[W]$ , where  $I_p$  and  $P_b$  are beam driven current and beam injection power, respectively. Device and plasma parameters are also shown

### 3.3 Self-Consistent Plasma Profile of Beam Driven High $\beta$ Plasma

#### 3.3.1 Computational Procedure

The high beta tokamak discharge with the NBI current drive has been studied by using the library system for the 1.5 dimensional (1.5 D) tokamak transport code: LIB2D. The code system consists of an axisymmetric equilibrium code, a magnetic-surface-averaged tokamak transport code, a localized MHD stability code and an NBI deposition and current drive code. The basic role of each step is as follows:

##### (1) Equilibrium step

An axisymmetric MHD equilibrium equation (see Appendix A.6)

$$\Delta^* \psi = -R^2 \mu_0 \frac{dp}{d\psi} - F \frac{dF}{d\psi}$$

is solved for prescribed values of  $q(\psi)$  and  $v(\psi) = p_T(\psi)(\partial V/\partial p)^\gamma$ , where  $q$ ,  $p_T$ ,  $V$  and  $\gamma$  are the safety factor, the total plasma pressure including the beam and  $\alpha$  particle components, the volume surrounded by the magnetic surface  $\psi$  and the adiabatic constant ( $\gamma = 5/3$ ), respectively. The code solves this equation as a generalized differential equation by using a combination of the Bunneman DCR method and the Green function method.

##### (2) Transport step

In this step, the plasma parameters of density  $n_j$ , temperature  $T_j$  and poloidal field  $B_{p0}$  are advanced by solving the magnetic-surface-averaged transport equations:

$$\frac{\partial n_j}{\partial t} = \frac{1}{r} \frac{\partial}{\partial r} \left( \langle |\nabla r|^2 \rangle r D_j \frac{\partial n_j}{\partial r} \right) + \langle S_j \rangle$$

$$\frac{3}{2} \frac{\partial p_j}{\partial t} \frac{1}{r} \frac{\partial}{\partial r} \langle |\nabla r|^2 \rangle r \left( n_j \chi_j \frac{\partial T_j}{\partial r} + \frac{5}{2} D_j T_j \frac{\partial n_j}{\partial r} \right) + \langle Q_j \rangle + \langle Q_{jk}^{equ} \rangle$$

$$\frac{\partial B_{p0}}{\partial t} = \frac{\partial}{\partial r} n_{//} (\langle j_{//B} \rangle - \langle j_{//B}^{ext} \rangle)$$

$$\langle j_{//B} \rangle = \frac{1}{\mu_0} \left( \frac{1}{\langle R^{-2} \rangle} \frac{\partial r}{\partial V} \right)^2 r \frac{\partial}{\partial r} \left( \langle R^{-2} \rangle \left| \frac{\nabla V}{R} \right|^2 \frac{B_{p0}}{r} \right)$$

where  $p_j = n_j T_j$  and  $B_{p0} = \Phi_a r / (\pi R_0 q)$ , and the angular bracket  $\langle X \rangle$  is the surface averaged value

$$\langle X \rangle = \oint \frac{dr}{B_p} \frac{X}{r} / \oint \frac{dr}{B_p} ;$$

where  $\chi$  denotes the poloidal direction. The radial coordinate  $r$  is defined by  $\Phi = \Phi_a r^2$ , where  $\Phi$  and  $\Phi_a$  are the toroidal magnetic flux and its value at the plasma surface, respectively. The other quantities,  $S_n$ ,  $Q_j$ ,  $Q_{jk}^{equ}$  and  $j_{//}^{ext}$  are the particle source, energy source, energy equipartition and externally driven plasma current parallel to the magnetic field, respectively. In these equations, we omitted the terms for the temporal change of the plasma volume which are included in the equilibrium code. These equations are solved by the finite element approximation and the Crank-Nickolson time integration scheme.

### 3) Stability step

Stabilities against the ballooning mode and Mercier mode are checked for the given equilibrium profile, and the threshold values of the pressure gradient against these modes are calculated. As an option, the code enhances the plasma transport in the unstable region so that the plasma is in a marginally stable state for these modes.

### 4) NBI step

The particle deposition profile is calculated by the Monte-Carlo scheme, and the heat deposition profiles to electrons and ions are evaluated with Stix's formula. The beam-induced current parallel to the magnetic field is also evaluated by using Start's analytic expression neglecting the trapped particle effect on beam ions.

## 3.3.2 Calculated Results

In the following, the time evolution of the FER plasma with a 50-50% D-T mixture is simulated by using a hydrogen plasma with an equivalent mass number of 2.5. The employed transport coefficients are  $D_e = 1.0 \times 10^{19} / n_e \text{ m}^2 \text{ s}^{-1}$ ,  $\chi_e = 5.0 \times 10^{19} / n_e \text{ m}^2 \text{ s}^{-1}$  and  $\chi_i = 3.0 \times \chi_i^{NC}$ , where  $\chi_i^{NC}$  is the neo-classical ion thermal conductivity (see Appendix 1). The simulation is started from the MHD equilibrium of the Joule heated plasma with an average plasma density  $\bar{n}_e = 5.0 \times 10^{19} \text{ m}^{-3}$ , total plasma

current  $I_p = 5.0$  MA and flat current density profile with  $q_{axis} = 1.5$ , and then the plasma parameters are advanced in time by solving each step mentioned above in turn. The average plasma density and the plasma current are kept constant during the simulation by adjusting the gas-puffing and by controlling the OH-coil current. The NBI heating power is also controlled so that the OH current in the initial phase is replaced by the beam-driven current in the steady state phase.

Figure 3.3.1 shows the plasma parameter profiles in the final stage of the simulation, where the plasma current is driven by the NBI and the toroidal electric field is almost zero in the whole region of the plasma. The fusion energy multiplication factor  $Q$  and the toroidal beta value  $\beta_T$  [%] are  $Q \sim 4.0$  and  $\beta_T \sim 4.3$  [%], respectively. In this simulation, enhancement of the transport due to the ballooning instability is not taken into account and the plasma is unstable in the narrow region. Because of the off-axis injection of the neutral beam, the safety factor profile remains very flat with  $q_{axis} > 1$ , and the marginal stability analysis predicts the beta value to be more than 6 for this  $q$  profile.

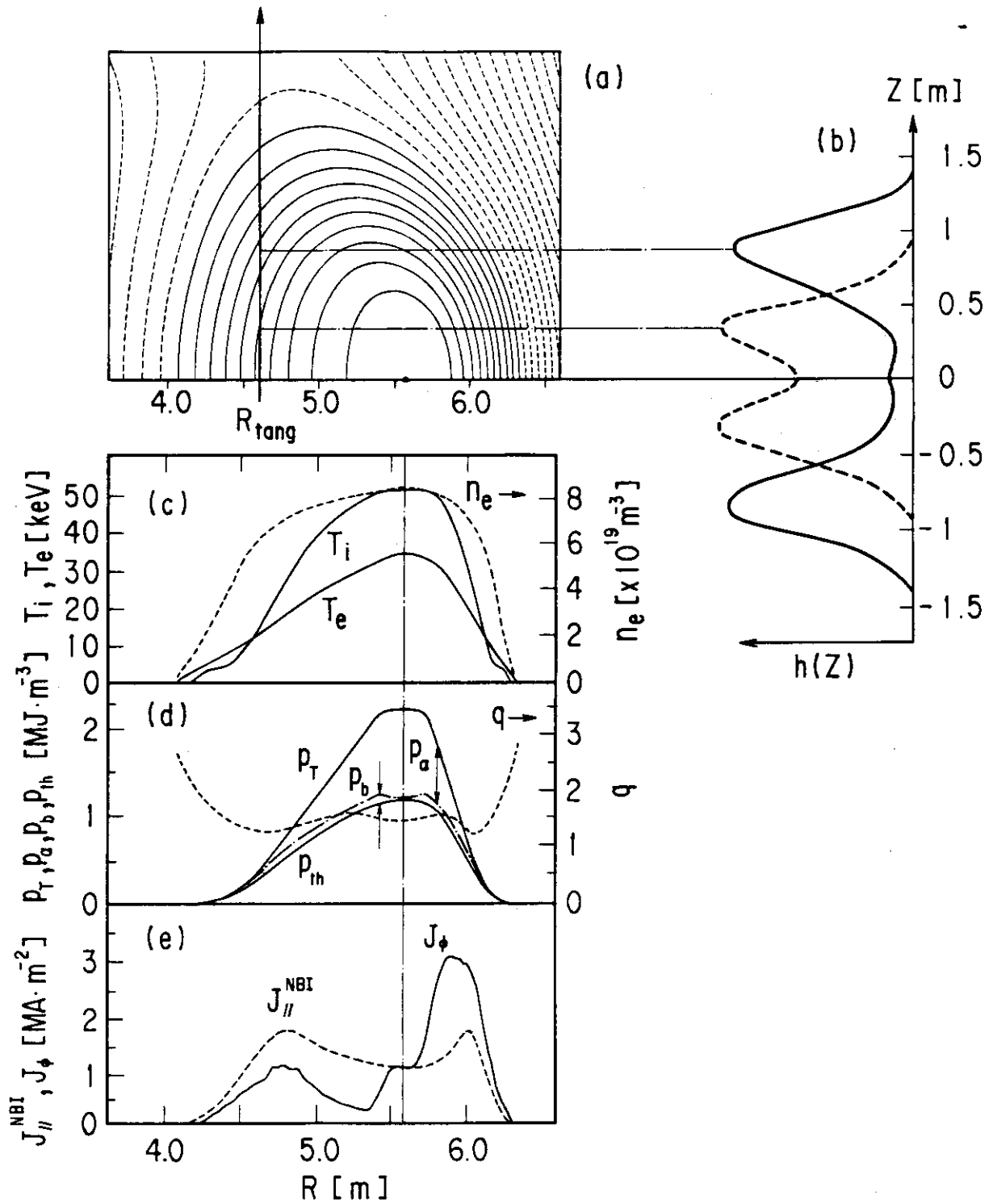


Fig. 3.3.1 Self-consistent high- $B$  plasma profile. (a) Magnetic surface, (b) Beam power profile  $h(z)$ . Plasma profiles of (c) Electron density  $n_e$ , electron temperature  $T_e$  and ion temperature  $T_i$ ; (d) Total plasma pressure  $p_T$ , thermal plasma pressure  $p_{th}$  and safety factor  $q$ . (e) Profiles of beam-driven current density  $J_{||}^{NBI}$  and toroidal component of plasma current density  $J_\phi$ . Device parameters are the same as shown in Fig. 3.2.2.

### 3.4 Current Ramp-Up Operation

An operational scenario, in which the plasma current is ramped up from 2 MA to 8 MA by the NBI current drive without OH-assist, is investigated with physical limitations on  $\beta_T$  and  $\beta_p$  and with an engineering restraint on the beam shine-through taken in account. The time evolutions of the plasma parameters are obtained using 0-D transport equations, the steady-state 2-D Fokker-Planck equation, and the plasma circuit equation. The beam-driven current is calculated time-dependently with a formula obtained by Mikkelsen and Singer [15,24].

#### 3.4.1 Simulation Model and Formulation

The plasma current ramp up scenario by the NBI current drive is studied with simple time-dependent 0-D transport equations, the steady-state 2-D Fokker-Planck equation, and the plasma circuit equation. The transport equations deal with the following power balance equations and the particle balance equations. The density and temperature profiles for ions are assumed to be the same as those for electrons, which are given by  $n(r) = n(0) \times [1 - (r/a)^2]^{0.5}$  and  $T(r) = T(0) \times [1 - (r/a)^2]$ , respectively.

The power balance equations for electrons and ions are given by

$$\frac{dW_e}{dt} = P_\alpha^e + P_{NBI}^e + P_{OH} - P_{ei} - P_{syn} - P_{imp} - P_{conv}^e$$

$$\frac{dW_i}{dt} = P_\alpha^i + P_{NBI}^i + P_{ei} - P_{conv}^i$$

where  $P_\alpha^e$  and  $P_\alpha^i$  are the alpha-heating power to the electrons and to the ions.  $P_{NBI}^e$  and  $P_{NBI}^i$  are the beam-heating power to the electrons and to the ions.  $P_{OH}$  is the Joule heating power;  $P_{ei}$  is the energy transferred from the electrons to the ions;  $P_{syn}$  is the synchrotron radiation loss;  $P_{imp}$  is the radiation loss due to impurities.  $P_{conv}^e$  and  $P_{conv}^i$  are the electron and the ion energy transport losses. The energy confinement

time for the electrons  $\tau_{E,e}$  is calculated by Kaye-Goldston scaling (see Appendix 1).

The ion energy confinement time  $\tau_{E,i}$  is calculated using ion thermal diffusivity  $\chi_i$ , which is taken to be ten times the neoclassical value as calculated by Change and Hinton (see Appendix 1).

The global energy confinement time,  $\tau_{E,g}$ , is calculated:

$$\frac{W_e + W_i}{\tau_{E,g}} = \frac{W_e}{\tau_{E,e}} + \frac{W_i}{\tau_{E,i}}$$

The particle balance equations are also solved time-dependently for D, T, He, and impurities individually. Argon is assumed to be the only impurity here. The charge state of argon  $Z_k$  is calculated from a polynomial fitting function given by Post[25].

The particle balance equations for D, T, He, Ar, and the electrons are:

$$\frac{d\bar{n}_D}{dt} = \frac{1}{V} (S_D + S_{NBI} - S_f) - \frac{\bar{n}_D}{\tau_p} (1 - R_e)$$

$$\frac{d\bar{n}_T}{dt} = \frac{1}{V} (S_T - S_f) - \frac{\bar{n}_T}{\tau_p} (1 - R_e)$$

$$\frac{d\bar{n}_\alpha}{dt} = \frac{1}{V} S_f - \frac{\bar{n}_\alpha}{\tau_p} (1 - R_e)$$

$$\frac{d\bar{n}_{imp}}{dt} = \frac{1}{V} S_{imp} - \frac{\bar{n}_{imp}}{\tau_p} (1 - R_e)$$

$$\frac{d\bar{n}_e}{dt} = \frac{d\bar{n}_p}{dt} + \frac{d\bar{n}_T}{dt} + 2 \times \frac{d\bar{n}_\alpha}{dt} + Z_{imp} \times \frac{d\bar{n}_{imp}}{dt}$$

where  $\bar{n}_D$ ,  $\bar{n}_T$ ,  $\bar{n}_\alpha$ ,  $\bar{n}_{imp}$  and  $\bar{n}_e$  are the volume averaged densities for D, T, He, Ar, and the electrons, respectively. The number of D, T, and Ar particles fueled per second are represented by  $S_D$ ,  $S_T$  and  $S_{imp}$ , and  $S_{NBI}$  is the number of beam particles injected into the plasma.  $S_f$  is the number of D or T (or He) particles spent (or produced) in the following fusion reaction:  $D + T \rightarrow \alpha + n$ .

The particle recycling rate,  $R_e$ , is assumed to be the same for D, T, He and Ar for simplicity. This is assumed to be 0.85 and is set constant. The particle confinement time  $\tau_p$  is defined as twice as large as  $\tau_{E,g}$ , where  $\tau_{E,g}$  is the global energy confinement time.

The energy balance equations and the particle balance equations are solved by the Runge-Kutta-Gill method and the plasma parameters are obtained time-dependently. The global beam driven current efficiency,  $\eta$ , is calculated by the formula obtained by Mikkelsen and Singer[15]:

$$\eta \left[ \frac{\text{Amp}}{\text{watt}} \right] = \frac{I_{\text{NBI}}}{P_{\text{NBI}}} = \frac{1}{2\pi R_0 / (\text{m})} \frac{\bar{\eta}}{88.92} \frac{T_e / (\text{keV})}{n_e / (10^{20} / \text{m}^{-3})} \bar{\xi}_0 (1 - f_s)$$

$$\bar{\eta} = 140.06 F(Z_b, Z_{\text{eff}}, \bar{\epsilon}) J(x, y)$$

$$\bar{\xi}_0 = R_0 / R_{\text{tang}}, \quad \bar{\epsilon} = a / 2R_0$$

where  $f_s$  is the shine-through fraction calculated by a beam power deposition code;  $J(x, y)$  is a function of the normalized beam velocity parameter  $x$  and the pitch-angle scattering parameter  $y$ ; and  $F(Z_b, Z_{\text{eff}}, \epsilon)$  is the correction factor for the current carried by the electrons in response to the beam ion current.  $F(Z_b, Z_{\text{eff}}, \epsilon)$  also contains the correction for trapped electrons. Thus the global beam driven current,  $I_{\text{NBI}}$ , can also be obtained time-dependently.

The voltage applied by the external field can be given by the following equation, if the inductance of the beam current is assumed to be the same as that of the inductive current:

$$V_L = R_p I_{\text{OH}} + \frac{d}{dt} (L_p I_p) \quad (1)$$

where  $L_p$ ,  $R_p$ , and  $I_{\text{OH}}$ , are the plasma inductance, the plasma resistance, and the inductive current, in which the return current is taken into consideration. Since the total plasma current,  $I_p$ , is supported by the beam driven current,  $I_{\text{NBI}}$ , in this scenario,  $I_p$  can be represented by the sum of  $I_{\text{NBI}}$  and  $I_{\text{OH}}$  as follows:  $I_p = I_{\text{NBI}} + I_{\text{OH}}$ . Therefore,  $V_L$  can be rewritten as:

$$V_L = R_p (I_p - I_{\text{NBI}}) + \frac{d}{dt} (L_p I_p)$$

The magnetic flux supplied by the external field  $\psi_{ex}$  is obtained by integrating  $V_L$  in Eq. (1) .

Note that in order to noticeably save the flux swing, the beam driven current  $I_{NBI}$  should always be larger than the plasma current, and it is also necessary to make  $V_L$  as small as possible. A smaller  $V_L$  results from higher plasma resistance to ramp up the plasma current while the electron temperature is low. The beam power  $P_{NBI}$  should be controlled properly.

### 3.4.2 Current Ramp-up under $\beta_T$ and $\beta_p$ Limitations

Since high energy and high power NB is injected during the NBI current ramp-up, care must be taken to satisfy the conditions on  $\beta_T$  and  $\beta_p$ , and the beam shine-through stated hereafter.

$$1) \quad \beta_T(\text{toroidal beta}) \leq \beta_{cr}$$

where  $\beta_{cr}$  represents the Troyon's beta limit which is given by Troyon[7].

$$\beta_{cr}(\%) = C_T \frac{I_p [\text{MA}]}{a [\text{m}] B_T [\text{T}]}$$

where  $I_p$ ,  $a$ , and  $B_T$  are the plasma current, plasma minor radius, and the toroidal field strength, respectively. The Troyon's beta scaling coefficient  $C_T$  is taken to be 4 in this calculation. Although the pressure produced by the fast beam ions is anisotropic ( $P_{//} \gg P_{\perp}$ ), while the background thermal pressure is isotropic, the total plasma pressure is defined as the sum of the beam pressure and the thermal pressure in this calculation. So the total beta toroidal is given by the sum of the beam beta and the thermal beta, that is,  $\beta_T = \beta_{beam} + \beta_{th}$ . The kinetic beam pressure is defined by  $P = \dot{n}_b \tau_b \langle E_b \rangle$ , where  $\dot{n}_b$  is the particle density input rate due to the injection,  $\tau_b$  is the beam ion life time[15], and  $\langle E_b \rangle$  is the averaged energy of the circulating beam ions.

$$2) \quad \beta_p \text{ (poloidal beta)} < A = R/a_p \text{ [plasma aspect ratio]}$$

Beta poloidal  $\beta_p$  is given by:

$$\beta_p = \beta_T A^2 q^2 \frac{2}{1+\kappa^2}$$

where  $\kappa$  and  $A$  are the plasma elongation and the aspect ratio. The safety factor  $q$  is represented by:

$$q = \frac{5aB_T(1+\kappa^2)}{2A I_p}$$

Thus, if we use the relation  $R B_T = \text{constant}$ ,  $\beta_p$  can be expressed by

$$\beta_p = C_1 C_T \left( \frac{1+\kappa^2}{2} \right) \frac{1}{A I_p}$$

where  $C_1$  is a constant. This equation for  $\beta_p$  shows that  $\beta_p$  is dependent not only on  $I_p$  but also on  $\kappa$  and  $A$ . So it is possible to ramp the plasma current up keeping  $\beta_p$  smaller than the aspect ratio, if  $\kappa$ ,  $R$ , and  $a$  can be changed properly.

### 3) Allowable beam shine-through rate

The allowable beam shine-through rate during the current ramp-up phase depends on the engineering design (see Subsection 5.3.2). The electron density is the main control means for the beam shine-through. The electron density  $n_e$  and the effective charge  $Z_{\text{eff}}$  are mainly controlled by gas fueling.

The current drive efficiency is inversely proportional to the plasma density. Therefore, it is preferable to keep the plasma density as low as possible. However, note that it is required to keep the density adequately high in order to suppress the beam shine-through and also to make a cold and dense divertor plasma.

The effective charge,  $Z_{\text{eff}}$ , is controlled by impurity fueling. Since high power beam is injected into the plasma while low electron temperature is preferable for reducing the resistive backward electron current due to negative voltage,  $Z_{\text{eff}}$  should be kept high so that the radiation loss due to impurity can be large enough to keep the electron

temperature low.  $Z_{\text{eff}}$  is preferable to be controlled at about 4.5 during the current ramp up.

### 3.4.3 Full Non-Inductive Current Ramp-up

In the previous section, the importance of controlling the NBI power and energy are described so that both the total beta,  $\beta_T$ , and the poloidal beta,  $\beta_p$ , are limited within the Troyon limit and the aspect ratio, respectively. These restraints limit the speed of the plasma current ramp-up, otherwise OH-assist is required for fast current rise.

In this subsection the OH-assist is removed resulting in  $V_L=0$  during the NBI current drive. It is not so easy to solve Eq.(1) even if  $V_L=0$ , because the plasma resistance,  $R_p$ , and the NBI driver current,  $I_{\text{NBI}}$ , are non-linear functions of  $T_e$ , and  $T_e$  is one of the quantities to be solved in each time step. To avoid this difficulty, the rate of change of the plasma current is estimated for obtaining the value at the next time step by the next equation in spite of solving Eq.(1).

$$\frac{dI_p}{dt} = - \frac{R_p}{L_p} (I_p - I_{\text{NBI}}) \quad (2)$$

This procedure clearly requires slow changes of  $R_p$ ,  $L_p$  and  $I_{\text{NBI}}$ . At the very beginning of the NBI current drive, the  $V_L = 0$  supposition is slightly violated. The plasma current is ramped up from 2 MA to 8 MA. The  $D^0$ -pencil beam is injected at:

$$R_{\text{tang}} = R - \frac{1}{2} a$$

Since Troyon's beta limit is proportional to the plasma current and since the total beta is defined as the sum of the beam beta and the thermal beta, it is not allowed to inject a high power beam into the plasma when the plasma current is small. So it is required to increase the beam power as the plasma current becomes larger.

The NBI energy maintained at 500 keV throughout the current ramp-up phase. The density will continue to increase gradually due to the gas fueling effect of the NBI. A lower energy beam reduces the shine-through rate because the interaction cross section between the beam

particle and the background plasma increases as the beam energy decreases. From a gas fueling point of view, a lower energy beam supplies more particles for the same NBI power, hence the density will increase more rapidly, which will deteriorate the current drive efficiency.

Figure 3.4.1 shows the time evolution of the plasma current, total beta, density,  $Z_{\text{eff}}$  and beam shine-through, for two different NBI power controls to compare its effect on the poloidal beta. Throughout the current ramp-up total beta is within the Troyon limit. In Fig. 3.4.1b,  $\beta_p$  limit violation has been avoided by beam power control, therefore there is no necessity of controlling  $\kappa$  and  $A$  (see Sub-section 3.4.2).

The power due to beam shine-through is well suppressed below the design value for the shine-through armor plate. Time evolution of the ion and electron temperatures and the loop voltage calculated by Eq. (1) are also shown in Fig. 3.4.1. Loop voltage is a measure of accuracy when approximating the change rate of the plasma current as Eq. (2). The flux consumption during plasma current ramp-up from 2 to 8 MA is 0.2 - 0.3 VS which is less than 0.5% of the inductive storage  $\Delta(LpI_p)$ .

Table 3.4.1 summarizes the results for two different manners of the NBI power control at the initial stage of the NBI current ramp-up. Case 1 corresponds to the Fig. 3.4.1a in which  $P_{\text{NBI}}$  is controlled so that the total beta  $\beta_T$  is maintained closed to the Troyon's beta limit. The poloidal beta  $\beta_p$  exceeds the aspect ratio for the first 50 seconds. In case 2, both NBI power and its rate of change are decreased, thus resulting in the suppression of  $\beta_p$  at the level around the half of the aspect ratio. Note that the case 2 requires longer rise time ( $t_r$ ) and larger energy ( $P \cdot t_r$ ) for plasma current ramp-up. Other conditions such as initial electron density  $\bar{n}_e(t = 0)$  and  $Z_{\text{eff}}$  are set exactly or approximately same.

Since NBI current drive efficiency is basically proportional to  $\bar{T}_e/\bar{n}_e$ , the NBI driven current is maximized in the high temperature but low density plasma. On the other hand, a return electron current, which cancels the driven current, increased rapidly at high electron temperature because of  $\bar{T}_e^{-3/2}$  dependence of the plasma resistivity. There exists, therefore, an optimum electron temperature to minimize the plasma current ramp-up rate. The importance of controlling the energy

and particle confinement times separately should be noted from this view point.

In the present analysis, the beam pressure contribution to the plasma pressure is taken into consideration by defining the total pressure as the sum of the beam pressure and the thermal pressure. If such an anisotropic beam pressure may be neglected when considering instabilities, it will be much easier to ramp up the plasma current. A further study on the effect of the anisotropic beam pressure on instabilities is required in order to establish the current ramp up scenario.

Table 3.4.1 Plasma parameters and summary

	Case 1	Case 2
R (m)	4.9	4.9
a (m)	1.3	1.3
$\kappa$	1.7	1.7
Lp ( $\mu$ H)	10.72	10.72
A = R/a	3.77	3.77
I <sub>p</sub> (MA) (t = t <sub>r</sub> )	8.0	8.0
B <sub>T</sub> (T)	5.0	5.0
$\beta_p$ - MAX	5.45	2.5
t <sub>r</sub> (sec)	3625	4525
P · t <sub>r</sub> (GJ)	15.915	17.31
P - MAX (MW)	500	48.02
P <sub>sh</sub> - MAX (MW)	2.053	1.645
$\bar{n}_e$ ( $\times 10^{19} \text{m}^{-3}$ ) (t=0)	0.861	0.861
Z - effective	4.657	4.775

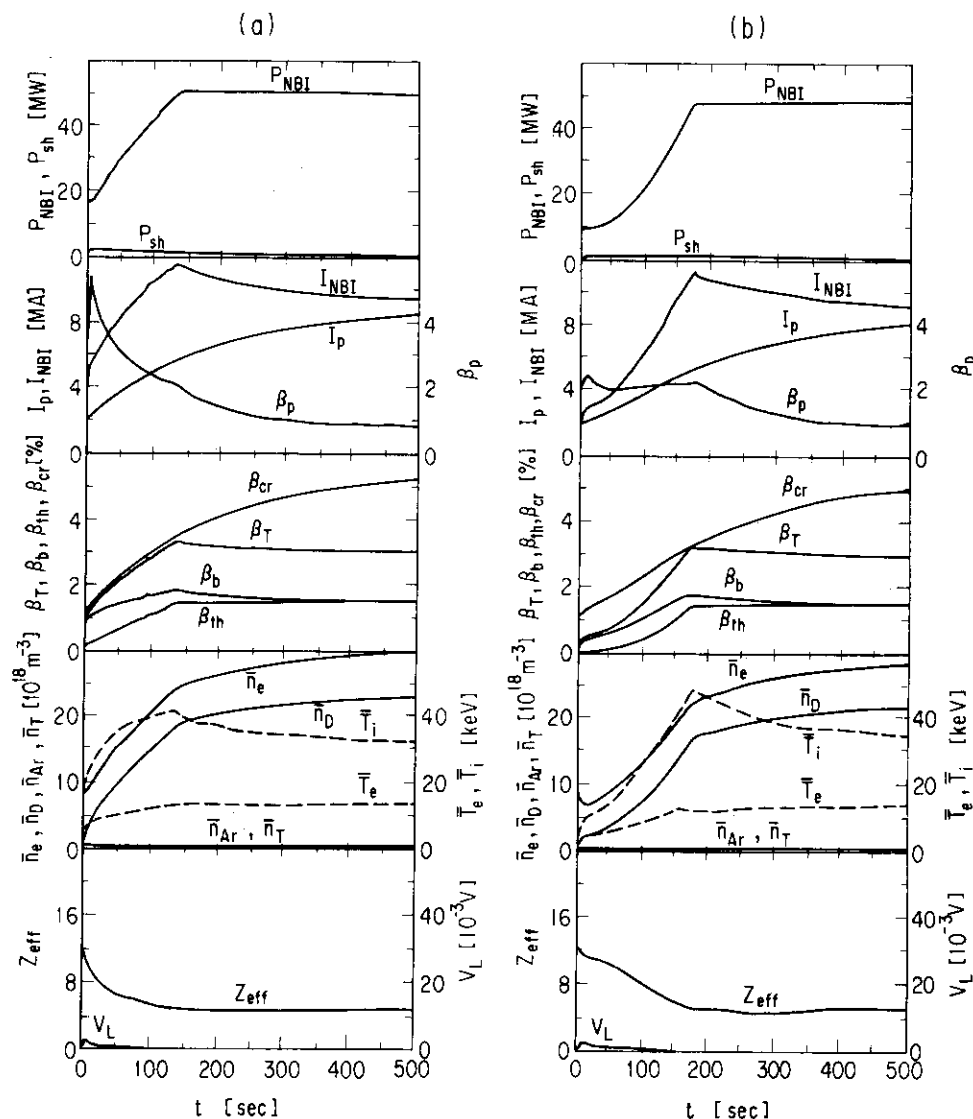


Fig. 3.4.1 Time evolution of the plasma parameters for two cases of different NBI power control; (a) NBI power is controlled in proportion to the plasma current up to 50 MW, (b) the rate of NBI power increase at the beginning is suppressed to decrease at this phase. Beam energy  $E_b$  is 500 keV. Beam power  $P_{NBI}$ ; beam shine through power  $P_{sh}$ ; beam driven current  $I_{NBI}$  and plasma current  $I_p$ ; critical beta value  $\beta_{cr}$ , total toroidal beta value  $\beta_T$ , including beta value due to thermal populations  $\beta_{th}$ , due to suprathermal alpha particles  $\beta_\alpha$  and due to ion beam particles  $\beta_b$ . Critical beta value  $\beta_{cr}$  is assumed to follow Troyon beta scaling law, expressed as  $\beta_{cr} = C_T I_p [MA] / a_p [m] B_T [T]$ . (Scaling coefficient  $C_T$  is 4), poloidal beta value  $\beta_p$ ; electron density  $\bar{n}_e$ , deuterium density  $\bar{n}_D$ , tritium density  $\bar{n}_T$  and argon density  $\bar{n}_{Ar}$ . Time variation of loop voltage is also shown. The loop voltage is given by  $V_L = R_p I_{OH} + \frac{d}{dt} (L_p I_p)$ , where  $L_p$ ,  $R_p$ , and  $I_{OH}$  are the plasma inductance, the plasma resistance, and the inductive current, where the return current taken into consideration.  $Z_{eff}$  is the effective charge state defined as  $Z_{eff} = \sum_i n_i Z_i^2 / n_e$

### 3.5 Quasi-steady State Operation

In FER, a quasi-steady state operation scenario was proposed, based on plasma heating and current drive by an RF system [26] and various problems were discussed [27]. In this operation, as shown in Fig. 3.5.1, the plasma current is non-inductively ramped-up by LHRRF [28]. In the ignition approach phase, LHRRF or ICRF is used for plasma heating. In the burning phase, the current is inductively maintained by the OH coils and plasma profile control is performed by ECRF. After the burning, the current is ramped-down to the same former appropriate value and then non-inductively maintained by LHRRF in low density plasma. During this phase, the transformer coils are recharged. The engineering advantages of introducing the RF-assisted quasi-steady state operation were discussed [29] and may be summarized as follows; 1) reduction in machine size without decreasing burn time, and 2) remarkable reduction in cyclic stress due to the over-turning force on the TF coil. The same engineering advantages are expected in the quasi-steady state operation scenario based on the NBI system. In this operation scenario, only the NBI system is used for heating, current drive and current profile control during all the phases, except for the plasma initiation phase by ECRF with about 3 MW power and the current growing-up phase up to 2 MA helped by OH coils. Figure 3.5.2a shows typical plasma parameters during the burn phase and the recharge phase. A beam input power  $P_b$  of 40.9 MW with  $E_b$  of 500 keV is injected. Xenon impurity is used to improve the current drive efficiency and to decrease the recharge time. By full using the prepared heating power for the ignition approach, relatively high density plasma can be used for a target plasma. Thus, a cold and dense divertor plasma tends to be obtained. The plasma poloidal beta  $\beta_p$  during the recharge phase is about one third of that of the burn phase. If the plasma current is reduced to 5.4 MA from 5.9 MA, the time variation for the over-turning force on the TF coils can be reduced significantly [29]. The heat load on the divertor plate during the recharge phase is about half of that for the burn phase, which leads to a reduction of the cyclic heat load on the divertor plate compared to the pulsed operation. The shine-through fraction  $f_s$  is 0.2. To reduce the heat load due to the shine-through beam particles, a parametric survey was performed. Figure 3.5.2b shows the  $\bar{n}_e$ -dependence of the beam

driven current  $I_b$ , electron temperature  $\bar{T}_e$  and  $f_s$ . The injection power,  $P_b$  is fixed to be 40.9 MW. Figure 3.5.2c shows the  $P_b$ -dependence of  $I_b$ ,  $\bar{T}_e$  and  $f_s$ . The plasma density is fixed to be  $1 \times 10^{19} \text{ m}^{-3}$ . Figures 3.5.2b and 3.5.2c suggest that a plasma density of  $2 \times 10^{19} \text{ m}^{-3}$  seems to be a more preferable target plasma density, from an engineering viewpoint, even though more injection power is necessary.

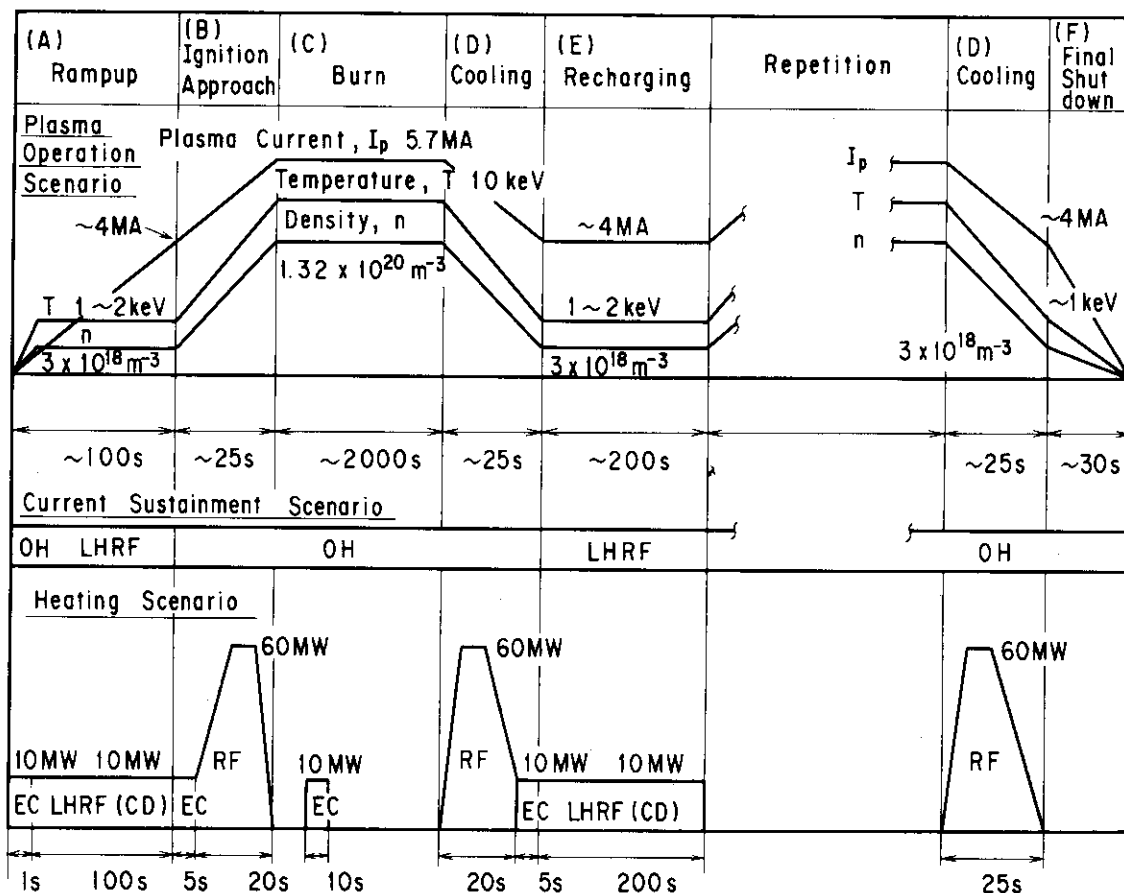


Fig. 3.5.1 Example of quasi-steady state operation, based on RF systems.

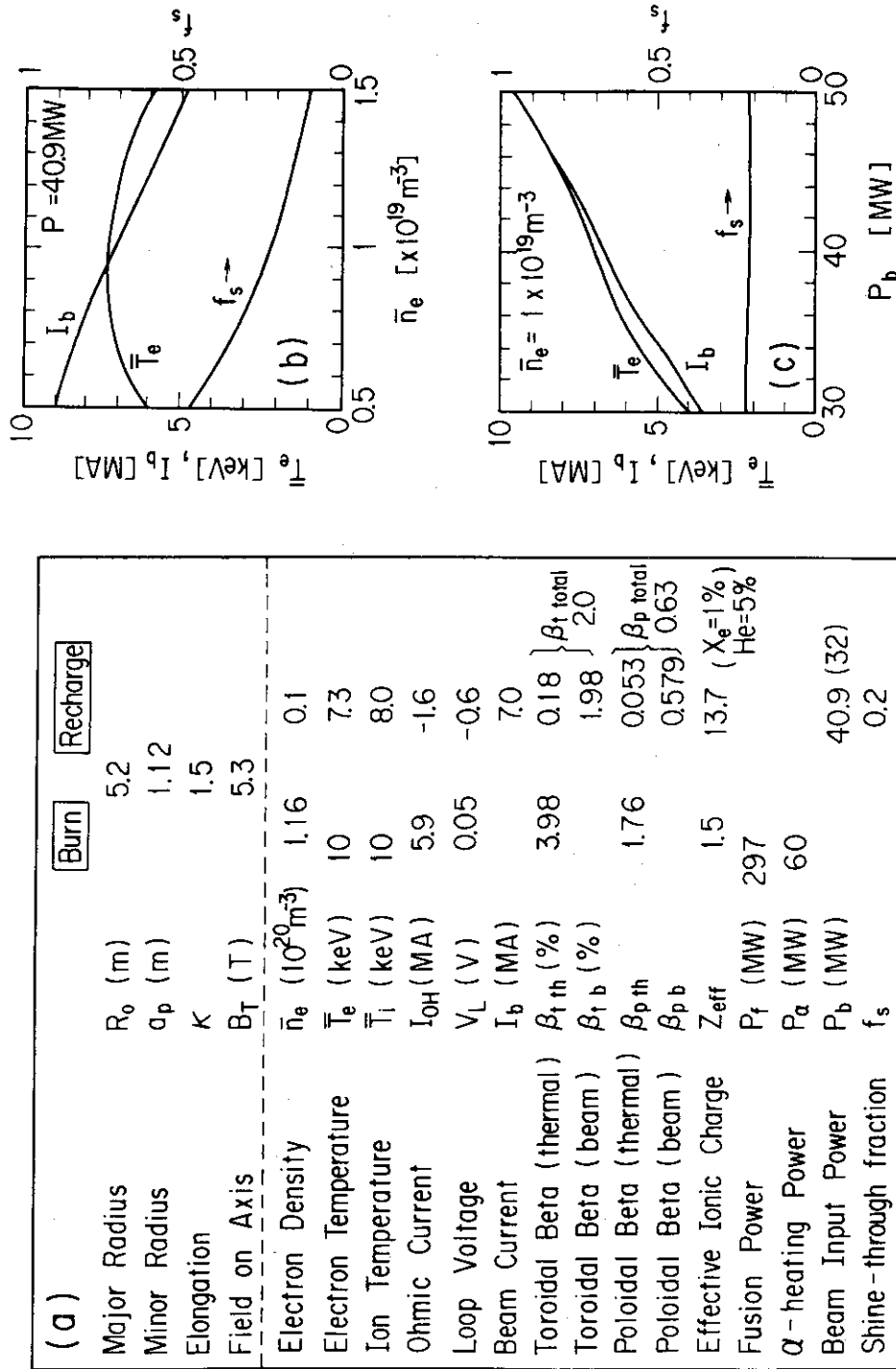


Fig. 3.5.2

Quasi-steady state operation in next generation tokamak. Beam energy  $E_b$  is 500 keV. (a) Plasma parameters during burn phase and recharge phase. (b) Plasma density  $\bar{n}_e$ -dependence of electron temperature  $\bar{T}_e$ , beam-driven current  $I_b$  and shine-through fraction  $f_s$ . Beam input power  $P_b$  is 40.9 MW. (c)  $P_b$ -dependence of  $\bar{T}_e$ ,  $I_b$  and  $f_s$ . Plasma density  $\bar{n}_e$  is  $10^{19} m^{-3}$ .

### 3.6 Cold and Dense Divertor Plasma during Non-Inductive Current Ramp-Up and Quasi-Steady State Operation

The formation of a high recycling divertor plasma, that is, a high density and low temperature divertor plasma, is preferable for plasma production and maintainability of the divertor plate due to the reduction of the impurity release from the divertor plate. When the main plasma density is high, a high recycling divertor tends to be easily obtained. On the other hand, the current driving efficiency is inversely proportional to the plasma density. As already described in the preceding section, the target plasma with a density of around  $(1 - 2) \times 10^{19} \text{ m}^{-3}$  is available in the NBI case. In this section, we examine the properties of the divertor plasma during non-inductive current ramp-up and quasi-steady state operation with the NBI.

#### 3.6.1 Calculational Procedure

Particle balance among the main, scrape-off and divertor plasmas is shown schematically in Fig. 3.6.1 [30]. The neutral flux flowing from the scrape-off plasma region into the main plasma region is balanced with the ion diffusive flux at the boundary between both regions. On the other hand, the neutral flux flowing from the divertor region back to the scrape-off region, a part of which is reionized in the scrape-off region (the probability is assumed to be  $\exp(-b/\lambda_M)$ ) and accelerated back again to the neutralizer plate, is balanced with the incoming ion flux flowing into the divertor region at the boundary.

We describe the divertor plasma by the conservation equation for the particle, momentum and energy along the field line projected on a poloidal cross section. Details of these analytical models are presented in Ref.[30], so only a brief description is given here. The analytical solution for the particle conservation equation can be expressed as follows,

$$F(z) = n_p(z)V(z) = F(z_{thr}) + F(z_L)n(z) \quad (1)$$

where

$$\eta(z) = \left[ \exp\left(\frac{z - z_L}{\lambda_{//}}\right) - \exp\left(\frac{z_{thr} - z_L}{\lambda_{//}}\right) \right] \left[ 1 - \eta_{esc} \exp\left(-\frac{b}{\lambda_{\perp}}\right) \right] \quad (2)$$

where

$$\lambda_{//} = \frac{v_{th}(z_L)}{n_p(z_L) \langle \sigma v \rangle (T(z_{thr}))} \quad (3)$$

$$\lambda_{\perp} = \frac{v_{th}(z_L)}{n_p(z_L) \langle \sigma v \rangle (T(z_L))} \quad (4)$$

$z$  is the coordinate along the poloidal magnetic field line,  $z_{thr}$  indicates the location of the throat entrance and  $z_L$  the neutralizer plate. The quantities  $n_p$ ,  $v$ ,  $F$  and  $T$  are the plasma density, the flow velocity, the ion flux and the plasma temperature, respectively. In Eqs. (3) and (4),  $\lambda_{//}$  and  $\lambda_{\perp}$  are the mean free paths for the neutral particles to move along and across the divertor channel.  $\eta_{esc}$  is the probability for a neutral particle emerging from the divertor plasma to escape from the divertor chamber.  $b$  is the width across the divertor channel.  $v_{th}$  and  $\langle \sigma v \rangle$  are the thermal velocity and the electron impact ionization rate. The physical meaning of  $\eta(z)$  is the ionization probability of the neutral particles emerging from the divertor plate.

The analytical solution for the momentum conservation equation is given as follows.

$$v(z) = v_S(z) (K(z) - \sqrt{K(z)^2 - 1}) \quad (5)$$

where

$$v_S(z) = \frac{B_p}{B_T} \sqrt{\frac{2T(z)}{mj}} \quad (6)$$

$$K(z) = \frac{F(z_L) v_S(z_L)}{F(z) v_S(z)} \quad (7)$$

where  $v_S$  is the sound velocity, and  $B_p$  and  $B_T$  are the poloidal and toroidal magnetic field. The sheath boundary condition (sound velocity) at the plate is used to derive Eq.(5).

The analytical solution for the energy conservation equation is given as follows.

$$\begin{aligned}
 T(z) = & \left[ T(z_L)^{7/2} + \frac{7}{2x_{//}} \left\{ Q_D(z_{thr})(z_L - z) \right. \right. \\
 & \left. \left. - \alpha F(z_L) \left[ 1 - \eta_{esc} \exp\left(-\frac{b}{\lambda_L}\right) \right] \right. \right. \\
 & \left. \left. \times \left[ \lambda_{//} \left( 1 - \exp\left(-\frac{z - z_L}{\lambda_{//}}\right) \right) - (z_L - z) \exp\left(-\frac{z_{thr} - z_L}{\lambda_{//}}\right) \right] \right\} \right]^{2/7} \quad (8)
 \end{aligned}$$

where

$$T(z_L) = [Q_D(z_{thr}) - \alpha \{F(z_L) - F(z_{thr})\}] / \gamma F(z_L) \quad (9)$$

$$x_{//} = 10^3 \left( \frac{B_p}{B_T} \right)^2, \quad (10)$$

$Q_D$  is the power flow,  $\alpha=13.6\text{eV}$  and  $\gamma=7.8$ . In deriving Eq.(8), we have used the sheath condition  $Q_D(z_L)=\gamma T(z_L)F(z_L)$ . These simple analytical models have been shown in Ref.[16,18] to well describe the features of the divertor plasma, if several parameters, e.g.,  $\eta_{esc}$ , are properly adjusted.

Next, we model the particle balance in the main plasma as follows.

$$-\frac{1}{r} \frac{\partial}{\partial r} \left( r D_M \frac{\partial n_M}{\partial r} \right) = S_M(r) = S_0 \exp \left[ -\frac{r - r_B}{\lambda_M} \right] \quad (11)$$

where

$$\lambda_M = \frac{v_{th}(z_{thr})}{n_M(r_B) \langle \sigma v \rangle (T(z_{thr}))} \quad (12)$$

$$\int_{V_p} S_M(r) dV_p = I_M = I \exp \left( -\frac{b}{\lambda_M} \right) \quad (13)$$

and  $r_B$  is the position between the scrape-off and the main plasma. If we assume the diffusion model in the main plasma as,

$$D_M = [h(r) \cdot n_e(r)]^\alpha, \quad (14)$$

where  $h(r)$  expresses the  $r$  dependence of  $D_M$  except for  $D_e(r)$ , but it is assumed to be constant in practical calculations here. We can easily obtain the solution as follows:

when  $\alpha \neq -1$

$$n_e(r) = \{n_e(r_B)^{\alpha+1} + (\alpha+1) \frac{I_M}{4\pi^2 R} g\left(\frac{r_B}{\lambda_M}\right) x\}^{\frac{1}{\alpha+1}} \int_r^{r_B} \frac{1}{n(r) \cdot r} \left[1 + \left(\frac{r}{\lambda_M} - 1\right) e^{\frac{r}{\lambda_M}}\right] dr \quad (15)$$

and when  $\alpha = -1$

$$n_M(r) = n_M(r_B) \exp\left\{ \frac{I_M}{4\pi^2 R A} g\left(\frac{r_B}{\lambda_M}\right) \left[f\left(\frac{r_B}{\lambda_M}\right) - f\left(\frac{r}{\lambda_M}\right)\right] \right\} \quad (16)$$

where

$$f(x) = \exp x - 1 + 0.57721 + \ln x - \bar{E}_1(x) \quad (17)$$

$$g(y) = \frac{\exp(-y)}{y - 1 + \exp(-y)} \quad (18)$$

It will be more convenient to use the average density by integrating Eqs.(15) or (16), since the current drive efficiency in the experiments is usually expressed in terms of the average density. Thus, we introduce the average density  $\bar{n}_e$  defined as

$$\bar{n}_e = \frac{2}{r_B^2} \int_0^{r_B} n_M(r) r dr \quad (19)$$

### 3.6.2 Calculated Results

The solution in the main plasma gives the relations among the edge electron density in the scrape-off layer  $n_{thr}$ , the ion out-flux across the separatrix surface into the scrape-off layer  $I_M$  and the average main electron density  $\bar{n}_e$ . According to a recent experimental result [31] it is observed that the particle confinement time decreases as the average

main electron density increases. Hence, we assume the diffusion model defined in Eq.(14) and search a reasonable index  $\alpha$  consistent with the observed particle confinement time in the JT-60 experiment. We will obtain the main plasma solution by using various values of  $\alpha$ . Figure 3.6.2 shows the particle confinement time  $\tau_p$  as a function of the average main electron density with the edge density as a parameter for the diffusion model  $\alpha=0.5$ . The lower cross marks are the result of JT-60. The essential point to be examined is the density dependence of  $\tau_p$ , since the diffusion model of Eq.(14) contains an unspecified numerical coefficient. Thus, we arbitrarily plot the upper crosses, which represent  $3\tau_p$ , to examine the density dependence of  $\tau_p$ . Results for  $0 < \alpha < 1$  reproduce the experimental characteristics. Hence we use  $\alpha=0.3$ , which is hardly different from the condition  $\alpha=0.5$ .

The main plasma solutions consistent with the divertor solutions are shown in Fig. 3.6.3. The calculation result suggests that it is very difficult to make a divertor plasma temperature below 10 eV in non-inductive current ramp-up while satisfying the required plasma current.

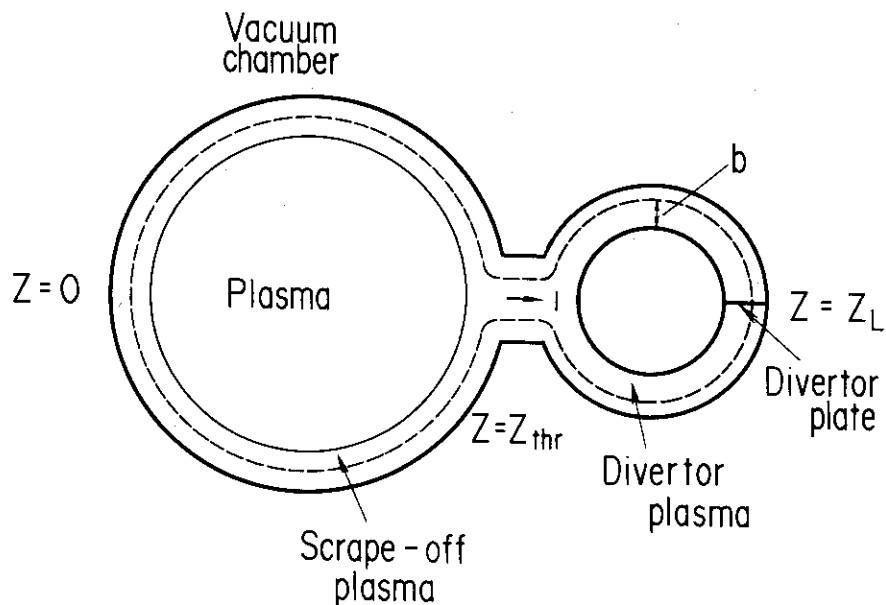


Fig. 3.6.1 Poloidal cross-section of divertor tokamak [30].

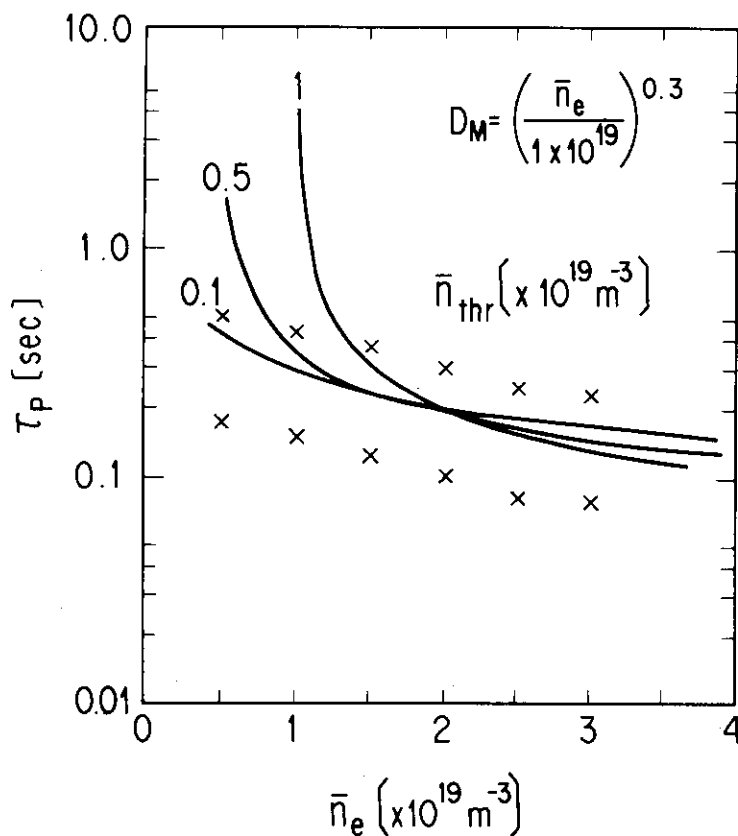


Fig. 3.6.2 Particle confinement times are as a function of average main electron density with electron density at throat entrance as a parameter when diffusion model in main plasma is  $\alpha=0.5$ . Cross marks indicate experimental results in JT-60 (lower) and  $3\tau_p$  (upper).

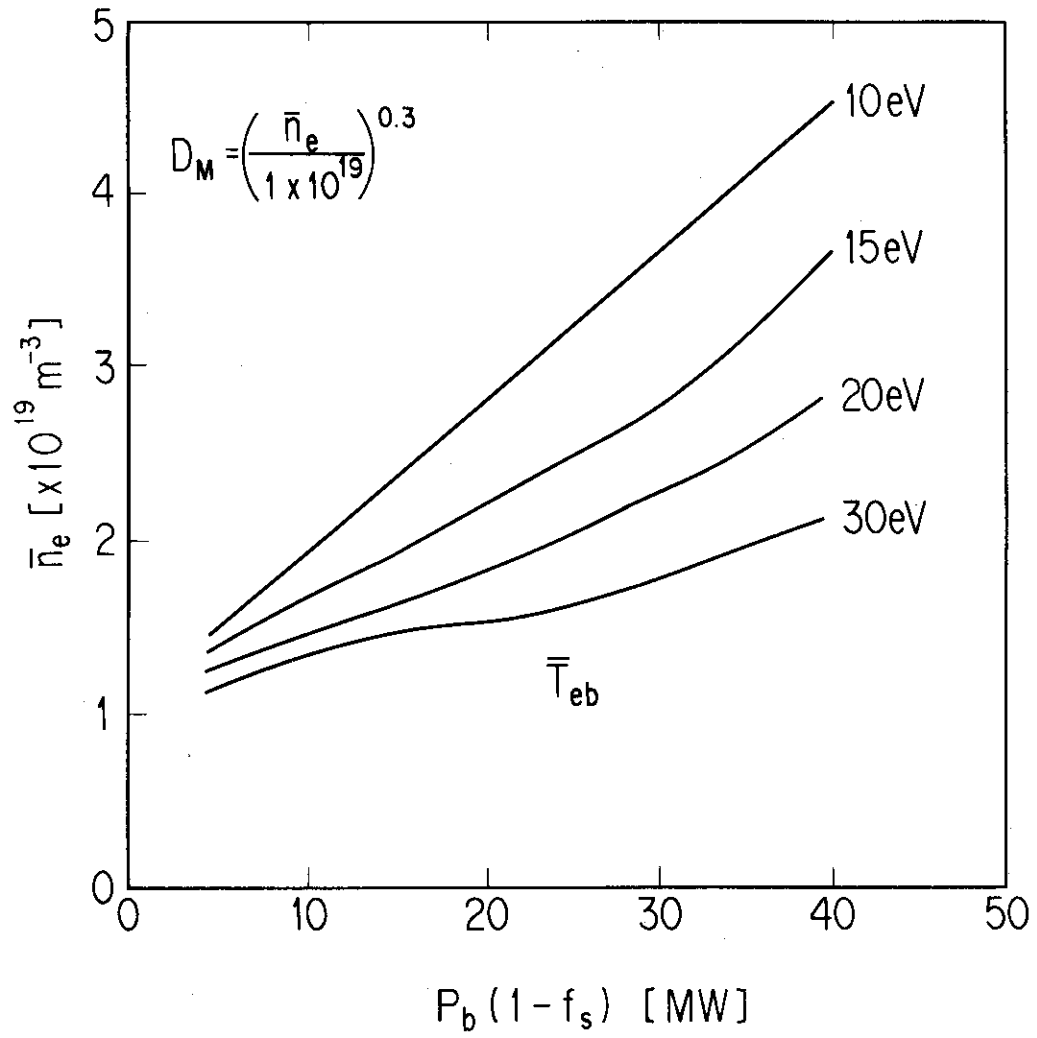


Fig. 3.6.3 Main plasma solutions consistent with the divertor solution.

### 3.7 Steady State Operation

#### 3.7.1 Steady State Operation for Next Generation Tokamak

We now consider the steady state operation scenario for the FER, using the heating power prepared for the ignition approach. Figure 3.7.1a shows an equi-contour map for the minimum heating power  $P_b$  [MW]. The plasma temperature and plasma density profiles are assumed to be  $T(r) = T(0) \times [1 - (r/a)^2]^{0.6}$  and  $n(r) = n(0) \times [1 - (r/a)^2]^{0.5}$ , respectively. The beam energy  $E_b$  is 500 keV. Figure 3.7.1b shows the relation between the Q values and other plasma parameters, corresponding to the contour denoted by the dashed-and-dotted line in Fig. 3.7.1a. The Q value includes the fusion output due to beam-target interaction. The dotted line in Fig. 3.7.1b shows the contour, corresponding to the Troyon beta scaling, expressed as  $\beta_{cr} = C_T I[\text{MA}] / a[\text{m}] B_T[\text{T}]$ , where I, a and  $B_T$  are the plasma current, plasma radius and toroidal field strength, respectively. In this case,  $C_T$ , the coefficient of the Troyon beta scaling, is assumed to be 5. This value is well expected when the current profile is controlled, as shown in Section 3.3. If the total beta value  $\beta_T$  is restricted by this Troyon scaling, the attainable Q value in FER is around 5. The pressure due to suprathermal alpha particles and ion beam particles amounts to 40 to 50 % of the total pressure.

#### 3.7.2 Steady State Operation for Power Reactor

The performance of the fusion plasma is often denoted by the Q value. But, for indicating the performance of the fusion power plant, the following parameter seems to be more appropriate.

$$\alpha_p = P_f / P_{\text{net}}^E$$

where  $P_f$  is the fusion power and  $P_{\text{net}}^E$  is the net electrical power. Figure 3.7.2 shows the relationship between Q and  $\alpha_p$  with a schematic drawing of the power flow in a fusion plant. In a present fission power plant, the circulation power ratio is about 2%. Here, we assume that the circulation power ratio, excluding the NBI power, is 5% and the thermal efficiency is 30%. In both cases of the NBI efficiency  $\eta_b = 0.5$

and  $n_b=0.7$ ,  $\alpha_p$  decreases up to  $Q \approx 15$  but in the region of  $Q > 15$ , the variation of  $\alpha_p$  is rather mild.

A future fusion power plant seems to require a net electrical output of about 1000 MWe with a reasonable beta limit. Under the reactor scale of  $R_p = 6.75$  m,  $a_p = 2$  m,  $\kappa = 1.6$  and  $B_T = 5.2$  T [32], the beam energy  $E_b$  is assumed to be 1 MeV, which seems to be a reasonable value after the 500 keV injection system is completed for the next generation tokamak. How should the operation point be decided?. The beam driven current efficiency is good in high temperature and low density plasma for any given beta. A high plasma temperature (about 30 keV) ensures a maximum Q value, but the fusion output is rather small within a certain beta limit. On the other hand, a low temperature (about 10 keV) ensures maximum fusion output. In this case, however, most of the fusion output is spent for the NBI system.

The above-mentioned relationships are summarized in Fig. 3.7.3. An electron temperature  $\bar{T}_e$  of 20 keV ensures a maximum net electrical output. But this point does not ensure a high Q. Therefore  $\bar{T}_e$  of 25 keV is chosen as a compromise between the requirements of a high net electrical output and a high Q. As a result, a Q value of more than 15 is realized and a net electrical output of more than 700 MWe is expected with a total NBI efficiency of 0.5.

Figure 3.7.4a shows the  $C_T$ -dependence of the Q value and other parameters. The plasma density and plasma temperature profiles are assumed to be  $n(r) = n(0) \times [1 - (r/a)^2]^{\alpha_n}$  and  $T(r) = T(0) \times [1 - (r/a)^2]^{\alpha_T}$ , respectively. In Fig. 3.7.4a,  $\alpha_n = 0.3$  and  $\alpha_T = 1$  are adopted. The influence of density and/or temperature profiles on the Q values is shown in Fig. 3.7.4b. A broad density profile gives a relatively low Q value compared to the peaked density profile, when the total beta value is fixed to be almost the same value. In Fig. 3.7.4a, the beam driven current can be decreased in accordance with the enhancement of the critical beta value under the condition of constant plasma temperature and plasma density, namely, constant fusion output. This results in a reduction in beam input power  $P_b$  and, hence, in an increment of the Q value. It is expected that  $C_T$  for a tokamak plasma with a conventional cross-section is improved more than two times, compared to the normal case, as shown in Section 3.3, owing to current profile controllability with the NBI system. In addition, a maximum field strength on the TF

coil  $B_{\max}$  of 16T may be possible with expected future progress [33]. As a result, a Q value of more than 20 is realized and a net electrical output of more than 700 MWe is expected with an overall efficiency of 0.5. In Fig. 3.7.4a, the toroidal beta value and poloidal beta value are also shown. The pressure due to suprathermal alpha particles and ion beam particles amounts to 30 to 40% of the total pressure. The pressure due to suprathermal alpha particles and ion beam particles may improve the MHD stability and raise the critical beta [34]. In addition, if the bootstrap current can be considered as a realistic aid in the current drive for a steady state tokamak [4,45], the required power for the current drive will be reduced. In the following section, the effect of the bootstrap current on the Q value will be described.

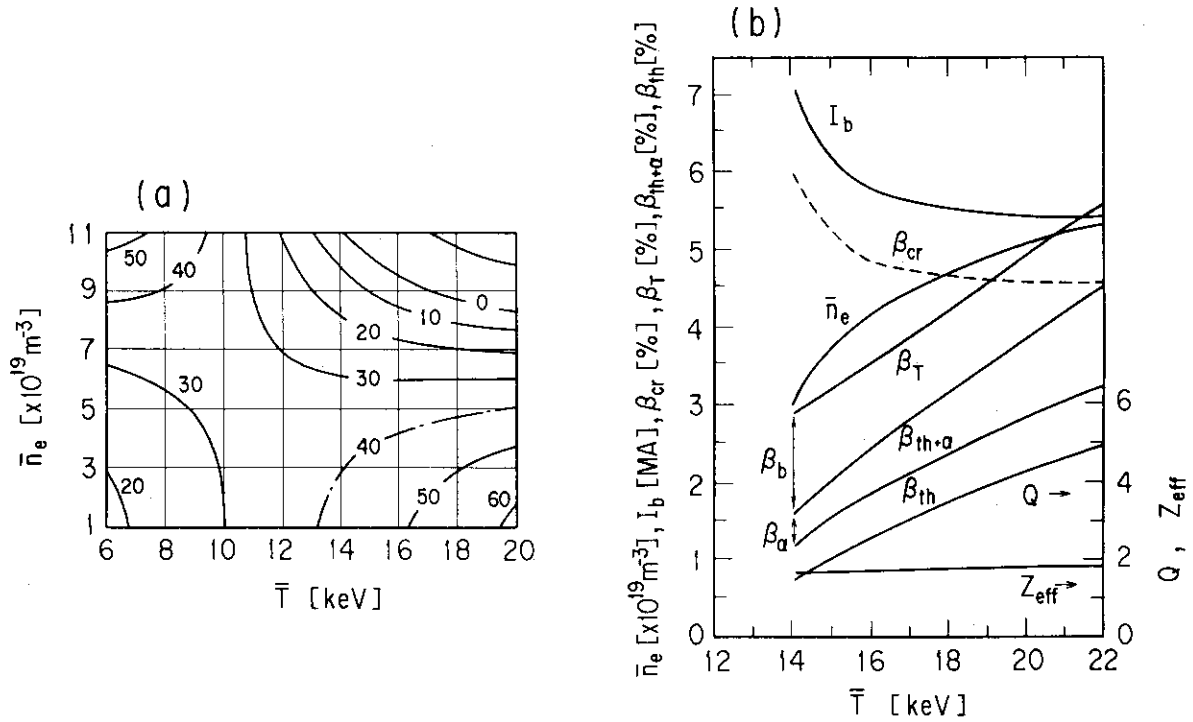


Fig. 3.7.1 Steady-state operation in next generation tokamak. Beam energy  $E_b$  is 500 keV. (a) Equi-contour map for minimum heating power  $P$  [MW] on a density and temperature plane, calculated from a point model of power balance with INTOR-Alcator scaling law as electron energy confinement. Xenon impurity fraction of 0.04% and helium impurity fraction of 5% in the ion density are assumed. (b) Maximum attainable  $Q$  value. Parametric survey is performed along the contour denoted by dashed-and-dotted line in Fig. 3.7.1a. Critical beta value  $\beta_{CT}$  is assumed to follow Troyon beta scaling, described in Fig. 3.4.2 (Scaling coefficient  $C_T$  is 5).  $\beta_T$ : total toroidal beta value, including beta value due to thermal populations  $\beta_{th}$ , due to suprathermal alpha particles  $\beta_\alpha$  and due to ion beam particles  $\beta_b$ .

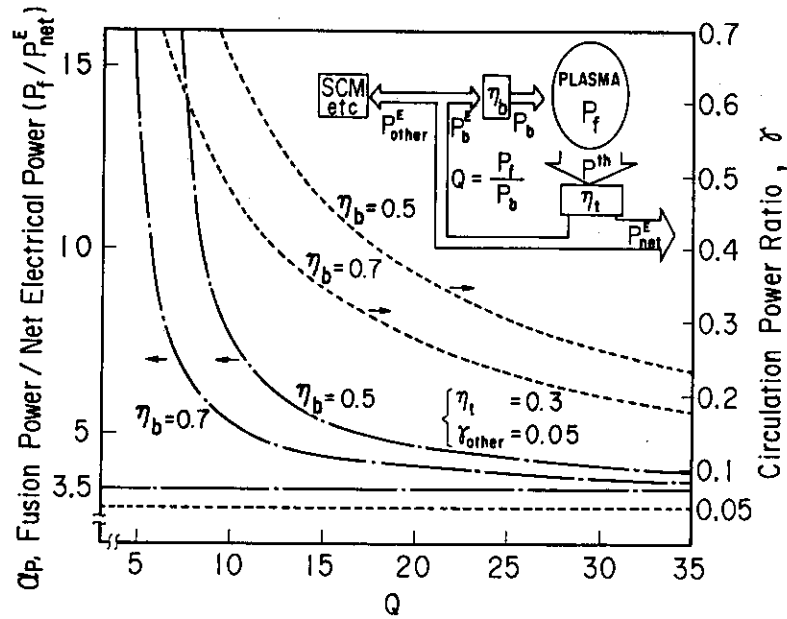


Fig. 3.7.2 Energy multiplication factor  $Q$ -dependence of  $\alpha_p$  and  $\gamma$ . Power flow in a fusion power plant is also shown in this figure  $\alpha_p = P_f / P_{net}^E$ : ratio of fusion power  $P_f$  to net electric power  $P_{net}^E$  and  $\gamma = \gamma_b + \gamma_{other}$ : total circulation power ratio. The definition of notations are as following;  $P_b$ : beam injection power,  $p_{th}$ : thermal output ( $P_f + P_b$ ),  $\eta_{th}$ : thermal efficiency,  $\eta_b$ : NBI efficiency,  $P_b^E$ : circulation power for current drive,  $P_{other}^E$ : circulation power for other,  $\gamma_b + \gamma_{other}$ .

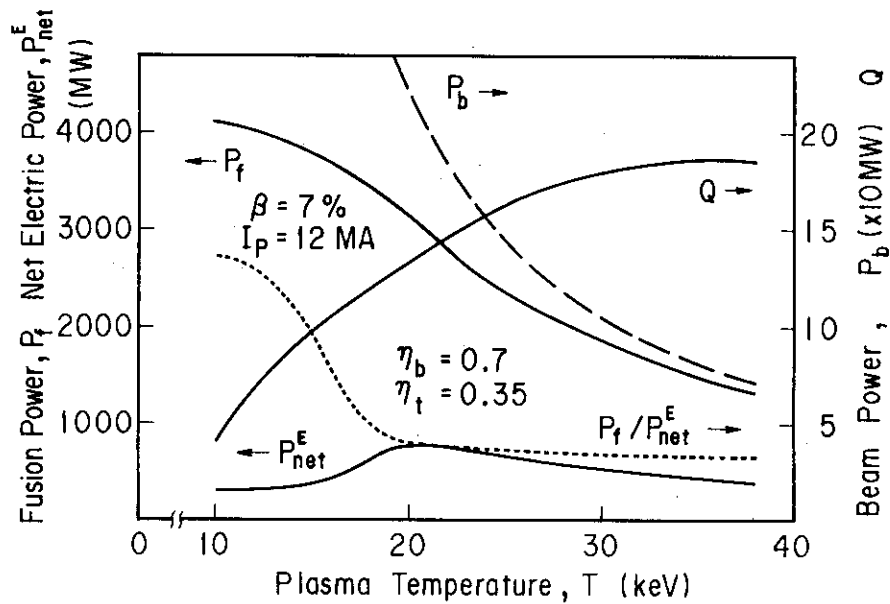


Fig. 3.7.3 Operation point of fusion power plant. Notations are the same as shown in Fig. 3.7.2

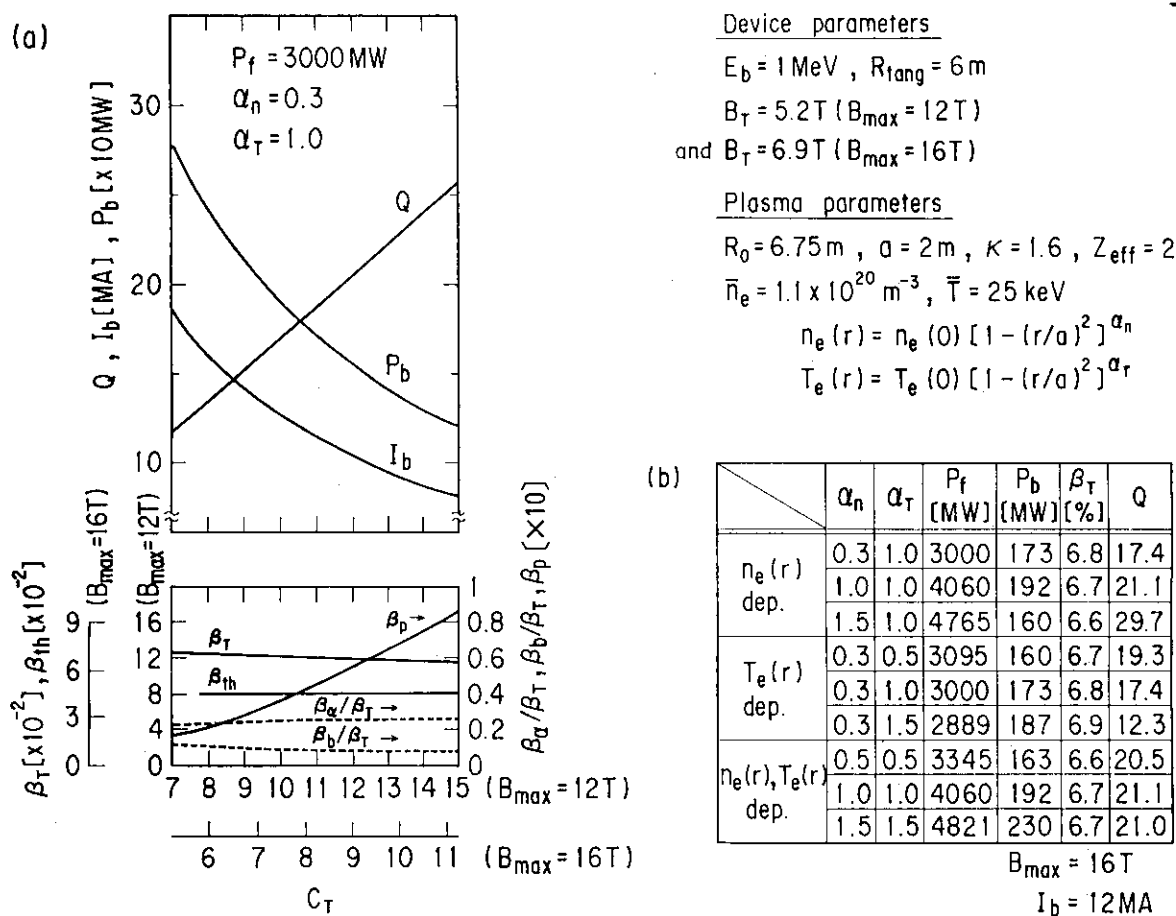


Fig. 3.7.4 Steady state operation in power reactor ( $R_0 = 6.75 \text{ m}$ ,  $a = 2 \text{ m}$ ,  $\kappa = 1.6$ ). Beam energy  $E_b$  is 1 MeV. Plasma density and plasma temperature profiles are assumed to be  $n(r) = n(0) \times [1 - (r/a)^2]^{\alpha_n}$  and  $T(r) = T(0) \times [1 - (r/a)^2]^{\alpha_T}$ . (a)  $C_T$ -dependence of  $Q$  values and other parameters. Plasma temperature and plasma density are fixed to obtain constant fusion output. The maximum field strength on TF coil  $B_{\text{max}}$  is 12 T and 16 T. The pressure due to suprathermal alpha particles and ion beam particles amounts to 30 to 40% of the total pressure. (b) Influence of density and/or temperature profiles on  $Q$  values. Total beta value is fixed to be almost the same value.

### 3.8 Bootstrap Current Effect

Recent experimental measurements in TFTR have shown that substantial plasma currents are created by neutral-beam injection parallel to the magnetic field [4]. In addition, a large fraction (sometimes more than 50%) of the plasma current can only be explained by including theoretically predicted neoclassical (bootstrap) effects. Theory has predicted that radial diffusion induces a current (bootstrap current) in the toroidal direction and that the current becomes large in the banana region [35,36,37].

The origin of the bootstrap current is as follows. Electrons in the collisionless region  $v_{ei} < v_b$  make complete circuits of a banana orbit. When a density gradient exists, there is a difference in the number of particles on a neighboring banana orbit passing through a point A, as shown in Fig. 3.8.1. The difference is  $(dn_t/dr)\Delta_b$ ,  $\Delta_b$  being the width of the banana orbit. When the component of the velocity parallel to the magnetic field is denoted by  $v_{//}$ , its value for the banana particles is  $v_{//} = \epsilon^{1/2} v_T$ , where  $v_T$  is the thermal velocity. Consequently, the current density due to the trapped particles is

$$j_{bt} = (e v_{//}) \left( -\frac{dn_t}{dr} \Delta_b \right) = -\epsilon^{3/2} \frac{1}{B_p} \frac{\partial p}{\partial r}$$

The untrapped particles start to drift in the same direction as the trapped particles due to the collisions between them, and the drift becomes steady-state due to the collision with ions. The drift velocity  $V_b$  of untrapped particles in a steady state is given by

$$v_{ei} m_e v_b = \left( \frac{v_{ee}}{\epsilon} \right) m_e \left( \frac{j_{bt}}{-en_e} \right),$$

where  $v_{ee}/\epsilon$  is the effective collision frequency between trapped and untrapped electrons. The current density due to the drift velocity  $v_b$  of the untrapped electrons is

$$j_b = -0.33 \epsilon^{1/2} \frac{1}{B_p} \frac{\partial P}{\partial r} \propto (a/R)^{1/2} \beta_p$$

Since  $\beta_p$  should be about unity in next generation devices such as the FER, a substantial fraction of the current could come from neoclassical effects.

Inspired by the above mentioned experimental results, we analyze the beam driven current with bootstrap effects. The expression for the neoclassical current is the Hinton-Hazeltine smoothed banana-plateau formula [38]. We develop an algorithm to solve the beam driven current, being consistent with MHD equilibrium. The algorithm is shown in Fig. 3.8.2. There are two options; one is the case with the regulation of injection power for a fixed plasma current, and the other is the case with the regulation of plasma current for a fixed injection power. Notations in Fig. 3.8.2 are the same as those in Section 3.3 and a detailed description is given in Appendix 6. An example of convergence of the equilibrium plasma current in the calculation is shown in Fig. 3.8.3. Usually the number of iterations  $N_{it}$  is within 10. We have carried out calculations for the FER Option C reactor described in Section 5. The radial density and temperature profiles are used:  $n \propto (1-\psi/\psi_s)^k$  and  $T \propto (1-\psi/\psi_s)^m$ , where  $k = 0.5$  and  $m = 1.0$ . Table 3.8.1 shows the numerical results with neoclassical effects and without neoclassical effects. Plasma current regulation is used. For  $I_p = 7$  MA, a required power is 103.9 MW without neoclassical effects and 55.6 MW with neoclassical effects in the case of  $E_b = 500$  keV and  $Z_{eff} = 2$ . The Q value with neoclassical effects increases from 2.8 to 5.42. The total output  $P_T$ , including the thermal output  $P_{th}$  and the fusion output due to beam-target interaction, is also shown.

The bootstrap effect on the Q value in a power reactor ( $R_o=6.75$  m,  $a=2$  m,  $\kappa=1.6$ ,  $B_T=6.9$  T,  $R_{tang}=6$  m) is also examined. The beam energy  $E_b$  is 1 MeV. The plasma density and plasma temperature profiles are assumed to be  $n = 1.75 \times 10^{20} [m^{-3}] x (1-\psi/\psi_s)^{0.3}$  and  $T = 50 [keV] x (1-\psi/\psi_s)$ . The calculation results are shown in Fig. 3.8.4. Notations are the same as those in Fig. 3.3.1. For a fixed plasma current of  $I_p = 15$  MA, the required power is 282 MW without neoclassical effects and 127 MW with neoclassical effects. In the case with bootstrap effects, the total output, the Q values and Troyon coefficient  $C_T$  are 3075 MW, about 24 and 6.21, respectively. In the case without bootstrap effects, these values are 3129 MW, about 11 and 6.47, respectively. The Q value with neoclassical effects increases from 11 to 24.

Table 3.8.1 Calculation results with and without bootstrap effects for the FER.

	w. B.S	w/o B.S	Op. C
R [m]	4.92		
a [m]	1.32		
K	1.7		
$\delta$	0.2		
B <sub>T</sub> [T]	4.68		
$\bar{T}$ [keV]	16	15	12
$\bar{n}_e$ [ $10^{20} \text{ m}^{-3}$ ]	0.72	0.67	1.09
P <sub>b</sub> [MW]	55.6	103.9	
P <sub>th</sub> [MW]	262	219	459
P <sub>TCT</sub> [MW]	39.8	71.9	
P <sub>T</sub> [MW]	302	291	
$\beta_p$	1.84	1.85	
$\beta_T$ [%]	5.74	5.83	4.9
I <sub>b</sub> [MA]	3.76	7	7
I <sub>BS</sub> [MA]	3.24		
I <sub>p</sub> [MA]	7	7	8.69
C <sub>T</sub>	5.1	5.1	3.5
Q	5.42	2.8	$\infty$

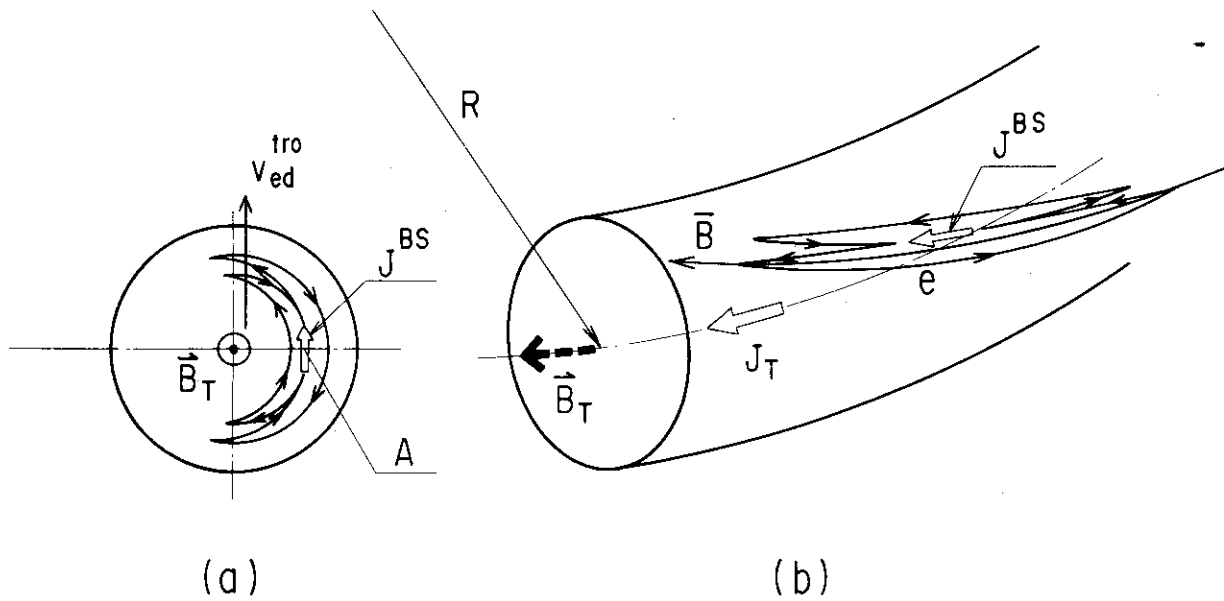


Fig. 3.8.1 Banana motion of electrons that induce the bootstrap current.

$I_p$  : fixed by  $P_b$  regulation  
 or  $P_b$  : fixed by  $I_p$  regulation

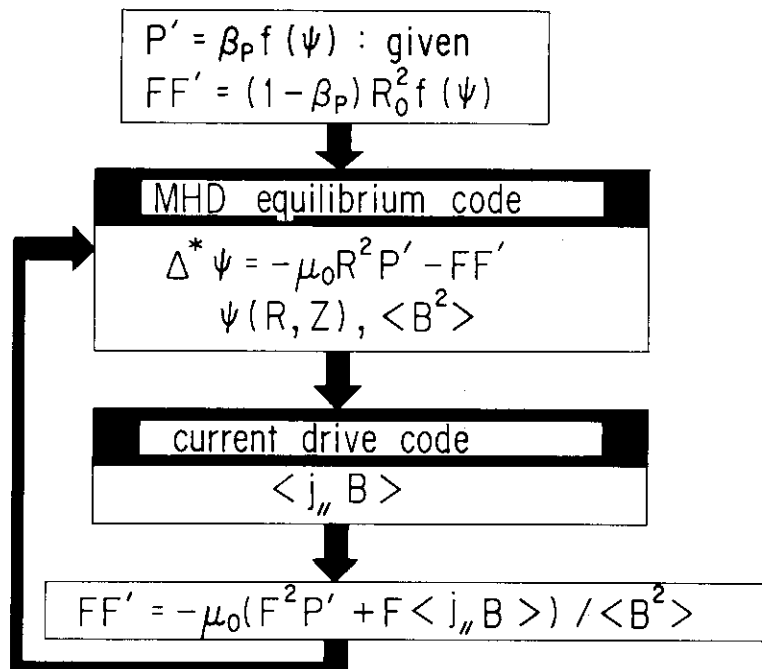


Fig. 3.8.2 Algorithm to solve the beam driven current, being consistent with MHD equilibrium.

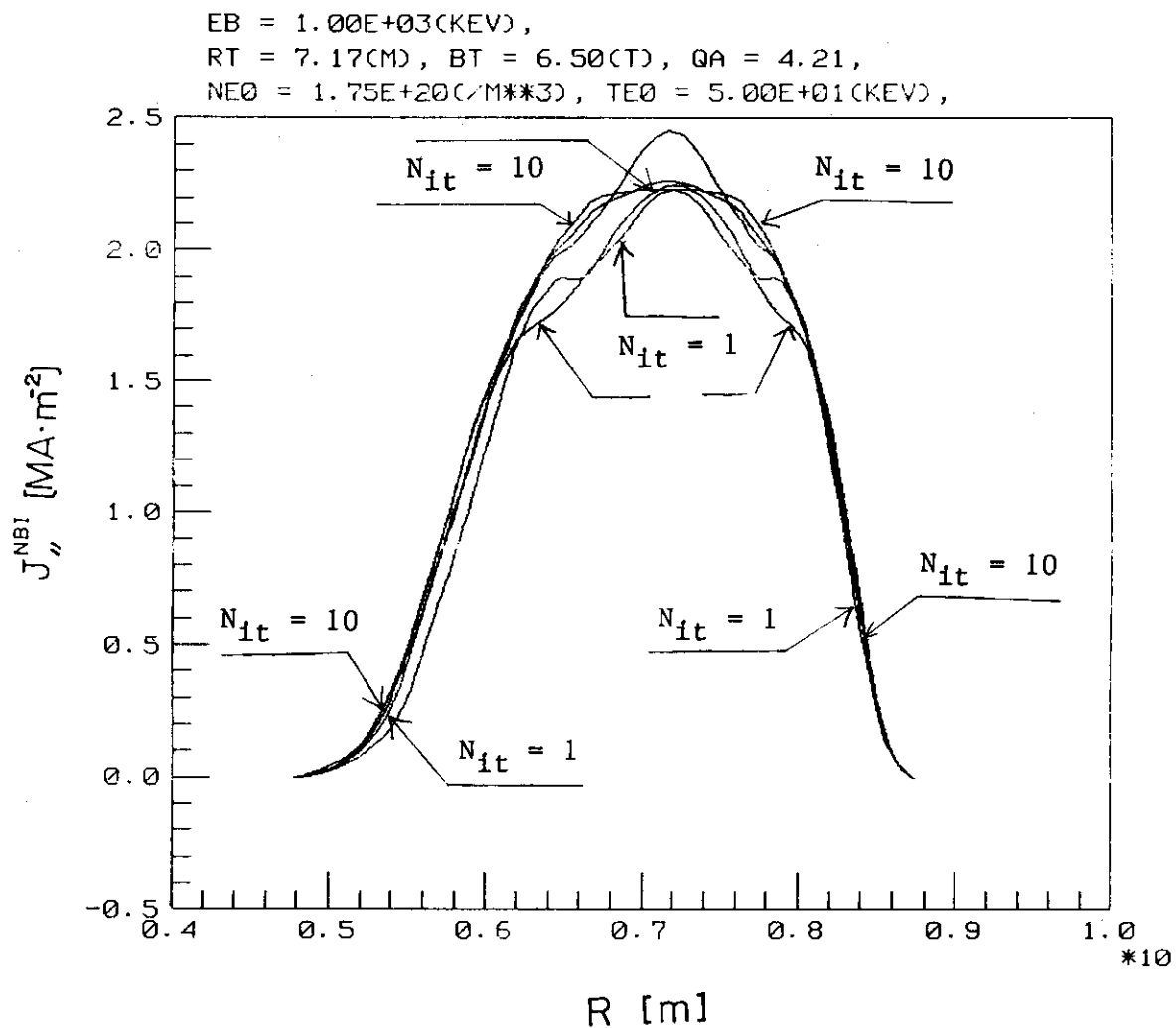


Fig. 3.8.3 Example of convergence of equilibrium plasma current in the calculation.  $N_{it}$  denotes the number of iterations.

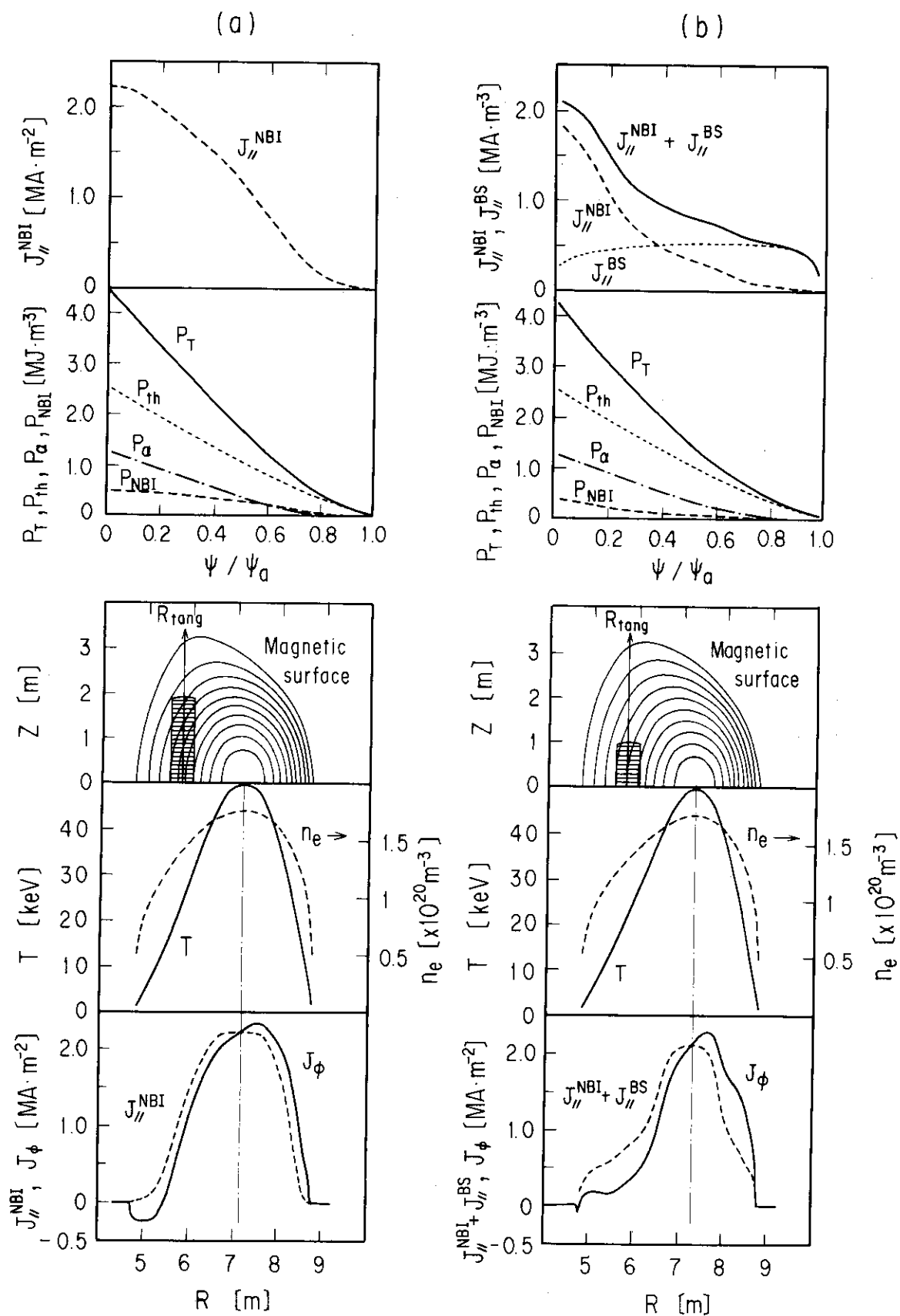


Fig. 3.8.4 Calculation results with and without bootstrap effect for the fusion power reactor.

### 3.9 Plasma Rotation Effect

In this section, plasma rotation effects on plasma confinement and the beam driven current efficiency are described. In the JFT-2 tokamak, the toroidal plasma rotation induced by the momentum input associated with unbalanced beam injection was studied to clarify the possible effects on the transport processes [39]. There was no difference between the incremental energy with co-injection, with counter injection and with balanced injection. Figure 3.9.1 shows the experimental results obtained in D-III [40]. The toroidal rotation speed was measured in a series of discharges by a spectrometer with a wavelength shift of 0.8 Å lines on an NBI beam path. For a constant value of plasma density and heating power, the peak rotation speed just before the onset of  $H_\alpha$  peripheral disruption has a linear correlation with the ion temperature, as is shown in Fig. 3.9.1. The rotation speed measured by a Doppler system is consistent with the toroidal phase velocity of the  $B_p$  fluctuation. The points at high  $T_i(0)$  correspond to the H-mode discharge and the lower  $T_i(0)$  values correspond to the L-mode discharge because the points shown in Fig. 3.9.1 are for almost the same heating power. The data for limited discharges are plotted on the same line. This suggests that the phenomenon, at least in the central region of the plasma, are continuous from limited to H-mode discharge. Discharges with confinement have a large rotation velocity, suggesting a close relationship between energy confinement and momentum confinement. The above mentioned experimental results suggest that plasma rotation effect of plasma confinement is small.

On the other hand, a new mode of enhanced energy confinement, the so called super shot, has been observed for TFTR with near-balanced injection [41]. The super shot exhibits improved electron stored energy, as well as improved beam and thermal ion stored energy. Peaked density profiles observed in this regime appear. A number of classically expected factors may lead to reduced density peaking and poorer heating efficiency at high rotation speed with unidirectional injection. In a rotating plasma frame the beam ions, and especially the fractional energy component beam ions (which constitute about one half of the total beam in the TFTR), have considerably reduced energy. This results in larger atomic cross-section for beam deposition and a larger

fraction of the deposition on hydrogenic species in the form of charge-exchange rather than impact ionization as shown in Fig. 3.1.1. A lowered beam velocity in the plasma frame results in a strong reduction in the beam-target and beam-beam fusion neutron yields; unidirectional injection reduces beam-beam neutron production as well.

In the FER, beam energy is 500 keV. Even if the plasma rotates with an ion thermal velocity  $v_{Ti}$ , the atomic cross-section for beam deposition is effectively in the form of impact ionization. Thus, confinement properties will be independent of the injection method.

Next, we consider the plasma rotation effect on beam driven current efficiency. Numerical results are shown in Fig. 3.9.2. An effective beam speed is defined as the difference between the injection velocity  $v_b$  and plasma rotation speed  $v_\phi$  and the effective beam energy is  $E_{eff} = m(v_b - v_\phi)^2/2$ . Solid and open dots correspond to the case of  $v_\phi = v_{Ti}$  and  $v_{Ti}/2$ , respectively, where  $v_{Ti}$  is the ion thermal velocity.  $I_b(E_{eff})/I_b(500\text{keV})$  means the ratio of the induced plasma current with an effective beam energy  $E_{eff}$  to the current with 500 keV. The current drive efficiency is reduced within 10 to 20 percent. Owing to the estimation by Goldston, the maximum rotation speed in the next generation machine will be below 20 percent of the ion thermal velocity when the injection energy is 500 keV [42]. In this case, the rotation effect on the beam driven current efficiency is negligibly small.

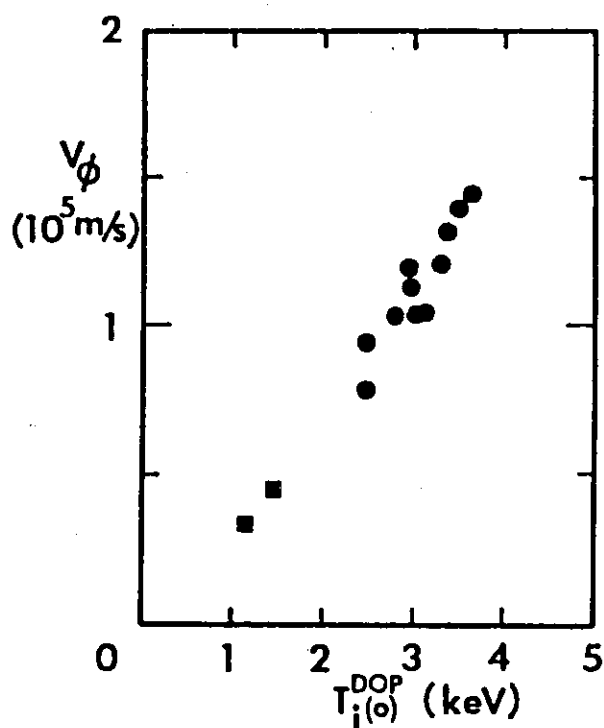


Fig. 3.9.1 Toroidal rotation speed versus central ion temperature observed in D-III [40]. ● Divertor discharge, ■ limiter discharge,  $P_{inj}=4.5-5.0$  MW,  $\bar{n}_e=(5-7)\times 10^{13} \text{cm}^{-3}$ ,  $I_p=750-830$  kA,  $B_T=2.0-2.6$  T.

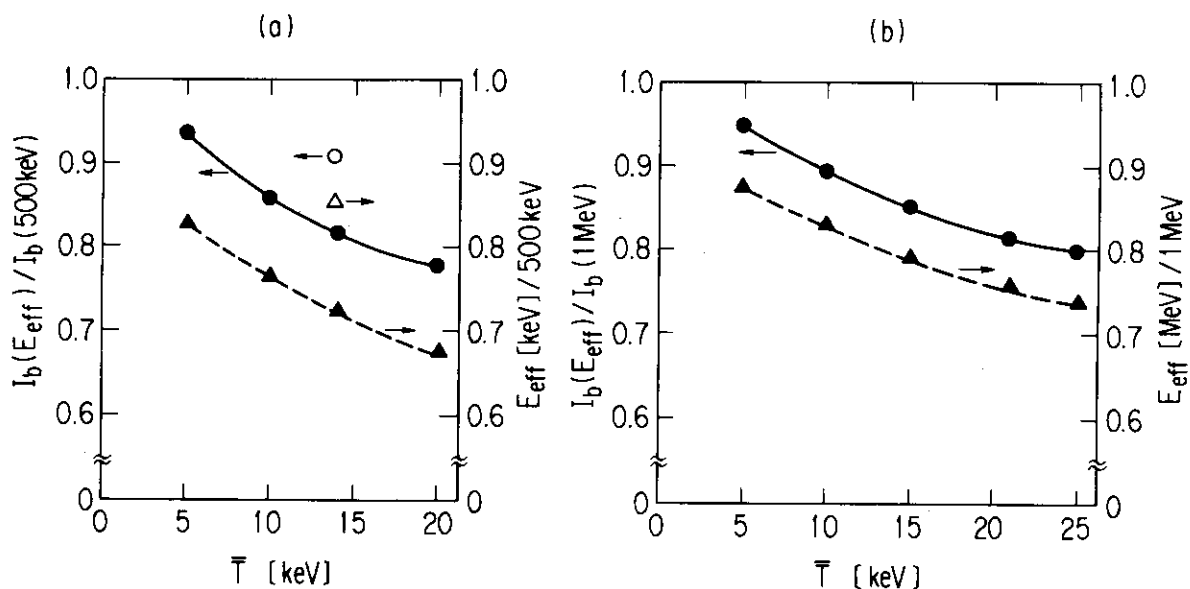


Fig. 3.9.2 Effect of plasma rotation on beam driven efficiency. Effective beam speed is defined as the difference between injection velocity  $v_b$  and plasma rotation speed  $v_\phi$  and effective beam energy is  $E_{eff}=m(v_b-v_\phi)^2/2$ . Solid and open dots correspond to the case of  $v_\phi=v_{Ti}$  and  $v_{Ti}/2$ , respectively, where  $v_{Ti}$  is ion thermal velocity.  $I_b(E_{eff})/I_b(500\text{keV})$  means ratio of induced plasma current with effective beam energy  $E_{eff}$  to the current with 500 keV.

### 3.10 Summary

The operation scenario, based on plasma heating and current drive by a 500 keV/20 MW negative-ion-grounded NBI system, has been proposed as one of the operation scenarios for the FER. Applying the NBI system technology with a beam energy of 500 keV to the FER represents a reasonable step from the present database. The system may be used for plasma heating, current drive and current profile control, concurrently. The quasi-steady state operation by the NBI system realizes nearly steady state conditions for the reactor structural components. Steady state operation can also be demonstrated by using an injection power of 40 MW, prepared for the ignition approach. Q values of around 5 can be expected in this steady state operation, if the coefficient of Troyon beta scaling is increased from 3.5 to 5. According to numerical results, this beta enhancement can be realized when the beam driven current profile is controlled. The control of the current profile is easily performed by this system. The impact of the NBI system on the reactor structural configuration and maintenance is favorable. The steady state operation scenario in the power reactor is also considered. The beam energy for the NBI system in the power reactor is assumed to be 1 MeV. This value seems to be reasonable, after the 500 keV injection system is completed for the FER. The critical beta value for the tokamak plasma with a conventional cross-section is expected to be improved more than two times, compared to the normal case, when the beam driven current profile is controlled by the NBI system. In a steady state operation for the power reactor with a fixed fusion output, the required current for equilibrium and stability can be reduced, when the critical beta value is increased. This results in a reduction in the required beam power, hence, in an enhancement of the Q value. In addition, if the maximum field strength on the TF coil is increased from 12 T to 16 T, a Q value of more than 20 is realized within a reasonable beta value.

Two critical issues are drawn for the NBI current ramp-up, i.e., the beta limitation (especially poloidal beta in low plasma current), and the density build-up combined with excessive electron heating. NBI power control in the early stage of plasma current ramp-up is quite effective for both the total beta and the poloidal beta suppressions,

while this control tends to expand current ramp-up time. One possibility to shorten the ramp-up time while keeping poloidal beta limitation is a small minor radius start-up with a constant low  $q_\psi$  value. A lower  $q_\psi$  value increases the plasma aspect ratio for a given plasma current, maximum toroidal field and elongation. The problem for this scenario is adjusting the beam line and shinethrough. It should be addressed that the possibility of the direct control of the energy and particle confinement times will be a future study for attaining fast and effective NBI current ramp-up.

The bootstrap current effect on the Q value is examined. We develop an algorithm to solve the beam driven current with the bootstrap current, being consistent with MHD equilibrium. If the bootstrap current can be considered as a realistic aid in current drive for a steady state tokamak, the required power for current drive will be reduced. In the FER, the plasma rotation effect on plasma confinement and beam driven current drive efficiency are expected to be small.

#### 4. A 500 keV/20 MW Negative-Ion-Grounded Neutral Beam Injection System

This NBI system consists of a beam line, a 500 keV power supply system, an evacuating system including a tritium handling system, a cooling water circulating system and auxiliary sub-systems [43]. The beam line consists of an intense negative ion source, a beam profile controller, a long gas neutralizer, an ion beam dump, a neutron shutter and an injection port of the torus. In both the ion source room and the beam dump room (or ion dump room), cryopanel is mounted. The neutralizer and the ion source room are shielded magnetically, and the beam line is covered with neutron shields.

##### 4.1 Beam Line Design

The ion source produces a 500 keV, 100 A negative deuterium ions. The profile of the extracted ion beam is changed by the beam profile controller before the ions enter the gas neutralizer. In the neutralizer, about 60% of the ion beam is converted to neutrals by collisions with the background deuterium molecules. The residual ions ( $D^-$ ,  $D^+$ ) are deflected by the tokamak poloidal field in the downstream region of the neutralizer exit and guided to the ion beam dump. The neutral beams are injected to the plasma through the torus injection port. Figure 4.1.1 shows a power and gas flow of the system at a beam energy of 500 keV. Out of 120 A  $D^-$  ions extracted from the ion source, 92 A  $D^-$  ions are accelerated to 500 keV, while 28 A  $D^-$  ions are lost by the gas collisions in the accelerator. In addition, 7 A  $D^-$  ions are lost by colliding with the side walls of the neutralizer. The equivalent current of neutrals going through the neutralizer exit is 50.2 A. Unneutralized negative ions (13.2 A) and re-ionized positive ions (21.6 A) are deflected towards the ion beam dump. In the injection port region, 3.8 A deuterium neutrals are lost due to direct interception by the port, and 2.0 A neutrals are lost by re-ionization. After all, 44.4 A equivalent neutrals whose power is 22.2 MW are injected into the FER tokamak, which corresponds to 46% of the acceleration beam power. The  $D_2$  gas is introduced into the ion source with a rate of 11.7 Pa·m<sup>3</sup>/s. The gas is evacuated by cryopumps located

at the ion source room and the beam dump room. The pumping speeds are 700 m<sup>3</sup>/s and 150 m<sup>3</sup>/s, respectively, resulting in pressure distribution, as shown in Fig. 4.1.1. It seems to be unnecessary to control the line density in the neutralizer for the purpose of obtaining a maximum neutralization efficiency in the energy range of 200 keV to 500 keV, because the optimum line density does not change so much in this energy range. However, control will be required in order to keep the heat flux on the beam dump surface below a permissible value, because the power fractions of the D<sup>-</sup> beam and D<sup>+</sup> beam are sensitive to the gas line density. Table 4.1.1 summarizes the major performance characteristics of the present NBI system.

The design is a little conservative so as to be realized in the near future. However, this injector has several prominent characteristics as follows:

- (1) Due to the long, slender gas neutralizer (0.3 meter wide by 24 meters long), the gas load to be handled and the neutron irradiation in the ion source room can be reduced considerably.
- (2) The plasma current profile can be controlled by changing the neutral beam profile. The beam profile is changed by applying a transverse magnetic field at the entrance of the neutralizer.
- (3) In order to deflect the residual ions (D<sup>-</sup>, D<sup>+</sup>) to the ion beam dump, poloidal magnetic fields are used. Hence, the conventional bending magnet, which takes much space in the reactor, can be eliminated.
- (4) In the design of the acceleration power supply system, an AC switch coupled with a high frequency AC line (~5 kHz) is used instead of a DC switch. This will improve the reliability of the power supply system.
- (5) The beam energy and power can be controlled individually during the beam injection phase.

In the next section, major beam line components will be described.

Table 4.1.1 Major performance characteristics of the present 500 keV/20 MW injection system.

## Overall

Neutral Beam power	22.2 MW
Power Density	16.4 MW/m <sup>2</sup> (average)
Beam Energy	200-500 keV
Pulse Length	10 sec - DC
Ion Species	D
Power Efficiency	46 % (at 500 keV)
Acceleration	96 %
Neutralization	59 %
Geometrical	85 %
Re-ionization	96 %

## Ion Source

Number	1
Type of D <sup>-</sup> Source	Volume Production
Size	0.2m x 2.4 m (grid)
Extracted Current	120 A
Accelerated Current	96 A
Current Density	50 mA/cm <sup>2</sup>
Divergence (e-folding half width)	5 mrad
Transparency	50 %

## Neutralizer

Size	(0.26-0.4)m x (2.4-1.4)m x 24 m
Line Density	$7.5 \times 10^{15}$ molecules/cm <sup>2</sup>
Pressure	$1.6 \times 10^{-2}$ Pa (at entrance)

## Injection Port

Size	(0.44-0.5)m x (1.8-2.8)m x 11 m
Pressure	$4 \times 10^{-3}$ Pa (at entrance)
Gas Flow into Torus	0.13 Pa m <sup>3</sup> /s

## Cryo-Pump

Source Chamber	700 m <sup>3</sup> /s
Beam Dump Chamber	150 m <sup>3</sup> /s

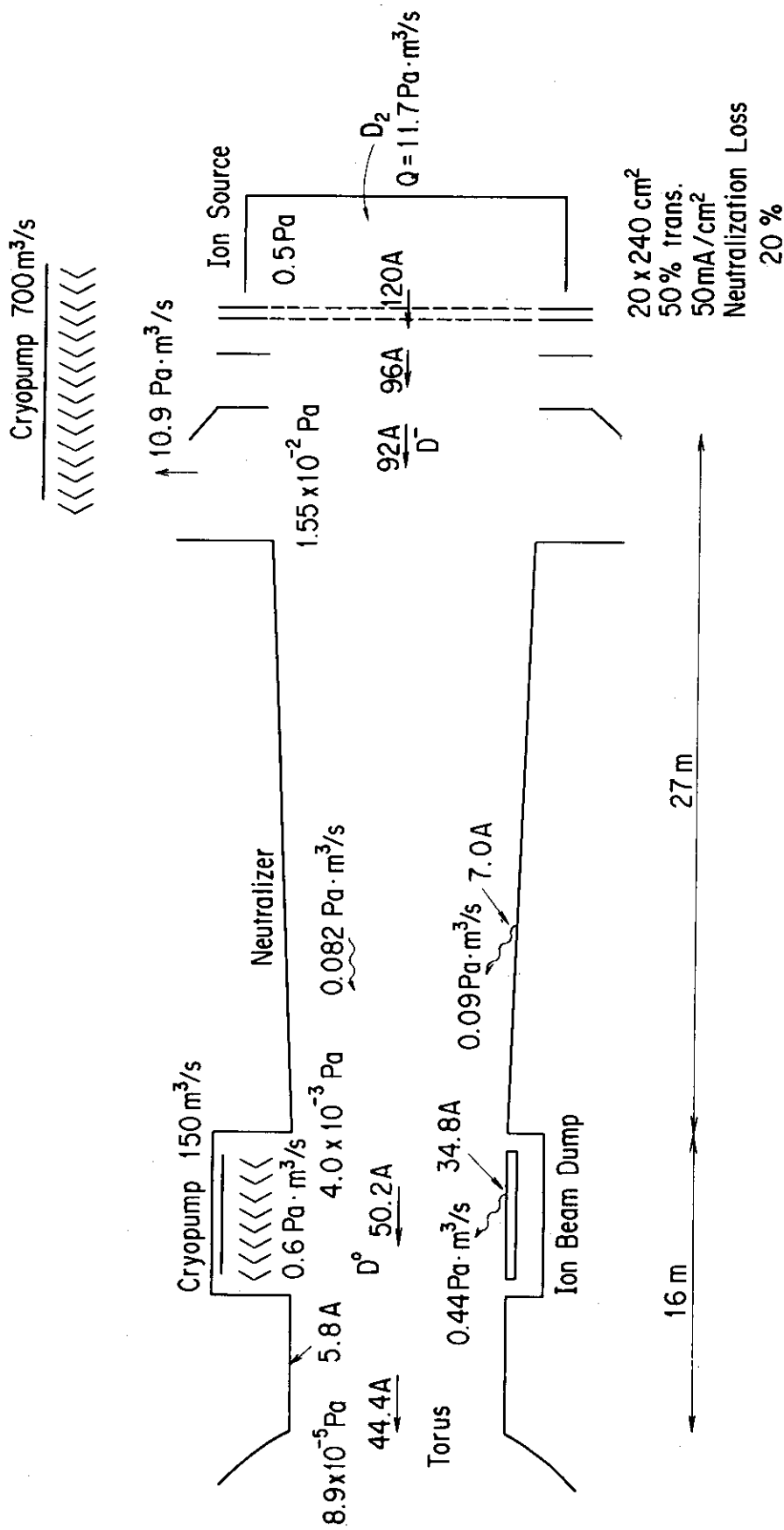


Fig. 4.1.1.1 Power flow and gas flow of the system

## 4.2 Major Components of Beam Line System

### 4.2.1 Ion Source

#### <H<sup>-</sup> Production>

In this design, a volume produced D<sup>-</sup> ion source is employed. Out of several approaches to produce D<sup>-</sup> ion beams, volume production has big advantages over other methods, such as the charge exchange method and the surface production method.

1. The extracted beam has good beam qualities: i.e., low emittance, high brightness, and low impurity content.
2. Since no cesium is required, the associated voltage breakdown problems resulting from cesium contamination of the accelerator column are avoided.
3. The structure is simple enough to scale up.
4. Stable and reliable operation has been demonstrated experimentally.

These advantages make the volume production method the most attractive for use in future injectors. The present status of negative ion source is summarized in Appendix 3. In the volume production type source, an H<sup>-</sup> beam with a current of 1.26 A was already produced at JAERI using the source shown in Fig. A3.2 of Appendix 3. However, the current density was still as low as 10 mA/cm<sup>2</sup>. At the lower extraction current, on the other hand, a higher current density of more than 50 mA/cm<sup>2</sup> is obtained. Hence, in the present design, a single, big volume ion source, which has dimensions of 0.2 m × 2.4 m for the extraction grid size, is applied to obtain D<sup>-</sup> ions of 120 A with a current density of 50 mA/cm<sup>2</sup>. The technology for sophisticated high current positive ion sources, i.e., large area plasma production, can be applied to develop such a big negative ion source. The most important point in developing the source is that the D<sup>-</sup> ions must be produced in a low filling pressure of around 0.5 Pa in order to suppress the neutralization loss in the accelerator.

#### <Pre-accelerator>

When the D<sup>-</sup> ions are extracted from a volume source, a large amount of electrons are accompanied. In order to prevent these electrons from

entering the main accelerator, they must be handled in the pre-accelerator. Figure 4.2.1 shows one of the optimized pre-acceleration systems where the electrons are deflected to the electron recovery electrode by a transverse magnetic field. The magnetic field is produced by two magnets inserted in the electrode. Only the  $D^-$  ions go straight to the main accelerator without being disturbed by the magnetic field ( $\leq 100$  Gauss-cm). It is important to minimize the heat flux on the surface of the electron recovery electrode.

#### <Main accelerator>

The accelerator of existing high current positive ion sources is composed of multi-aperture grids. If the negative ion accelerator is designed in the same manner as those of the positive ion accelerators, the negative ion loss becomes very large due to beam-gas collisions, because the cross section for electron stripping of  $D^-$  in  $D_2$  gas is unfortunately very large. The loss was estimated to be 40%, provided the pressure in the source plasma generator is 0.5 Pa. In order to minimize the loss, we adopted an accelerator shown in Fig. 4.2.2. Unlike the pre-accelerator composed of multi-aperture grids, the main accelerator consists of grids with large bore apertures or slots so as to increase the conductance for pumping. The  $D_2$  gas flowing from the plasma generator is evacuated from the apertures as well as from both sides of the main accelerator grids. Figure 4.2.3 shows the distribution of the gas pressure and electrical potential along the beam axis when the pressure in the arc chamber is 0.5 Pa. The stripping loss of negative ions is 17% in the pre-accelerator and 4% in the main accelerator. Since the beam energy is small in the pre-accelerator, the loss of 17% does not affect very much on the total power efficiency.

Another important point in designing the main accelerator is to produce a very convergent beam with an e-folding half-width divergence angle of less than 5 mrad in order to obtain a high geometrical transmission efficiency. Figure 4.2.4 shows one of the optimum acceleration systems, where three beamlets from the pre-accelerator are merged in the main accelerator. The maximum electric field strength between the grids is less than 5 kV/mm, which will make it possible to operate the accelerator stably. The slot geometry is preferable in that

it gives not only large gas conductance than the aperture geometry but also higher optimum perveance for a fixed electric field strength between the gaps. The merged beams are focused at a point about 40 meters from the ion source by curving the grids or by shifting the axis of the slot. The beam energy and beam power can be controlled individually during an injection pulse by varying the gap length of the accelerator and the potentials of each grid. The cross section view of the ion source room is shown in Fig. 4.2.5.

#### 4.2.2 Beam Profile Controller

Control of the plasma current profile is possible by changing the spatial intensity distribution of the neutral beams. The ion source produces a sheet beam with a cross section of 0.2 meter wide by 2.4 meters high. The beam is focused at the entrance of the torus injection port, which is about 40 meters from the ion source. In order to control the current profile efficiently, the focused beam must be deflected vertically by about 25 mrad, which corresponds to a shift of 1.2 meters at the target plasma 48 meters from the ion source. The beam can be deflected by applying a transverse magnetic field between the exit of the accelerator and the entrance of the neutralizer. The upper half and lower half beams are deflected in opposite directions by applying inverse magnetic fields to each beam, so that crossed beams can be formed, as shown in Fig. 4.2.6a. Hence, it is possible to produce various kinds of beam profiles from a Gaussian-like profile to a hollow profile at the plasma.

The vacuum pressure is typically  $1.55 \times 10^{-2}$  Pa in the region between the exit of the accelerator and the entrance of the neutralizer. Therefore, only a small amount of deuterium negative ions are neutralized before the ions are deflected by the controller.

The transverse field is produced by four modified solenoid coils as shown in Fig. 4.2.6a. The coils are deformed near the beam axis in order to reduce the vertical component of the magnetic field which increases the beam divergence. The return magnetic field is minimized by enclosing the coils with mild steel in order to decrease the required ampere-turn of the coils and to reduce the stray magnetic field in the ion source region. By optimizing the shape and size of both the coils

and the mild steel, the upper and lower beams are deflected by 25 mrad with a coil current of about 2000 ampere-turns, as shown in Fig. 4.2.6b.

#### 4.2.3 Neutralizer

There are three options for the neutralization of negative deuterium ions; i.e., (a) laser photo-neutralization, (b) plasma neutralization, and (c) gas neutralization. The laser neutralizer strips the negative ions by photodetachment in a laser resonator. Though nearly 99% neutralization is possible by this method, the required laser power is estimated to be about 1 MW, provided the reflectivity of the mirror is the 99.95% and the transparency of the window is 99.5%. Considering the production efficiency of the laser (<10%), the required power input to the laser is estimated to be greater than 10 MW. Thus, photo-neutralization is impractical in our design as far as it is based on the present technology of the laser. In the case of the LBL design mentioned above, photo-neutralization might be practical because the ion beam is strongly focused by transverse field focusing, and thus the transverse dimension of the laser resonator is small resulting in a small laser power (75 kW).

The plasma neutralizer provides up to 87% neutralization efficiency in a fully ionized plasma and about 70% neutralization with 10% ionized plasma. However, it is difficult to generate such a highly ionized plasma over a wide area. Based on the efficiency of producing a plasma in a multicusp plasma generator, the required power to produce the 10% ionized deuterium plasma was estimated to be a few MW, which cancels the merit of plasma neutralization. Using high atomic mass gases (e.g. xenon) seems to be a better way in realizing the plasma neutralization especially in our present design, because these impurity gases will be easily pumped out due to small conductance of the beam line. Multiple ionization of these gases leads to higher stripping efficiency, which will reduce the required power. However, such a plasma neutralizer has not been developed yet and we do not have a sufficient database at this time. In addition, the utilization of gases will require an extra handling system for the radio-activated gases.

Thus, we chose conventional gas neutralization in the present design. The fast negative ions are converted to neutrals and positive

ions by collisions with the neutral gas by processes of stripping and charge exchange. The converted fraction is shown in Fig. 4.2.7 as a function of the neutral gas line density at 500 keV. The fraction was calculated by using the cross section data collected by Nakai, et al. [44]. It is shown that the optimum line density which makes the neutral fraction maximum is about  $7.4 \times 10^{15}$  molecules/cm<sup>2</sup>, where the neutralization efficiency is 59%.

The minimum pressure in the neutralizer is determined by the effect of space-charge-expansion. The space-charge-effect of negative ion beams is different from that of positive ion beams and is not investigated in detail so far. In our recent experimental results using a low current H<sup>-</sup> ion beam, the space-charge-effect was observed below the pressure of  $5 \times 10^{-3}$  Pa and this result agrees with theoretical estimation. In the downstream region of the neutralizer, the space-charge-effect will be mitigated due to the production of positive deuterium ions. Hence, we chose the pressures at the entrance and the exit of the neutralizer to be  $1.55 \times 10^{-2}$  Pa and  $0.4 \times 10^{-2}$  Pa, respectively. When the length of the neutralizer is 24 meters, the optimum line density can be obtained.

It is necessary to shield the neutralizer against the stray magnetic field from the tokamak. The beam deflection angle  $\Delta\theta$  due to the magnetic field is given by

$$\Delta\theta = e B_{\perp} L / (2 m E)^{1/2} .$$

where,  $B_{\perp}$  is the component of the magnetic field perpendicular to the beam axis.  $L$  is the length of the neutralizer,  $m$  is the mass of the D<sup>-</sup> ions, and  $E$  is the beam energy. In order to suppress the deflection angle below the permissible value of 1 mrad which is fairly smaller than the beam divergence,  $B$  should be reduced to 0.048 gauss at  $E=500$  keV. Since the maximum value of the stray field is estimated to be 1000 Gauss at the exit of the neutralizer, the required shield factor is 20,000. The shield is composed of two layers. The inner shield is made of 4 cm thick mumetal, while the outer is of 20 cm thick mild steel. Both shields also act as a part of the neutron shield.

#### 4.2.4 Ion Dump

The unneutralized negative ions and the re-ionized positive ions are deflected by the poloidal magnetic field from the tokamak toward the ion dump in the beam dump room. Both the beam energy and the poloidal magnetic field vary during a pulse, according to the operation scenario of the FER tokamak. Hence, the trajectories of the ions also change during a pulse. The structure of the ion dump is designed so as to receive all those ions at all phases in a pulse by calculating the trajectories in the energy range of 200-500 keV. The inner dimensions of the ion dump are 3.0 meters in length, 0.5 meter in width and 2.0 meters in height. Figure 4.2.8 shows an example of the 3-D trajectory calculation for 500 keV deuterium ions. While the average heat flux dissipated in the ion dump is  $76 \text{ W/cm}^2$ , the peak heat flux is estimated to be  $4 \text{ kW/cm}^2$ . Since that of an existing neutral beam injector, for instance JT-60, is  $0.5 \text{ kW/cm}^2$ , the development of a high heat flux ion dump is the subject for future study (see Appendix A.7) An externally finned swirl tube is one of the promising candidates for the beam dump element.

Utilization of an energy recovery system is a better solution for the heat removal problem, though it is not applied in the present design. The softlanding of ions on the ion dump decreases the heat flux and also improves the total power efficiency of the injector. In addition, it will prolong the lifetime of the ion dump which is determined by sputtering and blistering caused by high energy ion bombardment. A preliminary study on the energy recovery system shows the possibility of energy recovery for both positive and negative ions by means of an electrostatic recovery system.

#### 4.2.5 Cryopump

There are two cryopumps in both sides of the ion accelerator. Each has a pumping speed of  $350 \text{ m}^3/\text{s}$ . In the beam dump chamber is a smaller cryopump whose pumping speed is  $150 \text{ m}^3/\text{s}$ . The required pumping speed is small compared with the existing injectors. The total pumping speed is  $850 \text{ m}^3/\text{s}$  for 20 MW injection, while that of the JT-60 NBI is, for example,  $1400 \text{ m}^3/\text{s}$  for 1.4 MW beam injection. The dimensions of the

cryopump are 1.6 m×2.2 m in the ion source room and 1.3 m×1.3 m in the beam dump room. The dimensions are determined so that the pumping speed per unit area becomes  $100 \text{ m}^3/\text{s}\cdot\text{m}^2$ . This is a reasonable value because the pumping speed per unit area is  $100 \text{ m}^3/\text{s}\cdot\text{m}^2$  in the JT-60 NBI for hydrogen gas, which corresponds to  $70 \text{ m}^3/\text{s}\cdot\text{m}^2$  for deuterium, and there is possibility to increase the pumping speed by employing an open-structure cryopump which is used in JET NBI [44].

The most important point which differs from the existing system is that the cryopump should be operated quasi-continuously. Since the cryopump should be re-generated periodically, an alternatively operated cryopump system is now proposed for DC operation.

#### 4.2.6 Power Supply System

The power supply system is composed of three units, each of which has a 500 keV, 100 A acceleration power supply and several minor power supplies for plasma production, etc. Figure 4.2.9 shows the arrangement of three beam lines and their associated three power supply units around the tokamak. In designing the acceleration power supply, it is important to protect not only the ion source but also the power supply itself against a breakdown in the ion source. The protection has been maintained by a high speed DC switch and a surge suppression system so far. However, the DC switch used in the JT-60 NBI and the 200 keV helium beam diagnostic system will not be available, because the system requires many switching elements and becomes too complex to control these elements at a high potential of 500 keV. Instead of the DC switch, an AC switch coupled with an inverter system is used in the design as shown in Fig. 4.2.10. The frequency of the inverter is determined by the permissible cut-off speed and the ripple of the beam energy or beam current. To obtain a cut-off speed of less than  $100 \mu\text{s}$  and a ripple of about 3%, the frequency in the AC power line must be increased up to 5 kHz.

Another critical point in designing the system is to suppress the energy dissipation in the ion source grid in the case of breakdown. The stray capacitance exists primarily in the insulating transformer of the plasma production power supplies. Therefore, instead of utilizing many insulating transformers for each source power supply, we use a

single, big insulating transformer combined with the inductance, which has a parallel resistance to suppress the zero-phase-sequence current. This concept makes it possible to reduce the surge current and consequently the size of the surge block core. By utilizing a 1.2 mH inductance, it is possible to suppress the surge current and the energy input to the ion source down to 1 kA and 1 joule, respectively. The volt-second of the surge block core is 0.2 volt-second. This value makes the size of the surge block core one ninth the size without the inductance.

#### 4.3 Summary

Taking advantage of the good beam quality of the volume negative ion source we have designed a 500 keV, 20 MW negative-ion-based neutral beam injector for the FER. The most significant feature of this design is to transport the high energy beams over a distance of more than 40 m through the narrow neutralizer and the beam drift duct. This design offers several advantages including the following items:

- (1) All beam line components installed near the tokamak are simple and small.
- (2) Tangential beam injection is possible because of the high beam energy and the narrow beam drift duct.
- (3) Since complicated beam line components such as the ion source are situated at a place far from the tokamak (or in a separate room), difficulties on neutronics will be reduced considerably and maintenance will be easy.
- (4) Magnetic shield of the beam line is easy.
- (5) The required pumping speed for the cryopump is small.

In this design, the total injection efficiency is 0.45 at 500 keV. This efficiency has a possibility of becoming higher by employing a plasma neutralizer and/or an energy converter system. The most important R&D component in realizing this design is the intense deuterium negative ion source. The source will be developed in the Advanced Injector Test Stand (AITS) which we are planning to construct.

\* 0- ION EXTRACTOR 5MM SLOT \* 9KG 3W 4T X=+20,-20 Z=18MM (NEGEX04)

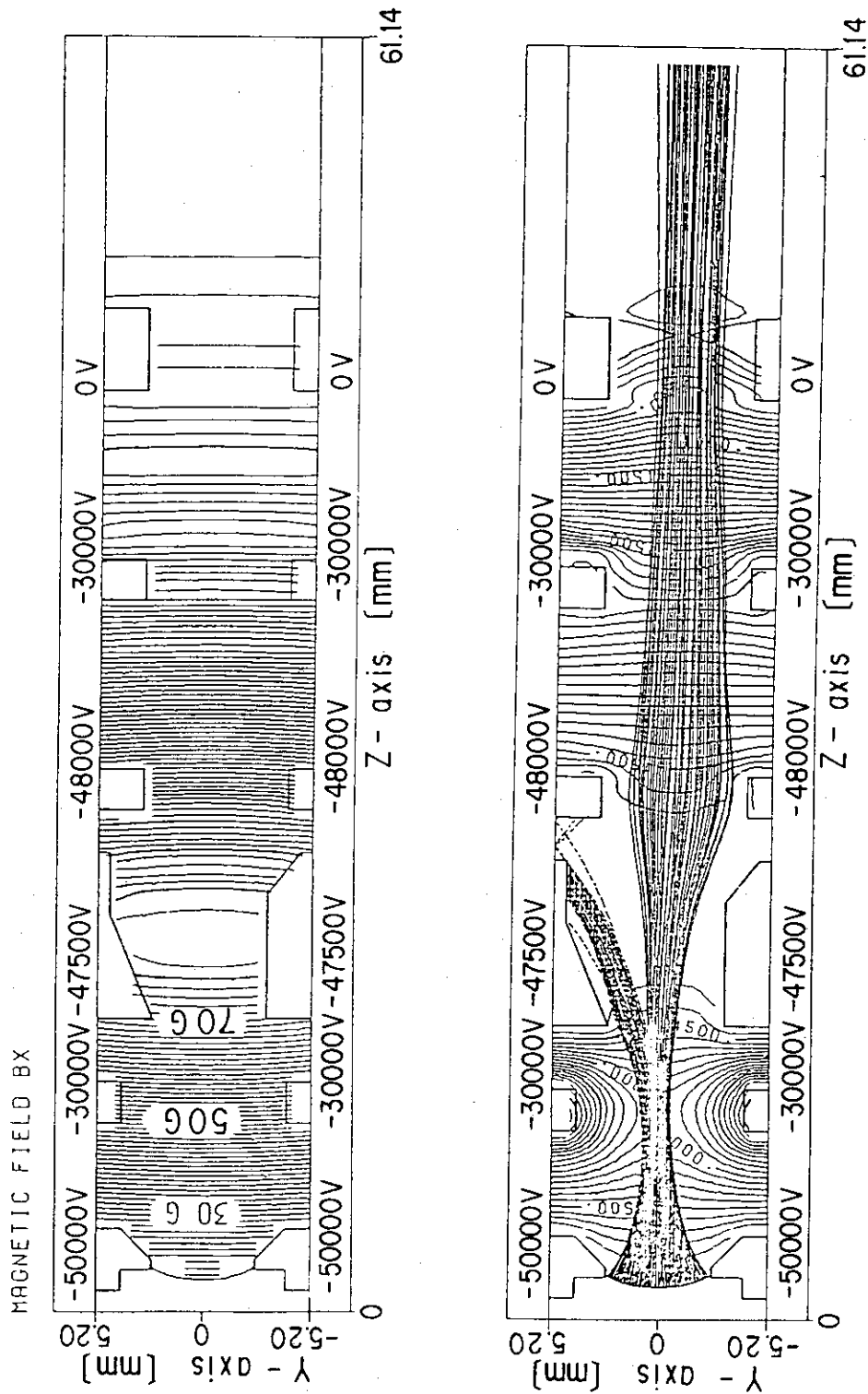


Fig. 4.2.1 Optimized pre-acceleration system. The electrons are deflected to the electron recovery electrode by the transverse magnetic field.

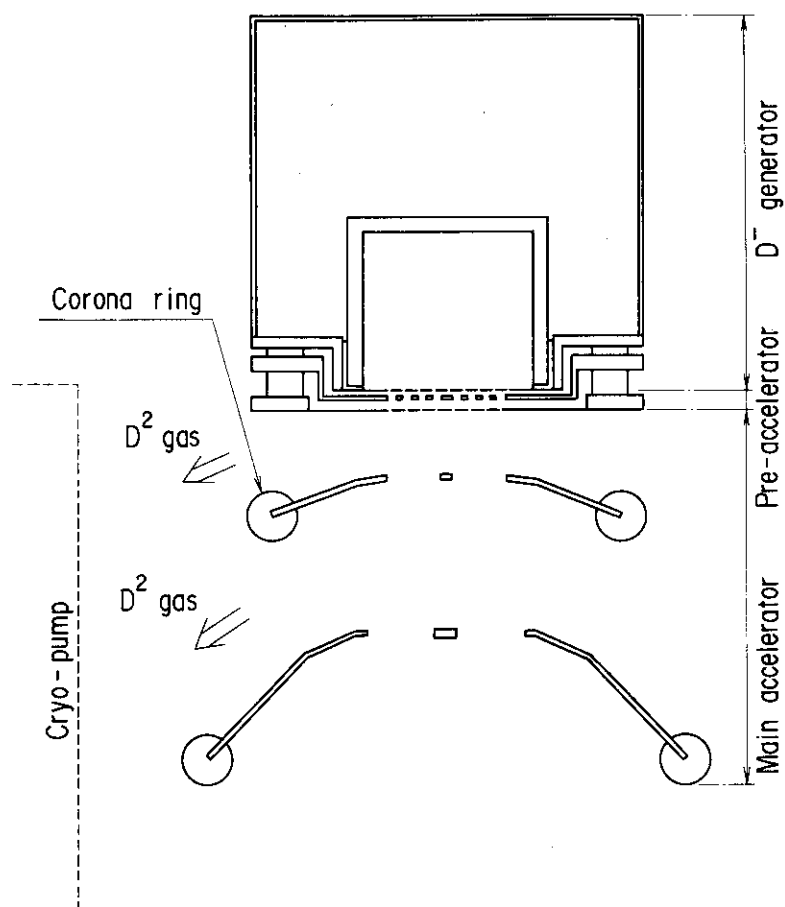


Fig. 4.2.2 Cross-sectional view of main accelerator

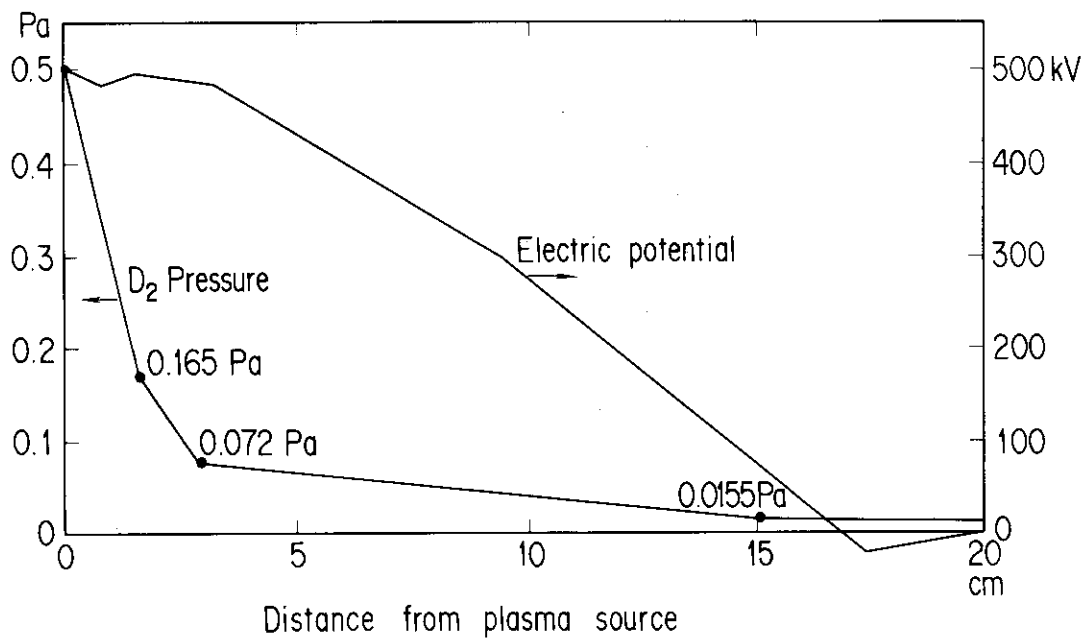


Fig. 4.2.3 Distribution of the gas pressure and electrical potential along the beam axis. The pressure in the arc chamber is 0.5Pa.

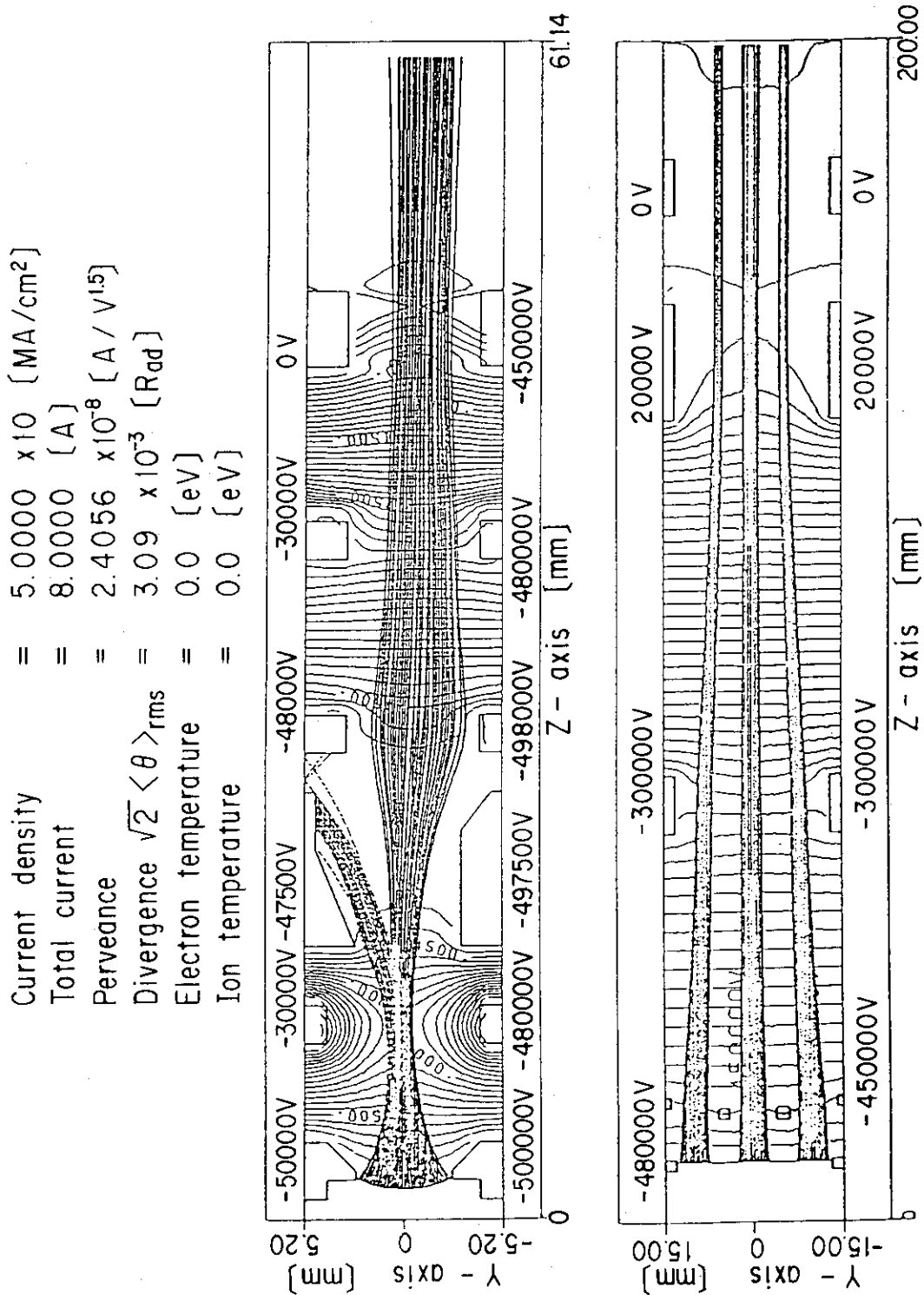


Fig. 4.2 4 Optimized acceleration system.

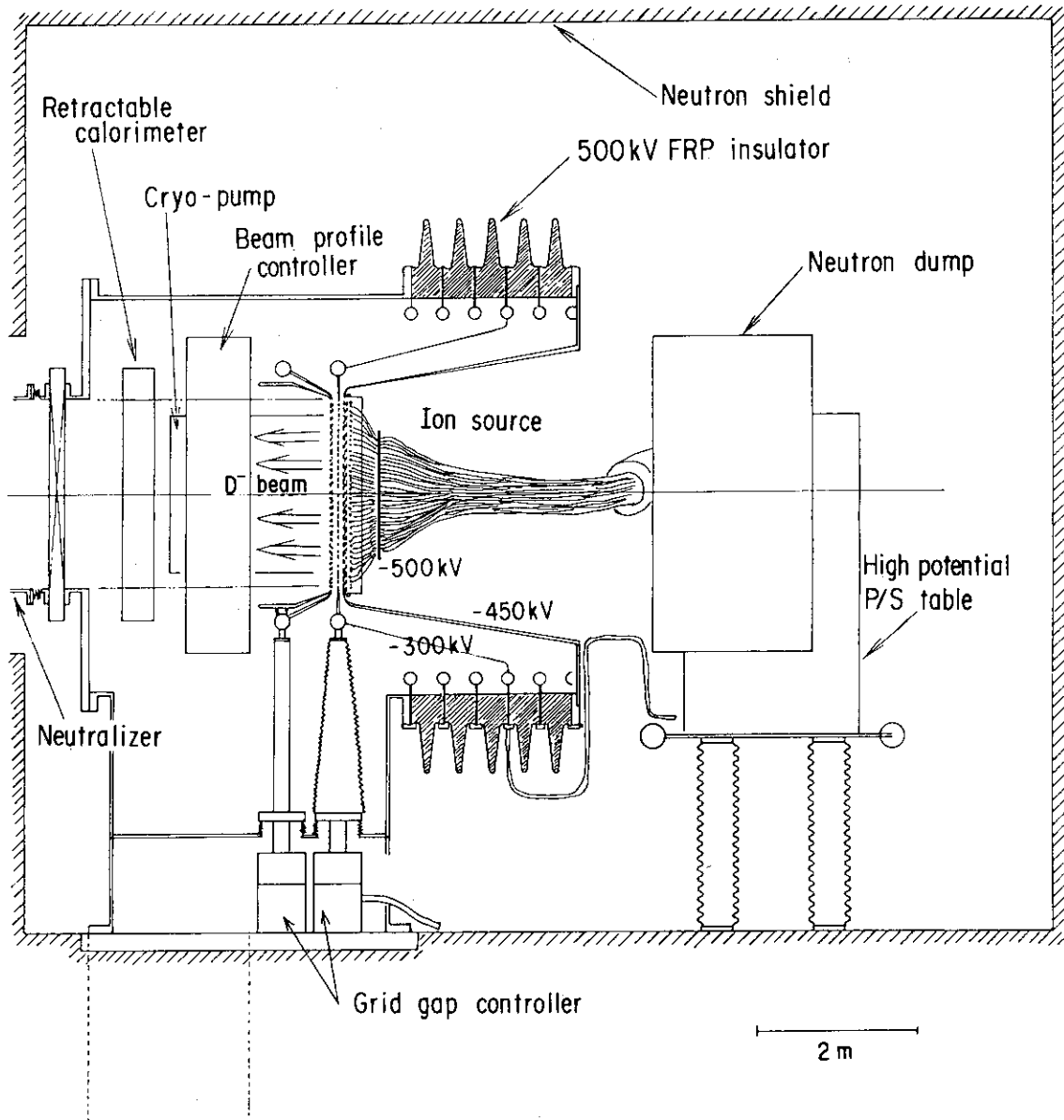


Fig. 4.2.5 Cross-section of ion source room

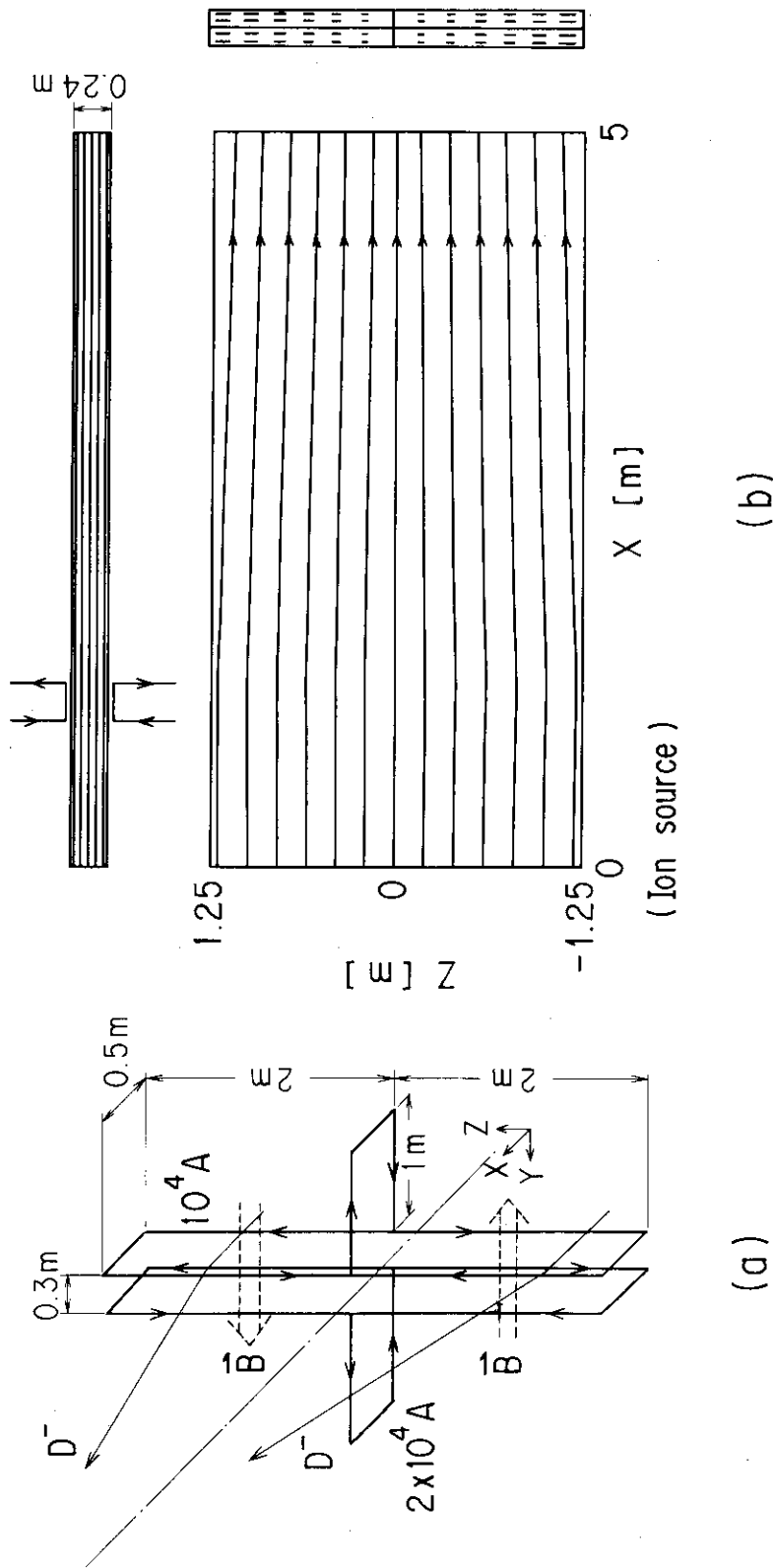


Fig. 4.2.6 (a) Beam profile controller and (b) calculated beam path under the transverse magnetic field for current profile control.

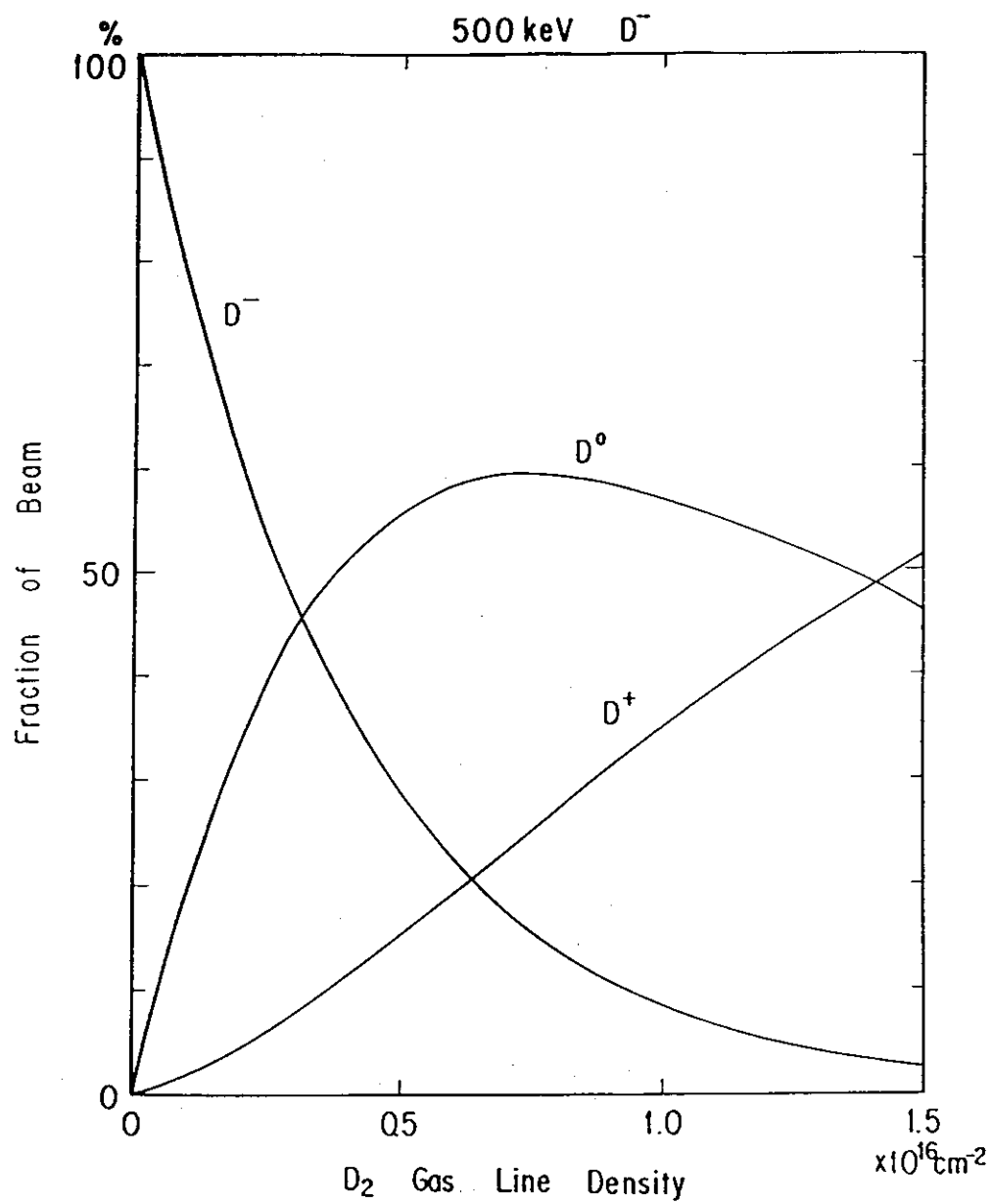


Fig. 4.2.7 Dependence of neutralization efficiency of 500 keV  $D^-$  ion on neutral gas line density

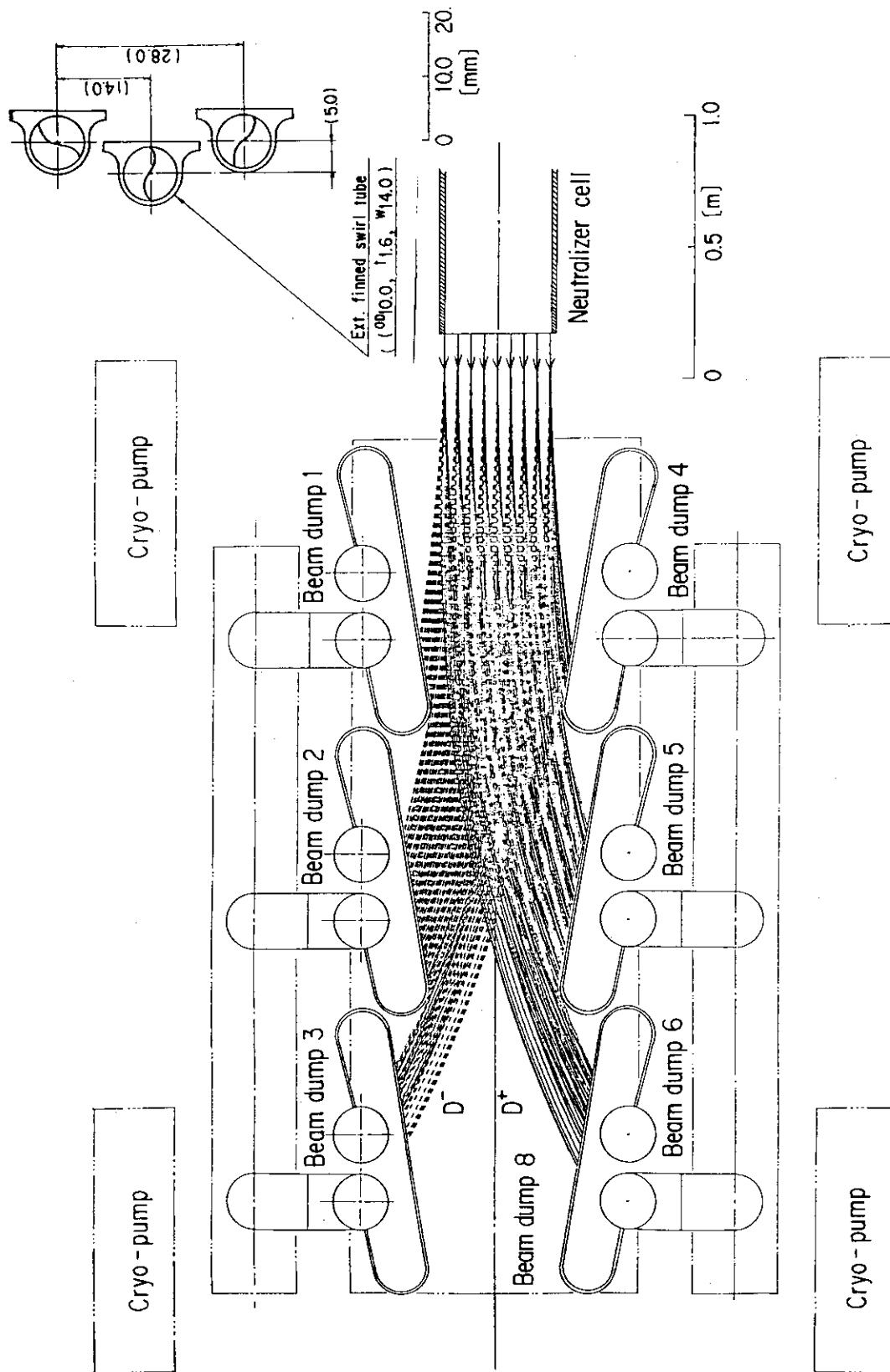
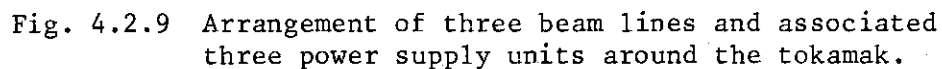


Fig. 4.2.8 Calculated 3-D trajectory of 500 keV deuterium ions, flowing into the ion beam dump.



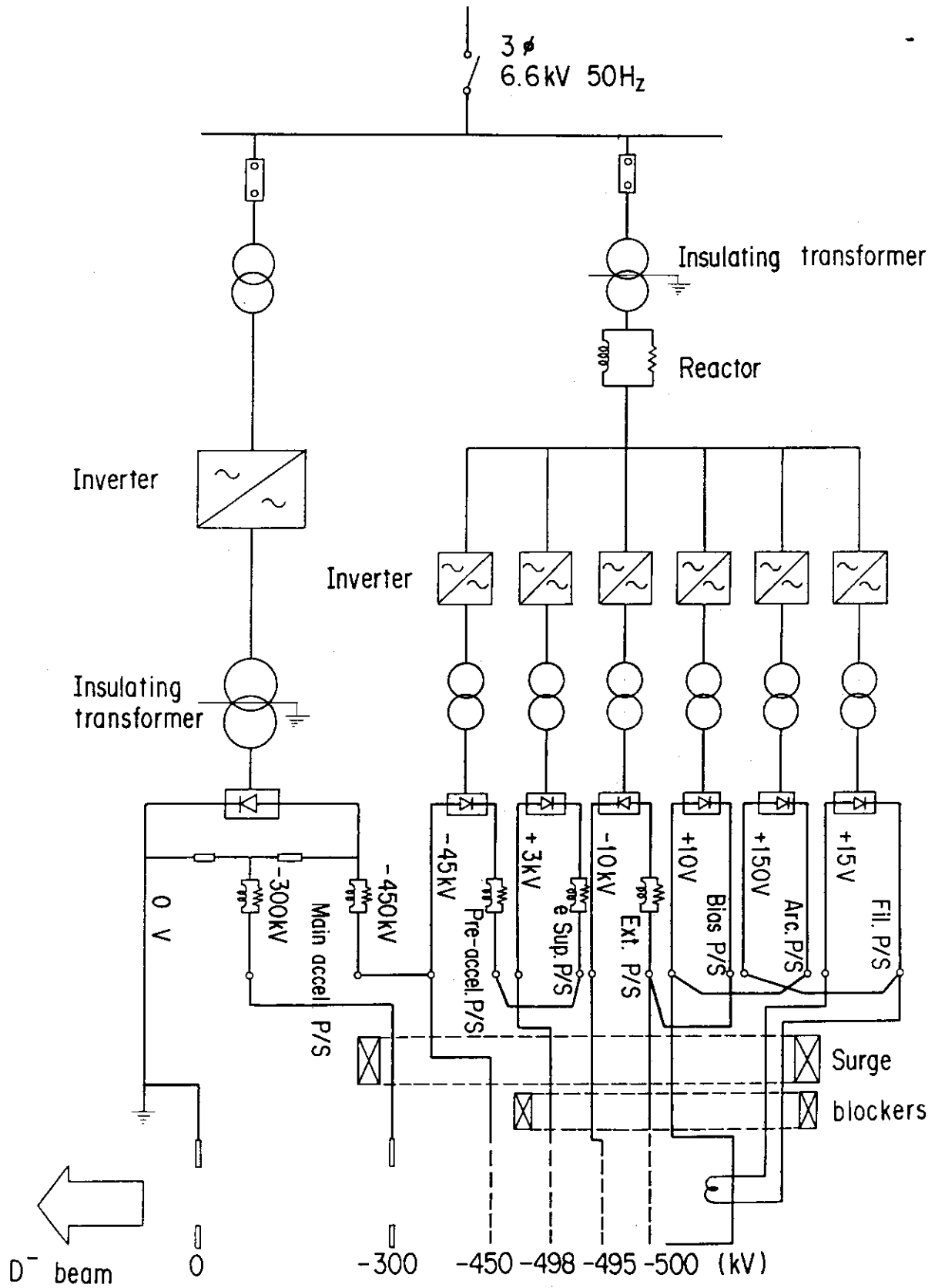


Fig. 4.2.10 Power supply system. AC switch coupled with an inverter system is used.

## 5. Reactor Design

### 5.1 Mission of Next Generation Tokamak (FER)

Since 1980, the FER ( Fusion Experimental Reactor ) has been designed as a next step machine to JT-60, with different levels each year, changing design emphasis and philosophy. In 1986, "the subcommittee on the next step device" in the Nuclear Fusion Council discussed and established the physics and engineering missions and the major specifications for the next step machine. The specifications for the FER is shown in Table 5.1.1. The physics missions of the FER are realization of self-ignited plasma and control of plasma stability for a long burn time ( $10^2 \sim 10^3$  sec). The engineering missions are development and test of the fusion technology, including the tritium fuel cycle, superconducting magnet, remote maintenance and breeding blanket test modules. The new FER design has been developed based on the subcommittee's conclusions with the main emphasis on increasing its cost performance considering the allowable budget for the machine. Five types of the reactor design concept have been examined [45,46]. Pulsed operation is chosen as the basic scenario option, while full use of non-inductive current ramp-up is adopted to reduce OH capability, which results in the reduction in the reactor size. The 500 keV/20 MW negative-ion-grounded neutral beam injection system is applied to one of these five reactors, the so called Option C type reactor. The Option C reactor is not necessarily optimized for the application of the NBI system. The basic performance parameters of the Option C type reactor are shown in Table 5.1.2. One of the operation scenarios based on plasma heating and current drive by the NBI system is shown in Fig. 5.1.1. In the following sections, the impact of the NBI system on the reactor structural configuration and maintenance will be described, including the design of the injection port and shine-through armor plate, the estimation of the neutron flux distribution and the  $\gamma$ -ray dose distribution in the ion source room and the ion beam dump room and the selection of the tritium processing system.

Table 5.1.1 Specifications of the FER

Items selected	Specifications
Long pulse burning	Burning duration : $\sim 800\text{sec}$ . (D/T burning)
Self ignition	Energy multiplication rate : more than 20 $\sim$ 30
Impurity control	Poloidal divertor
Operation mode	Pulse operation
Heating · Current drive	Neutral beam injection, Radiofrequency
Wall loading	Neutron wall loading : $\sim 1\text{MW}/\text{m}^2$
Neutron fluence	$\sim 0.3\text{MW Year}/\text{m}^2$
Magnet	Superconducting (partially normal conductor available)
Blanket	Partial module
Maintenance	Disassembling repair : divertor, first wall, part of shieldings
Power source	Combined use of utility power line and flywheel motor generator
Effective use of JT-60	Flywheel motor generator, DC convertor, heating device power source, measurement diagnostic device, etc.
Reactor technology development test items	Tritium fuel cycle : fuel injection, gas exhaust, purification, isotope separation, storage Superconducting coil : system engineering Blanket : tritium breeding, continuous recovery and high temperature high pressure test by using modular size blanket Material testing : irradiation of breeder and superconducting magnet materials Neutronics : shielding experiment, etc. Remote handling : first wall in-situ replacement, disassembling, pulling out and replacement of divertor / limiter Other items : measurement and control equipment testing, first wall material development, etc.

Table 5.1.2 Performance parameters of the Option C type reactor

Major radius	$R$	4.92 m
Minor radius	$a$	1.32 m
Aspect ratio	$A$	3.7
Elongation	$K$	1.7
Triangularity	$\delta$	0.2
Toroidal field strength	$B_T$	4.68 T
Plasma current	$I_p$	8.69 MA
Average plasma temperature	$\bar{T}$	12.0 keV
Toroidal beta value (total)	$\beta_T$	4.94 %
Average electron density	$\bar{n}_e$	$1.09 \times 10^{20} \text{ m}^{-3}$
Average ion density	$\bar{n}_i$	$0.98 \times 10^{20} \text{ m}^{-3}$
Safety factor (95 %)	$q_\psi$	2.6
Cylindrical safety factor	$q_I$	2.0
Fusion power	$P_f$	459 MW
Wall load	$P_w$	$1.03 \text{ MW/m}^2$

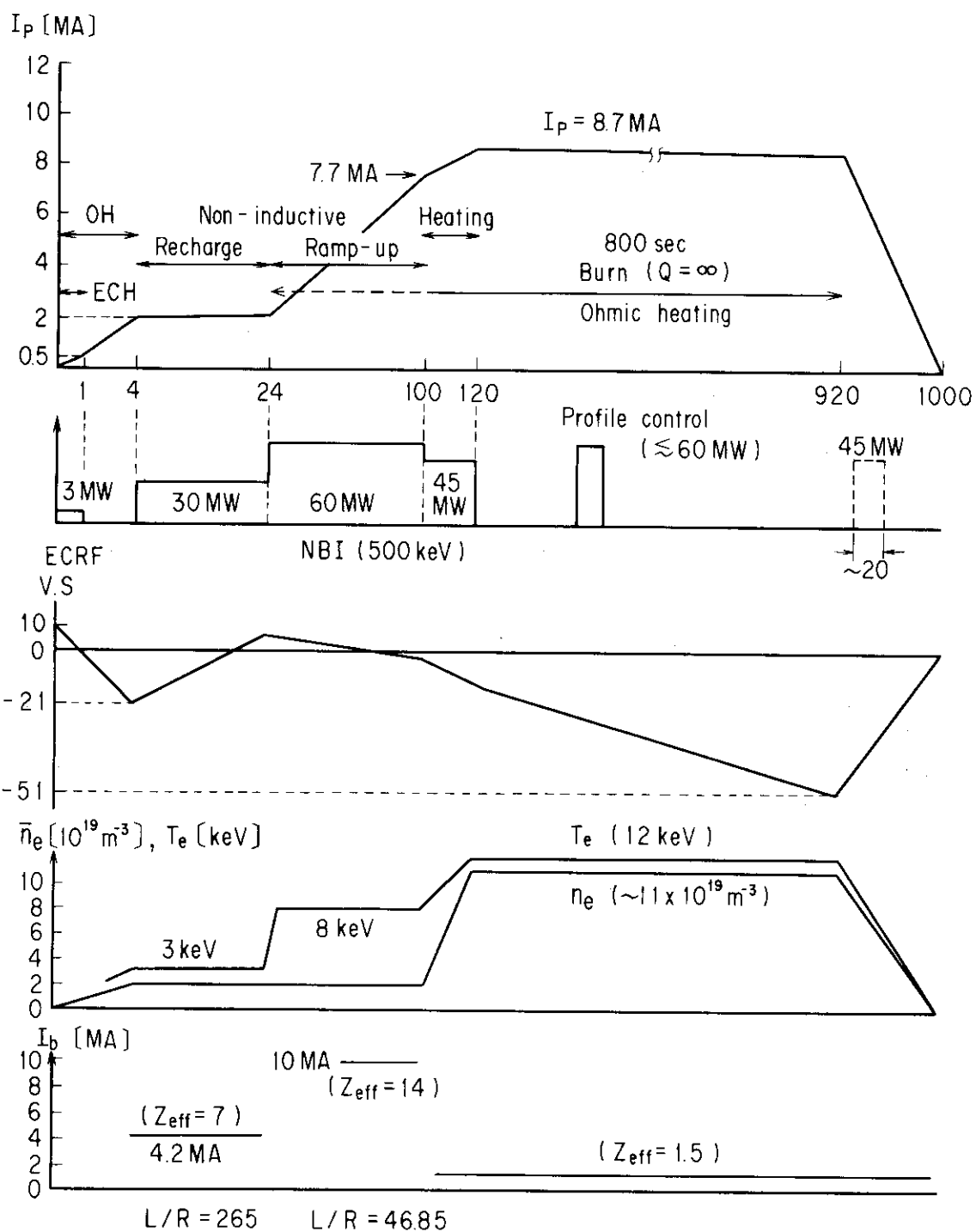


Fig. 5.1.1 Operation scenario based on plasma heating and current drive by the NBI system.

## 5.2 Location of Beam line System

Figure 5.2.1 shows the dependence of the normalized beam driven current  $I_p(R_{tang})/I_p(R_0)$  on  $R_{tang}$ , which is normalized by the beam driven current  $I_p(R_0)$  at  $R_{tang} = R_0$ .  $R_{tang}$  is the minimum major radius along the beam path. Using the code described in Section 3.8, the beam driven currents are solved, being consistent with the MHD equilibrium. The plasma density and plasma temperature profiles are assumed to be  $n = n(0)x(1-\psi/\psi_s)^{0.5}$  and  $T = T(0)x(1-\psi/\psi_s)$ , respectively.  $\psi$  is the magnetic surface (see Appendix 6) and  $\psi_s$  implies the outermost magnetic surface. The shine-through fraction  $f_s$  (that is,  $1-f_s$  corresponds to the net deposit power fraction) is also shown in Fig. 5.2.1a. Figure 5.2.1a shows the low density case, which corresponds to the non-inductive current ramp-up operation (see Section 3.4) or quasi-steady state operation (see Section 3.5). Figure 5.2.1b shows the relatively high density case, which corresponds to the steady state operation (see Section 3.7). In the low density case, the maximum current drive efficiency appears at  $R_{tang} = R_0 - \frac{1}{4}a$ . On the other hand, in the relatively high density case, there appears no maximum in the range between  $R_{tang} = R_0 - \frac{3}{4}a$  and  $R_{tang} = R_0 + \frac{1}{4}a$ . This comes from the shift in the magnetic axis to the outside of the torus due to the high poloidal beta value. In addition to the above mentioned current drive efficiency, the following items should be considered in the design of the beam line.

- (1) The drift duct (or injection port) should avoid interference with the passive shell conductor (copper shell shown in Fig. 5.2.3d) and the semi-permanent shield, as shown in Fig. 5.2.2. The passive shell conductor plays an important role in stabilizing of vertical position instability.
- (2) The shine-through armor plate should avoid interference with the drift duct.
- (3) The shield structure around the drift duct and the shine-through armor plate should avoid interference with the vacuum vessel of the TF coils and should have more than 600 mm shield thickness for the biological shield.

- (4) The shine-through armor plate should be able to be separately pulled out in one direction for the purpose of making its overhaul procedure simple.

In the present design work, the location of the beamline is determined by surveying the three dimensional geometry of the torus structure containing the beamlines by using a 3-D CAD. Figure 5.2.2a shows the plan views of the torus structure with beamlines. Figure 5.2.2b shows views from the direction along the beamline. The degree of interference of the beamline with the passive shell conductor and the permanent shield is reduced as the  $R_{tang}$  and the angle between the beamline and the datum reference line,  $\theta$ , decrease. The  $R_{tang}$  and the angle,  $\theta$ , are confined to  $R_{tang} < 4000$  mm and  $\theta \leq 2^\circ$ , respectively, in order to avoid the interference of the beamline with the passive shell. On the other hand, increase in  $R_{tang}$  reduces the interference of the shield structure around the drift duct and the shine-through armor plate with the vacuum vessel of the TF coils. The interference of the shine-through armor plate with the permanent shield and the drift duct can be avoided by a decrease in  $\theta$ .

However, the location of the beamline, which completely satisfied all the requirements mentioned above, could not be found. So, we put emphasis on avoidance from the interference of the beamline with the passive shell conductor (copper shell) and permanent shield structure, and located the beamline at  $\theta = 2^\circ$  and  $R_{tang} = 3928.5$  mm, of which value corresponds to  $R_{tang} = R - \frac{3}{4}a$ . In this case, the current drive efficiency of the low density case is reduced by about 20% compared with the optimized value, as shown in Fig. 5.2.1a. Figure 5.2.4 shows the dependence of the global current drive efficiency  $I_b[A]/P_b[W]$ , current drive efficiency  $\eta$ , shine-through fraction  $f_s$  and the required beam power for  $I_p = 7$  MA on plasma density. The plasma density and plasma temperature profiles are assumed to be  $n = n(0)x(1-\psi/\psi_s)^{0.5}$  and  $T = 16[keV]x(1-\psi/\psi_s)$ , respectively.

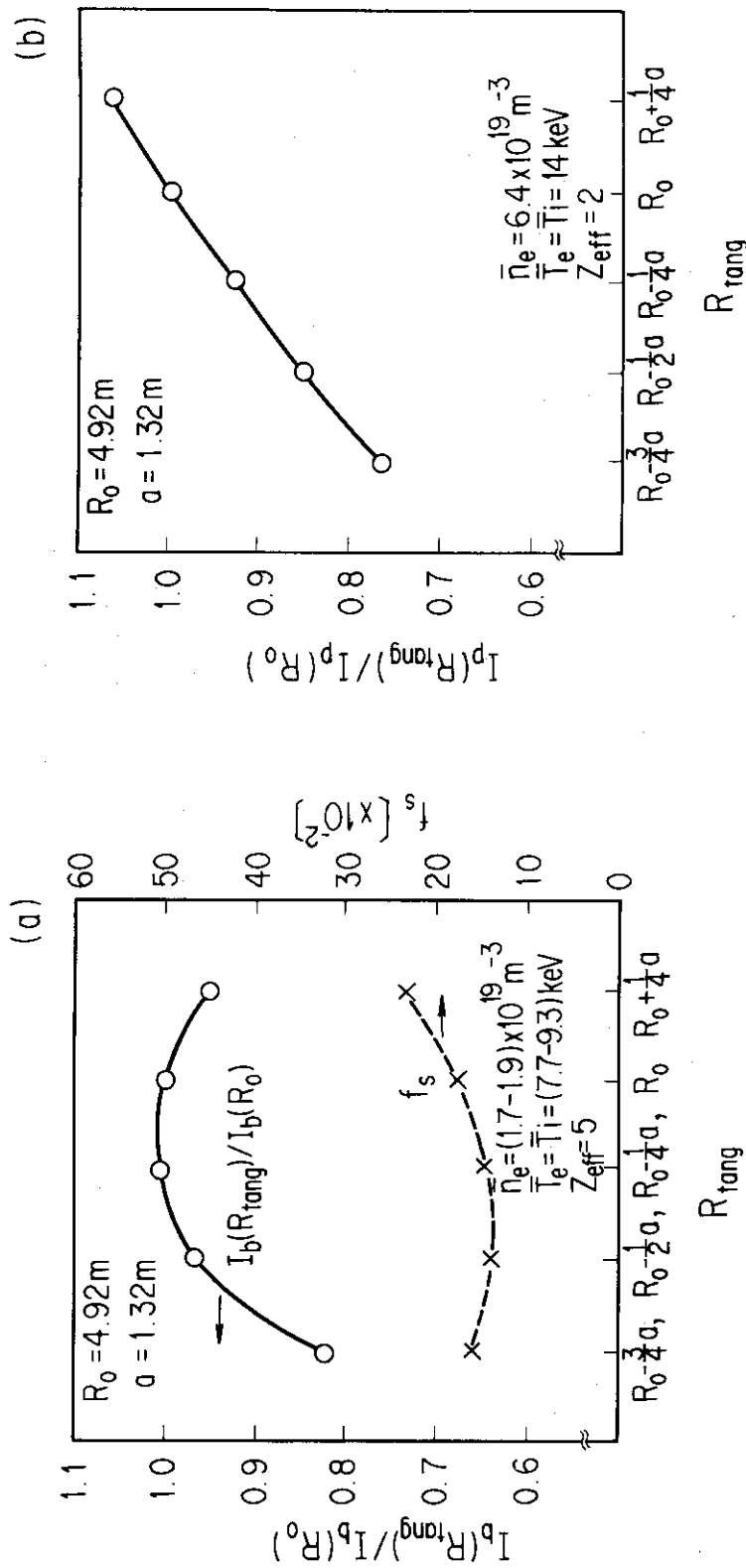


Fig. 5.2.1 Dependence of normalized beam driven current  $I_p(R_{tang})/I_p(R_0)$  on  $R_{tang}$ , which is normalized by the beam driven current  $I_p(R_0)$  at  $R_{tang}=R_0$ .  
 (a) low density case, which corresponds to the non-inductive current ramp-up operation or quasi-steady state operation. (b) relatively high density case, which corresponds to the steady state operation.  $E_b = 500 \text{ keV}$ . Plasma density and plasma temperature profiles are assumed  $n=n(0)x(1-\psi/\psi_s)^{0.5}$  and  $T=T(0)x(1-\psi/\psi_s)$ , respectively. Shine-through fraction  $f_s$  is also shown in Fig. 5.2.1a.

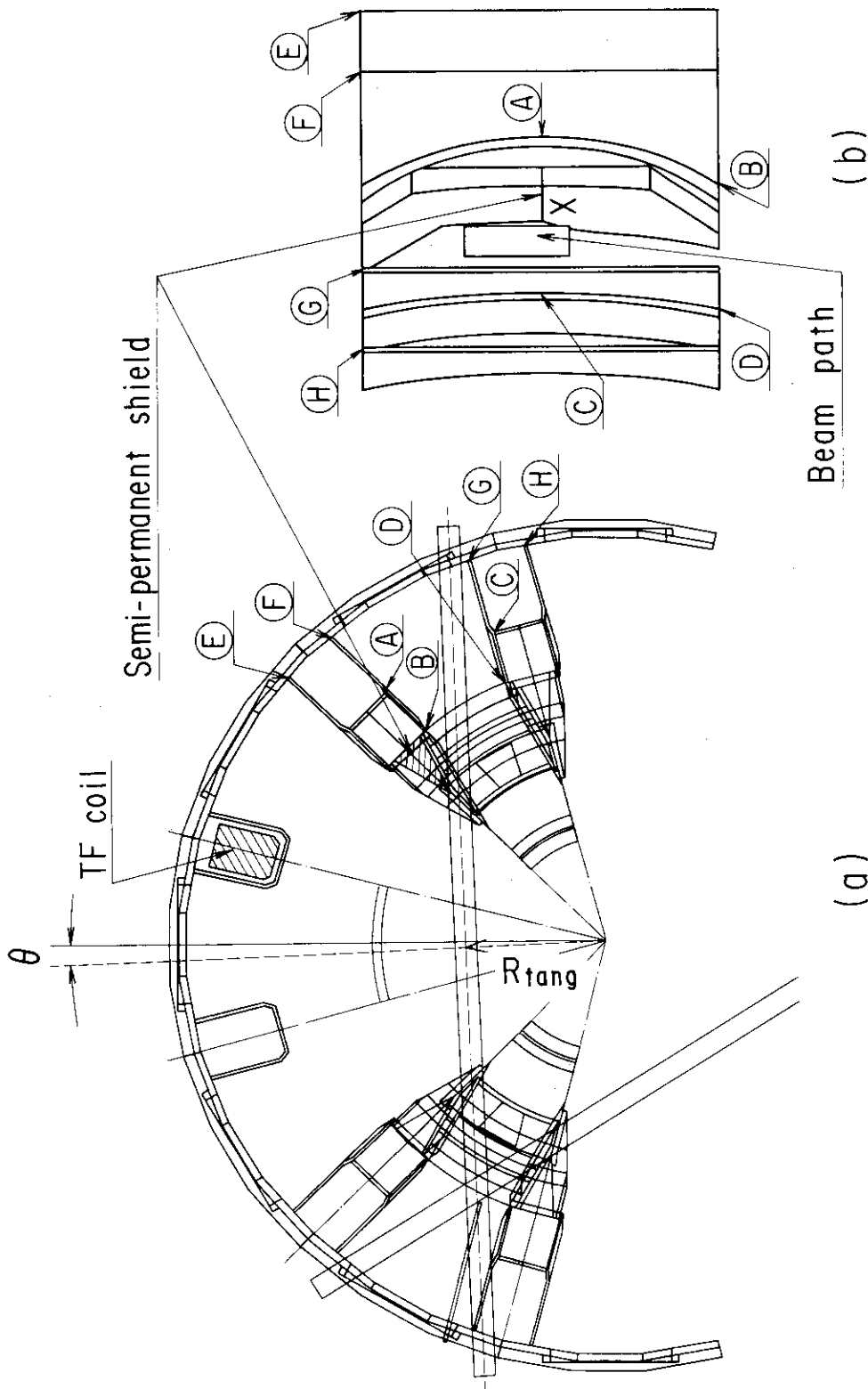


Fig. 5.2.2 Plane view of the torus structure with beam lines and view from the direction along the beam line. The location of the beamline is determined by surveying the three dimensional geometry of the torus structure containing the beamlines by using 3-D CAD. Notations as A, B, C and so on shown in Fig. 5.2.2a correspond to those in Fig. 5.2.2b.

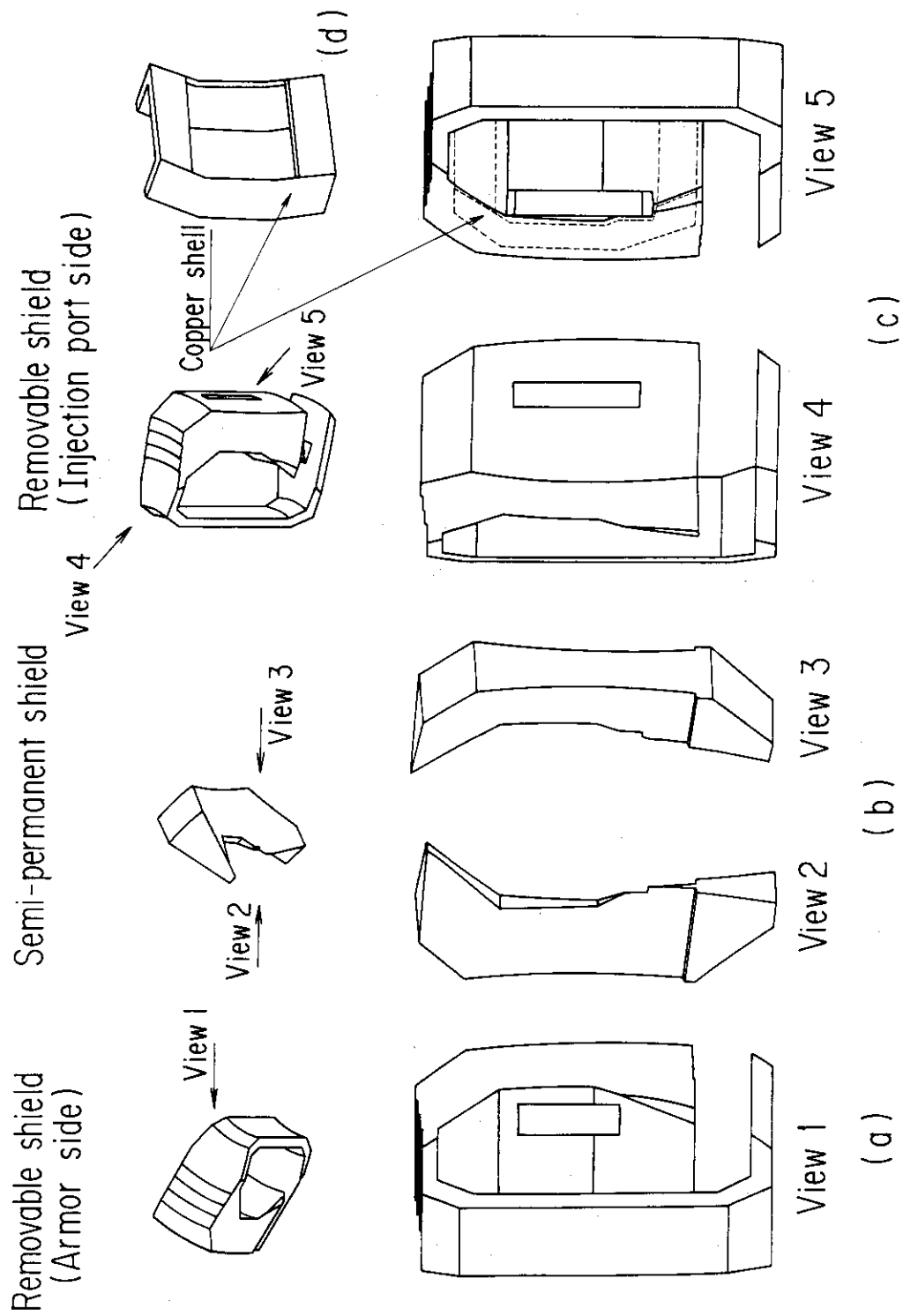


Fig. 5.2.3 Relative position of drift duct (or injection port) to the removable shield, semi-permanent shield and passive shell conductor (or copper shell).

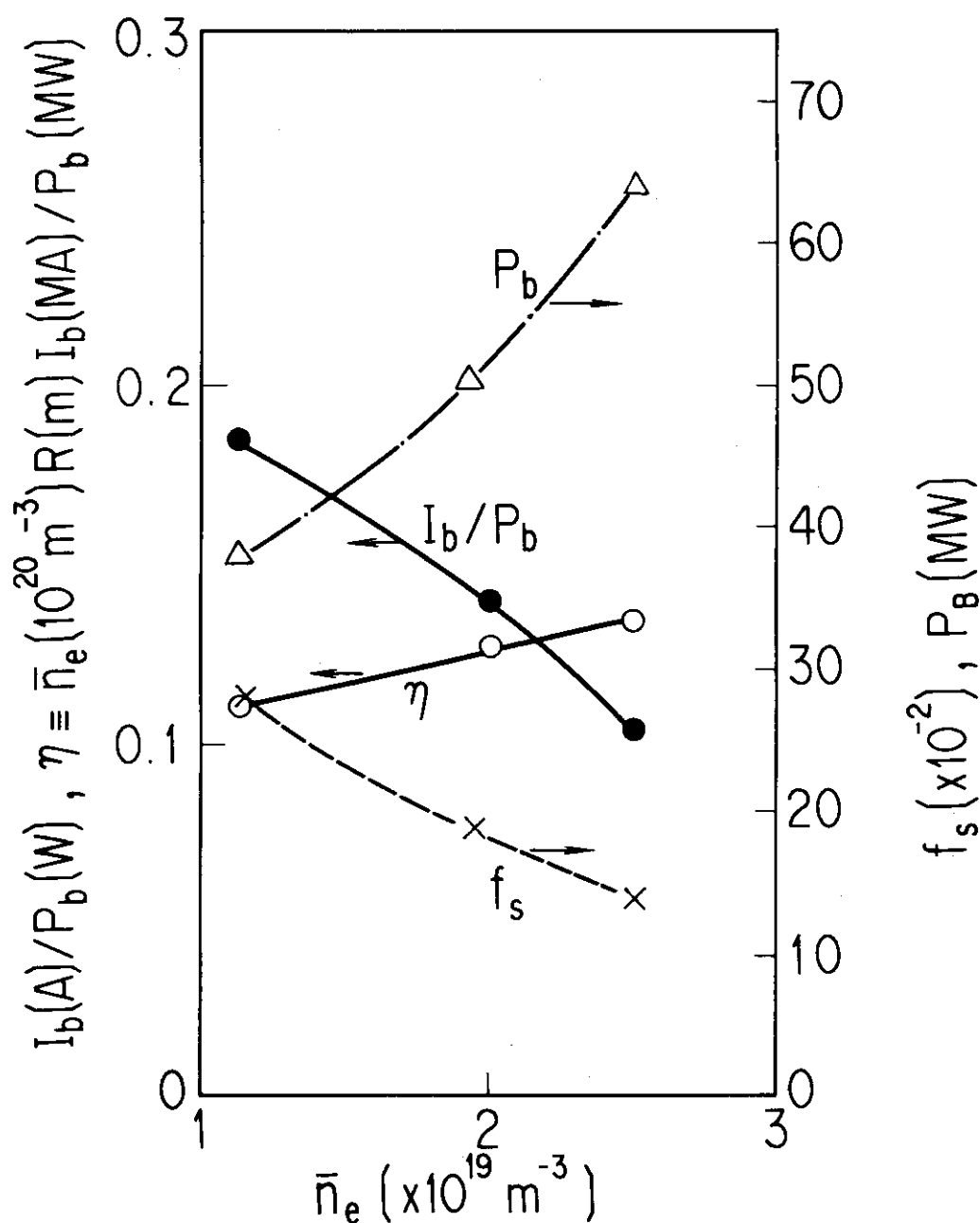


Fig. 5.2.4 Dependence of global current drive efficiency  $I_b[A]/P_b[W]$ , current drive efficiency  $\eta$ , shine-through fraction  $f_s$  and the required beam power for  $I_p=7$  MA on plasma density.  $E_b=500$  keV.  $Z_{eff}=5$ . Plasma density and plasma temperature profiles are assumed  $n=n(0)\times(1-\psi/\psi_s)^{0.5}$  and  $T=16[\text{keV}]\times(1-\psi/\psi_s)$ , respectively.

### 5.3 Injection Port and Shine-through Armor Plate

#### 5.3.1 Structural Concepts of Injection Port and Shine-through Armor Plate

The structural concept of the injection port (drift duct), designed on the basis of the location of the beamline determined above, has already been shown in Fig. 2.2.2. The drift duct penetrates the movable shield without crossing its side-wall where the connector between the upper and the lower shell conductor lies, as shown in Fig. 5.2.3c and d. The separated shield structure is also installed in the vacuum vessel of the TF coils where the required thickness of the shield structure around the drift duct and shine-through armor plate is insufficient. The interference of the drift duct with the permanent shield is so slight as to raise no serious structural problem except for cutting off the shield. The structural concept of the injection port involving the access door has been already shown in Fig. 2.2.5. The drift duct, shine-through armor plate and access door compose a monolithic construction.

The structural concept of the shine-through armor plate is shown in Fig. 5.3.1. The armor plate is extractable while keeping vacuum condition of the reactor vacuum chamber. It is 2.0 meters high and 2.3 meters long and located so as to make the incident angle  $65^{\circ}$ , considering the reduction in damage due to the heat load and erosion (see the next Subsection 5.3.2). Graphite and copper alloy can be applied to the surface material of the shine-through armor plate. The former is favorable from the viewpoint of impurity control and the latter is favorable from the viewpoint of the reliability in heat removal. In the present design work, we adopt a graphite armor structure because the self-sputtering and the blistering of the copper alloy has not yet been made clear. The graphite armor is brazed to the copper alloy heat sink by inserting a thin layer of molybdenum. It is fastened with bolts on a base plate of stainless steel. The surfaces of the graphite armors are slightly slanted in order to protect their edges from erosion damage. The shine-through armor plate has four cooling systems branching at a header installed in the base plate. The base plate has jogs near the access door against neutron streaming.

### 5.3.2 Thermal and Erosion Estimations of Shine-through Armor Plate

#### (1) Thermal estimation

The thermal estimation of the armor plate was carried out on the basis of the structure proposed in the previous section. The inlet temperature and pressure of the cooling water were matched with other cooling systems, that is,  $50^{\circ}\text{C}$  and  $8\text{ kg/cm}^2$ , respectively. The normal heat load on the shine-through armor plate during the current ramp-up phase with a duration time of 200 sec is  $4\text{ MW/m}^2$  with a peaking factor of 1.5. The dimension of the armor plate is shown in Fig. 5.3.1b. The length of the cooling channels is 2 meters. The flow rate is determined so as to keep the temperature of the copper alloy heat sink below  $150^{\circ}\text{C}$ .

The relation between the flow rate and the heating surface of the cooling channel is shown in Fig. 5.3.2. According to this figure, a flow rate of more than 7 m/sec is required in consideration of the temperature difference of  $15^{\circ}\text{C}$  in the copper alloy heat sink and to keep its maximum temperature below  $150^{\circ}\text{C}$ . The pulse length of 200 sec is long enough to be regarded as steady state. Steady state thermal analysis was carried out using the one dimensional model shown in Fig. 5.3.2b. The temperature at each position indicated in Fig. 5.3.2b is as follows;

$$\begin{aligned} T_w &= 130.5^{\circ}\text{C}, & T_1 &= T_{\text{max,graphite}} = 1678^{\circ}\text{C}, \\ T_2 &= T_{\text{max,molibdenum}} = 164^{\circ}\text{C}, & T_3 &= T_{\text{max,copper}} = 144^{\circ}\text{C} \end{aligned}$$

where, the thermal conductivity of graphite is  $0.151\text{ W/^{\circ}C}\cdot\text{cm}$ , molybdenum  $1.3\text{ W/^{\circ}C}\cdot\text{cm}$ , and copper alloy  $3.7\text{ W/^{\circ}C}\cdot\text{cm}$ . The outlet temperature of the cooling water is  $61.8^{\circ}\text{C}$ . The temperatures of the graphite and copper alloy are kept below their allowable temperature.

Experimental studies on the burnout heat flux in highly subcooled forced-convection boiling of water has been carried out in order to design beam dumps of a high power neutral beam injector for JT-60 [47]. From these results, the burnout heat flux is more than  $1\text{ kW/m}^2$  at a flow rate of 7 m/sec. The surface heat flux of  $0.54\text{ kW/m}^2$  in the present design work is much smaller than this value. The present cooling system has a sufficient margin to burnout.

Next, we consider the integrity of the shine-through armor plate for the plasma disruption case. When the plasma disrupts, a heat load of  $20 \text{ MW/m}^2$  with a peaking factor of 1.5 flows into the armor plate. Figure 5.3.3 shows the calculational result of temperature rise on the surface of the armor plate during the plasma disruption. A steady state thermal analysis based on a one dimensional model was used. The temperature  $T$  on the surface of an infinite plate is given by

$$T = 2Q \sqrt{\frac{t}{\pi \cdot c_p \cdot \rho \cdot \lambda}}$$

where  $Q$ ,  $t$ ,  $c_p$ ,  $\rho$  and  $\lambda$  are heat flux, time, specific heat, density and thermal conductivity [48]. Figure 5.3.3 shows that if the injection power is shut off within 0.5 sec, which is sufficient from the technical point of view, the carbon surface of the armor plate will maintain its integrity.

## (2) Erosion estimation

The surface erosion of the armor plate caused by physical sputtering and blistering is estimated. The normal particle load is  $5 \times 10^{19} / \text{m}^2 \cdot \text{s}$ , as shown in Fig. 5.3.4. Figure 5.3.4 shows the results of erosion estimations due to the physical sputtering of several candidate materials by using the DSPUT model [49].

This computer code has been developed to compute the physical sputtering yields for various plasma particles incident on candidate fusion reactor first wall materials. The code, which incorporates the energy and angular-dependence of the sputtering yield, treats both high- and low-Z incident particles bombarding high- and low-Z wall materials. The physical sputtering yield is expressed in terms of the atomic and mass numbers of the incident and target atoms, the surface binding energy of the wall materials, and the incident angle and energy of the particle. A low-z material is favorable from the impurity control point of view. Although the erosion thickness become large abruptly as the incident angle increases, the erosion thickness of graphite over its life time of  $2.4 \times 10^6$  sec is less than 1 mm at an incident angle of  $70^\circ$  and the erosion thickness of copper alloy is less than 1 mm at the

incident angle of  $50^{\circ}$ . By using bare copper alloy, the armor plate structure becomes simple and the reliability of heat removal is improved.

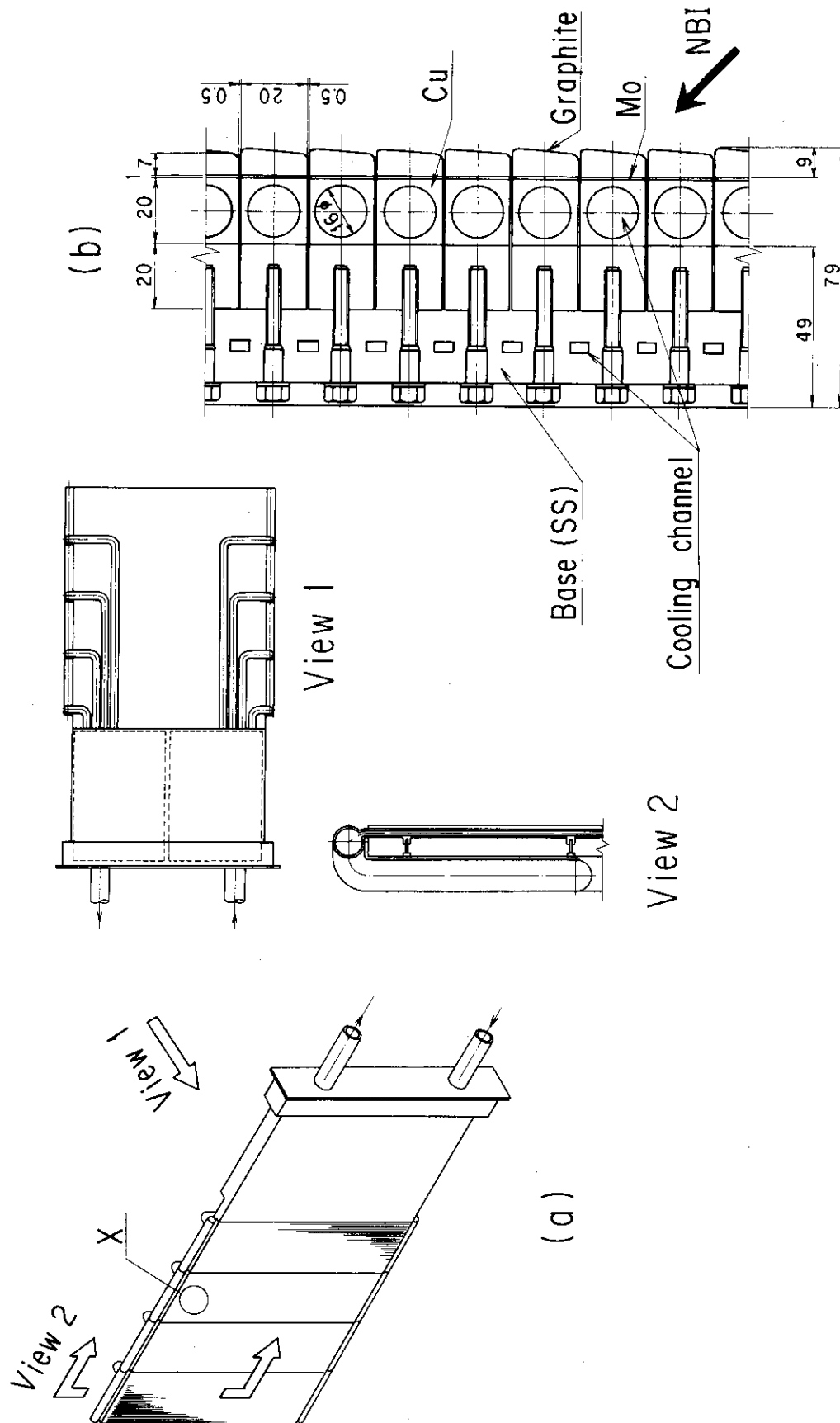


Fig. 5.3.1 Structural concept of the shine-through armor plate.

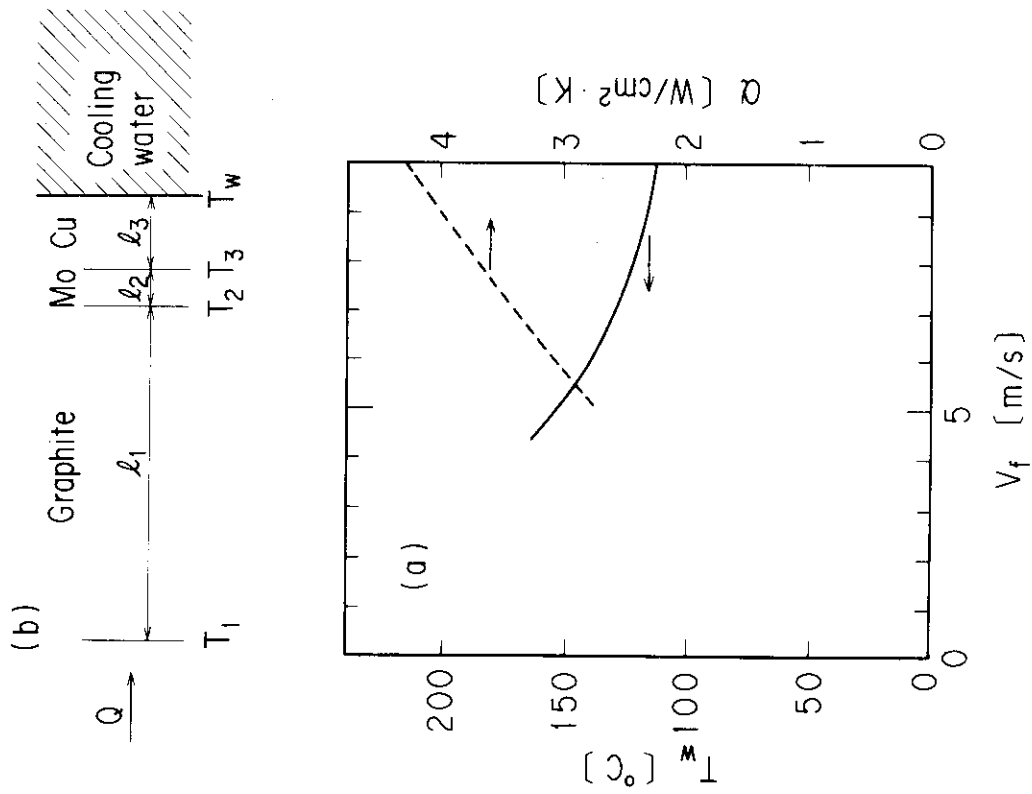


Fig. 5.3.2 Relation between flow rate and surface temperature of the cooling channel

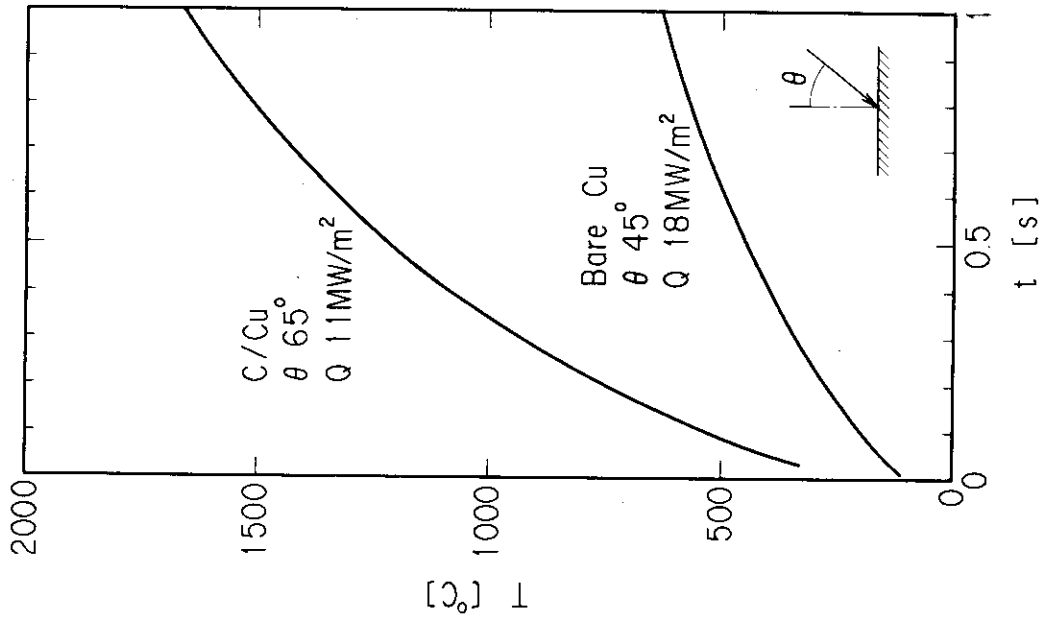


Fig. 5.3.3 Steady-state thermal analysis, based on the one dimensional model

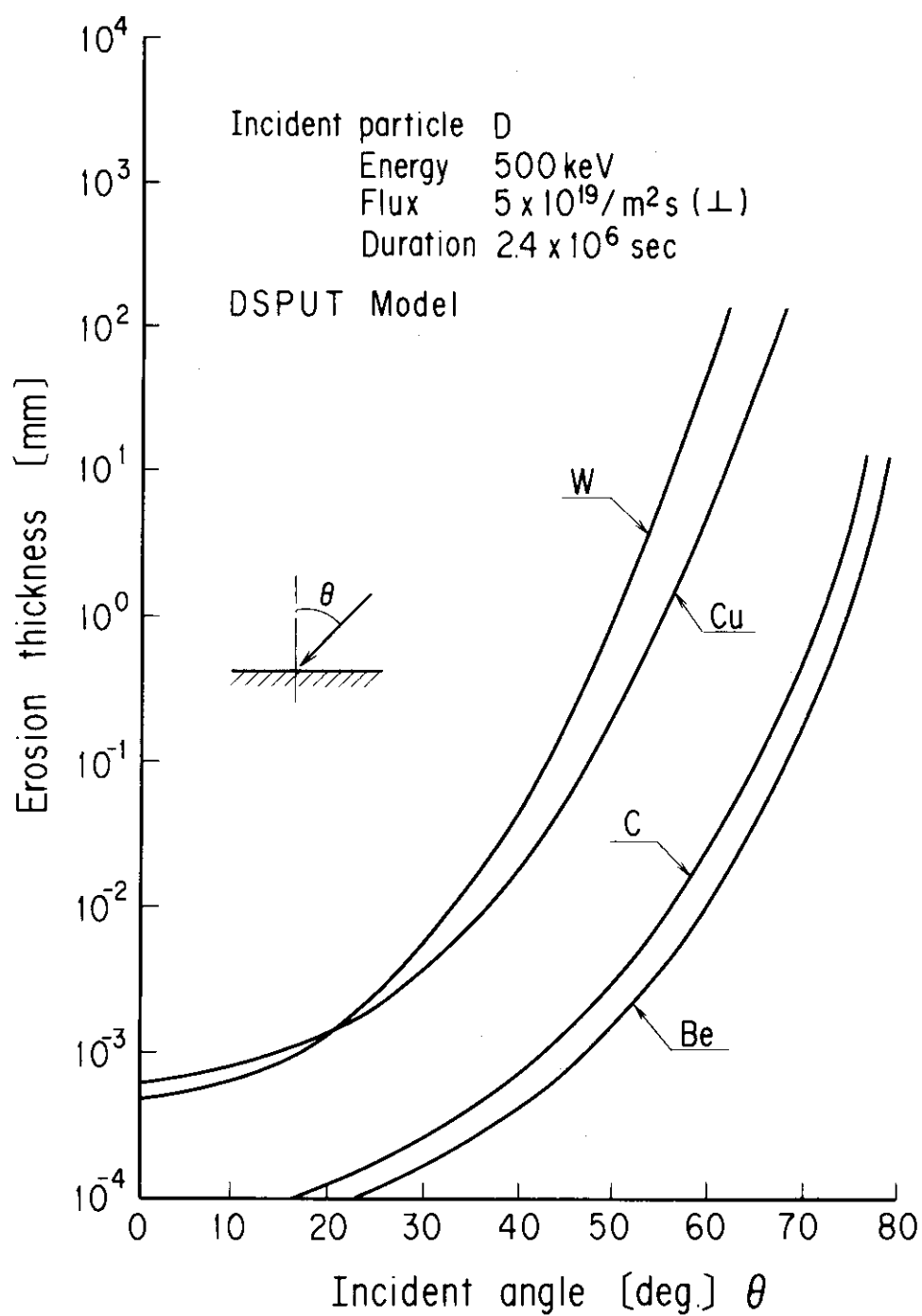


Fig. 5.3.4 Erosion estimation for armor plate. Calculation was performed by DSPUT model.

## 5.4 Neutron Shield Structure

The beamline is subjected to neutron irradiation and this limits accessibility and makes maintenance difficult. Therefore, it is a matter of concern to estimate the neutron-induced radioactivity and  $\gamma$ -ray dose rate distribution in designing the maintenance procedure as well as the beamline and its components. In the following section, the neutron flux distribution and the  $\gamma$ -ray dose distribution in the ion source room and the ion dump room will be described.

In this study, the D-D and D-T reactions at the D beam bombarded surface are not discussed.

### 5.4.1 Calculational Model

For the calculation of neutron and  $\gamma$ -ray transport in this study, a two-dimensional model may be applied and this helps reduce computational time. The Dot 3.5 code [52] is used mainly. To make a calculating model of the beamline, the following are concerned.

- 1) The drift duct is modeled in order to represent the transported neutron accurately.
- 2) The neutrons which are radiated directly and scattered a few times are calculated in order to estimate the life time of the components or the nuclear heating.
- 3) Each region volume is represented to be equal to that of the actual components.

Considering these requirements, the ion source room and ion dump room are modeled as shown in Figs. 5.4.1a and 5.4.5a. These two components are of prime concern to the maintenance design of the NBI system. The model is a two-dimensional axi-symmetrical (R-Z) one whose axis of symmetry coincides with the center line of the NBI beam line. The R dimensions were chosen in order to represent the component cross-section or the volume accurately. The Z dimensions were actual. In this model, the material compositions used were the same as in the actual components. In Figs. 5.4.1a and 5.4.5a, the region numbers represent the modeled components, and their material compositions are shown in Tables 5.4.1a and b, respectively.

#### 5.4.2 Calculation procedure

The neutron transport calculation was carried out with the DOT 3.5 code using an 18-group neutron cross-section set, a 7-group Y-ray cross section data set and  $44 \times 84$  spatial meshes. The generation and depletion of neucleides were estimated with an induced activity calculation code considering an operating pattern. The Y-ray transport calculation using the decay Y-ray source, which was calculated in the former step, was carried out to obtain the dose distribution. The DOT 3.5 code was again used in the calculation with a 54-group Y-ray cross-section set. The calculated Y-ray flux distribution was converted into the dose distribution using the flux-to-dose conversion factors. This procedure is shown in Fig. 5.4.2. To estimate the neutron source, it was assumed that the neutrons were yielded uniformly and radiated isotropically from the plasma region. The neutron density was estimated as  $5.7 \times 10^{11}$  n/s·cm<sup>3</sup>. It was also assumed that the neutrons, radiated inside of the solid angle through the drift duct, might arrive at the input point of the calculating region and be well collimated. Therefore, the neutrons radiated into the region were supposed to have the same divergence as that (solid angle). The geometrical position of the ion-source and the ion-dump chamber are illustrated in Fig. 5.4.3, and the source conditions are also described in the figure.

#### 5.4.3 Results

##### (1) Ion source room

The neutron flux distribution for the 14 MeV neutrons is shown in Fig. 5.4.1b, and the distribution for components higher than 1 MeV is in Fig. 5.4.1c. In these figures, the distribution of the near axis region and the chamber wall is considered to be reasonable. In the electrode insulator region, the neutron flux is estimated as  $\sim 10^6$  n/s·cm<sup>2</sup>. Assuming a 5 hour operation (18 times burning) per day, the Y-ray dose distribution for one day after shutdown following a two-year operation is shown in Fig. 5.4.1d. It is shown that the electrode region and the back wall have a high dose rate of up to 1 rem/h. Fig. 5.4.4 shows the

decay of the induced activity for the generated nuclides. The dose rate in the electrode depends on the decay of  $^{64}\text{Cu}$  which is generated from the  $^{65}\text{Cu}(n,2n)^{64}\text{Cu}$  reaction.

But the chamber wall has long life nuclides, such as  $^{55}\text{Fe}$  and  $^{57}\text{Co}$ , and it is expected that its material and volume will be reselected.

## (2) Ion dump room

The same calculation procedure and operating assumptions were used for the neutron flux distribution and the  $\gamma$ -ray dose distribution as for the ion dump chamber. The results are shown in Figs. 5.4.5b to d. The outside dose rate of the chamber is permissible. However, the neutron flux becomes up to  $\sim 10^9$  n/s $\cdot$ cm $^2$  at the beam dump which is supposed to be subjected to a high heat flux of several kW/cm $^2$ . So life time estimation may be important. In the maintenance process, a remote handling machine and work time limitation may be necessary.

One of the concerns in maintenance is the life estimation of the ion source insulation, for which FRP is used. In this design, the ion source was distant from the reactor and the neutron flux in that region was estimated to be under  $10^7$  n/cm $^2$  $\cdot$ s for neutrons above 1 MeV.

The database on which to judge the performance limits of the NBI components, especially for organic materials, is poor [53]. Concerning mechanical strength, the radiation exposure limit under  $\gamma$ -ray irradiation for epoxy may be supposed to be 1 MGy or less. Then, under neutron irradiation, assuming that the irradiation limit value for mechanical life time estimation is  $10^{16}$  n/cm $^2$ , it may be expected to have a life time (operation time) of  $10^9$  s magnitude. But, on electrical resistivity the limit value has a tendency to be reduced by a few orders of magnitude. Thus, it is desirable that the ion source insulator has enough distance from the axis to have a moderate life time.

For an operation time of  $10^7$  s magnitude (several years), it may be expected that there would be only few times of exchanging of the ion source insulator.

Table 5.4.1 Material compositions: (a) Ion source room,  
(b) Ion dump room.

(a)

Region	Region name	Composition (Volume fraction)
1	Vacuum chamber	SS (1.0)
2	Insulator	FRP (1.0)
3	Electrode	Cu (0.5) + Vacuum (0.5)
4	Neutralizer	Cu(0.052) + H <sub>2</sub> O(0.216) + SS(0.109) + Permalloy(0.05) + Vacuum(0.573)
5	Ion source chamber wall	SS (1.0)
6	Vacuum	Vacuum (0.5)

(b)

Region	Region name	Composition (Volume fraction)
1	Vacuum	Vacuum (1.0)
2	Beam limiter	Cu (0.8) + H <sub>2</sub> O (0.2)
3	Neutron shield	SS (1.0)
4	Neutron shield	H <sub>2</sub> O (1.0)
5	Ion dump room	H <sub>2</sub> O (0.8) + SS (0.2)
6	Ion dump	Cu (0.5) + H <sub>2</sub> O (0.5)
7	Neutralizer	SS (0.33) + H <sub>2</sub> O (0.67)
8	Magnetic shield	Permalloy (1.0)
9	Magnetic shield	Fe (1.0)

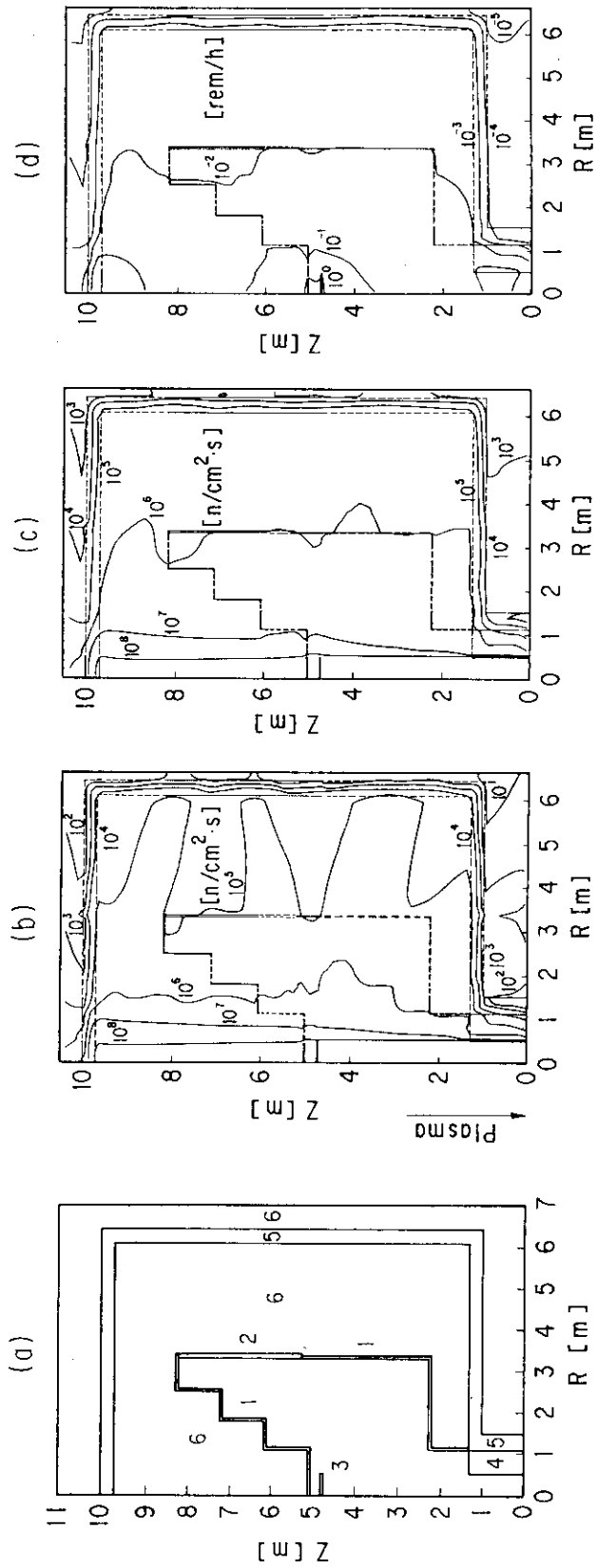
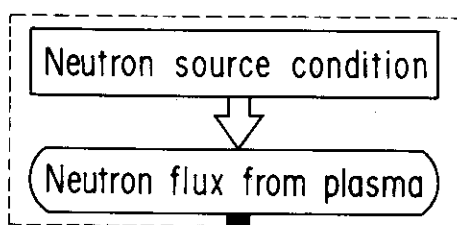


Fig. 5.4.1 Neutron and  $\gamma$ -ray transport in ion source room.  
 (a) Modeling of ion source room. Region numbers represent the modeled components and their material composition, described in Table 5.4.1a. (b) Neutron flux distribution for 14 MeV neutrons. (c) Neutron flux distribution for higher than 1 MeV. (d)  $\gamma$ -ray dose distribution for one day after shutdown following a two-year operation.

## Plasma



2D neutron flux distribution

&lt;DOT 3.5&gt;

Neutron flux distribution during discharge

Radioactivity after shutdown

&lt;CINAC&gt;

 $\gamma$ -ray source distribution2D  $\gamma$ -ray flux distribution

&lt;DOT 3.5&gt;

— note —

..... Calculation/Analysis

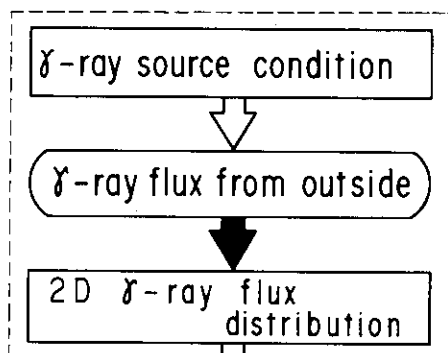
..... Result

..... Out put

..... In put

&lt; &gt; ..... Code name

## Reactor



&lt;DOT 3.5&gt;

 $\gamma$ -ray flux distribution after shutdown

flux-dose conversion

 $\gamma$ -ray dose distribution after shutdown

Fig. 5.4.2 Calculational procedure

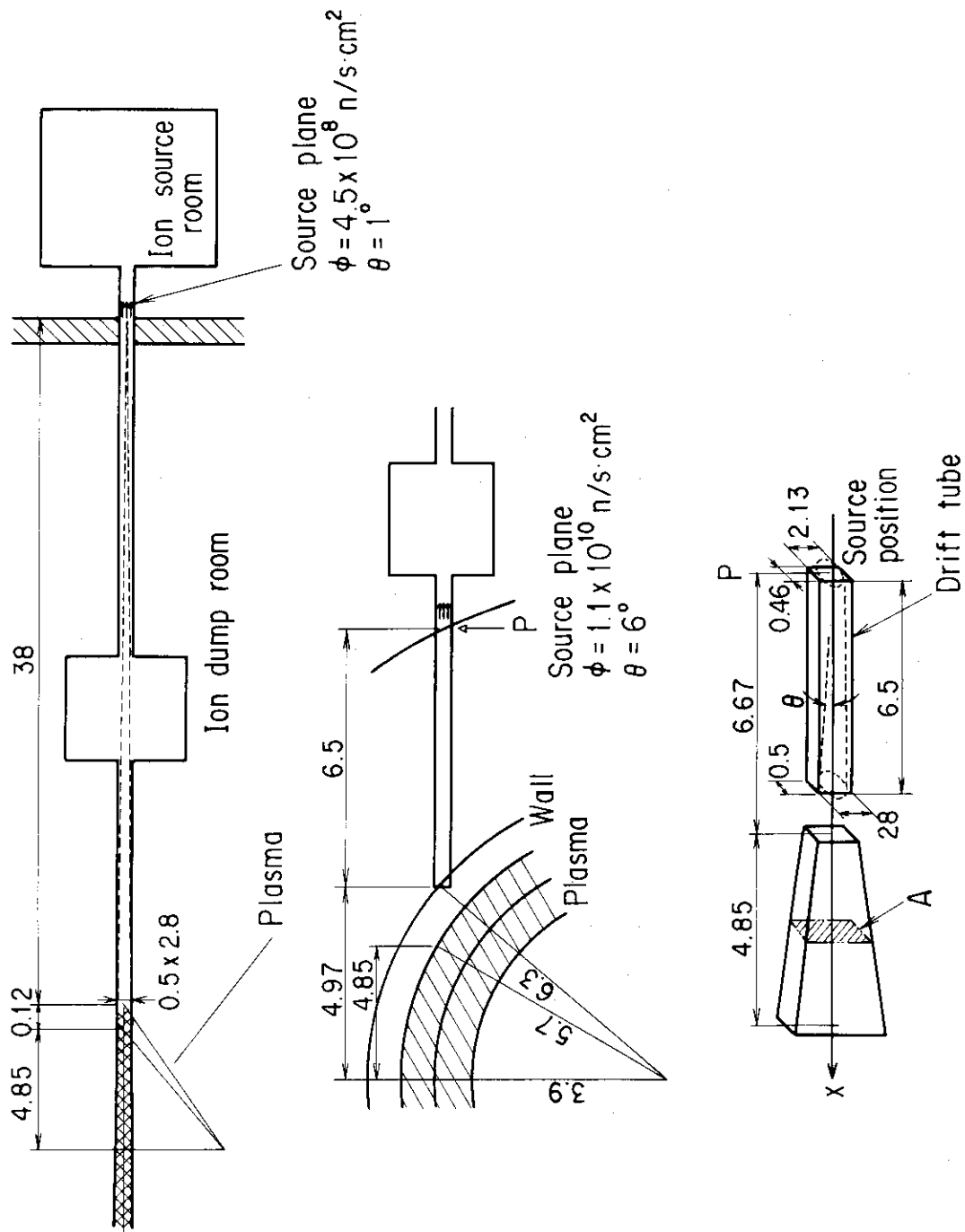


Fig. 5.4.3 Geometrical position of the ion source and the ion dump rooms. The source conditions are also shown in this figure.

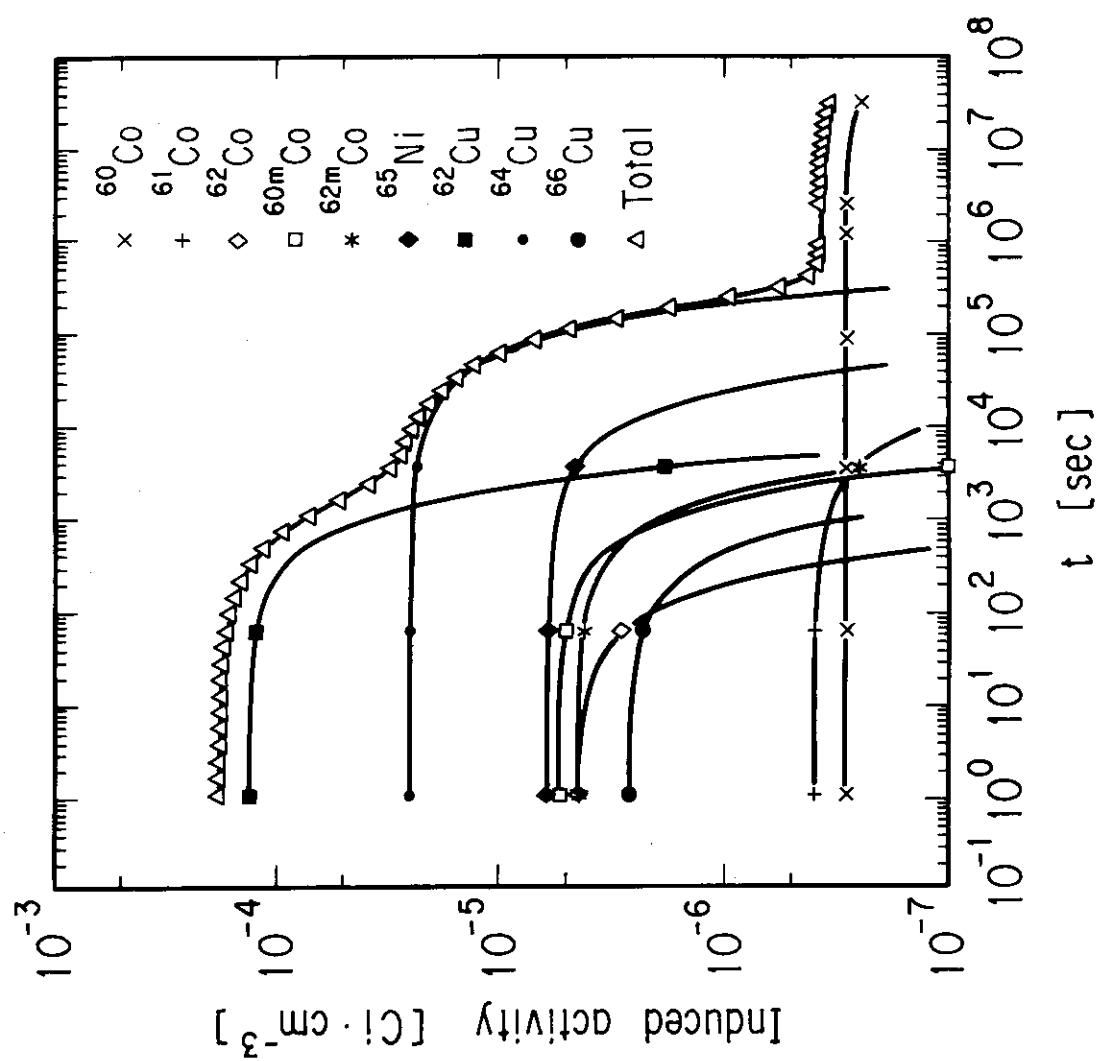


Fig. 5.4.4 Decay of induced activity for generated nuclides

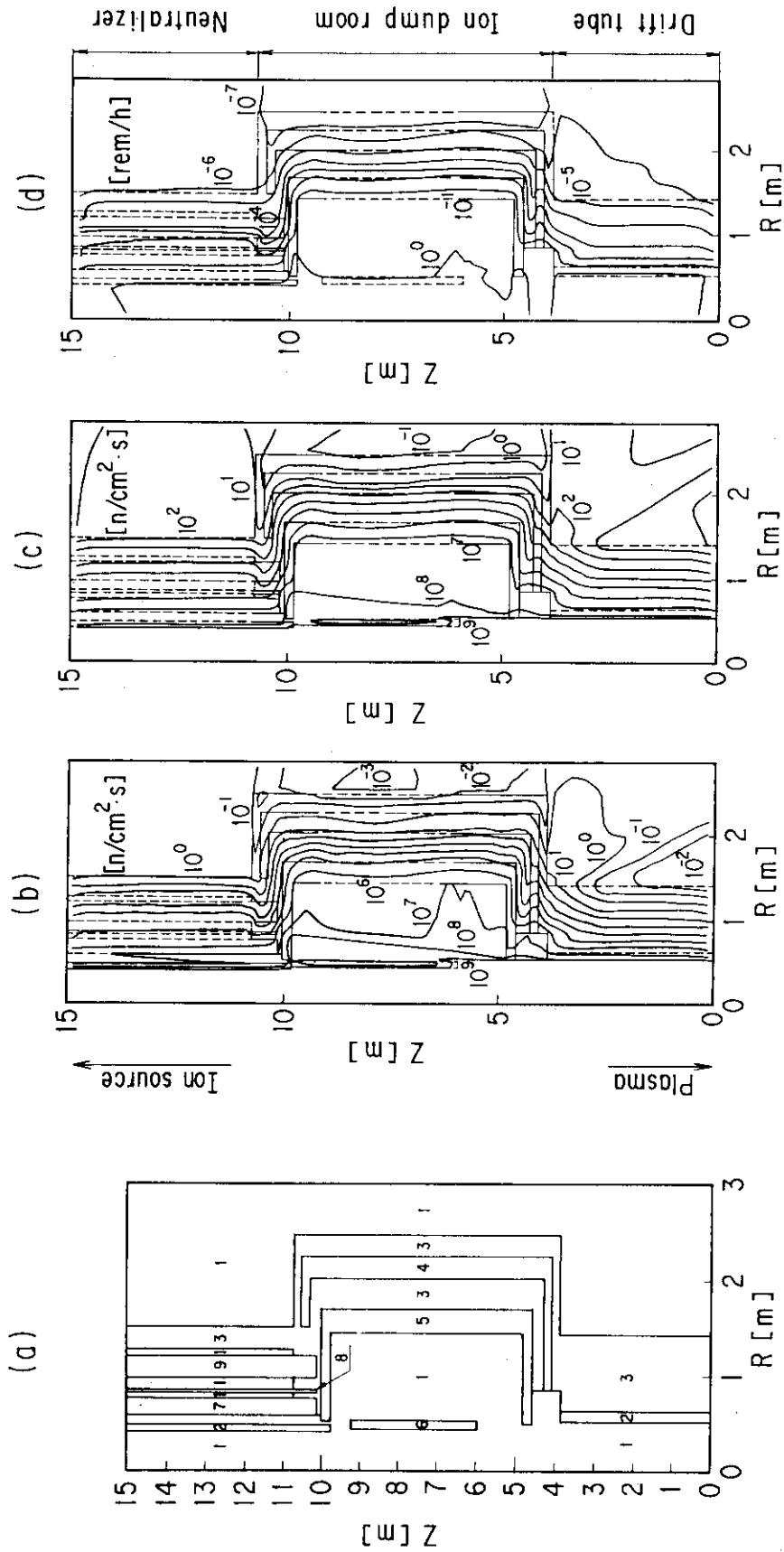


Fig. 5.4.5 Neutron and  $\gamma$ -ray transport in ion dump room.  
 (a) Modeling of ion dump room. Region numbers represent the modeled components and their material composition, described in Tables 5.4.1b.  
 (b) Neutron flux distribution for 14 MeV neutrons.  
 (c) Neutron flux distribution for higher than 1 MeV.  
 (d)  $\gamma$ -ray dose distribution for one day after shutdown following a two-year operation.

## 5.5 Tritium Processing System for Ion Source Room and Ion Dump Room

Plasma of D-T fusion reactors are expected to be heated to ignition temperature by deuterium neutral injection. Since D/T gas is the fusion fuel, the handling system is one of the major components of a fusion reactor. So neutral injectors for the heating plasma of D/T burning fusion reactors are subject to tritium contamination. Tritium contamination in deuterium neutral beam injection (NBI) systems results from particle backstreaming from the reactor vessel, and to a much lesser degree, from the  $D(d,p)T$  reaction at D-beam-bombarded surfaces. Therefore, the tritium aspects of gas pumping and recycling are of prime concern in NBI system design as well as in reactor fuel recycle system design. Here, we examine the tritium-related problem areas in the NBI systems, including discussions on deuterium injection, gas pumping, and recycling scenarios.

### 5.5.1 Operation Scenario and Mass Flows

The plasma operation pattern and NBI power required for each phase have already been shown in Fig. 5.1.1. The species of fuel gas injected into the plasma vacuum chamber in each operation phase are listed in Table 5.5.1. A schematic diagram of the NBI system, including the torus vacuum chamber, NBI gas evacuation and gas supply, is shown in Fig. 5.5.1. The tritium/deuterium mass flow in each operation phase is listed in Table 5.5.2. During the gas injection phase before start-up, the torus is filled with only deuterium gas. During the current ramp-up phase, only deuterium gas is injected from the pellet injector into the torus, and the deuterium gas effluent from the NBI is evacuated from the main vacuum system. During the ignition approach, burn phase and shut down phase, the tritium and deuterium are injected from the pellet injector into the torus. The unburned tritium and deuterium, injected from both the pellet injector and NBI are evacuated from the main vacuum system. During the burn phase (800 sec), the NBI is scheduled to be operated during 80 sec (8 sec $\times$ 10 times) at maximum for the purpose of profile control. A fast-acting shutter, instead of or in addition to the vacuum/shield valve is employed to substantially decrease the

tritium effluent from the torus into the NBI through the drift duct. The shutter is opened during neutral beam injection into the torus and the shutter is closed fast after injection. The primary source of tritium contamination is the backstreaming gas from the torus during each injection pulse. Most of the backstreaming tritium gas from the torus is trapped in the vacuum pump in the ion dump room, however, a small fraction of the tritium gas seems to penetrate into the ion source system and become trapped in the vacuum pump in the ion source room. The backstreaming rate depends on the gas pressure near the reactor wall, the local particle loss rate from the reactor plasma, and the cross-sectional area of the drift duct that connects the beam line to the torus.

Figure 5.5.2a shows the cross-section of the Option C plasma. The total tritium out flux  $I_T$  [ $s^{-1}$ ] from the main plasma is given by

$$I_T[s^{-1}] = (N_i/2)/\tau_p[s] \sim n_i[m^{-3}]V[m^3]/2\tau_p[s]$$

$$\sim 10^{20} \times 288 / (2 \times 0.2) \sim 7.2 \times 10^{22}$$

where  $n_i$ ,  $V$  and  $\tau_p$  are the ion plasma density, plasma volume and particle confinement time, respectively. The decay length of the back flow neutral particles from the divertor to the main plasma is about 0.2 m.

Using this value and the above-mentioned total tritium out flux, the maximum tritium flux  $\Gamma_T[m^{-2} \cdot s^{-1}]$  into the drift duct is estimated as follows.

$$\Gamma_T[m^{-2} \cdot s^{-1}] = I_T \exp(-1.3/0.2) / 2\pi R[m]d[m] \sim$$

$$\sim 7.2 \times 10^{22} \times 1.5 \times 10^{-3} / (2 \times 3.14 \times 5 \times 0.1) \sim 3.4 \times 10^{19}$$

where  $R$  and  $d$  are the mean major radius at the position of the plasma side wall of the drift duct and the distance from the separatrix to the first wall. The maximum neutral density  $n_T[m^{-3}]$  at the entrance of the drift duct is estimated as

$$n_T[m^{-3}] = \Gamma_T/v_T[m/s] \sim 3.4 \times 10^{19} / 10^3 \sim 3.4 \times 10^{16}$$

Conductance of the drift duct is  $48[\text{m}^3 \cdot \text{s}^{-1}]$ , which is shown in Fig. 5.5.2c. The back stream flux of tritium molecules from the torus into the drift duct is estimated as

$$\phi_{\text{Bd}}[\text{n/s} \cdot \text{unit}] = n_{\text{T}} C \sim 3.4 \times 10^{16} \times 48 \sim 1.6 \times 10^{18}$$

(3 NBI units for FER system)

The backstream flux of the tritium molecules into the ion source is estimated as

$$\begin{aligned} \phi_{\text{IS}}[\text{n/s} \cdot \text{unit}] &= \phi_{\text{Bd}} C[\text{m}^3 \cdot \text{s}^{-1}] / S_{\text{T}}[\text{m}^3 \cdot \text{s}^{-1}] \\ &\sim 1.6 \times 10^{18} \times 5.5 / 160 \sim 5.5 \times 10^{16} \end{aligned}$$

where  $C[\text{m}^3 \cdot \text{s}^{-1}]$  and  $S_{\text{T}}[\text{m}^3 \cdot \text{s}^{-1}]$  are the conductance of the neutralizer and the cryopump speed in the ion dump room, respectively.

(3 NBI units for FER system)

### 5.5.2 Gas Handling Conditions

The presence of tritium in the NBI system affects gas handling or the cycling scenario. The selection of the gas handling scenario should be done by considering the backstream tritium flux and D/T ratio. The tritium inventory on the ion dump cryo panel is estimated. Assuming a 5 hour operation per day, and 0.8 duty with 3 units.

$$I_{\text{BD}} = 3 \times 5 \times 3600 \times 0.8 \times \phi_{\text{BD}} = 1.2 \text{ g/day}$$

For tritium inventory on the ion source cryopanel with the same assumption,

$$I_{\text{IS}} = 3 \times 5 \times 3600 \times 0.8 \times \phi_{\text{IS}} = 0.024 \text{ g/day}$$

From the above results, the evacuated gas from both the ion dump vacuum system and the ion source vacuum system cannot simply be vented to the

environment. (The maximum permissible tritium evacuation rate to the environment is settled as 100 ci/day). Therefore, the evacuated gas should be recirculated until the buildup of tritium becomes a problem or the evacuated gas should be recirculated for processing. Table 5.5.3 shows the averaged D/T flux and ratio during 1000 sec in each vacuum port. From the above table, it is clear that the D-flux from the ion source vacuum system is about 3 times that of the main vacuum system and the T/D ratio for the gas in the ion source vacuum system is very small in comparison with the main vacuum system. Therefore, it is recommended that an independent gas cycling system should be used for the main vacuum system and ion source vacuum system.

### 5.5.3 Selection of Gas Handling Scenario

Several gas handling scenarios are considered for the NBI system as shown in Fig. 5.5.3.

- i) A total integration of the NBI gas cycle into the reactor fuel cycle system in which the tritium contaminated gas from the NBI system is treated in the same way as burnt fuel gas.
- ii) The NBI gas from the ion source is vented directly to the environment. The rest of the gas is integrated into the reactor fuel cycle system.
- iii) The NBI gas from the ion source is recirculated until the buildup of tritium becomes a problem. After a number of uses, the NBI gas from the ion source is transferred to the main reactor fuel recycle system or detritiation system.
- iv) This scenario is the same as iii) except for the addition of a purification system in the deuterium gas recirculating system.

Scenarios i) and ii) are not acceptable from the discussion in subsection 5.5.2. Scenarios iii) and iv) are similar except in the way of recirculating the gas. A purification system for the ion source will be required because of impurity contamination in the ion source. Therefore, scenario iv) is selected as the reference gas handling system. The flow diagram of this system is shown in Fig. 5.5.4.

Table 5.5.1 Species of fuel gas injection into plasma vacuum chamber during each operation phase.

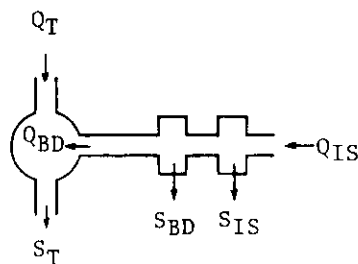
5 Phases for fuel gas injection	Fueling gas
① Gas injection phase before start up	D
② Current ramp - up phase	D
③ Ignition approach phase	D + T
④ Burn phase	D + T
⑤ Shut down phase	D + T

Table 5.5.3 Averaged D/T flux and ratio during 1000 sec in each vacuum port

	D-flux [n/s]	T-flux [n/s]	T/D Ratio
Main vacuum system	$1.3 \times 10^{21}$	$1.2 \times 10^{21}$	0.922
Beam dump vacuum system	$2.0 \times 10^{20}$	$1.85 \times 10^{18}$	0.009
Ion source vacuum system	$3.2 \times 10^{21}$	$4 \times 10^{16}$	0.001

Table 5.5.2 Tritium/Deuterium mass flow during each operation phase

		0~4 (4)	2~24 (20)	24~100 (76)	100~120 (20)	120~920 (720/800)	120~920 (80/800)	920~940 (20)	940~1000 (60)
$Q_T$	D	0	0	0	$0.78 \times 10^{21}$ n/s	$1.68 \times 10^{21}$ n/s	$0.48 \times 10^{21}$ n/s	$0.78 \times 10^{21}$ n/s	0
	T	0	0	0	$1.688 \times 10^{21}$ n/s	$1.68 \times 10^{21}$ n/s	$1.688 \times 10^{21}$ n/s	$1.688 \times 10^{21}$ n/s	0
	He	0	0	0	0	0	0	0	0
	C	0	0	0	0	0	0	0	0
	O	0	0	0	0	0	0	0	0
	N	0	0	0	0	0	0	0	0
	H	0	0	0	0	0	0	0	0
	etc.	0	0	0	0	0	0	0	0
$Q_{BD}$	D	0	$0.6 \times 10^{21}$ n/s	$1.2 \times 10^{21}$ n/s	$0.9 \times 10^{21}$ n/s	0	$1.2 \times 10^{21}$ n/s	$0.9 \times 10^{21}$ n/s	0
	T	0	0	0	0	0	0	0	0
	He	0	0	0	0	0	0	0	0
	C	0	0	0	0	0	0	0	0
	O	0	0	0	0	0	0	0	0
	N	0	0	0	0	0	0	0	0
	H	0	0	0	0	0	0	0	0
	etc.	0	0	0	0	0	0	0	0
$S_T$	D	0	$0.6 \times 10^{21}$ n/s	$1.2 \times 10^{21}$ n/s	$1.52 \times 10^{21}$ n/s	$1.52 \times 10^{21}$ n/s	$1.52 \times 10^{21}$ n/s	$1.52 \times 10^{21}$ n/s	0
	T	0	0	0	$1.52 \times 10^{21}$ n/s	$1.52 \times 10^{21}$ n/s	$1.52 \times 10^{21}$ n/s	$1.52 \times 10^{21}$ n/s	0
	He	0	0	0	$1.63 \times 10^{20}$ n/s	$1.63 \times 10^{20}$ n/s	$1.63 \times 10^{20}$ n/s	$1.63 \times 10^{20}$ n/s	0
	C	0	0	0	$1.63 \times 10^{19}$ n/s	$1.63 \times 10^{19}$ n/s	$1.63 \times 10^{19}$ n/s	$1.63 \times 10^{19}$ n/s	0
	O	0	0	0	$1.63 \times 10^{19}$ n/s	$1.63 \times 10^{19}$ n/s	$1.63 \times 10^{19}$ n/s	$1.63 \times 10^{19}$ n/s	0
	N	0	0	0	0	0	0	0	0
	H	0	0	0	$3.26 \times 10^{19}$ n/s	$3.26 \times 10^{19}$ n/s	$3.26 \times 10^{19}$ n/s	$3.26 \times 10^{19}$ n/s	0
	etc.	0	0	0	0	0	0	0	0
$S_{BD}$	D	0	$5.1 \times 10^{20}$ n/s	$1.02 \times 10^{21}$ n/s	$7.65 \times 10^{20}$ n/s	0	$10.2 \times 10^{20}$ n/s	$7.65 \times 10^{20}$ n/s	0
	T	0	0	0	$8.37 \times 10^{19}$ n/s	0	$8.37 \times 10^{19}$ n/s	$8.37 \times 10^{19}$ n/s	0
	He	0	0	0	0	0	0	0	0
	C	0	0	0	0	0	0	0	0
	O	0	0	0	0	0	0	0	0
	N	0	0	0	0	0	0	0	0
	H	0	0	0	0	0	0	0	0
	etc.	0	0	0	0	0	0	0	0
$S_{IS}$	D	0	$1.8 \times 10^{21}$ n/s	$16.2 \times 10^{21}$ n/s	$12.15 \times 10^{21}$ n/s	0	$16.2 \times 10^{21}$ n/s	$12.15 \times 10^{21}$ n/s	0
	T	0	0	0	$3.32 \times 10^{17}$ n/s	0	$3.32 \times 10^{17}$ n/s	$3.32 \times 10^{17}$ n/s	0
	He	0	0	0	0	0	0	0	0
	C	0	0	0	0	0	0	0	0
	O	0	0	0	0	0	0	0	0
	N	0	0	0	0	0	0	0	0
	H	0	0	0	0	0	0	0	0
	etc.	0	0	0	0	0	0	0	0
$Q_{IS}$	D	0	$9.81 \times 10^{21}$ n/s	$19.62 \times 10^{21}$ n/s	$14.71 \times 10^{21}$ n/s	0	$19.62 \times 10^{21}$ n/s	$14.71 \times 10^{21}$ n/s	0
	T	0	0	0	0	0	0	0	0
	He	0	0	0	0	0	0	0	0
	C	0	0	0	0	0	0	0	0
	O	0	0	0	0	0	0	0	0
	N	0	0	0	0	0	0	0	0
	H	0	0	0	0	0	0	0	0
	etc.	0	0	0	0	0	0	0	0
NBI power Fueling gas			30MW D	60MW D	45MW D+T	D+T	60MW D+T	45MW D+T	



$Q_T$  : Injected fuel gas  
 $S_T$  : Evacuated fuel gas  
 $Q_{IS}$  : Gas supply for ion source  
 $S_{IS}$  : Gas evacuation from ion source  
 $S_{BD}$  : Gas evacuation from ion dump  
 $Q_{BD}$  : Gas flow from NBI to vacuum chamber

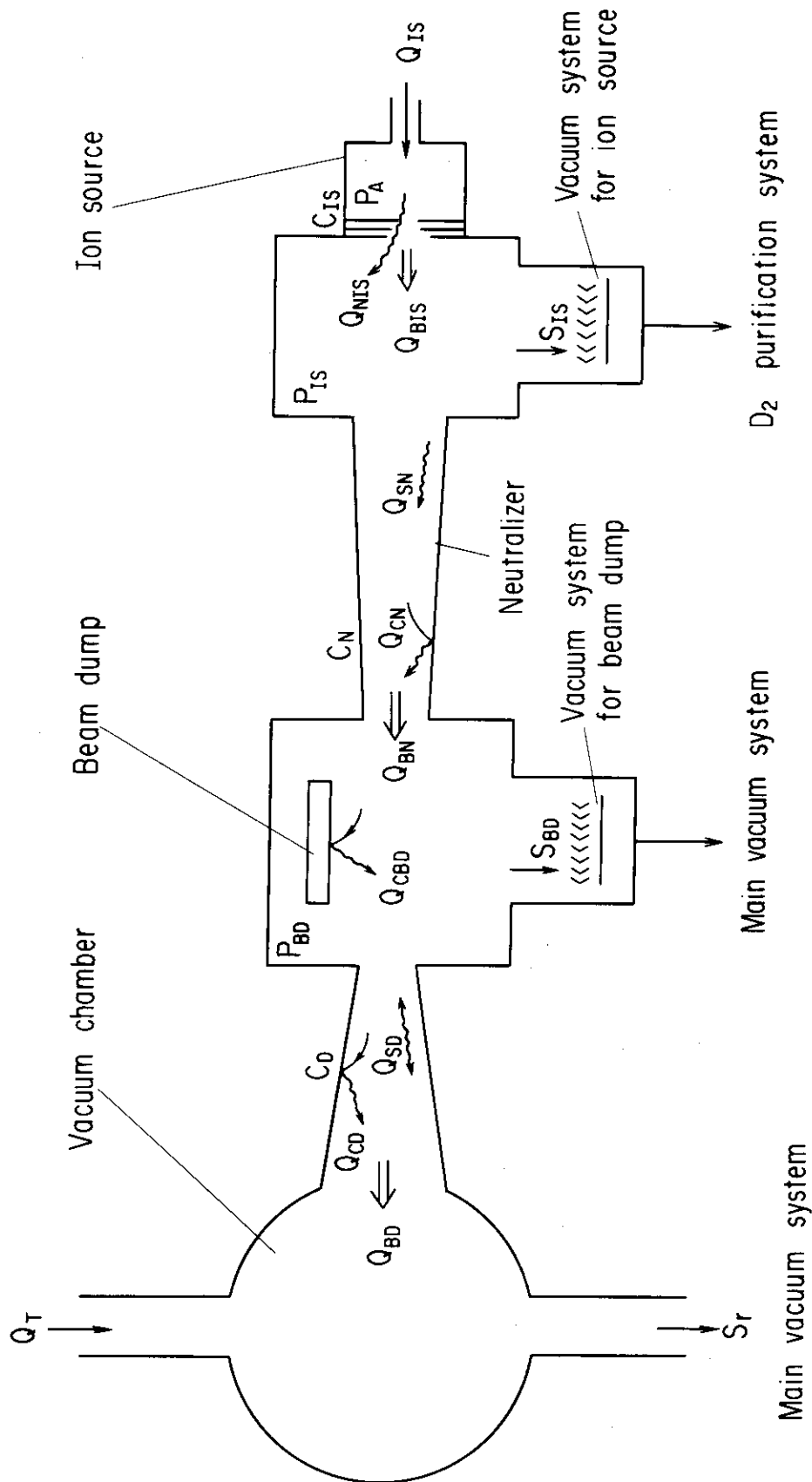
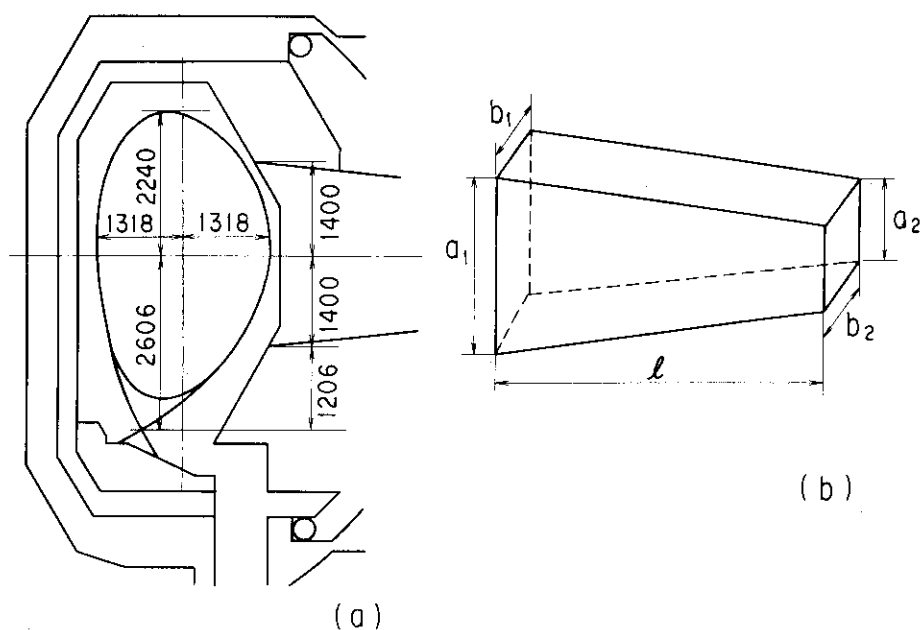


Fig. 5.5.1 Schematic diagram of NBI system, including torus vacuum chamber, NBI evacuation and gas supply.



(c)		Drift duct	Neutralizer
Plasma side	$a_1$ [cm]	280	140
	$b_1$ [cm]	50	40
Ion source side	$a_2$ [cm]	180	240
	$b_2$ [cm]	44	26
$l$ [cm]		600	2400
Correction factor $\alpha$		1.3	1.3
Conductance $C$ [ $\text{m}^3\text{s}^{-1}$ ]		48.0	5.5

Fig. 5.5.2 Geometries of drift duct and neutralizer.  
 (a) Cross-section of Option C plasma.  
 (b) Tapered duct (c) Parameters of drift duct and neutralizer. Conductance  $C$  [ $\text{l}\cdot\text{s}^{-1}$ ] of a tapered rectangular duct is given by

$$C[\text{l}\cdot\text{s}^{-1}] = \frac{166}{\sqrt{M}} \frac{\alpha(a_1 \cdot b_1)(a_2 \cdot b_2)}{(\bar{a} + \bar{b})\{l + 8\alpha\bar{a}\bar{b}/3(\bar{a} + \bar{b})\}}$$

where  $\bar{a} = (a_1 + a_2)/2$ ,  $\bar{b} = (b_1 + b_2)/2$ ,  $\alpha$  is correction factor and  $M$  is molecular weight, respectively.

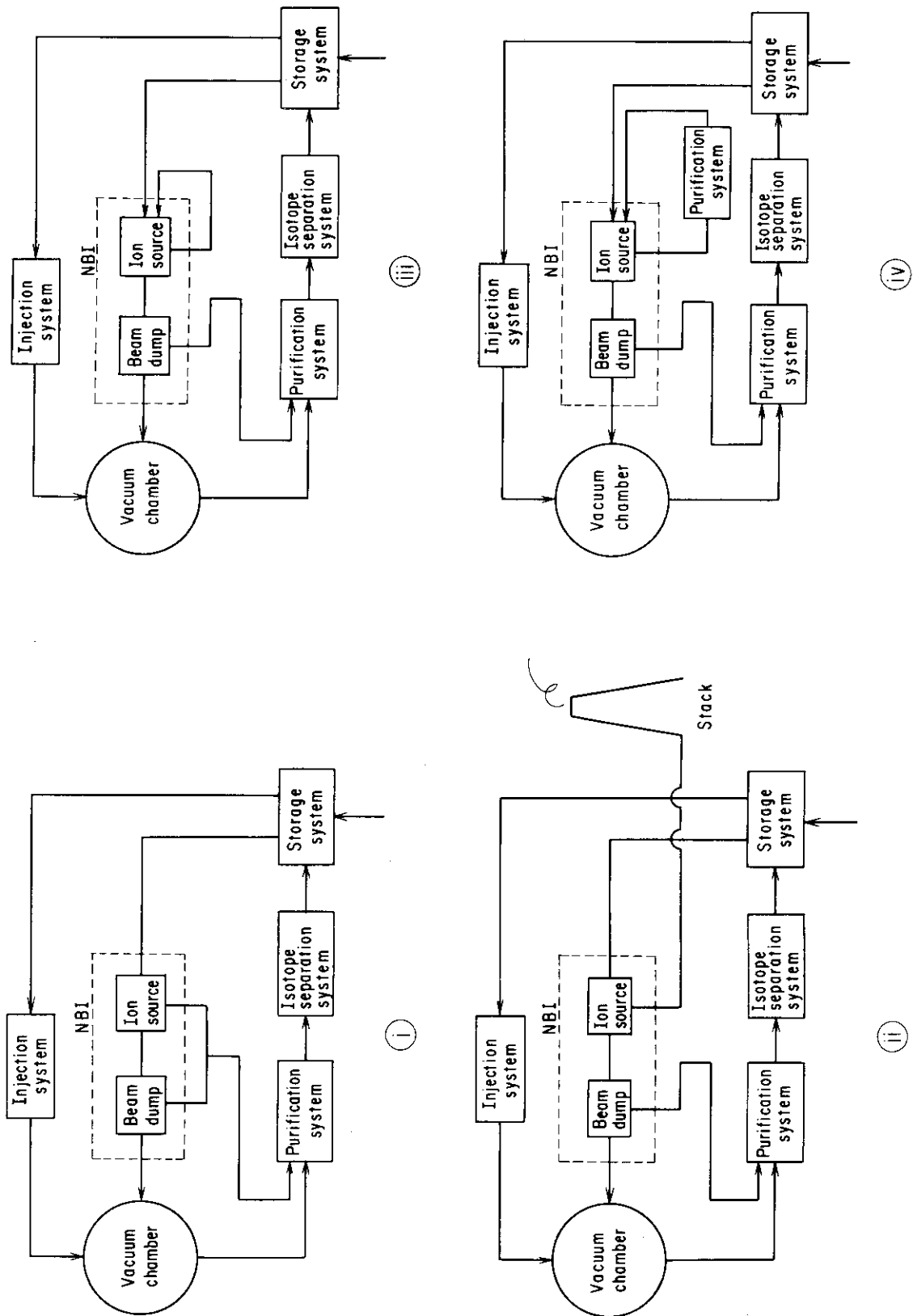


Fig. 5.5.3 Gas handling scenarios

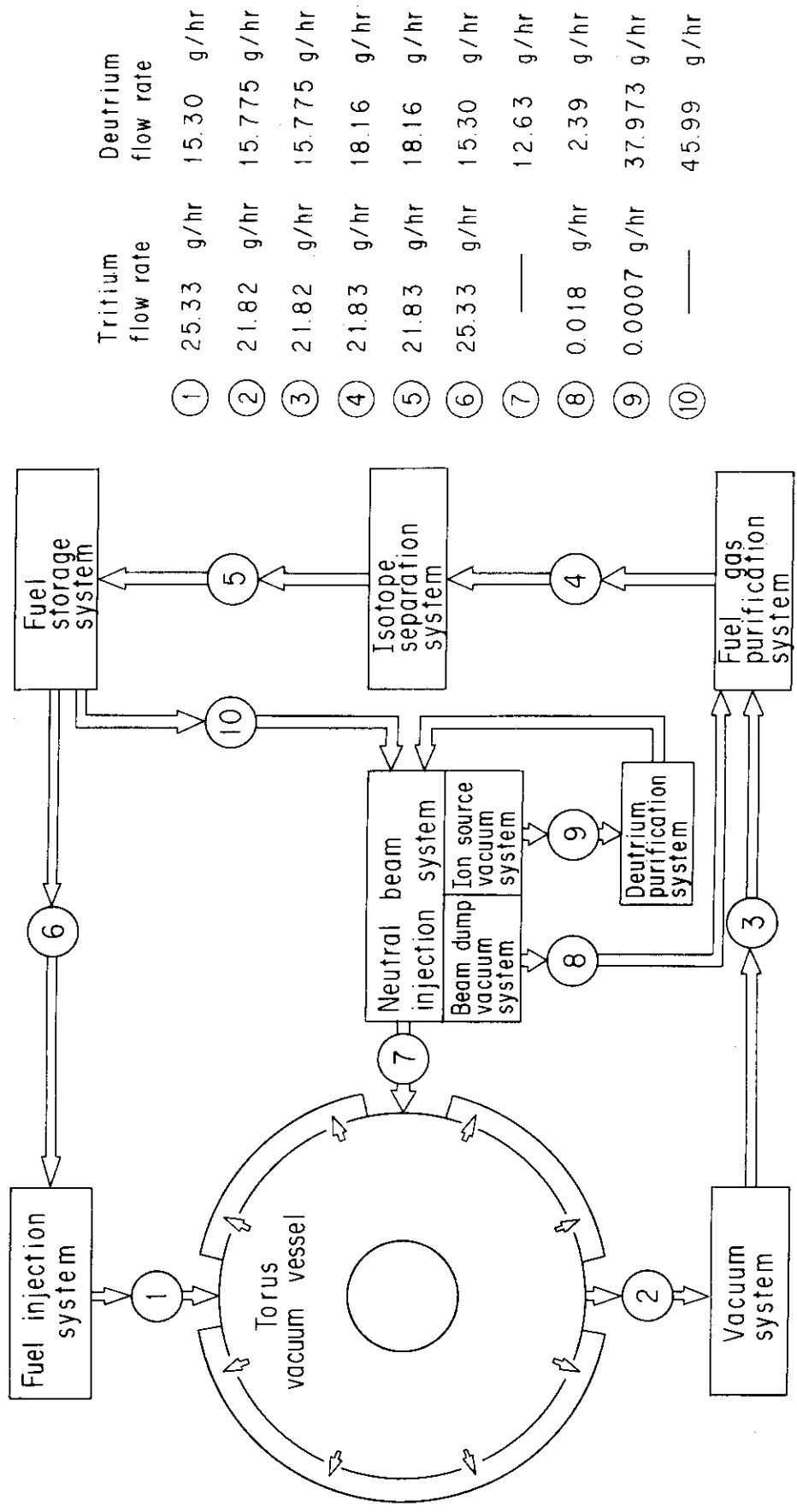


Fig. 5.5.4 Flow diagram of tritium processing system

## 5.6 Summary

The impact of the NBI system on the reactor structural configuration and maintenance was examined, including the design of the injection port and shine-through armor plate, the estimation of the neutron flux distribution and the  $\gamma$ -ray dose distribution in the ion source room and the ion dump room and the selection of the tritium processing system.

The NBI system is applied to the Option C reactor. The Option C reactor is not necessarily optimized for the application of the NBI system. However, tangential ports can be set without serious interference with the torus components.

The divertor segment is withdrawn without interference to the NBI system. The movable shield with the injection port (drift duct) is also withdrawn, after taking off only a part of the neutron shutter. Each shine-through armor plate is installed in each injection port, which keeps the number of ports employed by the NBI system to be minimum. The shine-through armor plate is extractable while keeping the vacuum condition of the reactor vacuum chamber.

The heat load on the shine-through armor plate during the current ramp-up phase is  $4 \text{ MW/m}^2$  with a peaking factor of 1.5. This value is permissible for the design of the armor. The heat load on the armor plate during plasma disruption is  $20 \text{ MW/m}^2$ . If the NBI is shut off within 0.5 sec, which is possible from the technical point of view, the armor plate will keep integrity.

From the estimation of the  $\gamma$ -ray dose distribution in the ion source room, it may be expected that it will be necessary to exchange the ion source insulator only a few times for an operation time of a magnitude of  $10^7 \text{ s}$  (for several years)

From the evaluation of the backstream of tritium molecules from the torus into the ion source room, the gas handling system is selected. The backstream into the ion source room is very low. Thus, the NBI gas from ion source is recirculated until the buildup of tritium becomes a problem. A purification system is used for impurities in the deuterium gas recirculating system. After a number of uses, the NBI gas from the ion source is transferred to the main reactor fuel recycle system or detritiation system.

## 6. Discussion and conclusions

In order to minimize the development cost and technological risk, phased operation and phased construction were proposed by the Atomic Energy Commission of Japan. The phase-to-phase check and review have to be sufficiently carried out. The phased operation is defined as follow.

- 1) Phase I: Facility function confirmation phase
- 2) Phase II: Burning experiment phase
- 3) Phase III: Full-rating operation phase

Figure 6.1.1 shows one example of the phased operation and phased construction adopted in the NBI reactor. The most important items are presented in the figure. Phase I (so called physics phase) with deuterium and/or hydrogen plasma (D/H plasma) is the important phase. During this phase, the plasma parameters are widely examined using a simple vacuum vessel without a neutron shield, as already shown in Fig. 2.1.2 and any modification of the mechanical configuration is done as necessary, in order to obtain an ignition relevant D/H plasma. Through these works, we realize a disruption free and self-ignited long burn plasma in Phase III. Thus, a simple and reliable operation scenario is preferable and the reactor should have sufficient flexibility.

Lawson derived his condition for ignition. Lawson's fusion parameter  $n_i T_i \tau_E$ , which should be above a critical value for ignition, is proportional to  $\beta_T \tau_E$ , where  $n_i$ ,  $T_i$ ,  $\tau_E$  and  $\beta_T$  are the ion plasma density, ion temperature, global plasma confinement time and toroidal beta value. Recent experimental results show that both the plasma confinement time and maximum attainable beta value are proportional to the plasma current. Thus, in order to have a required current and a required injection power as soon as possible after completion of the reactor, full inductive current ramp-up operation and NBI heating are adopted as the most efficient and reliable current ramp-up method and heating method, respectively.

The choice of the first wall material is one of the key factor in the design of the next machine. Recent experimental results show that a low-Z material is necessary for the production of a high performance plasma. However, for example, the erosion width of the graphite divertor plate of the FER is estimated to become several meters during the reactor life. In order to overcome such large erosion and offer

reliable maintainability, in-situ and vacuum repair of the divertor surface is adopted.

An NBI heated plasma offers good and reliable target plasma for the RF. One of the problems in RF is that the antenna-plasma coupling depends on the plasma property, especially on the scrape-off plasma and final aging of the transmission line including the antenna is finished, using an actual plasma. Thus, it is preferable to study the RF launcher using a simple structure without a neutron shield, for example, the RF launcher used in JT-60 or JT-60 up-grade. In this case, an unknown plasma can be studied using the well-known RF launcher like a well-accustomed diagnostic tool and obtain valuable information for the design of the RF launcher to be used in Phase III. The ECRF, from the point of coupling, the impact on the plasma edge conditions and absorption, is particularly simple. An ECRF with injection power of 3 MW and duration of 0.5 ms is used for the initial plasma production in the NBI reactor from Phase I. If the non-inductive current ramp-up by the LHCD is realized in Phase III, the burn time is remarkably prolonged in the reactor with relatively medium elongation and medium triangularity plasma, and many technological advantages are expected (see Section 3.5)

The 500 keV/20 MW negative-ion-grounded NBI system has many functions such as current ramp-up, transformer recharge or quasi-steady state, steady and current profile control. These functions will be tested in Phase I and used to increase plasma performance. If non-inductive current ramp-up by the NBI is available, the required power for the LHCD in Phase III is reduced. If the current profile control by the NBI is effective, a high  $\beta$  plasma is expected. Steady state operation by the NBI offers database for the DEMO reactor.

The NAVIGATOR concept has been proposed in this report. The NAVIGATOR concept is composed of three major elements, that is, reliable operation scenarios, reliable maintainability and sufficient flexibility of the reactor. The negative-ion-grounded advanced tokamak reactor based on a 500 keV/20 MW neutral beam injection system satisfies the above three components and well supports the ideas of phased operation and phased construction of the FER.

	Years of operation											
	1 , 2		3 , 4		5 , 6 , 7 , 8 , 9 , 10							
	Phase I		Phase II		Phase III							(Phase IV)
	H/D		D/T		D/T							
	5000shots		1000 shots ~0.01MW·y/m <sup>2</sup>		800 sec x 12000 shots ~ 0.3 MW·y/ m <sup>2</sup>							
<ul style="list-style-type: none"><li>• Inductive ramp - up</li><li>Non inductive ramp-up (LHCD)</li><li>• Heating NBI</li><li>• Plasma initiation ECH</li><li>• Operation region (disruption free)</li><li>• Coupling LH ICRF (simple structure)</li><li>• Divertor C W (carbonization)</li><li>• Current profile control NBI</li></ul>											Steady state High $\beta$ High Q	
<ul style="list-style-type: none"><li>• Neutronics tests</li><li>• Tritium recovery tests Screening (short period) Irradiation effect on breed-er properties (long period)</li><li>• Blanket demonstration tests</li><li>• Material irradiation tests</li></ul>			[Port No.] #1,2,3,4									
			T/E -1									
					#1,2,3,4							
					T/E -2		# 4					
							T/E -2					
							# 1, 2, 3					
							T/M					
			# 5, 6									
			T/E - 3									

Number of test port : 6

Test element-1 : 2/port

Test module : 1/port

Test element-2 : 4/port

Test sector : TBD

Test element-3 : 4/port

Fig. 6.6.1 Phased operation and phased construction

## Acknowledgements

It is difficult to track down all the sources of the authors' ideas, but it would be inexcusable not to acknowledge the valuable discussions with persons described in the following. We are grateful for the helpful discussions we had with Dr. F. H. Coensgen of LLNL (at the 11th IAEA conference, Kyoto, 13th - 20th November 1986) concerning the mirror reactor, Prof. R. W. Conn of UCLA (at the 11th IAEA conference, Kyoto) concerning the plan on the FER, with Prof. B. Coppi of MIT (at the 11th IAEA conference, Kyoto) concerning the application of the negative ion injection system to the IGNITOR of the high field compact tokamak machine, with Dr. J. J. Foit of KfK (JAERI member, 1st June 1987 - 31st May 1988) concerning the alpha particle behavior in a self-ignited plasma, with Dr. R. J. Goldston of PPPL (JAERI member, 9th July 1987 - 3rd September 1987) concerning the effect of high energy beam pressure on the critical poloidal and toroidal beta values and of plasma rotation on plasma confinement and beam driven current efficiency, with Dr. B. G. Logan of LLNL (at the 11th IAEA conference, Kyoto) concerning the effect of the bootstrap current on the energy multiplication factor Q value in a steady state tokamak machine, with Dr. T. Ohkawa of GA Technologies Inc. (at the 11th IAEA conference, Kyoto) concerning the effect of the position of the X-point on the tokamak confinement, with Dr. F. Söldner of the Max-Planck-Institute für Plasma Physik, Garching (JAERI member, 1st August 1987 - 30th November 1987) and Dr. Y. Takase of MIT (JAERI member, 11th May 1987 - 31st October 1987) concerning the application of LHCD and LHH to the next generation tokamak machines and with Dr. H. Takahashi of PPPL (JAERI member, 6th September 1986 - 25th November 1986) concerning the magnetohydrodynamic (MHD) behavior of high beta plasma. The authors also wish to thank Drs. T. Ando and H. Takatsu for discussions on the flexibility of the reactor machine, Messrs. K. Anno, T. Arai, T. Shibata, T. Tokutake and Y. Matsuzaki concerning reactor maintainability, Drs. T. Imai, H. Kimura and T. Nagashima concerning the R&D of RF facilities, Drs. T. Matsuda, Y. Miura, H. Ogawa, S. Sengoku and T. Shoji on the H-mode plasma behavior in the JFT-2M tokamak machine, Drs. M. Maeno, T. Ogiwara, M. Saïdo and R. Yamada on the plasma-wall interaction

in the reactor, Dr. K. Nakamura concerning plasma controllability, Dr. S. Seki concerning the plan on JT-60 upgrade, Dr. J. Tateno concerning neutron and gamma irradiation effects on insulating materials for fusion, Drs. T. Takizuka, S. Tokuda, T. Tsunematu and T. Tuda on plasma physics, Drs. S. Shimamoto and H. Tsuji on the high field superconducting magnet, Drs. Y. Sawada of Toshiba Corporation, R. Saito of Mitsubishi Electric Corporation and Y. Itoh of Hitachi Ltd. concerning the FER design. Other members of the FER Design Team are also acknowledged. The authors wish to thank Dr. A. Kitsunozaki for his permission to use Fig. 7 in his paper {(Proc. 10th Int. Conf. London, 1984), Vol. 1, IAEA, Vienna (1985) 57} and Dr. S. Saito of Hitachi, Ltd. to use Fig. 1 in his paper {Nucl Fusion 25 (1985) 828}. We have obtained many ideas from books written by Prof. K. Miyamoto of the University of Tokyo (Plasma Physics for Nuclear Fusion, The MIT press, Cambridge, Massachusetts, and London, England, 1980) and by Prof. S. Takamura of Nagoya University (The Fundamentals of Plasma Heating, in Japanese, Nagoya University Press, Nagoya, Japan, 1986). The authors are indebted to Profs. Emeriti H. Itoh of Osaka University, H. Nishihara of Kyoto University and Prof. K. Uo of Kyoto University for many stimulating discussions on the fusion reactor concept, including the tokamak reactor and heliotron reactor. The authors gratefully acknowledge the discussion on feasible strategies with Drs. H. Maeda, H. Kishimoto, Y. Obata and Prof. Emeritus T. Sekiguchi of the University of Tokyo. One of the authors (S. Y.) is indebted to the late Dr. J. Uno (deceased, 18th June 1982) who led me to fusion research. The authors are grateful for the discussions we had with the late Drs. T. Itagaki (deceased, 6th August 1978), K. Takahashi (deceased, 26th August 1979) and K. Kumagai (deceased, 16th September 1980) concerning the future of fusion research. The authors wish to thank Mr. H. Kuroda of Hazamagumi Ltd. for providing us the concept on the reactor building, Mr. K. Koike, Miss A. Suzuki and Mrs. E. Yamamoto for providing informations of fusion research, Miss A. Koike for typing our paper and Mr. F. Umibe for his intensive and extensive effort in English proofreading. Thanks are also due to Mr. Y. Hirohara and Drs. T. Takeda, H. Shirakata, K. Inoue, S. Tamura, T. Iijima, M. Tanaka, M. Yoshikawa, K. Tomabechi, Y. Iso and S. Mori for support and encouragement.

## References

- [1] OKUMURA, Y., AKIBA, M., HORIIKE, H., ITOH, T., KAWAI, M. et al.: "Development of High-Performance Neutral-Beam Injection at JAERI", in Plasma Physics and Controlled Nuclear Fusion Research (Proc. 10th Int. Conf. London, 1984), Vol. 3, IAEA, Vienna (1985) 329.
- [2] JT-60 Team presented by M. Yoshikawa.: "Recent Experiments in JT-60", in Plasma Physics and Controlled Nuclear Fusion Research (Proc. 11th Int. Conf. Kyoto, 1986), IAEA, Vienna, IAEA-CN-47/A-I-1.
- [3] THE JET TEAM presented by REBUT, P.H., et al.: "JET Latest Results and Future Prospects", in Plasma Physics and Controlled Nuclear Fusion Research (Proc. 11th Int. Conf. Kyoto, 1986), IAEA, Vienna, IAEA-CN-47/A-I-2.
- [4] HAWRYLUK, R.J., ARUNASALAM, V., BELL, M.G., BITTER, M., BLANCHARD, W.R., et al.: "TFTR Plasma Regimes", *ibid.*, Paper IAEA-CN-47/A-I-3.
- [5] ANDERSON, O.A. and COOPER, W.S.: "Efficient, Radiation-Hardened, 400 and 800 keV Neutral Beam Injection Systems", Nucl. Tech./Fusion 4 (1983) 1418.
- [6] HORIIKE, H., OHARA, Y., OKUMURA, Y., SHIBATA, T. and TANAKA, S.: "Conceptual Design of Negative-Ion-Based 500 keV 20 MW Neutral Beam Injector", JAERI-M 86-064 (1986) (in Japanese).
- [7] TACHIKAWA, K., KOBAYASHI, T., IIDA, H., SAWADA, Y., ADACHI, J., et al.: "Maintenance of Torus Components for the Fusion Experimental Reactor (FER)", in Remote Systems and Robotics in Hostile Environments (Proc. Int. Topical Meeting, Pasco, 1987), ANS, (1987) 543.
- [8] YAMAMOTO, S., OKANO, K., NISHIO, S., SUGIHARA, M., SAITO, R., et al.: "Tokamak Reactor Operation Scenario Based on Plasma Heating and Current Drive by Negative-Ion-Based Neutral Beam Injector", in Plasma Physics and Controlled Nuclear Fusion Research (Proc. 11th Int. Conf. Kyoto, 1986), IAEA, Vienna, IAEA-CN-47/H-I-3.
- [9] OHKAWA, T.: "New Method of Driving Plasma Current in Fusion Devices", Nucl. Fusion 10 (1970) 185.
- [10] RIVIERE, A.C.: "Penetration of Fast Hydrogen Atoms into a Fusion Reactor Plasma", Nucl. Fusion 11 (1971) 363.
- [11] SWEETMAN, D.R.: "Ignition Condition in Tokamak Experiments and Role of Neutral Injection Heating", Nucl. Fusion 13 (1973) 157.

- [12] BRAGINSKII, S.I.: "Transport Process in a Plasma", Rev. of Plasma Physics Vol. 1, p205 (ed. by LEONTOVICH, M.A., Consultants Bureau, New York, 1966.).
- [13] START, D.F.H., CORDEY, J.G. and JONES, E.M.: "The Effect of Trapped Electrons on Beam Driven Currents in Toroidal Plasmas", Plasma Physics 22 (1980) 303..
- [14] START, D.F.H. and CORDEY, J.G.: "Beam-Induced Currents in Toroidal Plasmas of Arbitrary Aspect Ratio", Phys. of Fluids 23 (1980) 1477.
- [15] MIKKELSEN, D.R. and Singer, C.E.: "Optimization of Steady-State Beam-Driven Tokamak Reactors", Nucl. Technol./Fusion 4 (1983) 237.
- [16] GAFFEY, J.D. Jr.: "Energetic Ion Distribution Resulting from Neutral Beam Injection in Tokamaks", J. Plasma Phys. 16 (1976) 149.
- [17] CORDEY, J.G.: "Effects of Particle Trapping on the Slowing-Down of Fast Ions in a Toroidal Plasma", Nucl. Fusion 16 (1976) 499.
- [18] TANI, K., AZUMI, M., KISHIMOTO, H. and TAMURA, S.: "Effect of Toroidal Ripple on Fast Ion Behavior in a Tokamak", J. Phys. Soc. Japan 50 (1981) 1726.
- [19] TANI, K., TAKIZUKA, T., AZUMI, M. and KISHIMOTO, H.: "Ripple Loss of Suprathermal Alpha Particles During Slowing-Down in a Tokamak Reactor", Nucl. Fusion 23 (1983) 657.
- [20] TANI, K., SUZUKI, M., YAMAMOTO, S. and AZUMI, M.: "On the Analysis of Beam Driven Current in a Tokamak", to be published in JAERI-M.
- [21] See, e.g., the following papers: SEKI, S., TSUNEMATSU, T., AZUMI, M. and NEMOTO, T.: "Beta Enhancement of Tokamak Plasma with Nearly Circular Cross Section", Nucl. Fusion. 27 (1987) 330; YAMAZAKI, K., NAITOU, H., AMANO, T., TSUNEMATSU, T., TUDA, T., et al.: "Second Stability Access in Tokamak Plasmas", in Plasma Physics and Controlled Nuclear Fusion Research (Proc. 11th Int. Conf. Kyoto, 1986) IAEA, Vienna, IAEA-CN-47/E-I-2-1.
- [22] YAMAMOTO, S., AZUMI, M., TANAKA, Y. and TSUNEMATSU, T.: "Control of  $m=1$  Activity", Tokamak Concept Innovations, p 149-154, IAEA-TECDOC-373.
- [23] YAMAMOTO, S., MAENO, M., SUZUKI, N., AZUMI, M., TOKUDA, S., et al.: "Magnetohydrodynamic Activity in the JFT-2 Tokamak with High-Power Neutral-Beam-Injection Heating", Nucl. Fusion 21 (1981) 993.

- [24] OKANO, K., MASUZAWA, M., SAITO, R. and YAMAMOTO, S.: "Heating, Current-Drive and Plasma Control by Negative Ion Based Sub-MeV Beams"; Tokamak Concept Innovations, p 209-213, IAEA-TECDOC-373.
- [25] POST, D.E., JENSEN, R.V., TARTER, C.B., GRASBERGER, W. H and LOKKE, W.A.: "Steady-State Radiation Cooling Rates for Low-Density High-Temperature Plasmas", Atomic Data and Nuclear Data Tables, 20 (1977) 397.
- [26] TONE, T., FUJISAWA, N., SEKI, Y., IIDA, H., TACHIKAWA, K., et al.: "Conceptual Design of the Fusion Experimental Reactor (FER) Based on an Advanced Scenario of Plasma Operation and Control", in Plasma Physics and Controlled Nuclear Fusion Research (Proc. 10th Int. Conf. London, 1984), Vol. 3, IAEA, Vienna (1985) 287.
- [27] NISHIO, S. and SUGIHARA, M.: "Reduction of the Cyclic Stress Fatigue due to the Over-Turning Force on the Toroidal Field Coils by Quasi-Steady Operation in a Tokamak Fusion Reactor", Nucl. Eng. Design/Fusion 3 (1985) 59.
- [28] FUJISAWA, N. and FER PLASMA DESIGN TEAM, "Tokamak Start-Up", Physical Science, Vol. 26, Plenum Press, New York and London (1986).
- [29] NISHIO, S., SUGIHARA, M. and OKAZAKI, T.: "Enhancement of Engineering Advantages in Tokamak Reactor Operation Assisted by RF Waves", JAERI-M 85-141.
- [30] SAITO, S., KOBAYASHI, T., SUGIHARA, M., HIRAYAMA, T. and FUJISAWA, N.: "Bifurcated Confinement Solutions for Diverted Tokamak", Nucl. Fusion 25 (1985) 828.
- [31] JT-60 Team presented by M. Nagami.: "Energy and Particle Confinement of JT-60 Plasmas with High Power Heating", in Plasma Physics and Controlled Nuclear Fusion Research (Proc. 11th Int. Conf. Kyoto, 1986) Vol.1, IAEA, Vienna (1987) 89.
- [32] TONE, T., et al.: in Fusion Technology (Proc. 6th Topical Meeting on the Technology of Fusion Energy, San Francisco, 1985), Vol.8, No.1, Part 2(A) (1985) 731.
- [33] See, e.g., the following paper: SHIMAMOTO, S., HENNING, C., KOMAREC, P. and KOSTENKO, A.I.: "Advanced Magnetics", Tokamak Concept Innovations, p 243-284, IAEA-TECDOC-373.
- [34] TSANG, K.T. and SIGMAR, D.J.: "Stabilization of Ballooning Modes by Energetic Particles in Tokamaks", Nucl. Fusion 21 (1981) 1227.

- [35] BICKERTON, R.J., CONNOR, J.W. and TAYLOR, J.B.: "Diffusion Driven Plasma Current and Bootstrap Tokamak, Nature Physical Science 229 (1971) 110.
- [36] GALEEV, A.A. and SAGDEEV, R.Z.: "The Theory of Plasma Confinement in a Tokamak at High Temperatures", in Plasma Physics and Controlled Nuclear Fusion Research (Proc. 4th Int. Conf. Madison, 1971) Vol.1, IAEA, Vienna (1971) 481. [Nucl. Fusion Suppl. p45 (1972)].
- [37] KADOMTSEV, B.B. and SHAFRANOV, V.D.: "A Stationary Tokamak", in Plasma Physics and Controlled Nuclear Fusion Research (Proc. 4th Int. Conf. Madison, 1971) Vol.2, IAEA, Vienna (1971) 479. [Nucl. Fusion Suppl. p209 (1972)].
- [38] HINTON, F.L. and HAZELTINE, R.D.: "Theory of Plasma Transport in Toroidal Confinement System", Rev. of Modern Physics 48 (1976) 239.
- [39] YAMAMOTO, S., MAENO, M., SENGOKU, S., SUZUKI, N., KASAI, S., et al.: "Transport Studies in the JFT-2 Tokamak", in Plasma Physics and Controlled Nuclear Fusion Research (Proc. 9th Int. Conf. Baltimore, 1982), Vol. 1, IAEA, Vienna (1983) 73.
- [40] KITSUNEZAKI, A., ABE, M., HIRAYAMA, T., HOSHINO, K., KAMEARI, A. et al.: "High-Pressure Plasma with High-Power NBI Heating in Doublet III", in Plasma Physics and Controlled Nuclear Fusion Research (Proc. 10th Int. Conf. London, 1984), Vol. 1, IAEA, Vienna (1985) 57.
- [41] GOLDSTON, R.J., ARUNASALAM, V., BELL, M.G., BITTER, M., COHEN, S.A., et al.: "Energy Confinement and Profile Consistency in TFTR", in Plasma Physics and Controlled Nuclear Fusion Research (Proc. 11th Int. Conf. Kyoto, 1986), IAEA, Vienna, IAEA-CN-47/A-II-1.
- [42] GOLDSTON, R.J.: "Topics in Confinement Analysis of Tokamaks with Auxiliary Heating", Proc. Course and Workshop on Basic Physical Processes of Toroidal Fusion Plasmas, Vol. 1, Varenna (1985) 165.
- [43] OHARA, Y., AKIBA, M., ARAKI, M., HORIIKE, H., INOUE, T., et al.: "Design of a 500 keV, 20 MW Negative-Ion-Based Neutral Beam Injection System for Fusion Experimental Reactor", IAEA Technical Committee Meeting on Negative Ion Beam Heating, Culham Lab., July (1987).
- [44] NAKAI, Y, et al., Data on Collisions of Hydrogen Atoms and Ions with Atoms and Molecules (1), JAERI-M 83-013.

- [45] FUJISAWA, N., SUGIHARA, M., YAMAMOTO, S., MIZOGUCHI, T., HITOKI, S., et al.: "Main Physics Features Driving Design Concept and Physics Design Constraints -Conceptual Design Study of FY86 FER-", JAERI-M 87-093 (1987).
- [46] SAITO, R., KASHIHARA S., ITOH, S., NAKAYAMA, T., ADACHI, J., et al.: "Conceptual Design Study of Fusion Experimental Reactor (FY86 FER) -Plant System Design-", JAERI-M 87-091.
- [47] ITO, T., HORIIKE, H., MATSUOKA, M., MATSUDA, S., OHARA, Y., et al.: "Development of Helium Beam Injection for JT-60 Active Beam Diagnostic System", JAERI-M 86-114 (1986) (in Japanese)
- [48] CARSLow, H.S. and JAEGER, J.C.: "Conduction of Heat in Solids", p. 75-77, Clarendon Press, Oxford.
- [49] SMITH, D.L., BROOKS, J.N., POST, D.E. and HEIFETZ.: "A Physical Sputtering Code for Fusion Applications", Proc. 9th Symp. on Engrg. Problems of Fusion Research, IEEE, Pub. No. 81CH1715-2, p179, 1981.
- [52] RHOADES, W.A. and MYNATT, F.R.: "The DOT-III Two Dimensional Discrete Ordinates Transport Code", ORNL/TM-4280 (1973); Comments on the DOT 3.5 Version of DOT III by W. A. Rhoades (Nov. 1975) ORNL CCC-276.
- [53] See, e.g., the following paper: "Insulations for Fusion Applications", IAEA-TECDOC-417, 1987.

## Appendices

### A. 1 Confinement Scaling Law and H-Mode Phenomenon

#### 1) Energy flow pattern of tokamak discharge

The energy flow pattern of tokamak discharges is illustrated in Fig. A1.1. It is convenient from the energy flow point of view, to regard the plasma as consisting of the bulk plasma and the boundary plasma. The plasma is heated by ohmic heating, neutral beam injection (NBI) heating and/or radio frequency (RF) wave heating. The ohmic heating power mainly goes into the central bulk plasma electrons, and is transmitted to the ions via Coulomb collisions. The energy flow may be quite different when additional heating is applied. In both NBI and RF heating, the central bulk plasma can be heated under some appropriate condition. The electron energy is transported from the bulk region of the plasma to the boundary region principally by heat conduction and by the energy that accompanies mass transport, that is, convection. The ion energy loss from the bulk plasma is, in general, dominated by heat conduction and mass flow to the plasma boundary, but charge exchange is of comparable magnitude at low density as an energy loss mechanism. In the case of NBI heating with relatively low injection energy ( $< 40 - 50$  keV), the birth of fast ions is due to charge exchange between injected fast neutrals and bulk ions, as shown in Fig. 3.1.1. Thus, neutrals coming from bulk ions (so called Halo neutrals) are made in the central plasma region, and affect the energy loss from the bulk region. Electron and ion energy can go from the plasma boundary to the limiter or divertor plate by mass flow. Electron energy can flow to the limiter or divertor by heat conduction. Other important mechanisms to remove the energy of the boundary plasma are radiation and charge-exchange directly to the wall. When the dominant impurities are low Z (typically oxygen, carbon, and nitrogen), the bulk of the emitted radiation originates from the plasma boundary. However, in some discharges containing heavy metal impurities (such as tungsten or molybdenum from the first walls), the energy lost by radiation from the bulk plasma may be a significant fraction of the input power.

When there are large scale MHD modes, for example, sawtooth oscillation or  $m/n = 2/1$  tearing mode, it is impossible to define the

transport coefficients for electron and ion thermal diffusivities  $\chi_e$ ,  $\chi_i$  and the electron and ion particle diffusion coefficients  $D_e$ ,  $D_i$  around the region with large scale MHD instabilities. In addition, a discussion on transport in a region with large amount of radiation loss is meaningless. Generally, three confinement zones in a tokamak plasma can be distinguished in the radial direction, i.e., the central region (within the  $q = 1$  surface), the core region ( $r(q = 1) \leq r \leq r(q = 2)$ ) and the outer region. Sawtooth oscillation dominates the transport in the central region. When we solve the transport equation under the given  $\chi_e$ ,  $\chi_i$ ,  $D_e$  and  $D_i$ , we should take account of the MHD effect. (For example,  $\chi_e \rightarrow \infty$  or  $\partial T_e / \partial r = 0$  in the region of  $0 \leq r < r_1$ ,  $q(r_1) = 1$  and  $r_2 \leq r < a$ ,  $q(r_2) = 2$ .) Large scale MHD instabilities restrict the plasma profile. Thus, sometimes, nearly the same scaling law is derived for each electron thermal diffusivity  $\chi_e$ , which is different from each other in physical properties. The energy transport in a tokamak plasma is dominated by electron thermal diffusivity  $\chi_e$ . The ion transport is dominated by ion thermal diffusivity  $\chi_i$ , which is close to its neoclassical value or within several times of the value given by Chang and Hinton [1]. The experimental result does not necessarily imply that ions follows the neoclassical theory. It seems that anomaly in the ion transport does not affect, because the neoclassical value of  $\chi_i$  is intrinsically very large compared with the neoclassical value of  $\chi_e$ .

## 2) Confinement scaling law

The energy confinement time is of practical importance in tokamak performance, and the possibility that it might scale with other experimental quantities in a predictable manner is of considerable interest both for interpreting the results of existing experiments and for the design of future devices. Various empirical scaling laws for the energy confinement time, reflecting primarily anomalous electron transport, have been proposed. The most commonly adopted scalings are listed in Table A1.1. The energy confinement time is defined by  $\tau_E = W/P_{\text{loss}}$ , where  $W$  is the sum of the electron ( $W_e$ ) and ion ( $W_i$ ) energy, and  $P_{\text{loss}}$  is the total power lost from the plasma. Since, in steady state,  $P_{\text{loss}}$  is equal to the total power input ( $P_{\text{in}}$ ),  $\tau_E$  is equal to  $\tau_E = W/P_{\text{in}}$ . The latter quantity is often called the gross energy confinement time (or the energy replacement time), and commonly used as

a measure for tokamak performance. In order to separate the electron and ion energy balance, the electron and ion energy replacement times are defined by  $\tau_{Ee} = W_e / (P_{OH} + P_e - P_{ei})$  and  $\tau_{Ei} = W_i / (P_i + P_{ei})$ , where  $P_{OH}$  is the ohmic heating power,  $P_{ei}$  the heat transfer from electrons and ions, and  $P_e(P_i)$  the power input to electrons (ions) directly from additional heating. In the ohmic heating case,  $\tau_{Ee}$  follows neo-Alcator scaling in plasma density below some critical value of  $n_{cr}$ . However, a clear saturation of the confinement time with density is observed above the critical density. This saturation is considered to arise from the enhancement of ion thermal diffusivity  $\chi_i$  due to the  $\eta_i$ -mode, resulting in the dominant loss channel in plasma transport. The effect based on neoclassical theory is not necessarily excluded. The observation of a neoclassical bootstrap current is reported by the TFTR group [2]. If there exists neoclassical bootstrap current, the Ware pinch should exist, because of the Onsager symmetry relation. However, there is no experimental evidence on the Ware pinch.

In the additional heating case, two different types of discharges can develop. In one case, the reduction in confinement lasts through the NBI or RF heating. Because of the low values of  $\beta_p$  achieved during these discharges, they are called L-type discharges. In the other case, the particle and energy confinements suddenly improve during the NBI or RF pulse. As a higher value of  $\beta_p$  is obtained, this discharge type is called H type [6]. Both the confinement properties at values of beta much smaller than the beta limit and when the beta limit is approached should be analyzed. No precise scaling is available yet. The global energy confinement time in an H-mode discharge seems to follow the Kaye-Goldston scaling, as long as the plasma beta does not approach the beta limit and the value is twice or three times larger than that of the L-mode discharge. Recently, an optimized confinement time was proposed at JAERI [3]. The parametric dependence of the H-mode confinement is different from that of ohmic plasma, but the energy confinement time of an optimized H-mode  $\tau_E^H$  is equal to the optimized ohmic confinement time  $\tau_E^{OP}$ , as shown in ASDEX, D-III(JAERI), JFT-2M and D-III-D with  $q_{cy} \leq 2.2$ . The optimized ohmic confinement time is the saturated value of  $\tau_E^{OH}$  given by the neo-Alcator scaling, i.e.  $\tau_E^{OH} \propto n_e R^2 a_p q_{cy}^{-1} \kappa^{0.5} \tau_E^{OH}$ .  $\tau_E^{OH}$  saturates at  $n_e \approx 6.7 \times 10^{19} q_{cy}^{-1} B_T^{-1} A^{0.5}$  and  $\tau_E^{OP} = 0.045 R a_p B_T \kappa^{0.5} A^{0.5}$ . Therefore, the optimized H-mode plasma with  $q_{cy} \leq 2.2$  has the following confinement time,

$$\tau_E = 0.045 R a_p B_T \kappa^{0.5} A^{0.5}.$$

An excellent review of anomalous transports in tokamak plasmas can be found in Ref.[4].

### 3) Improved confinement

It was a great relief when in the ASDEX divertor experiments a new type of beam-heated discharges with confinement times comparable with those in ohmic discharges was found [6-16]. High confinement discharges have also been obtained in JFT-2M [17-22], PDX/PBX [23-27], D-III/D-III-D [28-37], JET [38, 39], TFTR [40] and JT-60 [41-43]. In the following, the experimental conditions and the range of plasma parameters which allow the development of the H regime are described [5].

- i) There is a threshold power for transition into the H-mode.
- ii) Even under the condition of the power being below the threshold, H-transition is often triggered by an internal sawtooth that transports energy into the boundary plasma zone.
- iii) The discharge begins as an L-type. Transition into the H mode occurs suddenly after a short L-phase.
- iv) The transition from the L-mode to the H-mode is also found in both hydrogen and deuterium plasma, although the power threshold is higher in hydrogen plasma. In addition, there is a dependence of the power threshold on the safety factor, plasma density and so on. However, the H-mode also has been obtained over a wide range of plasma parameters, and there seems to be no serious restriction in the parameter space typical for tokamak operation. In particular, there is no obvious restriction on low  $q$  ( $q_s \geq 2.0$ ) or high currents. The observed lower density limit has no practical consequences, whereas the upper density limit seems to be a power limit and can be improved by pellet fueling.
- v) There is a dependence of the power threshold for the H-mode on the number and location of the x-points on the separatrix.
- vi) An H-mode plasma is characterized by a large temperature gradient at the plasma edge, and a high temperature only a few centimeters inside the separatrix.
- vii) For the H-mode, a reduction in particle recycling around the plasma boundary is necessary. In the divertor configuration, this condition is easily satisfied.

- viii) In addition to a minimum heating power, the separation of the separatrix from the limiters or the wall,  $\Delta L$ , and of the x-point from the target plates,  $\Delta X$ , respectively, are required for the H-mode.
- ix) The H-mode is usually accompanied by strong fluctuations at the plasma edge (edge localized modes, "ELM", or edge relaxation phenomena, "ERP").
- x) Numerical simulation of the broad  $n_e$  and  $T_e$  profiles, typical for the H-mode plasma, indicate a reduction in electron thermal diffusivity by a factor of typically 2 in the plasma center and by a factor of over 5 at the plasma boundary. The H-mode energy confinement time are found to scale linearly with the plasma current. The parameter dependence of the H-mode scaling law is nearly the same as the Kaye-Goldston law.
- xi) It is interesting that H-mode discharge can be obtained with limiters. For limiters at the outside of the torus the minimum clearance,  $\Delta L$ , ranges from 2 to 5 cm in different experiments, roughly equivalent to twice the e-folding length of the power flow in the scrape-off layer. The required separation is smaller for limiters at the top or bottom of the machine and can even become zero for limiters on the inner side of the torus as demonstrated by the recent JFT-2M limiter H-mode results. A tentative explanation for this strong poloidal variation of the required clearance would be the following: particle and energy transport are maximum in the plasma at the outer side, giving maximum thermal insulation from the contact point for limiters on the inner side. The elongation of the plasma cross-section increases the connection length and therefore improves the thermal insulation.

Many theoretical works have been done to interpret the H-mode [44-61]. Review of theories on the H-mode is given in Ref.[5]. Attention is paid to the following experimental results.

- i) The high edge temperature and density with a steep radial gradient a few centimeters inside the separatrix, i.e., the high pressure with a steep pressure gradient.
- ii) The finite edge current density due to the above results described in i).
- iii) The effect of the separatrix

- iv) Control of the boundary plasma (recycling, divertor functions, etc)
- v) Why the global energy confinement becomes strongly dependent on the boundary energy transport ?

An outstanding feature of the H-mode is the occurrence just inside the separatrix of very steep density and temperature gradients, and therefore the pressure gradients. Since pressure gradients can be limited by the onset of the ballooning and interchange modes, it is of interest to examine how the stability properties of such modes are modified by the presence of the separatrix. Bishop examined the stability of a model tokamak equilibrium for the MHD ballooning and interchange modes [47, 55]. He showed that the combined effects of the magnetic separatrix and a finite edge current density can result in coalescence of the first and second stable regions, and this leads to a picture of the H-mode in which the observed steep edge pressure gradients result from the modified ballooning stability properties. Harm and Diamond showed that the principal effect of separatrix geometry on resistive fluid turbulence is a decrease in the characteristic radial scale length (step size) caused by increased global shear [59]. However, it is very difficult to determine whether the stabilizing effect of the separatrix is important for H-transition or not, because the limiter H-mode is obtained in JFT-2M [21]. Hinton suggests that the transition into the H-mode might be triggered by the neoclassical transport properties of the ions [44, 46, 51]. A study of the plasma conditions during the preceding L-phase just before the H-transition indicates that the electron temperature at the plasma edge plays a crucial role. In order for the electron temperature to rise above the critical threshold, Hinton conjectured that the ion temperature at the plasma edge has to rise, which should be possible in the low-recycling conditions of the divertor configuration. When charge-exchange and convective losses at the edge are negligible, the edge ion temperature is governed by neoclassical transport across the separatrix, and bifurcation in the time evolution of the ion temperature, and subsequently in the confinement properties, is possible. The most important aspect of Hinton's theory with respect to the H-mode bifurcation, which could be tested experimentally, is the deteriorating effects of enhanced recycling, the role of the collisionality conditions at the plasma edge, the advantage of the asymmetric topology of the

single-null (SN) over the double-null (DN) configuration, and the role of the ion grad B-drift direction. The increased H-mode accessibility of the single-null configuration requires the ion grad B-drift direction to be towards the stagnation point. The experimental observations in ASDEX [14] are in agreement with the theory of the H-transition by Hinton.

One of the puzzling observations in the H-mode discharges is that the core energy confinement also improves, even though the H-mode is associated with changing plasma boundary conditions. Ohya, et al., explained this puzzle in that a higher edge temperature due to lower thermal conductivity ( $\kappa_{out}$ ) makes possible broader tearing mode stable profiles, leading to a higher core temperature and hence a higher  $\tau_E$  [33].

The need for a divertor in obtaining the H-mode suggests that the following conditions are necessary: (1) charge-exchange energy loss is practically absent, (due to the divertor refueling process, in which almost all of the recycling may be assumed to be confined inside the divertor chamber), and (2) the impurity concentration is low (for possibly the same reason). Then, the electron and ion temperatures are allowed to be higher near the edge. The fact that the H-mode can be prevented by too large an impurity concentration supports the consideration that a high electron temperature at the edge is necessary for the H-mode. Similarly, the fact that the H-mode confinement is degraded by excess gas puffing supports the hypothesis that a high ion temperature is also necessary. In Ref.[49], it is shown that a hysteresis relation between the particle flux into the divertor and the temperature and density of the divertor plasma exists.

To fully utilize the superior confinement properties of the H-mode, there are a number of problems that have to be solved. A better understanding, and possibly an optimization of energy confinement in large tokamaks, is essential for enhancing tokamak performance and to lay the grounds for extrapolation to a reactor-grade tokamak of the next generation machine.

In conclusion, a summary of the experiments on improved plasma confinements is presented in Table A1.2. Double solid circles denote good H-mode confinement times, which are twice or more larger than those of the L-mode. Solid circles imply that the confinement times are no better than the L-mode values, although there is still a clear signal of

an H-transition. Double dotted circles indicate that the confinement time is significantly improved, but the improvement is different from H-transition. Single dotted circles correspond to the case with slightly improved confinement, independent from the H-mode phenomenon. There seems to be no severe constraints on the heating method for getting into the H-regime. In fact, H-mode discharges have been obtained by various heating methods (NBI, ICRF, ECRF, NBI+ICRF and NBI+ECRF) and heating scenarios (co- and counter-injection; low- and high-field-side antennae, minority heating, mode conversion; with current-drive being dominant). The observed differences and difficulties seem to be only secondary effects related to differences, for example, in power deposition (primary to electron/ion, profiles) or impurity production associated with a particular heating method. The same is true for differences in wall conditions (eg. with or without carbonization) and fueling/pumping techniques (gas puffing, beam or pellet fueling, with or without gettering). The requirements for a transition to the H-mode are not changed fundamentally, but the power threshold, for example, might be affected.

## References

- [1] CHANG, C.S. and HINTON, F.L.: "Effect of Finite Aspect Ratio on the Neoclassical Ion Thermal Conductivity in the Banana Regime", Phys. of Fluids 25 (1982) 1493.
- [2] HAWRYLUK, R. J., ARUNASALAM, V., BELL, M.G., BITTER, M., BLANCHARD, W.R., et al.: "TFTR Plasma Regimes", in Plasma Physics and Controlled Nuclear Fusion Research (Proc. 11 th Int. Conf. Kyoto, 1986), Vol. 1, IAEA, Vienna (1987) 51, IAEA-CN-47/A-I-2.
- [3] SHIMOMURA, Y., SUZUKI, N., SUGIHARA, M., TSUDA, T., ODAJIMA, K. and TSUNEMATSU, T.: "Empirical Scaling of Energy Confinement Time of L-Mode and Optimized Mode and Some Consideration of Reactor Core Plasma in Tokamak", JAERI-M 87-080.
- [4] ITOH, K. and ITOH, S-I.: "Present Status of the Theory on Anomalous Transport Phenomena in Tokamak", KAKUYOGO KENKYU 57 (1987) 280 and 379.
- [5] OKAMOTO, M., AZUNI, M., NAGAMI, M., SUZUKI, N., MATSUMOTO, H.: "On the H-Mode in Tokamaks", KAKUYUGO KENKYU 58 (1987) 105.

## Related Experiments on Improved Confinements

## The ASDEX Experiments

- [6] WAGNER, F., BECKER, G., BEHRINGER, K., CAMPBELL, D., EBERHAGEN, A., et al.: "Regime of Improved Confinement and High Beta in Neutral-Beam-Heated Divertor Discharges of the ASDEX Tokamak", Phys. Rev. Letters 49 (1982) 1408.
- [7] WAGNER, F., BECKER, G., BEHRINGER, K., CAMPBELL, D., EBERHAGEN, A., et al.: "Confinement and  $\beta_p$ -Studies in Neutral-Beam-Heated ASDEX Plasmas", in Plasma Physics and Controlled Nuclear Fusion Research (Proc. 9th Int. Conf. Baltimore, 1982), Vol. 1, IAEA, Vienna (1983) 43.
- [8] KEILHACKER, M., BECKER, G., BERNHARDI, K., EBERHAGEN, A., EISHAER, M., et al.: "Confinement Studies in L and H-Type ASDEX Discharges", Plasma Physics and Controlled Fusion 26 (1984) 49.

- [9] WAGNER, F., KEILHACKER, M. and the ASDEX and NI Teams.:  
"Importance of the Divertor Configuration for Attaining the H-Regime in ASDEX", J. Nucl. Mater. 121 (1984) 103.
- [10] KEILHACKER, M., FUSSMANN, G., v. GIERKE, G., JANESCHITS, G., KORNHERR, M., et al.: "Confinement and  $\beta$ -Limit Studies in ASDEX H-Mode Discharges", in Plasma Physics and Controlled Nuclear Fusion Research (Proc. 10th Int. Conf. London, 1984), Vol. 1, IAEA, Vienna (1985) 71.
- [11] LACKNER, K., DITTE, U., FUSSMANN, G., GRAVE, T., JANESCHITZ, G., et al.: "Experimental and Theoretical Investigation of the ASDEX Divertor Scrape-Off Layer", in Plasma Physics and Controlled Nuclear Fusion Research (Proc. 10th Int. Conf. London, 1984) Vol. 1, IAEA, Vienna (1985) 319.
- [12] WAGNER, F., FUSSMANN, G., GRAVE, T., KEILHACKER, M., KORNHERR, M., et al.: "Development of an Edge Transport Barrier at the H-Mode Transition of ASDEX", Phys. Rev. Letters 53 (1984) 1453.
- [13] GRUBER, O., JILGE, W., BERNHARDI, K., EBERHAGEN, A., FUSSMANN, G., et al.: "Radial Energy Balance Analysis of ASDEX H-Mode Discharges", in Proc. 12th European Conference on Controlled Fusion and Physics, Budapest, Sept. 2-6, 1985. (Pergamon, New York, 1985) Part I, p.18.
- [14] WAGNER, F., BARTIROMO, R., BECKER, G., BOSCH, H.S., EBERHAGEN, A., et al.: "Experimental Evidence for Neoclassical ion Transport Effects in the H-Transition of ASDEX", Nucl Fusion 25 (1985) 1490.
- [15] NIEDERMEYER, H., WAGNER, F., BECKER, G., BUCHL, K., EBERHAGEN, A., et al.: "The Achievement of Regimes with High Density, Low  $q_a$  and Good Confinement on ASDEX", in Plasma Physics and Controlled Nuclear Fusion Research (Proc. 11th Int. Conf. Kyoto, 1986), IAEA, Vienna, IAEA-CN-47/A-II-5.
- [16] STEINMETZ, K., NOTERDAEME, J.-M., WAGNER, F., WESNER, F., BAUMLER, J., et al.: "Obsevation of a High-Confinement Regime in a Tokamak Plasma with Ion Cyclorton-Resonance Heating", Phys. Rev. Letters 58 (1987) 124.

## The JFT-2M Experiments

- [17] MATSUMOTO, H., OGAWA, T., TAMAI, H., ODAJIMA, K., HASEGAWA, M., et al.: "Improved Confinement during ICRF Heating on JFT-2M", JAERI-M 86-147, 1986.
- [18] MIURA, Y., KASAI, S., SENGOKU, S., HASEGAWA, K., SUZUKI, N., et al.: "Characteristics of Pellet and Neutral-Beam Injected Single Null Divertor Discharges of the JFT-2M Tokamak", JAERI-M 86-148, 1986.
- [19] ODAJIMA, K., FUNAHASHI, A., HOSHINO, K., KASAI, S., KAWAKAMI, T., et al.: "Confinement Studies of Additionally Heated Plasma in JFT-2M Tokamak", in Plasma Physics and Controlled Nuclear Fusion Research (Proc. 11th Int. Conf. Kyoto, 1986), IAEA, Vienna, IAEA-CN-47/A-III-2.
- [20] SENGOKU, S. and the JFT-2M Team.: "Confinement and Fueling Studies during Additional Heating Phase in the JFT-2M Tokamak", J. Nucl. Mater. 145-147 (1987) 556.
- [21] SENGOKU, S., FUNAHASHI, A., HASEGAWA, M., HOSHINO, K., KASAI, S., et al.: "Regime of Improved Confinement in Neutral-Beam-Heated Limiter Discharges of a Tokamak", Phys. Rev. Letters 59 (1987) 450.
- [22] HOSHINO, K., et al.: private communication.

## The PDX/PBX Experiments

- [23] KAYE, S.M., BELL, M., BOL, K., BOYD, D., BRAU, K., et al.: "High Confinement Discharges in PDX with Neutral Beam Injection", in Proc. 11th European Conference on Controlled Fusion and Plasma Physics, Aachen, Germany, Sept. 5-9, 1983 (Pergamon, New York, 1983) Part I, p.19.
- [24] FONCK, R.J., BEIRSDORFER, P., BELL, M., BOL, K., BOYD, D., et al.: "H-Mode Studies in PDX", in Proc. 4th Int. Symposium on Heating in Toroidal Plasmas, Rome, March 21-28, 1984, Vol.1, p.37.
- [25] KAYE, S.M., BELL, M.G., BOL, K., BOYD, D., BRAU, K., et al.: "Attainment of High Confinement in Neutral Beam Heated Divertor Discharges in the PDX Tokamak", J. Nucl. Mater. 121 (1984) 115.

- [26] BUDNY, R., BELL, M.G., BOL, K., BOYD, D., BUCHENAUER, D., et al.: "Initial Results from the Scoop Limiter experiment in PDX", J. Nucl. Mater. 121 (1984) 294.
- [27] McGUIRE, K., BEIRSDORFER, P., BELL, M., BOL, K., BOYD, D., et al.: "Divertor and Scoop Limiter Experiments on PDX", in Plasma Physics and Controlled Nuclear Fusion Research (Proc. 10th Int. Conf. London, 1984), Vol. 1, IAEA, Vienna (1985) 117.

#### The D III/D III-D Experiments

- [28] DOUBLET III PHYSICS, OPERATIONS and NEUTRAL BEAM GROUPS (Presented by K. H. BURRELL): "A Regime of Improved Energy and Particle Confinement in Neutral Beam Heated Divertor Discharges in DOUBLET III", in Proc. 11th European Conference on Controlled Fusion and Plasma Physics, Aachen, Germany, Sept. 5-9, 1983 (Pergamon, New York, 1983) Part I, p.11.
- [29] NAGAMI, M., KASAI, M., KITSUNEZAKI, A., KOBAYASHI, T., KONOSHIMA, S., et al.: "Energy Confinement of Beam-Heated Divertor and Limiter Discharges in DOUBLET III", Nucl Fusion 24 (1984) 183.
- [30] KITSUNEZAKI, A., ABE, M., HIRAYAMA, T., HOSHINO, K., KAMEARI, A., et al.: "High-Pressure Plasma with High-Power NBI Heating in DOUBLET III", in Plasma Physics and Controlled Nuclear Fusion Research (Proc. 10th Int. Conf. London, 1984) Vol. 1, IAEA, Vienna (1985) 57.
- [31] SHIMADA, M., WASHIZU, M., KAMEARI, A., SENGOKU, S., ITOH, K., et al.: "Divertor and Edge Plasma Characteristics of Beam-Heated D-III Discharges", in Plasma Physics and Controlled Nuclear Fusion Research (Proc. 10th Int. Conf. London, 1984) Vol. 1, IAEA, Vienna (1985) 281.
- [32] SENGOKU, S., ABE, M., HOSHINO, K., ITOH, K., KAMEARI, A., et al.: "Improvement of Beam-Heated Limiter Discharges by Continuous Pellet Fueling in DOUBLET III", in Plasma Physics and Controlled Nuclear Fusion Research (Proc. 10th Int. Conf. London, 1984) Vol.1IAEA, Vienna (1985) 405.
- [33] OHYABU, N., BURRELL, K.H., DeBOO, J., EJIMA, S., GROEBNER, R., et al.: "A Regime of Improved Energy Confinement in Beam-Heated Expanded-Boundary Discharges in DOUBLET III", Nucl. Fusion 25 (1985) 49.

- [34] SENGOKU, S., NAGAMI, M., ABE, M., HOSHINO, K., KAMEARI, A., et al.: "Improvement of Energy Confinement Time by Continuous Pellet Fueling in Beam-Heated DOUBLET III Limiter Discharges", Nucl. Fusion 25 (1985) 1475.
- [35] DeBOO, J.C., BURRELL, K.H., EJIMA, S., KELLMAN, A.G., OHYABU, N. et al.: "DOUBLET III Operating Regimes with Improved Energy Confinement", Nucl. Fusion 26 (1986) 211.
- [36] LUXON, J., ANDERSON, P., BAITY, F., BAXI, C., BRAMSON, G., et al.: "Initial Results from the DIII-D Tokamak", in Plasma Physics and Controlled Nuclear Fusion Research (Proc. 11th Int. Conf. Kyoto, 1986), IAEA, Vienna, IAEA-CN-47/A-III-3.
- [37] LOHR, J.M., PRATER, R., SNIDER, R., STALLARD, B.W., BURRELL, K.H., et al.: "Observation of H-mode Confinement in the DIII-D Tokamak with Electron Cyclotron Heating", to be published in Phys. Rev. Letters.

#### The JET Experiments

- [38] TANGA, A., KEILHACKER, M., BARTLETT, D., BEHRINGER, K., BICKERTON, R.J., et al.: "Experimental Studies in JET with Magnetic Separatrix Configuration", in Plasma Physics and Controlled Nuclear Fusion Research (Proc. 11th Int. Conf. Kyoto, 1986), IAEA, Vienna, IAEA-CN-47/K-I-1.
- [39] JACQUINOT, J.: private communication.

#### The TFTR Experiments

- [40] GOLDSTON, R.J., ARUNASALAM, V., BELL, M.G., BITTER, M., BLANCHARD, W.R., et al.: "Energy Confinement and Profile Consistency in TFTR", in Plasma Physics and Controlled Nuclear Fusion Research (Proc. 11th Int. Conf., Kyoto, 1986) Vol. 1, IAEA, Vienna (1987) 75, IAEA-CN-47/A-II-1.

## The JT-60 Experiments

- [41] TSUJI, S., SHIMIZU, K. and JT-60 Team.: "Relation between Particle Confinement Time and Energy Confinement Time in JT-60", Bull. Phys. Soc. Jpn. 4 (1987) 143.
- [42] KIMURA, H. and JT-60 Team.: "Heating and Beam Acceleration during Second Harmonic ICRF Experiment in JT-60", 14th Europ. Conf. on Controlled Fusion and Plasma Physics,
- [43] JT-60 Team presented by T. Imai.: "Improvement of Current Drive and Confinement by Combination of LHCD and NBI Heating in JT-60", *ibid.*, Vol. 1, IAEA, Vienna (1987) 563, IAEA-CN-47/F-II-7.

## Related theory of H-Mode

- [44] OHKAWA, T., CHU, M.S., HINTON, F.L., LIU, C.S. and LEE, Y.C.: "Thermal and Electrical Properties of the Divertor Channel of Tokamak Plasmas", Phys. Rev. Letters 51 (1983) 2101.
- [45] BECKER, G., CAMPBELL, D., EBERHAGEN, A., GEHRE, O., GERNHARDT, J., et al.: "Transport Simulation of Neutral-Beam-Heated ASDEX Plasma in the L and H Regimes", Nucl. Fusion 23 (1983) 1293.
- [46] HINTON, F.L., CHU, M.S., DOMINGUEZ, R.R., HARVEY, R.W., et al.: "Physics of the H-Mode", in Plasma Physics and Controlled Nuclear Fusion Research (Proc. 10th Int. Conf., London, 1984) Vol. 2, IAEA, Vienna (1985) 3.
- [47] BISHOP, C.M., KIRBY, P., CONNOR, J.W., HASTIE, R.J., TAYLOR, J.B.: "Ideal MHD Ballooning Stability in the Vicinity of a Separatrix", Nucl. Fusion 24 (1984) 1579.
- [48] QU, W.X. and CALLEN, J.D.: "Two-Dimensional Ballooning Mode Equation and its Solution Near an X-Point", Univ. Wisconsin Plasma Rep. UWPR 85-1, 1985.
- [49] SAITO, S., KOBAYASHI, T., SUGIHARA, M., HIRAYAMA, T. and FUJISAWA, N.: "Bifurcated Confinement Solutions for Diverted Tokamaks", Nucl. Fusion 25 (1985) 828.
- [50] OHYABU, N.: "A Phenomenological Model for H-Mode", Research Report of Plasma Phys. Lab., Princeton Univ., PPPL-2242, August 1985.

- [51] HINTON, F.L.: "Neoclassical Transport Effects and the H-Mode Transition", Nucl. Fusion 25 (1985) 1457.
- [52] FURTH, H.P.: "Enhancement of Confinement in Tokamaks", Plasma Phys. Contr. Fusion 28, No.9A (1986) 1305.
- [53] OHYABU, N., LEE, J.E. and de GRASSIE, J.S.: "A Simple Model of Energy Confinement in Tokamaks", Nucl. Fusion 26 (1986) 593.
- [54] OHKAWA, T.: "Combined Confinement System Applied to Tokamaks", KAKUYUGO KENKYU 56, No. 4 (1986) 274.
- [55] BISHOP, C.M.: "Stability of Localized MHD Modes in Divertor Tokamaks - A Picture of the H-Mode", Nucl. Fusion 26 (1986) 1063.
- [56] GRUBER, O., BECKER, G., v. GIERKE, G., GRASSIE, K., KLUBER, O. et al.: "MHD Stability and Transport of Beam-Heated ASDEX Discharges in the Vicinity of the Beta Limit", in Plasma Physics and Controlled Nuclear Fusion Research (Proc. 11th Int. Conf. Kyoto, 1986), IAEA, Vienna, IAEA-CN-47/A-VI-2.
- [57] KRASHENINNIKOV, S.I., KUKUSHKIN, A.S. and POZHAROV, V.A.: "Edge Plasma Oscillation in H-Mode, A Feature or the Cause?", in Plasma Physics and Controlled Nuclear Fusion Research (Proc. 11th Int. Conf. Kyoto, 1986), IAEA, Vienna, IAEA-CN-47/E-III-3.
- [58] OHKAWA, T.: "Effects of the Location of the X-Point on Edge Confinement", in Plasma Physics and Controlled Nuclear Fusion Research (Proc. 11th Int. Conf. Kyoto, 1986), IAEA, Vienna, IAEA-CN-47/E-III-24, and KAKUYUGO KENKYU 56 (1986) 427.
- [59] HAHM, T.S. and DIAMOND, P.H.: "Resistive Fluid Turbulence in Divertor Tokamaks and the Edge Transport Barrier in H-Mode Plasmas", Phys. Fluids 30 (1987) 133.
- [60] OZEKI, T., SEKI, S., NINOMIYA, H. and AZUMI, M.: "Kink Instability of the Divertor Configuration in JT-60", JAERI-M 87-004, 1987.
- [61] SEKI, S. and AZUMI, M.: "Maximum  $\beta$  Limited by Ideal MHD Ballooning Instabilities in JT-60", JAERI-M 86-025, 1986.

Table A.1.1 Confinement scaling law

Ion	1	$\tau_{Ei} = C_{Ei} \cdot 4.7 \times 10^{18} \frac{B_0^2 \sqrt{T_i} a_p^2}{A^{1.5} n_i q_\psi^2}$	Neo-classical
Electron	1	$\tau_{Ee} = C_{Ee} \cdot 1.1 \times 10^{-20} n_e a_p^2$	Alcator
	2	$\tau_{Ee} = C_{Ee} \cdot 1.15 \times 10^{-21} n_e a_p^{0.8} R^{2.3}$	Neo-Alcator
	3	$\tau_{Ee} = \frac{(\tau_{Ee}^A \cdot \tau_e^B)}{(\tau_{Ee}^A)^2 + (\tau_e^B)^2}$ $\tau_{Ee}^A = C_{Ee} \cdot 1.03 \times 10^{-21} n_e a_p^{1.04} R_p^{2.0} R_p^4 q_\psi^{0.5}$ $\tau_e^B = C_{Ee} \cdot 3.68 \times 10^{-5} I_p P^{-0.5} R^{1.75} a_p^{-0.37} K^{0.5}$	Goldston (L-mode) $P_h$ : Heating power
	4	$\tau_{Ee} : 2 \times \text{Goldston (L-mode)}$	Goldston (H-mode)
	5	$\tau_{Ee} = C_{Ee} \cdot 9 \times 10^{-27} I_p^{-0.61} n_e^{1.33} T_e^{0.75} R_p^{0.82} Z_{eff}^{0.07}$	Gill (H-mode)
	6	$\tau_{Ee} = C_{Ee} \cdot 1.45 \times 10^{-7} a_p I_p$	JAERI
Global	1	$\tau_E = C_E \cdot 0.045 R a B_T K^{0.5} A^{0.5}$	Optimized

$$* Z_{eff} = (1 + f_Z \cdot Z^2) / (1 + f_Z \cdot Z)$$

$f_Z$ : ratio of the impurity ion density  $n_i$  to fuel ion density ( $= n_i / n_f$ )

Table A.1.1.2 Summary of experimental results concerning improved confinements

	ASDEX	JFT-2M	PDX/PBX	DM/DIII-D	JET	TFTR	JT-60
NBI	⊙ Ref. [6-15]	⊙ Ref. [18-21]	○ Ref. [23-27]	⊙ Ref. [28-36]	⊙ Ref. [38]	⊙*1 Ref. [40]	○*2 Ref. [41]
ICRF	○*3 Ref. [16]	⊙*4 Ref. [17]			○*5 Ref. [39]		
LHH							
ECH				⊙ Ref. [37]			
NBI + ICRF	⊙ Ref. [16]						○*6 Ref. [42]
NBI + ECH		⊙ Ref. [22]					
NBI + LHH							○*7 Ref. [43]

\* 1 Super shot (Peaked density) ; Limiter.

\* 2 Outside X point.

\* 3 Outside antenna ; Only one shot.

\* 4 Inside antenna ; Inside limiter H-Mode.

\* 5 Outside antenna ; Coupling problem.

\* 6 Ion high energy tail production.

\* 7 Current profile control ; H-mode like behavior.

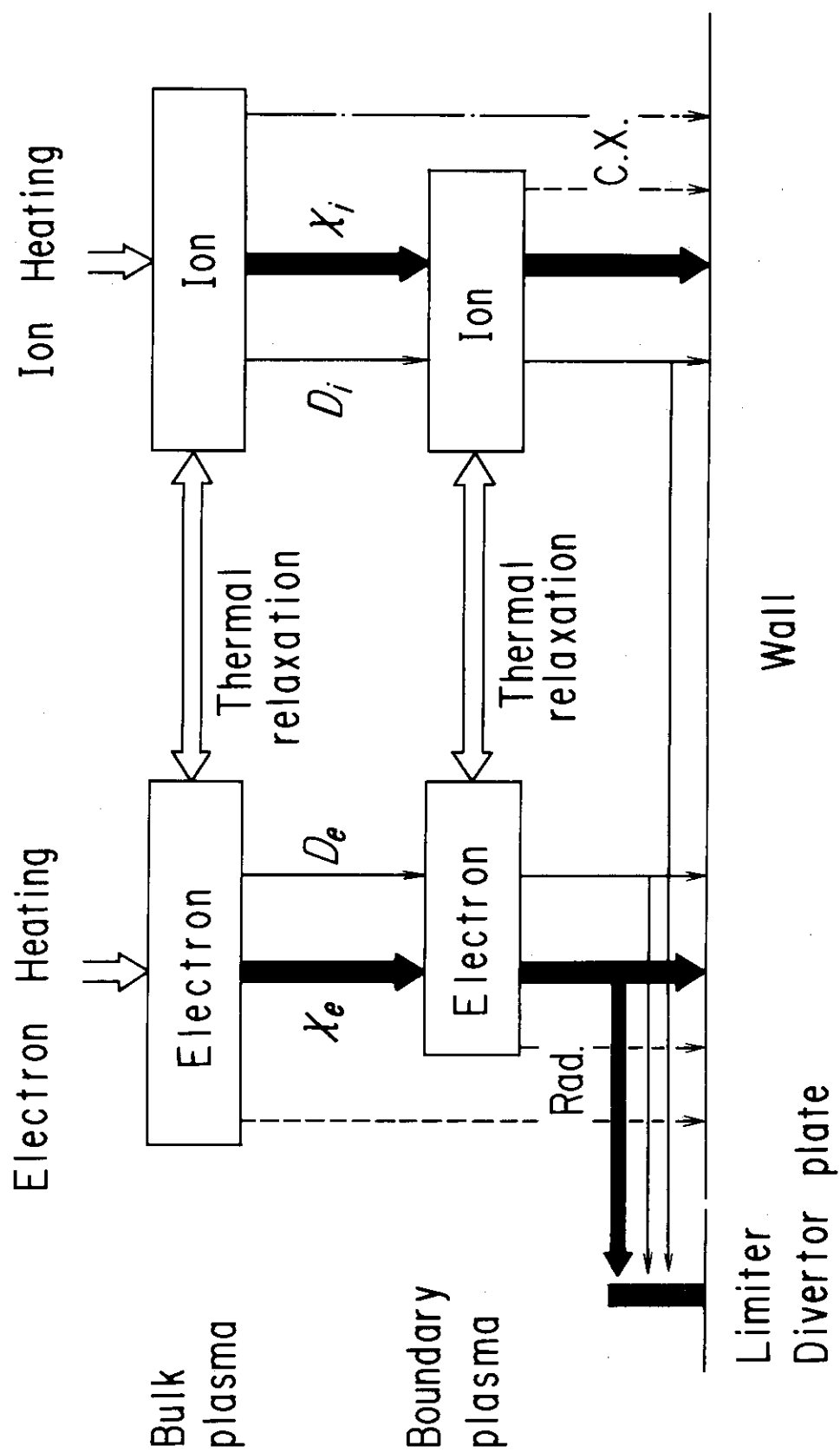


Fig. A.1.1 Energy flow pattern of tokamak discharge

## A. 2 Overall Efficiency of Heating and Current Drive Facilities

An engineering design guideline is provided for system capacity estimation on auxiliary heating and current drive systems. Two methods with neutral beam injection (NBI) and/or RF wave radiation are adopted in the next generation tokamak machines. There may be four candidates, that is, the negative ion-based NBI, and RF waves with a frequency range of the electron cyclotron (ECRF), lower hybrid (LHRF) and ion cyclotron (ICRF).

Table A2.1 summarizes typical values studied in the FER engineering design [1]. These systems are composed of four sections which are the drift duct or coupler, the neutralizer or transmission line, the ion beam or RF wave generator and individual power supplies.

The overall efficiency is described as

$$\eta = \eta_1 \cdot \eta_2 \cdot \eta_3 \cdot \eta_4$$

where  $\eta_j$  ( $j=1,2,3,4$ ) means the unit of efficiency for each section. Detailed descriptions of each  $\eta_j$  will be given in the following.

### 1) NBI (neutral beam injection)

A negative ion-based NBI system will be used for the next generation tokamak machines, due to the neutralization efficiency.

Deuterium ion beams with an energy of 500 keV has a neutralization efficiency of 0.58 ( $\eta_2$ ). There are many loss terms, for example, the re-ionization loss of neutralized beams in the drift duct, geometrical losses on the neutralizer and drift duct wall, and ion acceleration loss at the accelerating region. A design [2,3] shows each loss rate to be 0.05 to 0.1. The geometrical loss rate depends on the drift duct size, so it is preferable to assume it to be 0.15. The injection efficiency  $\eta_1$  is assumed to be  $0.95 \times 0.85$ . There is a loss of a few percent in power supplies. The overall efficiency may be expected to be more than 0.4 comparable to the ICRF system.

Positive ion beams have a poor neutralization efficiency and beams with the required energy of 200 keV for the next generation machines have an efficiency of 0.18. The overall efficiency may be around 0.1.

## 2) ECRF (electron cyclotron range of frequencies)

It is assumed that an oscillator with a unit size of 200 kW CW operating at about 150 GHz will be available and the waves are transferred through an oversized circular waveguide with mode converters, bends, windows and so on. The insertion loss due to these components may be about 3 dB. In such a system, the transmission efficiency  $\eta_2$  is estimated pessimistically to be 0.5. The oscillator may be a gyrotron and an efficiency of 0.2 to 0.45 is reported as the nominal value. So the available tube efficiency  $\eta_3$  may be expected to be 0.35. The output waves have many modes. A value of 0.1 is assumed as the mode impurity. There is a loss fraction of a few percent in the power supplies and a comparative loss in the coupling section should be considered. The overall efficiency may be around 0.15.

## 3) LHRF (lower hybrid range of frequencies)

The Lower hybrid wave launcher is designed, using a phase-controlled grill antenna fed by a waveguide array. The reflection rate depends on the plasma conditions, especially on the scrape-off plasma conditions. In the FER design, the reflection rate is in the range from 0.4 to 0.8.

In estimating the system capacity, the coupling efficiency  $\eta_1$  is assumed to be 0.6, taking into account the reflection rate and the spectrum of the refractive index in the plasma. Waves in this range of frequencies are transferred through a rectangular waveguide. In addition, other components are inserted. The insertion losses due to these components accumulates to about 1.7 dB and the transmission efficiency  $\eta_2$  may be expected to be 0.7. The RF wave conversion efficiency  $\eta_3$  in the case of the high power klystron is assumed to be 0.5 on the basis of a few nominal data. There still remains another loss of a few percent in power supplies. The overall efficiency may be around 0.2.

## 4) ICRF (ion cyclotron range of frequencies)

The frequency of the deuteron second harmonic (which from 70 to 90 MHz for the next generation tokamak machines) is chosen. The net

deposition power into the plasma depends on plasma parameters and antenna properties. In the case of  $2 \times 2$  loop array antenna, the transferable power fraction  $\eta_1$  is 0.8 to 0.9. In this estimation, it is assumed that waves with a velocity higher than that of light is ineffective.

Waves in this frequency range are transferred through the coaxial cable and such components as power combiners, tuners and so on. The accumulated insertion losses of these components are estimated to be about 0.6 dB and the transmission efficiency  $\eta_2$  may be expected to be 0.9. The RF wave conversion efficiency  $\eta_3$  in the case of the tetrode is assumed to be 0.65, because the nominal data of the candidates show a efficiency range from 0.45 to 0.7. In the estimation of the overall efficiency, the input power to the preamplifiers and the loss in power supplies should be considered. The efficiency  $\eta_4$  may be evaluated to be 0.85. The overall efficiency may be expected to be in the range of around 0.4.

#### References

- [1] SAITO, R., KOBAYASHI, T., YAMADA, M., MIKI, N., NAKASHIMA, K., et al.: "Main Engineering Features Driving Design Concept and Engineering Design Constraints -- Conceptual Design Study of FY86 FER --", JAERI-M 87-137.
- [2] SHIBATA, T., HORIIKE, H., MATSUDA, S., OHARA, Y., OKUMURA, Y. and TANAKA, S.: "Conceptual Design of a 500 keV, 20 MW Negative-Ion-Based Neutral Beam Injector for FER", Kakuyugo Kenkyu 56 (1986) 124 (in Japanese).
- [3] OHARA, Y., et al.: "Design of a 500 keV, 20 MW Negative-ion-based Neutral Beam Injection System for Fusion Experimental Reactor", 12th Symp. on Fusion Engrn., Monterey, Oct. 12-16 (1987) 10-07.

Table A.2.1 Overall efficiency of heating and current drive facilities in the FER

Energy source	Efficiency ( $\eta$ )	Injection or Coupling ( $\eta_1$ )	Neutralization or Transmission ( $\eta_2$ )	Ion beam or Wave generation ( $\eta_3$ )	Power supply or Auxiliary system ( $\eta_4$ )	Overall $\eta_1 \cdot \eta_2 \cdot \eta_3 \cdot \eta_4$	Out put level of an unit size
Particles	NBI (0.5 MeV negative ion - based beams with deflection)	0.95 (reionization) x 0.95 ~ 0.85 (geometrical)	0.58 (ideal)	0.95 (acceleration)	$\lesssim 1$	0.43	50 MW (ion beams)
	NBI (0.2 MeV positive ion - based)	0.95 (reionization) x 0.95 (geometrical)	0.18 (ideal)	0.95 (acceleration) x 0.9 (ion impurity)	$\lesssim 1$	0.13	20 MW (ion beams)
	ECRF bundle of waveguides with reflectors (140 GHz)	$\lesssim 1$ (assumed)	0.5 (assumed)	0.35 (gyrotron) x 0.9 (mode impurity)	$\lesssim 1$	0.15	0.2 MW (cw gyrotron)
Waves	LHRF grill of open waveguides (2 GHz)	0.35 ~ 0.8 (reflection and effective spectrum)	0.7 (assumed)	0.5 (klystron)	$\lesssim 1$	0.20 ( $\eta_1 = 0.6$ )	1 MW (cw klystron)
	ICRF loop type antenna with 2x2 arrays (70 MHz)	0.8 ~ 0.9 (reflection and effective spectrum)	0.9 (assumed)	0.65 (tetrode)	0.85 (include auxiliary power)	0.42 ( $\eta_1 = 0.85$ )	2 MW (cw tetrode)
Remarks (components)	Drift duct Antenna	Neutralizer Transmission line	Ion source Hard tube	DC power supply Preamplifier etc.			

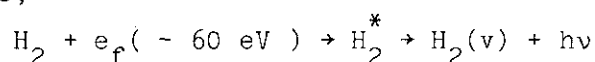
### A. 3 Present Status of Negative Ion Source Development

Here, a brief review on negative ion source development is provided. More detailed information is given in Ref.[1].

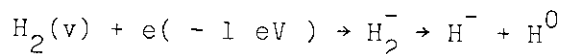
There are three main methods to produce high current negative hydrogen (deuterium) ion beams; i.e., the charge exchange method [2-4], surface production method [5-8] and volume production method [9-18]. In the charge exchange method, the negative ion beams are produced by double charge exchange of positive ion beams passing through an alkali-metal vapor cell. On the other hand, in the surface production method, plasma particles (positive ions and fast atoms) hitting a low work function cesiated surface capture electrons and reflect as negative ions. In the volume production, the negative ions are generated by a collisional process in gas discharge. Out of these methods, volume production is the most attractive for use in future neutral beam injectors. This is because, 1) the method needs no cesium, which offers 2) stable and reliable operation of the source. In addition, 3) the structure is simple to scale up and 4) good beam quality is produced. Owing to these advantages, current developmental efforts throughout the world are mainly concentrated on volume production.

Table A3.1 summarizes the typical parameters achieved in these three production methods. Although the beam current obtained in the volume production method is still lower than the maximum values obtained in the other two methods, significant progress has been made in the volume production method these years. Among them, high current density ( $\geq 20 \text{ mA/cm}^2$ )  $\text{H}^-$  ion beam extraction has been achieved in various types of volume ion sources, [9, 10, 15, 16]. Recently, a more than one ampere  $\text{H}^-$  ion beam has been produced at JAERI [18]. It is also found that the produced beam has good beam quality; the beam optics is extremely good and the impurity content in the beam is as low as one percent [18]. We consider that these recent results demonstrate the potential of the volume negative ion source for neutral beam application.

In the volume production method, the negative ions are formed through two-step processes. In the first step, vibrationally excited hydrogen molecules are produced by collisions between the molecules and fast electrons;



There are several other processes for the production of excited molecules. In the second step, negative ions are produced by the dissociative attachment of low energy electrons to the excited molecules;



Again, there are other processes for forming the negative ions, but the production rate is considered to be much smaller than the above mentioned process.

Figure A3.1 shows the one ampere volume  $\text{H}^-$  ion source developed at JAERI. The source consists of an ion generator and an accelerator column. The  $\text{H}^-$  ion generator is divided into two regions by a magnetic filter. In the first region, a dense plasma of  $10^{12} - 10^{13} \text{ cm}^{-3}$  is produced by arc discharge between hot tungsten filaments and a magnetic multicusp discharge chamber. The excited molecules are formed in this region. Although these excited molecules can diffuse to the second region, energetic electrons emitted from the filaments cannot go through the magnetic filter due to the transverse magnetic filter field. As a result, the electron temperature becomes to be in the order of 1 eV in the second region, where  $\text{H}^-$  ions are formed by dissociative attachment. The produced  $\text{H}^-$  ions are extracted and accelerated by a multi-aperture grid system in the accelerator column. This type of volume source, which is called "magnetically filtered multicusp source", has been developed at LBL [9], Culham [10], Ecole Polytechnique [11], FOM-Institute [12], Yamaguchi Univ [13] and also at TRIUMF [14] for accelerator application. Other types of volume source have been developed at ORNL [15] (reflex discharge), Nagoya Univ. [16] (plasma sheet) and Grenoble (ECR) [17].

It is necessary to develop a 500 keV/ 100 A  $\text{D}^-$  ion source for the negative-ion-grounded neutral beam injector for the FER. At JAERI, we are going to develop such a high intensity negative ion source according to the plan shown in Fig. A3.2. In the first step, basic research on the negative ion source was made in the ITS-2 test stand. And then, advanced research and scaling up of the negative ion source are now going on in the ITS-2M test stand. An advanced test stand (AITS) will be constructed for the development of a high energy and high current  $\text{D}^-$  ion source of 500 keV/ 25 A, which is 1/4 scale of the ion source for the FER.

## References

- [1] OKUMURA, Y.: "Development of High Intensity Negative Ion Source for Neutral Beam Injectors", in Proc. of 11th Symp. on Ion Source and Ion-Assisted Technology, Tokyo, June 1987, p. 2676
- [2] JACQUOT, C., LUDWIG, P., ROCCO, J. C. and ZADWORNÝ, F.: "Intense  $H^-$  Ion Source by Charge Exchange with Cesium", Proc. of the IAEA Technical Committee Meeting on Negative Ion Beam Heating, Grenoble, March 1985, p. 113.
- [3] HOOPER, E. B., POULSEN, P and PINCOSY, P.A.: Jour. Appl. Phys. 52 (1981) 7027.
- [4] KUZNETSOV, V.V., SEMASHKO, N.N., KRYLOV, A. I., ILUNIN, I. A. and FIRSOV, P. S.: Proc. of the IAEA Technical Committee Meeting on Negative Ion Beam Heating, Grenoble, March 1985, p110.
- [5] BEL'CHENKO, YU, I. and DIMOV, G. I.: "Pulsed Multiampere Source of Negative Hydrogen Ions", Proc. 3rd Symp. on Production and Neutlization of Negative Ions and Beams, Brookhaven, 1983, p.363
- [6] PRELEC, K.: "Report on the BNL  $H^-$  Ion Source Development", *ibid.*, p. 333.
- [7] KWAN, J.W., ACHERMAN, G. D., ANDERSON, O.A., CHAN, C.F., COOPER, W.S., et al.: "One-Ampere, 80-keV, Long-pulse  $H^-$  Source and Accelerator", Rev. Sci. Instrum. 57 (1986) 831.
- [8] DAMMERTZ, G. and PIOSZYK, B.: "Development Work on  $H^-$ -Ion Sources", Proc. 4th International Symp. on Heating in Toroidal Plasma, Rome, 1984, p. 1087.
- [9] KWAN, J, W., ANDERSON, O.A., CHAN, C.F., COOPER, E.S., LEUNG, K.N., et al.: "Volume Produced  $H^-$  Beam Experiment at LBL", 2nd IAEA Technical Committee Meeting on Negative Ion Beam Heating, Culham, July 1987.
- [10] HOLMES, A.J.T., DAMMERZ, G. and GREEN, T.S.: "The Design and Operation of a 30 keV Accelerator for Negative Ion Beams", Rev. Sci. Instrum. 57 (1986) 2402.
- [11] BACAL, M. and HILLON, F.: "Extraction of Volume-Produced  $H^-$  of Ions from a Hybrid Magnetic Multicusp Source", Rev. Sci. Instrum. 56 (1985) 2274.
- [12] BONNIE, J.H., EENSHUISSTRA, P.J. and HOPMAN, H.J.: "Measured Densities and Rotational Temperatures of Metastable  $H_2$  in a Multicusp Ion Source", Phys. Review Letters 57 (1986) 3265.

- [13] FUKUMASA, O. and SAEKI, S.: "Effect of Wall Material on Negative Ion Production in a Hydrogen Plasma", J. Phys. D: Appl. Phys. 20 (1987) 237
- [14] KENDALL, K.R., McDONALD, M., MOSSCROP, D.R., SCHMOR, P.W., YUAN, D., et al.: "Measurements on a DC Volume  $H^-$  Multicusp Ion Source for TRIUMF", Rev. Sci. Instrum. 57 (1986) 1277.
- [15] DAGENHART, W.K., TSAI, C.C., STIRLING, W.L., RYAN, P.M., SCHECHER, D.E., et al.: "Accelerated Beam Experiments with the ORNL Sitex and Vitex H-/D-Sources", 4th Int. Symp. on the Production and Neutralization of Negative Ions and Beams, Oct. 1986, BNL, (to appear in AIP Conf. Proc. 1987).
- [16] URAMOTO, J.: "Extraction of Volume Production  $H^-$  or  $D^-$  Ions from a Sheet Plasma I", Research Report of Institute of Plasma Physics, Nagoya University, IPPJ-645.
- [17] HELLBLOM, G. and JACQUOT, C.: "Extraction of Volume Produced  $H^-$  Ions from A Mirror Electron Cyclotron Resonance Source", Nuclear Instruments and Methods in Physics Research A243 (1986) 255.
- [18] OKUMURA, Y., HORIIKE, H., INOUE, T., KURASHIMA, T., MATSUDA, S., et al., "A High Current Volume  $H^-$  Ion Source with Multi-Aperture Extractor", Proc. 4th Int. Symp. on the Production and Neutralization of Negative Ion and Beams, Brookhaven, 1986.

Table A.3.1 Summary of typical parameters achieved in  
charge exchange method, surface production  
method and volume production method

Oct. 1987

Method	Laboratory	Current [A]	Beam energy [keV]	Pulse length [s]	Current density [mA/cm <sup>2</sup> ]	Reference
Charge exchange	Grenoble	0.35	21		22	[2]
	LBL	2.2	10.5	70	12	[3]
	Kurchatov	5.5	80	0.01	26	[4]
Surface production	Novosibirsk	11	25	$0.2-0.8 \times 10^{-3}$	180	[5]
	BNL	0.2-0.3	7.5	DC	40 - 100	[6]
	LBL	1.25	80	DC	10	[7]
	Karlsruhe	0.07	30	DC	53	[8]
Volume production	LBL	0.017	80	0.25	17	[9]
	Culham	0.13	83	30	30	[10]
	Ecole poly.	$0.1 \times 10^{-3}$	1	DC	0.3	[11]
	TRIUMF	$4 \times 10^{-3}$	25	DC	12	[14]
	ORNL	0.08	16.4	0.1	27	[15]
	Nagoya univ.	0.2	4.5	DC	28	[16]
	Grenoble				(20)	[17]
	JAERI	1.26	21	0.2	9.5	[18]

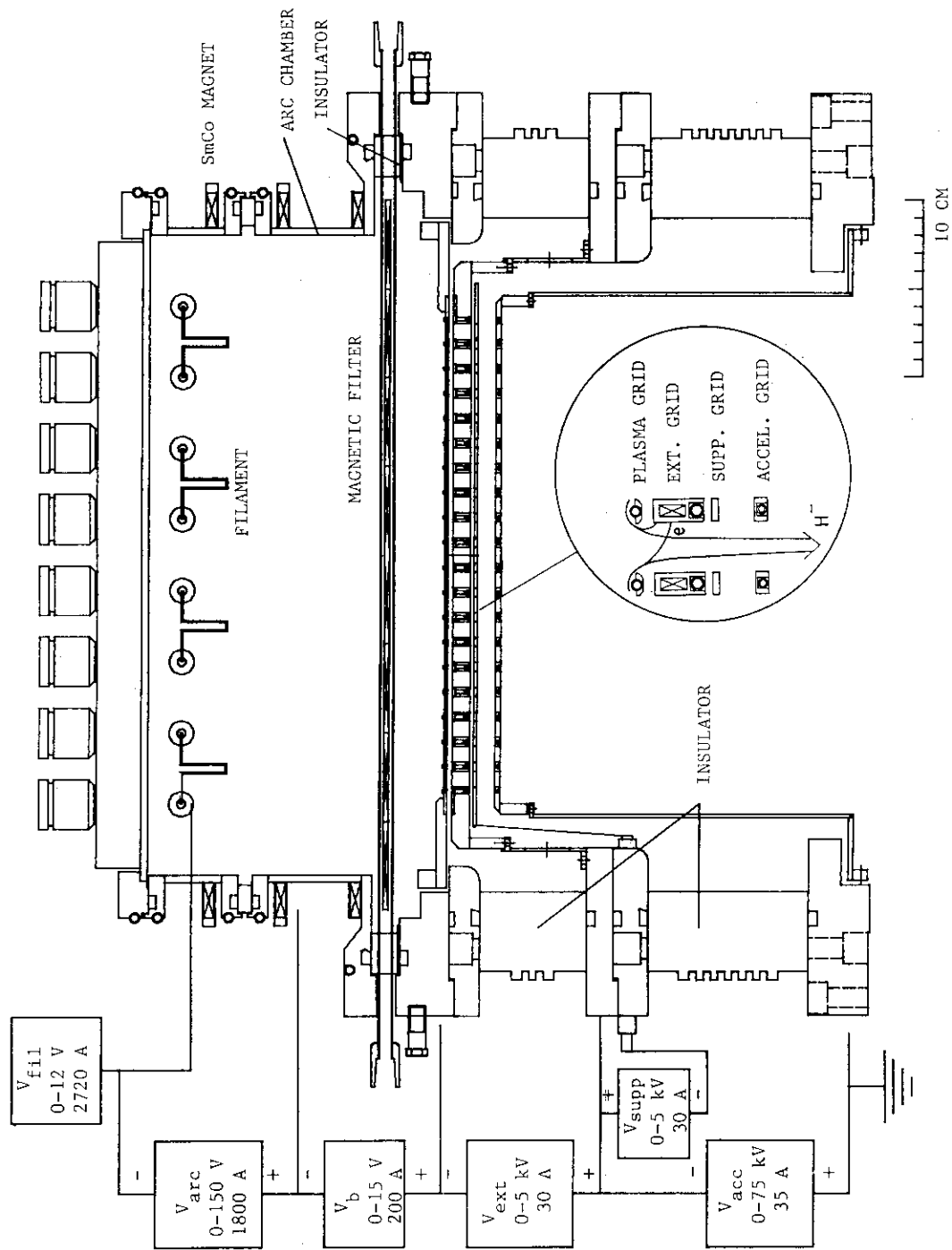


Fig. A.3.1 Cross sectional view of JAERI one-ampere volume  $H^-$  ion source and electrical connection of power supplies

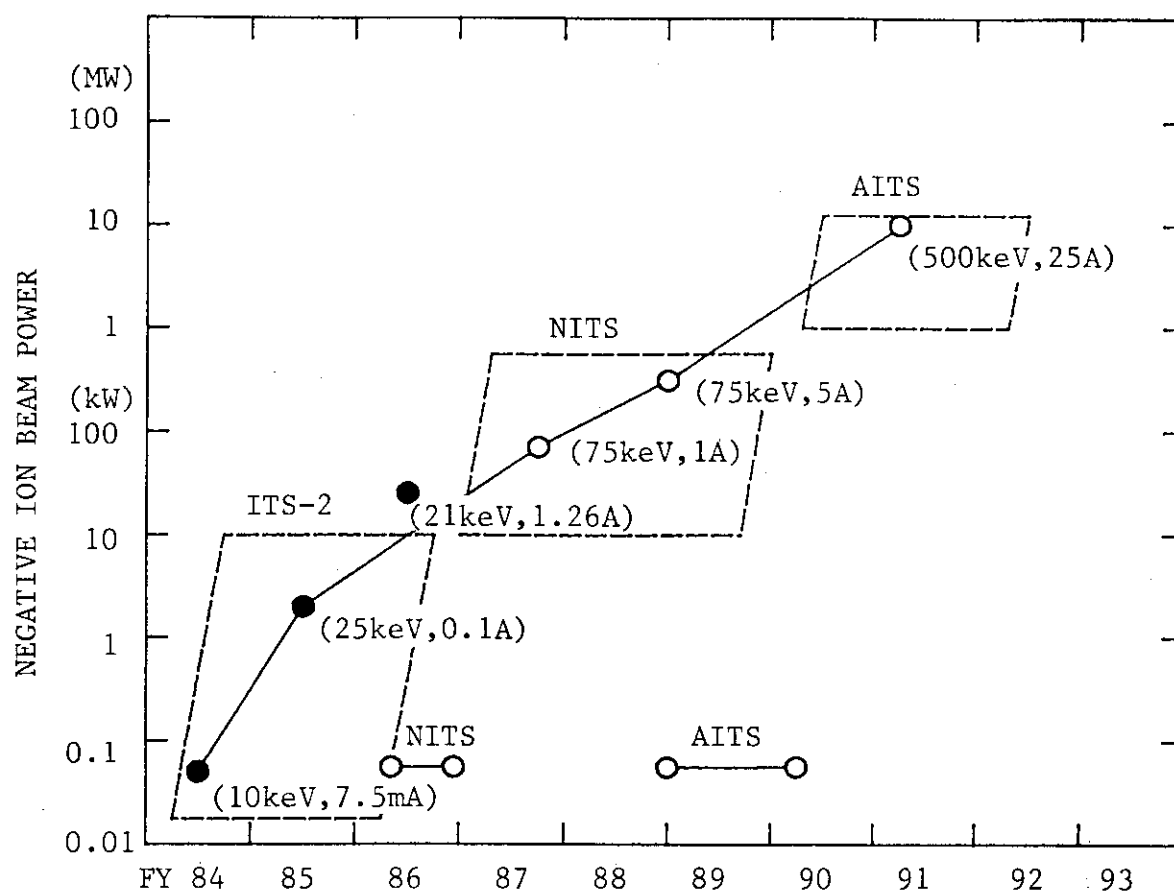


Fig. A.3.2 Long range plan for development of negative ion source at JAERI. This plan was set in 1984.

## A. 4 Beam Divergence in a Volume Negative Ion Source

Beam divergence is in general defined as the e-folding half width divergent angle of the beam profile. The divergence of a beam extracted from a plasma has a minimum value at the optimum perveance. The minimum divergence is determined by both the aberration of the electrostatic lens in the accelerator and the finite temperature of the plasma ions. Here, the minimum divergence  $\omega_{\min}$  is expressed as follows:

$$\omega_{\min}^2 = \omega_0^2 + \omega_T^2 \quad (1)$$

where  $\omega_0$  is the aberration-limited divergence and  $\omega_T$  is the temperature-limited divergence. When the ion temperature distribution function is Maxwellian,  $\omega_T$  is obtained by the following equation;

$$\omega_T = \frac{\sqrt{\pi}}{2} \cdot \sqrt{\frac{T_i}{E}} \quad (2)$$

where  $E$  and  $T_i$  are beam energy and ion temperature, respectively.

The minimum divergence of 3 mrad was obtained using a 200 keV, 3.5A helium ion source. Therefore, it will be possible to reduce the aberration-limited divergence below 3 mrad. On the other hand, we observed a beam divergence of 14 mrad for a 25 keV, 1.26A negative hydrogen beam. If we assume the aberration-limited divergence equals zero and the divergence 14 mrad is determined only by the ion temperature, the temperature is estimated to be 6.24 eV using Eq.(2). When the beam energy is increased up to 500 keV, the temperature-limited divergence decreases down to 3.53 mrad. Thus the minimum divergence calculated by Eq.(1) is expected to be 4.63 mrad at 500 keV. The design value of 5 mrad in the present design will be attainable from the viewpoint mentioned above.

## A. 5 Analytic Expression of Beam-Driven Ion Current

The fast ion current  $I_{fi}$  can be described by

$$I_{fi} = n_b \langle v_{\parallel} \rangle e Z_b = e Z_b \int_0^{\infty} v^3 dv \int_{-1}^{+1} f(v, \xi) \xi d\xi \quad (1)$$

where  $n_b$  is the beam density,  $v_{\parallel}$  the velocity component parallel to the magnetic field line,  $v$  the fast ion velocity,  $\xi = v_{\parallel}/v$  and  $f(v, \xi)$  the distribution function of fast ions in steady state. The distribution function  $f$  has been solved by J.D. Gaffey [1].

In general, variables of  $f$  can be separated as

$$f(v, \xi) = S \tau_s \sum_n a_n(v) \cdot c_n(\xi) \quad (2)$$

where  $S$  is the source of the NBI and  $\tau_s$  the Spitzer slowing down time [2]. In the velocity region  $v < v_b$ ,  $a_n(v)$  in Eq.(2) is simply given by

$$a_n(v) = \frac{1}{v^3 + v_c^3} \left( \frac{v^3}{v_b^3} - \frac{v_b^3 + v_c^3}{v^3 + v_b^3} \right) \frac{\beta}{3} \lambda_n$$

where  $v_c$  is the critical velocity, at which the drag exerted by the background electrons on the beam will equal that of the background ions,  $\beta = Z_{eff}/[Z]$ ,  $Z_{eff} = \sum_i n_i Z_i^2 / n_e$ ,  $[Z] = \frac{m_b}{\lambda n \Lambda_e \cdot n_e} \sum_j \frac{Z_i^2 \lambda n \Lambda_i}{m_j}$ ,  $m_b$  the beam particle mass and  $j$  denotes the  $j$ th species of bulk plasma ions. If fast ions are assumed to be stationary (no orbit effect),  $c_n(\xi)$  can be simply described by Legendre polynomial functions as

$$c_n(\eta) = \frac{n}{2} P_n(\xi_0) P_n(\xi) \quad (3)$$

where  $\xi_0$  is the initial pitch angle.

Three kinds of effects are taken into consideration in the new analytical model [3].

## 1) Velocity diffusion

Owing to collisions with faster moving electrons, some of the energetic ions will have velocities greater than the injection velocity

$v_b$ , and the energetic ion distribution will have a high energy tail rather than being sharply cut off at  $v = v_b$ .

The expression of the velocity diffusion term derived by J.D. Gaffey [1] is employed in the velocity region  $v > v_b$ , that is,

$$\alpha_n(v) = \frac{1}{v_b^3 + v_c^3} \exp [-g(v)] \quad (v > v_b) \quad (4)$$

where

$$g(v) = \frac{2(1 + v_c^3/v_b^3)}{T_e/E_b + T_i/E_b v_c^3/v_b^3}$$

## 2) Bounce average of $v_{//}$

The fast ion current can be calculated by integrating  $v_{//}$  with the weight of the distribution function over  $v$  and  $v_{//}$ . It must be noted that, in most of the old analytical treatments fast ions are assumed to be stationary at their birth point throughout the slowing down time. In a tokamak plasma, however, every particle makes its own particular bounce motion along a magnetic field line. Therefore, in order to calculate the fast ion current, we must integrate the bounce averaged  $v_{//}$ , that is,  $\langle v_{//} \rangle = H(v_{//}^*/v)$ , where  $v_{//}^*$  is the  $v_{//}$  defined in the midplane outer side of the turns.

The  $H$  function is shown in Fig. A5.1 by the dotted line. The solid line is the current weight function of an old analytical model.

## 3) Effect of particle trapping

Fast ions produced by a tangential co-injection of neutral beams undergo pitch angle scattering, and some of them diffuse into the banana trap region. On the way of diffusive motion crossing the banana-transit boundary, particles can easily get into the transit region of a negative pitch. This is because the transition probabilities of banana particles into co- and counter- transit particles are approximately 0.5:0.5. Therefore, the pitch angle scattering is effectively enhanced in the presence of a banana trapping region. J.G. Cordey has analyzed this effect [4].

The bounce averaged differential equation for  $c_n$  in Eq.(3) can be written as

$$\frac{1}{R(\eta, \eta_t)} \frac{d}{d\eta} \left[ (1-\eta^2) Q(\eta, \eta_t) \frac{dc_n}{d\eta} \right] + \lambda_n c_n = 0 \quad (5)$$

where

$$R(\eta, \eta_t) = \frac{2}{\pi} K \left[ \left( \frac{\eta_t}{h} \right)^2 \right] \eta,$$

$$Q(\eta, \eta_t) = \frac{2}{\pi} E \left[ \left( \frac{\eta_t}{h} \right)^2 \right],$$

$K$  : the complete elliptic integral of the first kind,

$E$  : the complete elliptic integral of the second kind,

and  $\eta_t$  is the pitch of a barely trapped particle. It must be noted that

$$\lim_{\eta \rightarrow \eta_t} R(\eta, \eta_t) = \infty$$

Assuming  $R \sim 1.0$  and  $Q \sim 1.0$ , Cordey solved the differential equation Eq.(5) and derived analytical eigenfunctions

$$c_n(\eta) = P_{v_n}(\eta) \quad (6)$$

where  $P_{v_n}(\eta)$  is the Legendre function and  $v_n$  is given by the boundary condition

$$P_{v_n}(\eta) = 0.$$

For a precise treatment of the distribution function of fast ions, the effect of a barely trapped particle, whose bounce time  $\tau_b = \infty$ , is taken into consideration. The eigenfunctions for  $R$  and  $Q$  with exact expressions in Eq.(5) are numerically derived by adopting a variational method. That is, we expand  $c_n$  in a series of

$$c_n(\eta) = \sum_m \alpha_{mn} (1-\eta)^{2m-1} \quad (7)$$

Then, eigenvalues  $\lambda_n$  are given as solutions of the following equation

$$|\alpha_{mn} + \lambda \beta_{mn}| = 0 \quad (8)$$

where

$$\begin{aligned}\alpha_{mn} &= \int_0^{1-\eta_t} [1-(\eta+\eta_t)^2] E(\kappa) (2m-1)(2m-2) \eta^{2m+2n-4} d\eta \\ &+ \int_0^{1-\eta_t} [-2(\eta+\eta_t)E(\kappa) - [1-(\eta+\eta_t)^2] \frac{dE(\kappa)}{d\kappa} \frac{2\eta_t}{(\eta+\eta_t)^3}] (2m-1) \eta^{2m+2n-3} d\eta \\ \beta_{mn} &= \int_0^{1-\eta_t} K(\kappa) (\eta+\eta_t) \eta^{2m+2n-2} d\eta \\ \kappa &= \frac{\eta_t^2}{(\eta+\eta_t)^2}\end{aligned}$$

With these eigenvalues  $\lambda_n$  and the boundary condition,

$$c_n(1) = \sum_m (1-\eta_t)^{2m-1} = 1.0 \quad ,$$

$\alpha_{mn}$  are easily obtained.

#### References

- [1] GAFFEY, J.D.: "Energetic Ion Distribution Resulting from Neutral Beam Injection Tokamaks", J. Plasma Phys. 16 (1976) 149.
- [2] SPITZER, J., The Physics of Fully Ionized Gases, P.128-129. Interscience.
- [3] TANI, K., SUZUKI, M., YAMAMOTO, S. and AZUMI, M.: "On the Analysis of Beam Driven Current in a Tokamak", JAERI- M 88-042.
- [4] CORDEY, J.G.: "Effects of Particle Trapping on the Slowing-Down Ions in a Toroidal Plasma", Nucl. Fusion 16 (1976) 499.

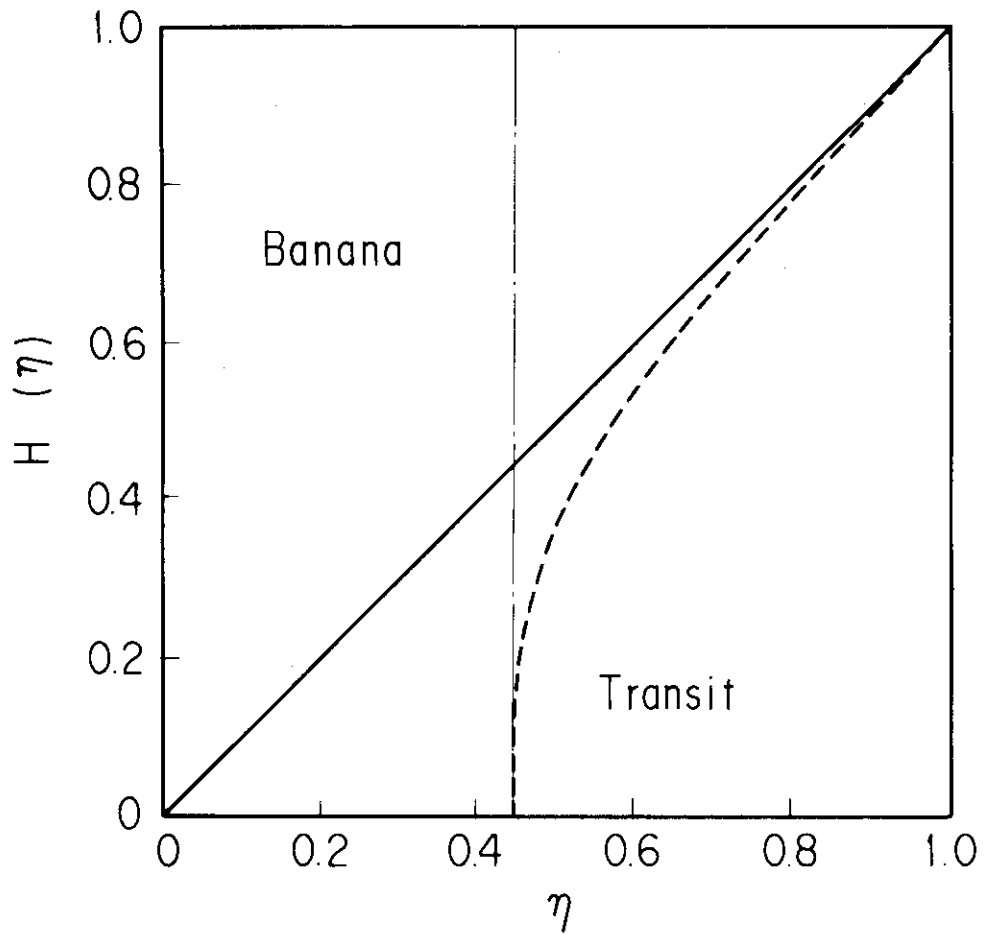


Fig. A.5.1 Dependence of H function defined by  $\langle v_{\parallel} \rangle = H(v_{\parallel}^*/v)$  on  $\eta = v_{\parallel}/v$ , where  $v_{\parallel}^*$  is defined in the midplane outer side of the torus. The solid line is the current weight function of an old analytical model.

## A. 6 Toroidal Equilibrium with Non-Inductive Current Drive

Let us consider an axisymmetric tokamak plasma with an orthogonal co-ordinate  $\Psi$ ,  $\chi$ , and  $\zeta$  (see Fig. A6.1a). The magnetic field and poloidal flux are given by

$$\vec{B} = F\nabla\zeta + \nabla\zeta \times \nabla\Psi/\pi \quad (1)$$

where  $F = RB_T$ ,  $\nabla\Psi = \hat{\Psi} / 2\pi RB_p$  and  $\nabla\zeta = \hat{\zeta}/R$  ( $\hat{\phantom{x}}$  indicates a unit vector).  $R$  is the distance from the symmetry axis, and  $B_T$  and  $B_p$  are, respectively, the toroidal ( $\zeta$ ) and poloidal ( $\chi$ ) field components. It is easily shown [1,2] that the equilibrium pressure and diamagnetism are function of only the poloidal flux, and that  $\Psi$  satisfies the Grad-Shafranov equation:

$$-(\mu_0 R^2 \frac{dP}{d\Psi} + F \frac{dF}{d\Psi}) = R^2 \nabla \cdot (\frac{\nabla\Psi}{R^2}) = -\mu_0 R j_T \quad (2)$$

The operator  $R^2 \nabla \cdot (R^{-2} \nabla \Psi)$  in a cylindrical co-ordinate is often written as  $\Delta^* \Psi$

$$\Delta^* \Psi = \frac{\partial^2 \Psi}{\partial R^2} - \frac{1}{R} \frac{\partial \Psi}{\partial R} + \frac{\partial^2 \Psi}{\partial Z^2} \quad (3)$$

The objective of our study is to find the function  $F(\Psi)$  which is generated by a non-inductively driven tokamak current, which, with the aid of Eq.(2), can be used to fully determine a two-dimensional equilibrium.

We begin by noting that, in equilibrium, the current density parrallel to the magnetic field is given by

$$j_{//} = \frac{-F}{B} \frac{dP}{d\Psi} - \frac{B}{\mu_0} \frac{dF}{d\Psi} \quad (4)$$

where the toroidal field  $B = |\vec{B}| = (B_T^2 + B_p^2)^{1/2}$ , and  $\mu_0$  is the free-space permeability. From this, we obtain:

$$\frac{1}{\mu_0} \frac{dF}{d\Psi} + \left[ \frac{1}{\langle B^2 \rangle} \frac{dP}{d\Psi} \right] F + \frac{\langle j_{//} B \rangle}{\langle B^2 \rangle} = 0 \quad (5)$$

where  $\langle \rangle$  denotes the flux surface average defined as

$$\langle x \rangle = \oint \frac{dr}{B_p} \frac{x}{B_p} / \oint \frac{dr}{B_p} \frac{x}{B_p} ;$$

$x$  denotes the poloidal direction.

The differential equation Eq.(5) provides a straight forward prescription for  $F$ , once  $\langle j_{\parallel} B \rangle$  is known. Notice, if Eq.(3) is substituted into Eq.(4), we find the following:

$$j_{\parallel} = \frac{dP}{d\psi} \left[ \frac{B}{\langle B^2 \rangle} - \frac{1}{B} \right] + \frac{B}{\langle B^2 \rangle} \langle j_{\parallel} B \rangle$$

The first term is the Pfirsch-Schlüter current. The  $\langle j_{\parallel} B \rangle$  includes inductive (Spitzer) as well as non-inductive current [3-5].

The origin of the Pfirsch-Schlüter current is simply described in Fig. A6.1b. In a simple torus without rotational transform (or without plasma current), ions and electrons drift in opposite directions along the  $Z$  axis. This drift is called toroidal drift. When the plasma current is induced and a rotational transform is created, the charge separation due to the toroidal drift is cancelled along the magnetic field lines. The induced current is the Pfirsch-Schlüter current. The direction of the current is opposite to that of the plasma current at the inside of the torus and the same at the outside of the torus, as shown in Fig. A6.1b. The surface average value becomes zero.

#### Reference

- [1] CALLEN, J.D. and DORY, R.A.: "Magnetohydrodynamic Equilibria in Sharply Curved Axisymmetric Devices", Phys. Fluids 15 (1972) 1523.
- [2] TOKUDA, S.: "Stability Analyses of Tokamak Plasmas by Computer Simulation", JAERI-M 84-040.
- [3] YAMAMOTO, S., OKANO, K., NISHIO, S., SUGIHARA, M., SAITO, R., et al.: "Tokamak Reactor Operation Scenario Based on Plasma Heating and Current Drive by Negative-Ion-Based Neutral Beam Injector", in Plasma Physics and Controlled Nuclear Fusion Research (Proc. 11th Int. Conf. Kyoto, 1986), IAEA, Vienna, IAEA-CN-47/H-I-3.
- [4] EAST, D. A.: "Toroidal Equilibrium with Low-Frequency Wave-Driven Current", Nucl. Fusion 25 (1985) 629.
- [5] EHST, D.A., EVANS, Jr. K., IGNAT, D.A.: "Tokamak MHD Equilibrium Generation by Narrow-Spectrum Fast-Wave Current Drive", Nucl. Fusion 26 (1986) 461.

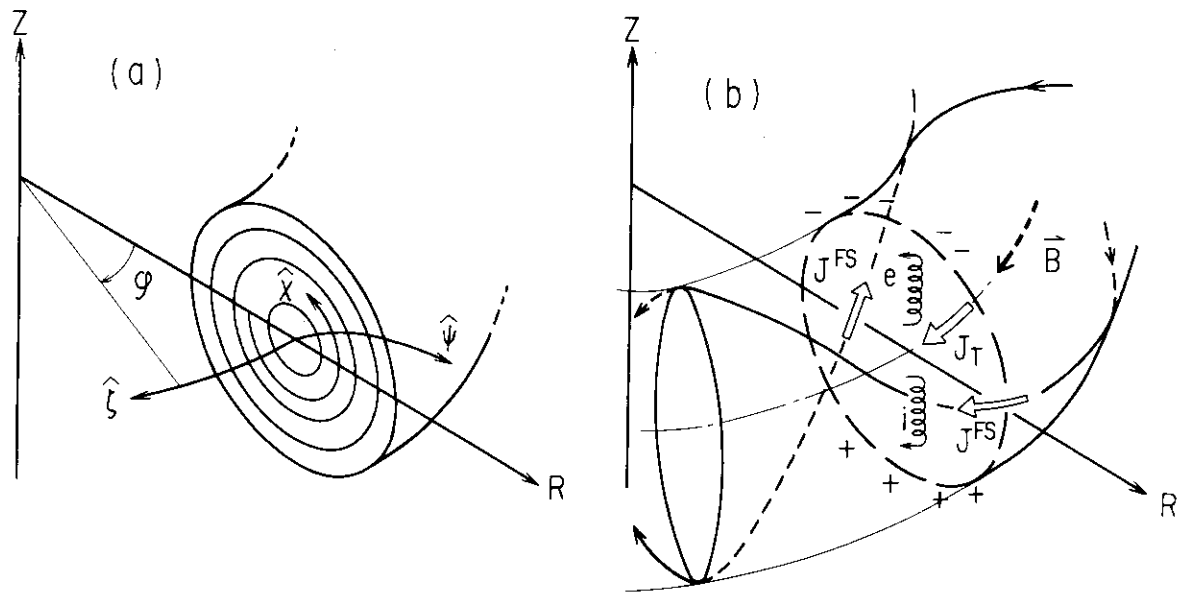


Fig. A.6.1 (a) Flux surface geometry. There is symmetry about the vertical axis. (b) Pfirsch-Schlüter current in a toroidal plasma.

## A. 7 High Heat Flux Components

Steady-state and high-heat flux beam stops will be required in the next generation injectors to handle multi-MW and multi-second particle beams. The peak heat flux densities normal to the beam axis amount to a few tens of  $\text{kW}/\text{cm}^2$ . It cannot be reduced below  $4\text{--}6 \text{ kW}/\text{cm}^2$  even if the surface of the beam stops are tilted. Various kinds of beam stops for high heat flux and/or steady-state heat removal have been investigated so far. A summary of recent findings is shown in Table A7.1. The values with and without parentheses indicate designed and measured values respectively.

There are two types of heat removal methods i.e., inertia cooling and forced cooling. The inertia type beam stops in Ref.[7] are used under the conditions of high heat flux but for short pulse length. They will be useful as the first wall in the tokamak vacuum vessel but cannot be used for steady-state heat removal.

Concerning the forced cooling method, there are two types of beam stop structures. One is a panel structure and another is a tube structure. The maximum heat flux on the surface of the panel structure seems to be limited to  $2 \text{ kW}/\text{cm}^2$  because of the low heat transfer coefficient. On the otherhand, the maximum heat flux which the tube structure can handle seems to be higher than  $4 \text{ kW}/\text{cm}^2$ . There are several types of tube structures depending on the cross section of the tube. In order to increase the equivalent heat transfer coefficient for forced convection, tubes with a swirl-tape or an internal helix fin are used. The beam stops based on the swirl tube have already achieved a removal of heat flux higher than  $5 \text{ kW}/\text{cm}^2$  with a pulse length of 30 sec [4]. The swirl tube and/or internally finned tube seems to be promising for beam stops required in the FER-NBI, though it is still necessary to investigate the reliability, manufacturing method and the life time of the tube.

References

- [1] HAANGE, R.: "Design of Calorimeter and Ion Dump for JET Neutral Injection Beam Line", Proc. 9th Symp. on Eng. Problems of Fusion Research, Chicago, p1352, 1982.
- [2] PATERSON, J.A., KOEHLER, G. and WELLS, R.P.: "The Design of Multi-Megawatt Actively Cooled Beam Dumps for the Neutral Beam Engineering Test Facility", Proc. 9th Symp. on Eng. Problems of Fusion Research, Chicago, p1666, 1982.
- [3] DAHLGREN, F.: "Steady-State Beam Dump for TFTR", Proc. 10th Symp. on Fusion Eng., Philadelphia, p1480, 1983.
- [4] COMBS, S.K., MILORA, S.L., BUSH, C.E., FOSTER, C.A., HASELTON, H.H., et al.: "Development of a High-Heat-Flux Target for Multimegawatt, Multisecond Neutral Beams at ORNL", *ibid.*, p526, 1983.
- [5] McFARLIN, D.J., BETZ, A.E., TOMPSON, C.C. and GOLDNER, A.: "Active Cooling System for the LLNL Mirror Fusion Source Test Facility", *ibid.*, p526, 1983.
- [6] AKIBA, M., ARAKI, M., DAIRAKU, M., HORIIKE, H., ITOH, T., et al.: "Beam Extraction at the Prototype Injector Unit for JT-60", *ibid.*, p2021, 1983.
- [7] ITO, T., HORIIKE, H., MATSUOKA, M., MATSUDA, S., OHARA, Y., et al.: "Development of Helium Beam Injection for JT-60 Active Beam Diagnostic System", JAERI-M 86-114.
- [8] ARAKI, M., et al.: "Conceptual Design of Beam Dumped for the FER-NBI", to be published.

Table A.7.1 Summary of heat flux components. The values with and without parentheses indicate design and measured values, respectively


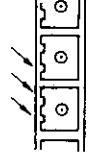


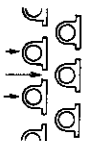
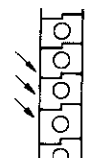

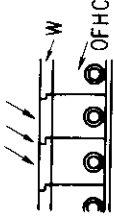
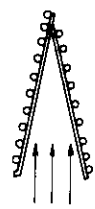

	HYPER-VAPOTRON <sup>(1)</sup> (JET)	Beam dump for <sup>(2)</sup> NBETF-NBI (LBL)	(DESIGN) Steady-state beam dump for TFTR-NBI (PPPL)	Beam target for <sup>(4)</sup> MEIF-NBI (ORNL)	Beam dump for <sup>(5)</sup> MFSTF-NBI (LLNL)	Rotating target
Max. heat flux (kW/cm <sup>2</sup> )	1.2 ~ 1.6 (1.0 ~ 2.0)	-1.6 (1.0)	1.0 ~ 2.0	-5.4 (3MW-30s)	-1.33 (8.0)	(20.0)
Material	1%Cr + Cu	0.2%Zr + Cu	Zr + OFHC or INCONEL	OFHC (tape: INCONEL)	Mo	
Size width height length	112 30 940(540)	215 — 200	OD: 19.1 t: 1.6 Int. finned tubes	OD: 9.5 t: 1.6 Swirl-tubes	OD: 5.0 t: 0.25 Int. finned tubes	
Cooling water	inlet	16.5	—	16.0	—	
	Press. outlet operat.	8.5 —	22.0	4.0 —	54.0	
Flow rate (l/min/tube)	166	220	29 (average) (max. 60)	20	5.4 (total: 2700)	
Press. drop (kg/cm <sup>2</sup> )	-0.5	-7.2	—	-11.0	—	
Pulse length (sec)	>10 (10)	30 (30)	>30	30 (30)	-0.4 (30)	
Life time (cycle)	(100000)	(> 25000)	—	30000 1000(LP)	(300000)	
Structure of surface	 V - shape	 V - shape	 Bowl - shape	 V - shape	V - shape	
Remarks	ION SOURCE 75keV, 10MW, D-BEAM (TOMSON CSF)	ION SOURCE 120keV, 50A, 30s, D (170keV, 65A, 30s) (MDAC)	ION SOURCE 120 keV, D-BEAM	ION SOURCE 75 keV, 40A, 30s (UNITED TECH.)	(UNITED TECH.)	

Table A.7.1 (Continued)

continue

	JT-60 NBI (JAERI)			Active diagnostics for JT-60 (JAERI) <sup>(7)</sup>		(DESIGN) <sup>(8)</sup> Beam dump for FER NBI (JAERI)
	Beam dump <sup>(6)</sup>	Water jacket	Calorimeter	Beam dump	Calorimeter	
Max. heat flux (kW/cm <sup>2</sup> )	0.5 (0.5)	0.4-0.5 (0.45)	-1.0 (1.0)	-7.5 (9.0)	3.7 (4.0)	(4.0) (17 MW)
Material	0.2%Ag + OFHC	0.2%Ag + OFHC	0.2%Ag + OFHC	W / OFHC	0.2%Ag + OFHC	0.2%Ag + OFHC (tape: INCONEL) ( or Ni )
Size width height length	OD: 14.0 Ext. finned tubes	16 x 16	30 36 30	49 50 49	140 260 20	OD: 10.0 Ext. finned swirl-tubes
	inlet	9.0	9.0	8.0	8.0	(20.0)
	outlet	5.0	5.0	-	-	-
	operat.	11.5	-	-	-	-
Cooling water	Flow rate (l/min/tube)	16.1 (average) (total: 1000)	9.3 (average) (total: 250)	4.5-11.0 (series)	1.6-2.0 (series)	(20.0-30.0)
	Press. drop (kg/cm <sup>2</sup> )	0.5-1.0	0.5-2.0	-	-	(10.0-15.0)
Pulse length (sec)	10 (10)	10 (10)	0.5-1.0 (0.5)	- 0.1 (0.1)	- 0.1 (0.1)	Continuous
Life time (cycle)	(10 <sup>6</sup> )	(10 <sup>6</sup> )	(10 <sup>6</sup> )			-
Structure of surface	 Bowl - shape	 Flat	 V - shape	 Flat	 V - shape	 Flat
Remarks	ION SOURCE 100 keV, 70A, 10s H-BEAM			ION SOURCE 200 keV, 35A, 0.1s He - BEAM		ION SOURCE 500 keV, 100A, Cont. D - BEAM